Technische Universität München European Southern Observatory

Near Infrared and bolometric properties of Type Ia supernovae

Suhail Dhawan

Vollständiger Abdruck der von der Fakultät für Physik der Technischen Universität München zur Erlangung des akademischen Grades eines

Doktors der Naturwissenschaften (Dr. rer. nat.)

genehmigten Dissertation.

Vorsitzender:		Univ.-Prof. Dr. Alejandro Ibarra
Prüfer der Dissertation:	1.	Hon.-Prof. Dr. Wolfgang Hillebrandt
	2.	Univ.-Prof. Dr. Stephan Paul

Die Dissertation wurde am 01.09.2016 bei der Technischen Universität München eingereicht und durch die Fakultät für Physik am 26.01.2017 angenommen.

To Nanima, the shining light, the guiding star, the transcender of cliches

Contents

1. Introduction **9**
1.1. A Brief Overview of Type Ia supernovae 11
1.1.1. Supernova Classification 11
1.1.2. Supernova Searches 12
1.1.3. Light curves and Spectra 14
1.1.4. Progenitor Scenario 18
1.1.5. Explosion Models 22
1.1.6. Peculiar Type Ia supernovae 25
1.2. Cosmology with Type Ia supernovae 26
1.2.1. Friedman-Lemaitre-Robertson-Walker Cosmology 26
1.2.2. Luminosity Distance and the matter-energy content of the universe 29
1.2.3. Luminosity Distance and the accelerating universe 31
1.2.4. Measuring the equation-of-state parameter of dark energy 34
1.3. Current Status and Recent Developments in Supernova cosmology 36
1.3.1. Sources of Systematic Uncertainties 37
1.3.2. Expanding the Wavelength Window 39
1.4. Organisation of the thesis 40

2. Near Infrared Light Curves of Type Ia supernovae: Studying the properties of the Secondary Maximum **43**
2.1. Introduction 43
2.2. Data 46
2.3. NIR Light Curve Morphology 47
2.3.1. Light curve fitting 47
2.3.2. The first maximum 50
2.3.3. The minimum 51
2.3.4. The second maximum 53
2.3.5. The late decline 53

2.3.6. NIR colours 53
2.4. Correlations 55
2.4.1. NIR light curve properties 58
2.4.2. Correlations with optical light curve shape parameters . 59
2.5. Discussion 62
2.5.1. A possible physical picture 64
2.5.2. Improved Distance Measurements? 68
2.6. Conclusions 68

3. A reddening-free method to estimate the ^{56}Ni mass of Type Ia supernovae 73
3.1. Introduction 73
3.2. Data 74
3.3. Results 76
3.3.1. Correlation between L_{max} and t_2 76
3.3.2. Deriving $M_{^{56}Ni}$ from L_{max} 79
3.3.3. Comparison of different methods 81
3.4. Test with well observed SNe Ia 84
3.5. The luminosity function of SNe Ia at maximum 88
3.6. Discussion and Conclusion 90

4. Near Infrared and bolometric properties of fast-declining SN Ia indicate sub-Chandra explosions 95
4.1. Data 97
4.2. Results 98
4.2.1. NIR light curve morphology near maximum 98
4.2.2. Late phase properties 103
4.2.3. ^{56}Ni and Ejecta mass 104
4.3. Discussion 109
4.3.1. NIR properties 109
4.3.2. Bolometric properties and ^{56}Ni mass 111
4.3.3. Ejecta mass 111
4.4. Conclusion 113

5. Nebular Phase Observations of Type Ia supernovae 117
5.1. Introduction 117

5.2. Near Infrared Spectroscopy in the Nebular Phase 119
5.2.1. Observations and data reduction 119
5.2.2. Analysis 120
5.2.3. Discussion 126
5.3. Conclusions and Current Work 128

6. Ejecta Masses of Type Ia supernovae 133
6.1. Introduction 133
6.2. Measurement of ejecta masses 134
6.3. Results 138
6.3.1. Host Galaxy Properties 142
6.4. Discussion 142
6.5. Conclusion 148

7. Forecasts of cosmological constraints with future observatories in the rest-frame Near Infrared 151
7.1. Introduction 151
7.2. Euclid Deep Drilling Fields 152
7.3. Creating Mock SN Ia data 154
7.3.1. Redshift Distribution 154
7.3.2. Creating the Mean Curve 156
7.4. Advantages of Sparse Sampling in the NIR 157
7.4.1. Precision on t_{max}(B) 159
7.5. Constraints on Cosmology 161
7.5.1. Variable w 164
7.5.2. Comparison with the Optical 165
7.5.3. Combined Constraints with Complementary Probes . . . 167
7.5.4. Impact of Deep Drilling Fields Cadence 172
7.6. $z>1$ constraints with James Webb Space Telescope 172
7.6.1. Constraints on cosmology 175
7.7. Discussion 181
7.7.1. Impact of K-correction errors on cosmology 182
7.7.2. Further extension of the high-z arm 187
7.7.3. Fitting for the intrinsic scatter 189
7.8. Conclusion 191

8. Conclusions and Future Outlook 193

Bibliography **199**

A. Nested Sampling for Cosmological Parameter Estimation **247**
A.1. Nested Sampling Algorithm 248
A.1.1. Stopping Condition 249

Abstract

Type Ia supernovae (SN Ia) are excellent distance indicators for cosmology. Their intrinsic luminsoities in the optical are found to vary systematically with the light-curve widths, providing an empirical calibration for precise distance measurements. Using this calibration, called the width-luminosity relation (WLR) led to the unexpected discovery of the current accelerated rate of cosmic expansion. Despite observations of large samples of SN Ia there are several fundamental physical properties that are still poor understood, for e.g. the progenitor system, progenitor mass, explosion mechanism.

In this thesis, I analyse the near infrared (NIR) and bolometric properties of SN Ia in order to understand their physical properties and to use them better as distance indicators in cosmology. I confirm their uniform behaviour near maximum light in the NIR and find that there is significant diversity in the NIR light curves at late phases. I find that there is a strong correlation between the timing of the second maximum in the NIR and the light curve width indicating that the diversity in the NIR is tied to the total amount of ^{56}Ni produced. I then use this measurement to derive the ^{56}Ni masses independent of the reddening from the host galaxy dust. I also analyse the NIR and bolometric behaviour of fast-declining SN Ia and find that their ejecta masses are significantly sub-Chandrasekhar and that there is possible evidence for two different sub-classes of fast-declining SN Ia.

I also present NIR spectra of the nearby SN 2014J at $\sim$ 400 days after maximum light. For the first time, I present estimates of the reddening from the host galaxy dust using spectra at such late phases. The NIR spectra prefer reddening properties that are similar to the Milky Way, whereas, maximum light colours suggest a steeper reddening law. This is further evidence that the dust in the environment of SN 2014J is atypical. Since the reddening from host galaxy dust is one of the dominant systematics for their use as distance indicators in cosmology, understanding the dust properties of their hosts is crucial to improving the constraints on cosmology.

A few weeks after maximum light, the NIR contributes significantly to the bolometric light curve. I construct bolometric light curves using observations from the u to H bands to account for the contribution of the NIR. Using these

bolometric light curves, I estimate the total ejecta mass for a sample of SN Ia, providing constraints on the possible progenitor channels that can explain the observed diversity of SN Ia.

Finally, I explore the use of future observatories (e.g. Euclid, James Webb Space Telescope) to measure distances to SN Ia in the *restframe* Near Infrared and find that sparsely-sampled NIR light curves, combined with prior information from the optical, provide precise constraints on the time-varying equation of state of dark energy. These constraints on the time-variability of dark energy

1. Introduction

Supernovae have revolutionised our understanding of the universe. The observation of a supernova in the constellation Cassopeia by Danish Astronomer Tycho Brahe in the year 1573 questioned the Aristotlean and Ptolemaic world systems. The Aristotlean viewpoint stated that all changes in the heavens must be within the lunar sphere, while the distant sphere containing all the fixed stars was immutable. The lack of parallax of this "new star", SN 1572 showed that the new star couldn't be part of the planetary sphere and had to be in the sphere of the fixed stars. Similarly, Kepler's supernova (SN 1604) showed a lack of parallax.

In 1885, Ernst Hartwig discovered a 'nova' in the Andromeda nebula. Knut Lundmark in 1925 [188] tried to separate a subclass of novae, which would be extremely bright, given extragalactic distances. The more luminous ones were at first called *upper-class* novae, which were much rarer, and about 10 magnitudes brighter than regular novae. These luminous novae were later termed "super-novae" in before Baade and Zwicky [12] described them as a separate class of objects.

Supernovae are amongst the most energetic stellar explosions in the universe. Supernovae that result from the thermonuclear disruption of a White Dwarf (Type Ia supernovae or "SN Ia" for short; see section 1.1.1 for the classification of supernovae) have typical energies of $\sim 10^{51}$ erg. Their large luminosities (4 -5 $\times$ 10^9 $L_\odot$, where $L_\odot$ denotes the luminosity of the sun; see Fig 1.1) results from photons generated in the decay chain of ^{56}Ni synthesised in the explosion. SN Ia have become an exceptional tool in modern astronomy. The recognition that the light curves of SN Ia can be used to calibrate their apparent peak luminosity, combined with the high peak brightness, prompted their use as distance indicators in cosmology. SN Ia have, hence, been instrumental in the discovery of the accelerated expansion of the universe [234, 251]. Along with

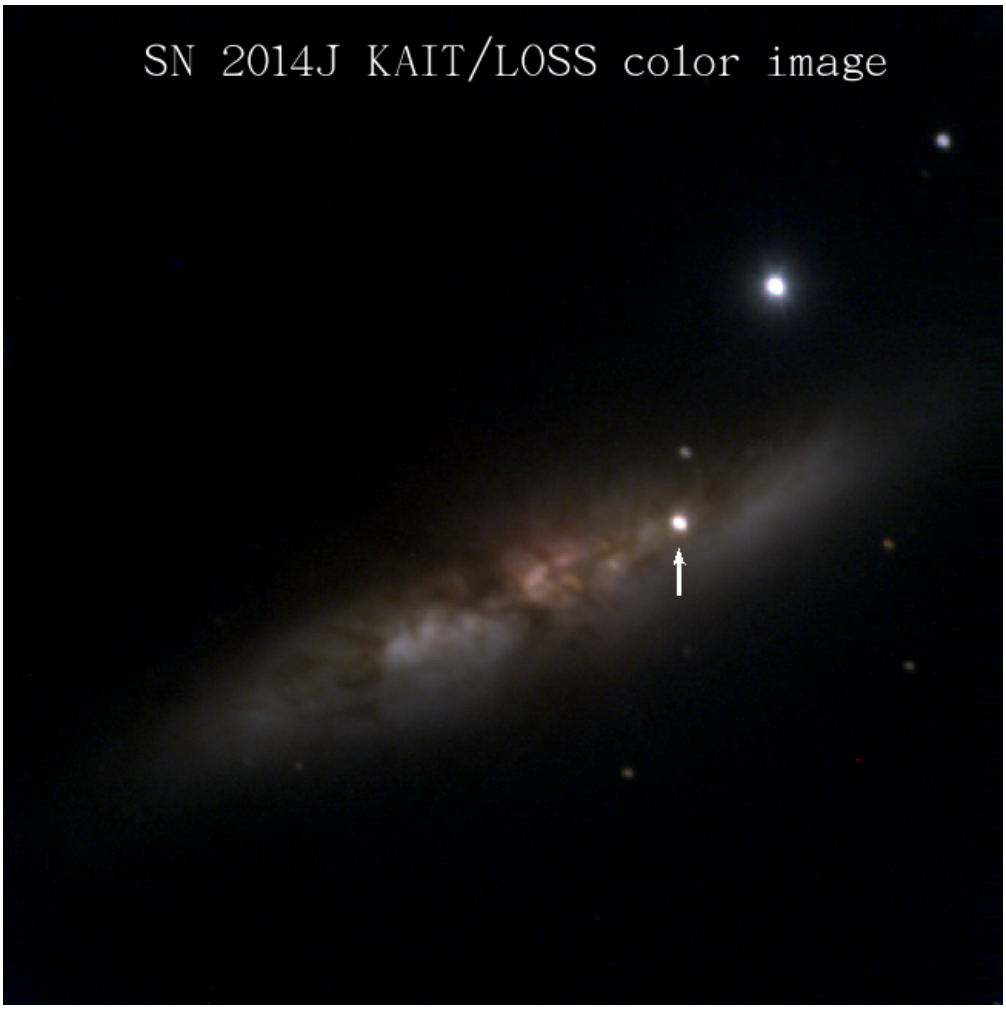

Figure 1.1.: SN 2014J, the nearest Type Ia supernova in over 40 years in M82. Credits: Lick Observatory Supernova Search.

their excellent use in cosmology, SN Ia are interesting as contributors to the chemical enrichment of galaxies and the synthesis of heavy elements in the universe and are important as endpoints of stellar/binary evolution scenarios.

In this Chapter we present a brief overview of Type Ia supernovae and their use in estimating cosmological parameters.

1.1. A Brief Overview of Type Ia supernovae

1.1.1. Supernova Classification

Supernovae were first classified as Type I (or SN I) and Type II (or SN II) by Minkowski in 1941 [209] on the basis of the absence or presence of hydrogen Calmer lines in the optical spectra. SN I were further divided into sub-classes based on the presence (Type Ia) or absence (Type Ib or Ic) of a deep absorption trough near 6150 Å, found to be due to the Si II $\lambda\lambda$ 6347,6371 doublet (see Wheeler & Harkness 1990 for details [319]). Although Type Ib and Type Ic supernovae are distinguish based on the presence or absence of He I in their spectra, respectively, whether they are physically distinct explosions is still heatedly debated (for e.g. because the nebular spectra of Type Ib and Ic supernovae look similar) and hence, some authors combine the classification as Type "Ib/c".

Type I supernovae have also been sub-classified into Type Ia and Ib/c by [70] based on Near Infrared light curves of a total of 13 SNe in 12 galaxies. This study also was the first to suggest the use of SN Ia in the NIR as distance indicators to the uniformity of the J and H band magnitudes at $\sim$ 2 weeks after maximum light.

Although all "Type I" supernovae (Ia/Ib/Ic) are defined by the absence of Hydrogen in their spectra, SN Ia arise from thermonuclear explosions whereas all other types of supernovae (Type Ib/c as well as Type II) arise from core-collapse in a massive star (see Fig. 1.2). There is significant diversity within the class of SN Ia explosions and various progenitor scenarios and explosion mechanisms have been proposed to explain the observed diversity (see Sections 1.1.4 and 1.1.5 for a summary). Several sub-classes of SN Ia are seen to deviate from the normal spectroscopic and photometric behaviour (properties of normal SN Ia are summarised in Section 1.1.3). We briefly discuss these subclasses in section 1.1.6.

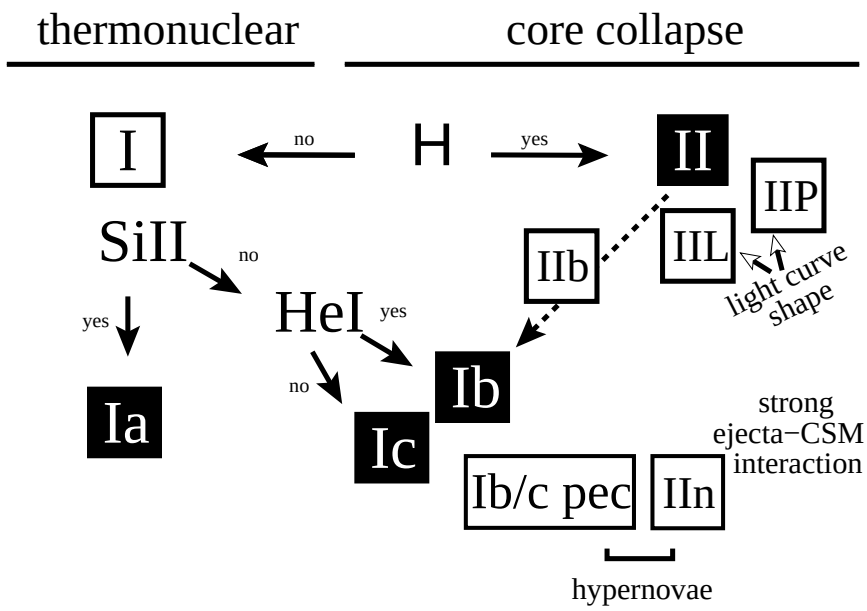

Figure 1.2.: Current classification scheme of supernovae, based on their early-time optical spectra. From a physical standpoint, Type Ia supernovae are thermonuclear disruptions of electron degenerate matter, whilst all other types result from the collapse of the core of a massive star. See text for a historical overview of the classification scheme. Credits [308]

1.1.2. Supernova Searches

The advent of charge coupled device (CCD) cameras, allowing pixel based image subtractions, has dramatically increased the number of supernovae discovered. Until 1996, $\sim$ 1000 SNe were discovered, while in 2015 alone, there were more than 1400 SN discoveries reported.

Searches for Type Ia supernovae can be segregated based on the redshift range they are targeting. A short summary of the recently concluded and ongoing supernova searches is presented here.

Low-redshift (z <0.1) Typically characterised by a redshift range of z <0.1, these searches often provide densely sampled light curves in multiple optical (and in some cases Near Infrared) light curves as well as detailed spectral time series for the SNe discovered. The low-z SNe are crucial to anchor the distance measurements to higher-z SN Ia in order to constrain cosmology. The Calan-Tololo SN survey was the first systematic search for low-z SN Ia by Hamuy et al. [112–114] Other low-z SN surveys include, the Lick Observatory Supernova Search (LOSS, [77]), CfA Supernova Survey [119], Carnegie Supernova Project (CSP) I and II, the Palomar Transient Factory (PTF, [250]) and its successor the intermediate Palomar Transient Factory (iPTF). One of the key factors influencing the precision of cosmological constraints from SN Ia is the cross-calibration between the low- and high-z SN Ia samples.

Intermediate-redshift (0.1 <z <0.4) The Sloan Digital Sky Survey (SDSS) supernova survey [93] found SN ia in the range 0.04 <z <0.42 [154], dramatically increasing the sample size in the redshift range 0.1 <z <0.3. The SDSS-II SN survey observed 103 SN Ia in *gri* filters, with an average of 48 measurements.

High-redshift (0.4 <z <1.0) The High-z Supernova Search team and the Supernova Cosmology Project presented the first evidence for an accelerated expansion with SN Ia out to z $\sim$ 0.6 - 0.8. There have been several follow-up high redshift supernova surveys, to confirm the findings and for precise constraints on the equation of state of dark energy (w). Some examples of these high-z searches are the ESSENCE survey [208, 325], the Supernova Legacy Survey (SNLS; [9, 50, 290])

The Carnegie Supernova Project conducted a high-redshift SN survey [89] in the *rest frame* i-band (observer frame Y and J bands) with PANIC on the Magellan telescopes. Before the CSP high-z survey, there had been a few individual supernovae at high-z observed in the rest-frame i-band by Riess et al. [253] and Nobili et al. [214]

The Dark Energy Survey (Bernstein et al. present simulations and strategies for the survey in [20]) has an ongoing supernova search to discover and follow-up $\sim$ 4000 SN Ia. Since it is unfeasible to obtain spectra for each SN to classify

them, only a subset of SNe will be spectroscopically classified, and the rest of the SNe will be classified using multi-band colour.

Very High-redshift (z >1) At high redshifts, the rest frame optical bands shift into the Near Infrared. Due to the high sky brightness in the NIR and contamination from atmospheric absorption features, NIR observations are best carried out from space-based observatories. Hence, nearly all very high-z SN searches have been carried out with the *Hubble Space Telescope (HST)* [58,257,258]. Cosmological constraints with z >1 discovered by the High-z SN search team were presented by Tonry et al. [303]. More recently, Rodney et al. [260] report the discovery of two SN Ia at redshift ~ 2 with the Wide Field Camera (WFC) aboard HST.

Future transient surveys, e.g. the Large Synoptic Survey Telescope (LSST) are designed to observe sizeable samples of SN Ia at redshifts z>1. in the optical Moreover, future space-based Infrared telescopes (e.g. Euclid, Wide-Field Infrared Space Telescope, James Webb Space Telescope) will present a unique opportunity to observe SN Ia at redshifts significantly greater than 1 and at longer rest frame wavelengths, making it an exciting era for precision cosmology constraints from SN Ia.

1.1.3. Light curves and Spectra

Light Curves

Light curves of SN Ia are an important tool to constrain the explosion energetics. They are characterised by a rise to maximum lasting $\sim$ 16 - 20 days [51,81,117,252]. The post-maximum decline is comparatively slower with the light curves settling onto an exponential decline at ~ 50 d after maximum light [53, 174].

Even at early times there exists a significant diversity in the light curve properties of SN Ia. Spectroscopically normal SN Ia reach absolute peak magnitudes in the B-band of $\sim$ -19.1 and obey the width-luminosity relation (WLR) that brighter supernovae also have broader light curves [237, 241] updated in [84]. The width of the light curves is characterised by the difference in magnitude

between peak and 15 d post-peak in the B-band ($\Delta m_{15}(B)$). Typical values of $\Delta m_{15}(B)$ range between 0.9 and 1.6 although spectroscopically peculiar SN Ia can have broader ($\Delta m_{15}(B)$<0.9) or narrower ($\Delta m_{15}(B)$>1.6) light curves. Details of the photometric properties of these subclasses of SN Ia are discussed in Section 1.1.6.

Near Infrared (NIR) light curves of SN Ia peak before t_{max}(B) (for e.g. see [84,151]). This is an effect of wavelength dependent ejecta opacity. The $YJHK$ bands also show a distinct secondary peak from 2 weeks to about a month after t_{max}(B) [70,84]. A similar behaviour is seen in the i band . The V and r bands show only a weak shoulder.

The optical $(B-V)$ colours evolves from blue around maximum light to red thereafter (from $\sim$ 0.1 before maximum light to $\sim$ 1.1 about 30 d after). The $B-V$ colour curves settle on a uniform decline at $\sim$ +35 d after maximum [183, 241], which is similar for different SN Ia. A recent study by Forster et al. [87], however, have shown deviations in the estimate of this late-time slope which they interpret as evidence for the presence of circumstellar material. Overall, the light curves of spectroscopically normal SN Ia, after correction for the light curve width, appear very homogenous.

Spectra

As described in Section 1.1.1, SN Ia spectra show absence of hydrogen and helium and the presence of a strong absorption line at $\sim$ 6150 Ådue to the Si II doublet $\lambda\lambda$ 6347,6371 at maximum light. A large fraction ($\sim$ 70% [181]) of the observed events show remarkably similar spectra at maximum light and almost identical spectral evolution as the example shown in Figure 1.3. These are so-called spectroscopically normal SN Ia. Prominent well-observed examples of this sub-class are SN 1994D, SN 2001el, SN 2005cf, SN 2011fe. Apart from the Si II doublet at $\sim$ 6150 Å, maximum light spectra of SN Ia show several other lines of intermediate-mass elements e.g. the H& K lines and the NIR triplet of Ca II at $\lambda\lambda$3934,3968 and $\lambda\lambda$8498,8542,8662, respectively. There are also prominent features of Mg II ($\lambda\lambda$4481), O I ($\lambda\lambda$7772,7774,7775) and S II ($\lambda\lambda$5468,5612,5654). In the NIR as well, the spectra are dominated at maximum light by features of Mg II, Si II and Ca II (a time series of NiR spectra from 14 days before to 75 days after t_{max}(B) is shown in Figure 1.4).

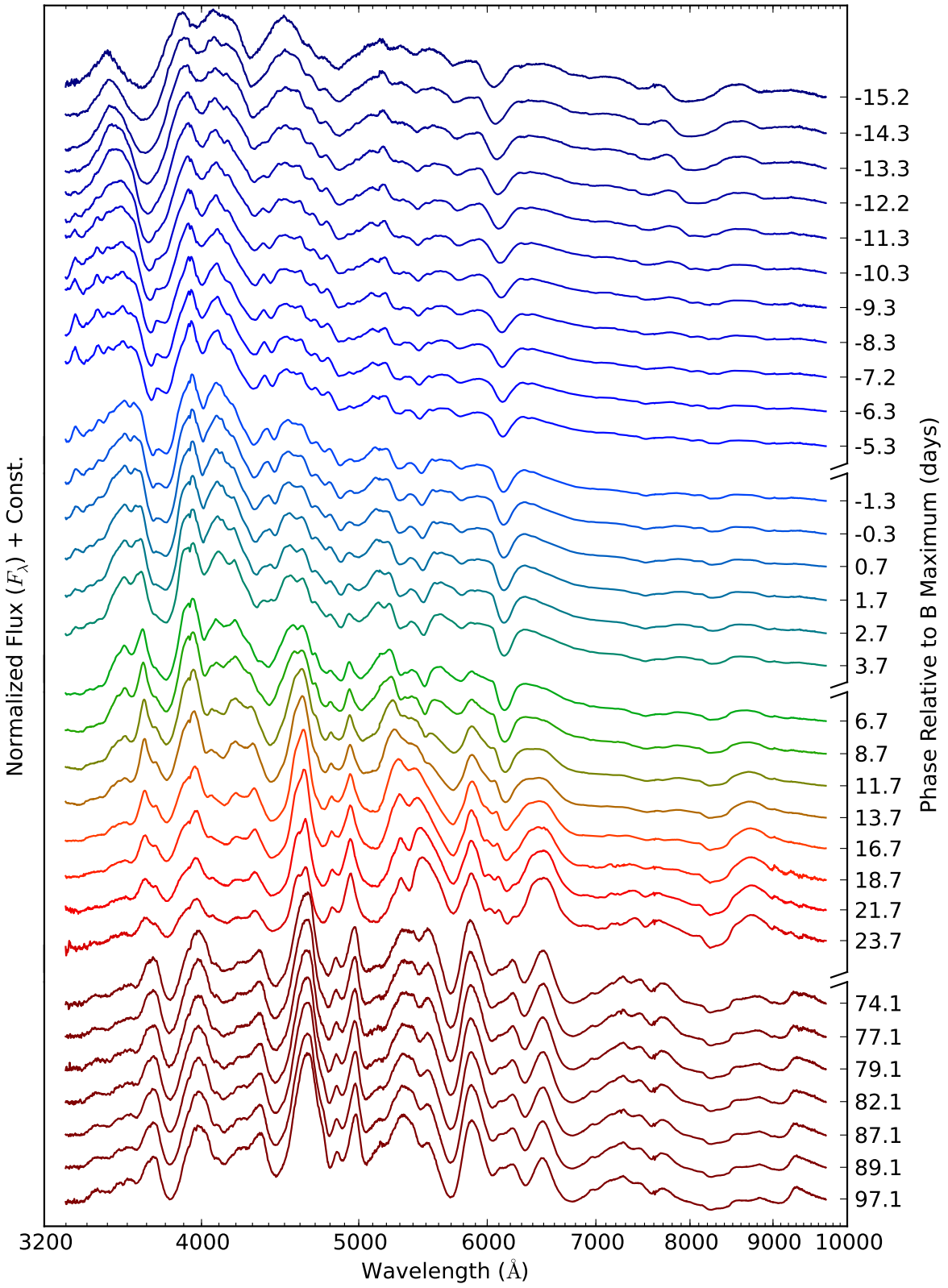

Figure 1.3.: Spectral evolution of the nearby, well-observed, normal SN 2011fe (spectra were obtained with the SNIFS spectrograph, from Pereira et al [233]). The kinks refer to the changes in the observing cadence. The spectra range in epochs from ~ 15 d before to ~ 100 d after maximum light.

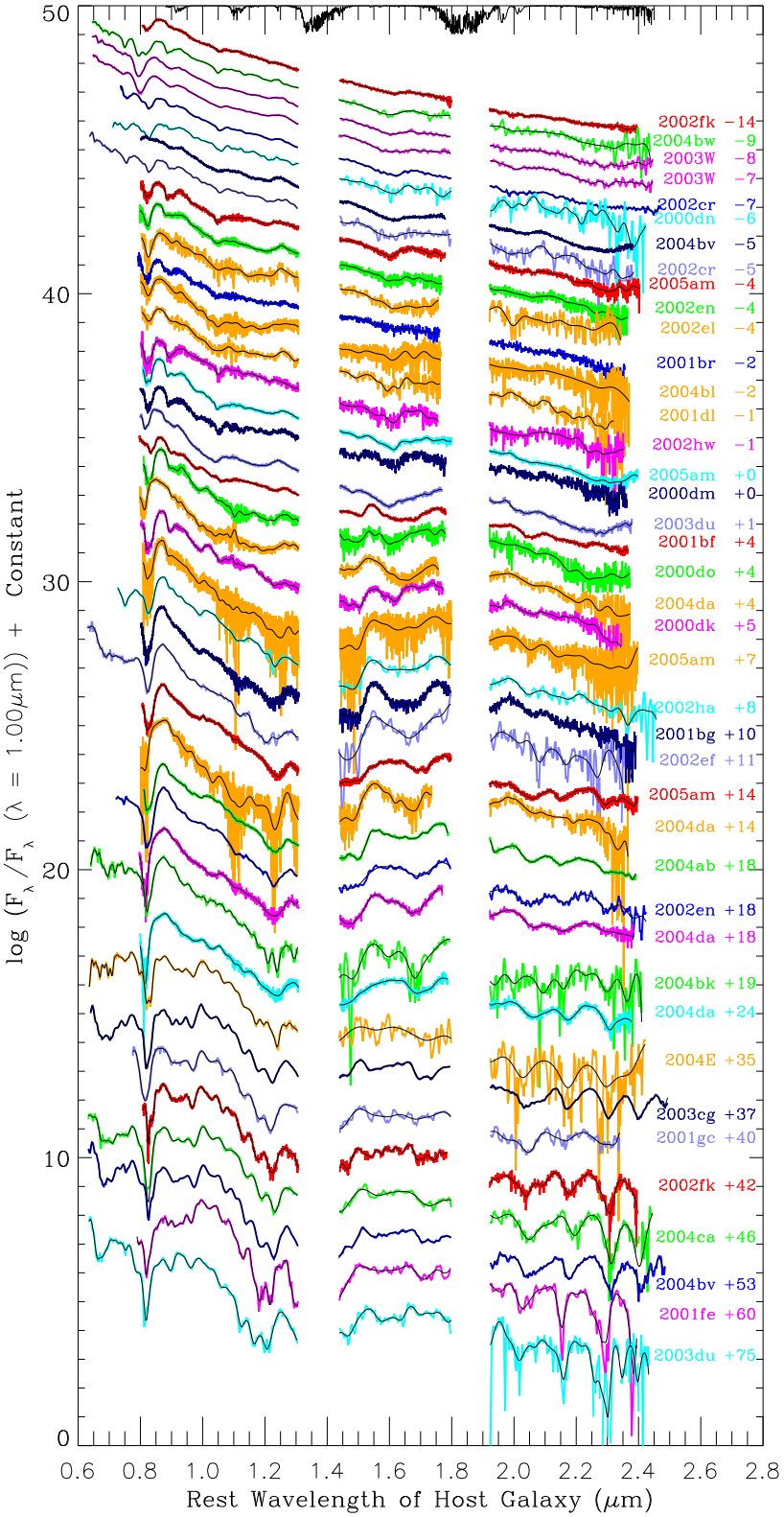

Figure 1.4.: An atlas of Near Infrared spectra from 14 days before to 75 days after maximum light presented in Marion et al. [198]. Wavelength regions between $\sim$ 1.3 - 1.4 μm and $\sim$ 1.8 - 1.9 μm have strong telluric absorption from the atmosphere.

The recession of the line-forming region causes the weakening (and finally, the disappearance) of the features associated with intermediate-mass elements. At this stage, the spectrum is dominated by a multitude of strongly blended features associated with singly-ionized iron-group elements (mostly Fe II, Co II), revealing the iron-group elements dominated composition of the ejecta core. At even later epochs ($\sim$ 1 year after explosion, referred to as the "nebular phase") the spectra are dominated by forbidden lines of doubly and singly ionised iron group elements ([Fe II], [Co II], [Fe III], [Co III]). At these phases the ejecta are optically thin and collisional de-excitations are too weak to balance the collisional excitations and the non-thermal excitations by the γ rays. [170] showed that the ratio of [Co III] to [Fe III] emission evolves according to the abundance ratio of cobalt and iron characteristic of the ^{56}Co $\rightarrow$ ^{56}Fe radioactive decay. Complementary evidence for radioactive decay was provided using NIR spectra at $\sim$ 1 year post explosion by [279] using the [Co II], and [Fe II],. Moreover, the width of the [Fe III], line at 4700 Å has been used as a tracer of the kinetic energy of the SN explosion [203]. Velocities of [Fe II], and [Ni II], lines in the nebular spectra have been used as a diagnostic of the asymmetries in the SN Ia explosion [189, 190]. Most studies of SN Ia spectra in the nebular phase have concentrated on the optical. [206] review the motivation for studying NIR nebular spectra. The [Fe II] and [Co II] features in the NIR are more isolated compared to the line blends in the optical. The [Fe II] 1.644 μm line has been used as an important diagnostic to estimate the total ^{56}Ni mass [279, 280]. Recently, NIR spectral features at $\sim$ 1 year post-explosion have been use to place constraints on the WD central density and the magnetic field in the ejecta [62, 232].

1.1.4. Progenitor Scenario

Hoyle & Fowler in 1960 [130] demonstrated that thermonuclear burning in an electron-degenerate stellar core can eventually lead to the disruption of the star. This led them to the conclusion that SN Ia are thermonuclear explosions of degenerate material in White Dwarfs (WDs). The progenitor white dwarf can have three possible chemical compositions depending on the evolution of the progenitor star [136]: (i) pure Helium WD, (ii) carbon-oxygen (C/O) WD and (iii) oxygen-neon-magnesium (O/Ne/Mg) WDs.

Since helium WDs are completely burnt to iron-group elements in a detonation when they reach $\sim 0.7\ M_{\odot}$ (e.g. [329]), their explosions cannot explain the observed spectra of SN Ia, and thus, they can be ruled out as progenitors. O/Ne/Mg WDs can be ruled out as progenitors since their number is not high enough to account for the observed supernova rate [186]. Moreover, simulations of this scenario suggest that the WD is more likely to undergo accretion induced collapse to a neutron star than a thermonuclear explosion when approaching the Chandrasekhar mass [217]. Therefore, the strongest candidate for an SN Ia progenitor is a C/O white dwarf.

White dwarfs are intrinsically inert, hence, the explosion needs to be induced externally, e.g. through interaction with a binary companion. The progenitor systems of SN Ia are characterised based on the companion star into two broad categories, the **single-degenerate** [321] and **double-degenerate** [135] scenario. In the single-degenerate scenario the companion can be a main-sequence, red giant or helium star. The WD accretes hydrogen-rich material or pure helium from the companion. In the double-degenerate scenario the companion can be a carbon/oxygen (C/O) or Helium WD. For each progenitor scenario, there are several different explosion mechanisms that can yield an SN Ia explosion. These are discussed in Section 1.1.5. The possible progenitor systems and observational constraints are reviewed in [121] and [194].

Single-degenerate In the most widely discussed version of this scenario, the C/O WD accretes hydrogen-rich material from the companion. The hydrogen is burnt to helium and further to carbon, increasing the WD mass. As the mass approaches the Chandrasekhar limit, the WD becomes unstable and explodes (the mechanism is discussed in Section 1.1.5). There is also a possibility that the a C/O WD accretes helium and explodes well below the Chandrasekhar mass limit. The detonation of the surface layer of Helium triggers a secondary carbon detonation at the center and unbinds the WD [296,330]. Details of this scenario are discussed in Section 1.1.5.

There are several observational constraints on this scenario. The hydrogen burning on the surface of the WD releases nuclear energy which is emitted in X-rays, hence, these systems should be visible as supersoft X-ray source [145]. The expected X-ray luminosity from these systems, without resolving individual objects, can also be a viable constraint for this scenario. [101] analysed

nearby elliptical galaxies and found that the total X-ray flux is not high enough to account for the rate of SN Ia from Chandrasekhar-mass, hydrogen accreting progenitor systems.

The presence of circumstellar material (CSM) was originally proposed as a key diagnostic of the SD scenario. CSM signatures have been detected through studies of time-varying Na ID absorption in near maximum light spectra (e.g. [227]). Statistical studies have shown that ~ 20 % of SN Ia show signs of CSM [191, 284], which is more common for more luminous SN Ia [191]. However, recent studies (e.g. [249]) have also shown, at least qualitatively that the Na ID absorption can also occur in the DD scenario, hence, casting doubts on the presence of CSM as a strong test to distinguish between the two leading progenitor scenarios .

A complementary method to trace the progenitor scenario of SN Ia is the presence of stripped/ablated hydrogen from a non-degenerate companion [196]. When the ejecta become optically thin (~ 1 year post explosion), this hydrogen should be visible in the SN spectra. Most attempts to model the nebular phase spectra (e.g. [273]) present no evidence for hydrogen, however, a study by Maguire et al. [192] demonstrated tentative evidence for the detection of hydrogen in SN 2013ct. More recently, [265] suggested that the Paschen β line at ~ 1.29 μm is a prominent feature in the J-band between ~ 1 -2 months post explosion. However, [265] do not find any trace of the Paβ line for a small sample of SNe with NIR spectra at the specific epoch, although this test would require a larger sample of SN Ia with NIR spectra.

Deep, early time radio observations can provide a crucial constraint on the SD scenario. For a nearby SN 2011fe in M101, [126] constrain the accretion rate using radio data (0.3 - 20 cm) as early as 1.3 days after the explosion date inferred by [219], excluding a circumstellar wind from a giant donor.

Early time optical and NIR light curves can provides constraints on the SD scenario. Marion et al . [197] present evidence for an early time luminosity excess in the V-band indicating possible interaction of the SN ejecta with a non-degenerate binary companion. Future experiments are designed to discover and obtain follow-up observations of SN Ia few hours to days post-explosion. These proposed data will be an essential test for the SD scenario.

Double-degenerate In the double-degenerate (DD) scenario, the companion star can be a helium or another C/O WD. Thus, intrinsically, there is no hydrogen around in the system, except old circumstellar material from the formation of the WDs. The merger process is initiated by emission of gravitational waves. As the WDs approach each other, one of them fill its Roche-Lobe and mass transfer sets in.

Within this scenario, if the companion star is a Helium WD, then the system is similar to the helium accreting single degenerate scenario. As the maximum He WD mass is $\sim 0.45\ M_{\odot}$and typical masses are lower, the amount of mass that the primary can accrete is limited. Hence, this scenario is mainly a candidate for sub-Chandrasekhar mass explosions [23, 106].

For the scenario with two C/O WDs, the more massive WD is generally thought to tidally disrupt and accrete its companion, initially through an accretion disk configuration, that finally takes on a more spherical geometry. The high accretion rate of carbon and oxygen would overcome the problem of inefficient mass growth and lead to a carbon ignition in the core. However, it has long been argued that the large accretion rate can induce off-center ignition of the C/O material and the burning of carbon to oxygen and neon. Further ignition and approach to M_{Ch} would drive electron capture on Mg and Ne, leading to an "accretion induced collapse" to a neutron star as described above.

Recent 3D hydrodynamical merger models have cast doubt on the picture of a merger remnant as an unperturbed primary-mass WD that accretes the remnants of a secondary WD. Instead, complex structures with regions of high temperature and density are found, in which explosive carbon ignition may occur. Pakmor et al. [222] find that such "violent mergers" can explain the observed display of peculiar, subluminous SN Ia, although the model light curves are too broad for this class of SN Ia . Van Kerkwijk et al. [311] argue that such mergers may lead to SN Ia even if the total mass is less than M_{Ch} . Details depend on the WD masses and the presence of He, which can facilitate ignition.

1.1.5. Explosion Models

In this section, we briefly summarise the explosion models that have been invoked to explain the observed display of SN Ia. These explosion models can be classified based on the mass of the exploding WD into Chandrasekhar mass, sub-Chandrasekhar mass and super-Chandrasekhar mass.

Chandrasekhar Mass Models A pure detonation of a C/O WD (e.g. [4]) burns the entire WD to iron-group elements and doesn't produce the amount of intermediate mass elements (IMEs) required to reproduce the observed spectrum at maximum light. Pure deflagrations on the other hand produce a maximum of $\sim 0.4\ M_{\odot}$ of ^{56}Ni in the explosion and hence cannot explain a majority of normal and over luminous SN Ia. Due to large Rayleigh-Taylor instabilities, the elements are highly mixed in the ejecta [261], which contradicts observations indicating that there is no carbon in the central parts of the ejecta. However, this explosion mechanism has been invoked to explain the peculiar class of SNe similar to SN 2002cx [141, 167, 240].

It has been proposed that in $\mathrm{M_{Ch}}$ models, the nuclear burning starts out as a deflagration and transitions to a detonation at a transition density [156]. The deflagration phase pre-expands the WD, leading to low enough densities that the detonation wave burns some of the material only to intermediate mass elements. Hence, the strength of the deflagration phase mainly determines the outcome of the explosion, since a longer deflagration phase leads to a higher IMEs production, whereas a shorter deflagration phase implies more of the WD is burnt to iron group elements.

Kasen et al. [148] find that an ensemble of models with different initial flame configurations and different metallicities can produce the range of ^{56}Ni masses for normal SN Ia. Synthetic observables calculated for these models could reproduce the observed Phillips relation between the luminosity and light curve width reasonably well. [28] find a good agreement between a suite of delayed detonation models with different ^{56}Ni masses and photometric and spectroscopic properties of SN Ia at maximum light. Futhermore. [27] compare the photometric and spectroscopic evolution of a broad-lined SN Ia (SN 2002bo) to one of their suite of models and find that the model reproduces the evolution of the SN well.

The main drawback of this model is that the formation of the detonation is poorly understood and the models to estimate the probability of the formation of a detonation are highly parameterised. As the properties of the explosion depend heavily on the timing of the detonations, the formation of the detonation must be understood in order to judge this scenario.

Sub-Chandrasekhar Mass Models In the sub-M_{Ch} models scenario, the primary WD is significantly below the Chandrasekhar mass. It accretes helium from a companion that can be main sequence star (single-degenerate scenario) or a helium WD (double-degenerate scenario). The surface layer of Helium undergoes a thermonuclear runaway, inducing a carbon detonation in the core (known as "double detonations" [330]). Recently, [80] concluded that even for small Helium shell masses ($<0.1\ M_{\odot}$), the helium detonations and subsequent carbon detonations can form.

More recently, [275] artificially detonated a suite of sub-M_{Ch} models with different primary mass and obtained a good agreement between the calculated synthetic observable . Moreover, these systems should be frequent enough to explain the observed SN Ia rate, hence, making them an exciting possibility to explain a large fraction of SN Ia.

The collision of two WDs as a possible explosion mechanism was proposed as early as 1989 by Benz et al. [18] and has recently been studied in [262]. Kozai resonances in triple systems are proposed as the mechanism to decrease delay time to a collision. Simulations show that the explosion ensues after collision and synthetic light curves and spectra show reasonable agreement with observations of normal SN Ia [262]. However, due to large uncertainties in the properties of triple systems, this mechanism makes no definite prediction for the expected absolute rate of collisions.

Super-Chandrasekhar Mass Models There are several SN Ia for which the ejecta masses are claimed to be higher than a Chandrasekhar-mass . One possibility to explain these events is a double-degenerate merger exploding during the merging process. Another scenario involves differentially rotating WDs. Similar to the M_{Ch} case, these objects may burn as a pure deflagration or pure detonations. [236] find that these systems lead to bright enough explosions

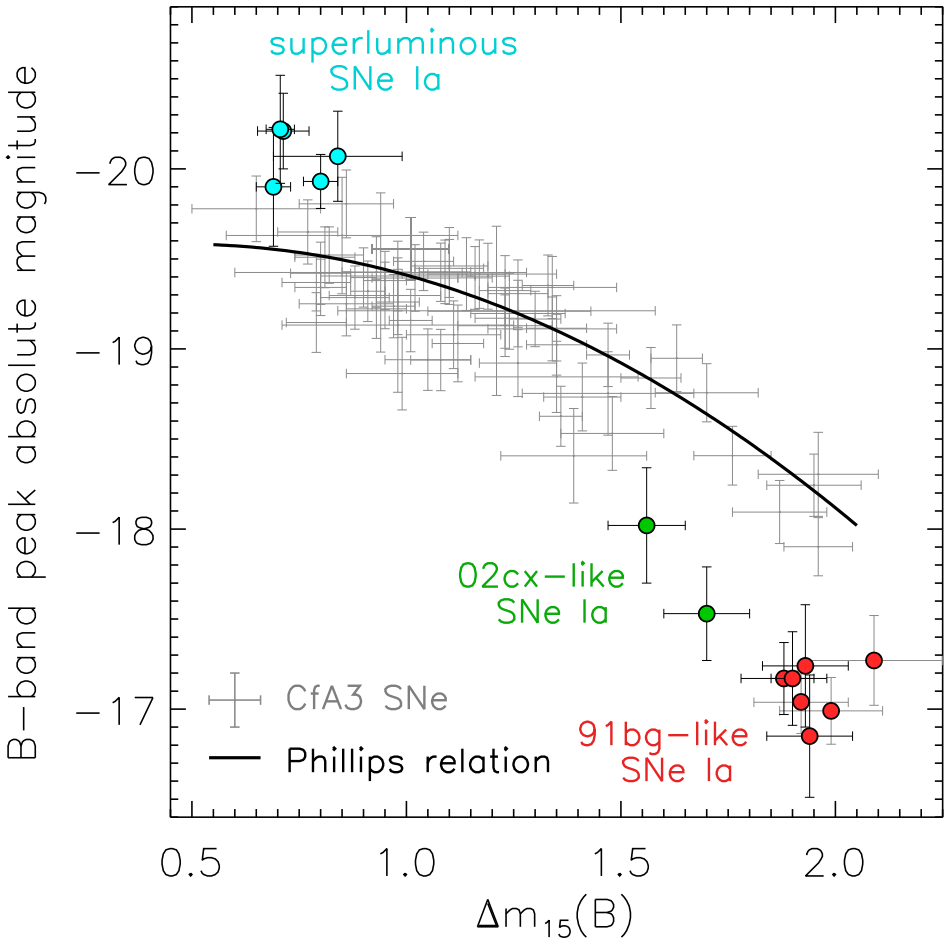

Figure 1.5.: The relation between the absolute B-band magnitude and the B-band decline rate ($\Delta m_{15}(B)$) is plotted for SN Ia observed as part of the CfA SN survey presented in Hicken et al. [118]. The peculiar SN Ia that are outliers on this relation are labeled and denoted in a different colour. SN 1991T-like events do not appear distinct from the relation for normal SN Ia. Credits: Hillebrandt et al. [120]

to explain superluminous SN Ia. However the ejecta are aspherical and have fast velocities in contradiction with the observations.

1.1.6. Peculiar Type Ia supernovae

Type Ia supernovae have diverse spectroscopic and photometric properties. Dedicated searches for SN Ia have revealed several sub-classes that show deviations from the 'normal' SN Ia. These sub-classes of SN Ia, typically named after the prototypical SN, are summarised below:

- **SN 1991T-like**: These SN Ia show features of doubly-ionized iron-group elements in their pre-maximum spectra and shallow SiII absorption, though their post-maximum spectra look like those of normal SN Ia. They have more slowly declining light curves ($\Delta m_{15}(B)$<0.9) and brighter peak luminosities ($M_B \sim$ -19.9; [79]) and are seen to obey the width-luminosity relation.

- **SN 1991bg-like**: They show prominent Ti II features in their near-maximum light spectra, having deep SiII absorptions [78, 299]. Early time spectra also show features from unburnt material. These SN Ia have fast-declining light curves and faint peak luminosities.

- **SN 2002cx-like or Type Iax SNe**: This class of SNe typically has lower, maximum light spectral line velocities. Their peak brightnesses are >1 mag fainter than normal SN Ia [85]. Their nebular spectra do not show forbidden emission lines of iron, but instead have P Cygni line profiles of Fe II and low-velocity OI lines [141] that are not seen in nebular spectra of normal SN Ia.

- **Super-Chandrasekhar (or superluminous) SN Ia**: For this subclass, the total inferred ejecta mass is significantly greater than the Chandrasekhar limit. They are brighter than the class of 1991T-like objects ($M_B \sim -20.5$). Their spectra at early times have C II lines which are normally attributed to normal or subluminous SN ia, indicating unburnt carbon in the ejecta. These SN Ia have slowly evolving light curves, but unlike the class of 1991T-like objects, they do not obey the width-luminosity and are brighter than their expected luminosity, extrapolating the relation for normal SN Ia.

The width-luminosity relation for normal SN Ia from [120] is shown in Figure 1.5 along with the peculiar subclasses of superluminous, SN 1991bg-like and SN 2002cx-like SNe over plotted for comparison.

1.2. Cosmology with Type Ia supernovae

In this section, we review the arguments to support the use of Type Ia supernovae as excellent distance indicators in cosmology. We first setup the 'standard model' of cosmology and define the distance measurements that have been used in the literature, as a function of the redshift and the cosmological density parameters.

1.2.1. Friedman-Lemaitre-Robertson-Walker Cosmology

The cosmological principle states that the universe is spatially homogenous and isotropic on the largest scales. Homogeneity implies an invariance of the system under translations and isotropy implies invariance under rotation. Large galaxy redshift surveys (e.g. CfA redshift survey, Sloan Digitial Sky Survey), combined with the impressive uniformity of the cosmic microwave background (as measured for example with the COBE satellite, and more recently and precisely by the WMAP and Planck satellites) gives a firm observational basis to this assumption.

The metric ansatz for a homogenous and isotropic universe, known as the Friedman-Lemaitre-Robertson-Walker (hereafter, FLRW) metric, has a line element ds given as:

$$ds^2 = -dt^2 + a^2(t)[\frac{dr^2}{1-kr^2} + r^2(d\theta^2 + sin^2\theta d\phi^2)] \tag{1.1}$$

where t is the coordinate time and (r, θ, ϕ) are the co-moving coordinates of a point in space.

Field Equations The field equations of general relativity, given below

$$G_{ab} + \Lambda g_{ab} = 8\pi G T_{ab} \tag{1.2}$$

encode the information relating the matter content (T_{ab}) and geometry (G_{ab}) of space-time. Λ is the cosmological constant, a fluid with constant density

and negative pressure that was introduced in order to make the solution to the field equations 1.2 static (see Chapter 4, section 2 of Bergstrom & Goobar 2004; [19]).

Inserting the FLRW metric and the expression for the stress-energy tensor, T_{ab} yields the two field equations. Λ is the cosmological constant.

$$(\frac{\dot{a}}{a})^2 = \frac{8\pi G\rho}{3} - \frac{k}{a^2} + \frac{\Lambda}{3} \tag{1.3}$$

$$\frac{\ddot{a}}{a} = -\frac{4\pi}{3}(\rho + 3P) + \frac{\Lambda}{3} \tag{1.4}$$

where a is the scale factor, ρ is the matter density, k is the signature for the curvature.

Fluid Equation The first law of thermodynamics states that the heat flow into or out of a system (Q) is equal to the change in internal energy E and the pressure multiplied by the change in the volume

$$\dot{Q} = (\dot{E}) + P\dot{V} \tag{1.5}$$

In a homogenous universe

$$\dot{E} = -P\dot{V} \tag{1.6}$$

The volume of a sphere with co-moving radius r_s is

$$V(t) = \frac{4\pi}{3} r_s^3 a^3(t) \tag{1.7}$$

and the energy is given by

$$E(t) = V(t)\rho(t) \tag{1.8}$$

Table 1.1.: Equation of State (EoS) values for non-relativisitic matter, radiation, cosmological constant

Energy Source	$w = P/\rho$
Non-relativistic matter	0
Radiation	1/3
Cosmological Constant	-1
strings	-1/3

taking a time derivative of equation 1.8

$$\dot{E} = \dot{\rho}V + \rho\dot{V} \tag{1.9}$$

Replacing the expression for $\dot{V}$ and equation 1.6 in equation 1.9, we get

$$\dot{\rho} + 3\frac{\dot{a}}{a}(\rho + P) = 0 \tag{1.10}$$

Equation of state The equation of state of a fluid is defined as the ratio of the pressure exerted by the fluid to its density, given by the following equation

$$P = w\rho \tag{1.11}$$

If we assume that w is constant for a given energy source, then we can use the relation between P and ρ to evaluate the expression for ρ as a function of the scale factor and hence for different equations of state, characterise the evolution of the density. A summary of the equation of state values for the energy sources in the universe is given in Table 1.1

For a given energy source (and hence, equation of state value), the density is related to the scale factor as

$$\rho(a) \propto a^{-3(1+w)} \tag{1.12}$$

Density Parameters We derive the dimensionless density parameters that can be constrained from several different observational datasets.

The Hubble parameter H is defined as:

$$H = \frac{\dot{a}}{a} \tag{1.13}$$

Hence, equation 1.3 can be written as

$$H^2 = \frac{8\pi G\rho}{3} - \frac{k}{a^2} + \frac{\Lambda}{3} \tag{1.14}$$

and re-arranged as

$$1 = \frac{8\pi G\rho}{3H^2} - \frac{k}{a^2H^2} + \frac{\Lambda}{3H^2} \tag{1.15}$$

defining the dimensionless matter density $\Omega_m = \frac{8\pi G\rho}{3H^2}$, vacuum (or cosmological constant) density $\Omega_\Lambda = \frac{\Lambda}{3H^2}$ and the curvature density $\Omega_k = -\frac{k}{a^2H^2}$, equation 1.15

$$\Omega_k = 1 - \Omega_m - \Omega_\Lambda \tag{1.16}$$

Defining $\Omega_{tot} = \Omega_m + \Omega_\Lambda$, we obtain,

$$\Omega_k = 1 - \Omega_{tot} \tag{1.17}$$

Which relates the energy sources of the universe to its geometry.

1.2.2. Luminosity Distance and the matter-energy content of the universe

In this section, we derive the expression for the luminosity distance. The luminosity distance to an astrophysical source can be calculated by knowing its intrinsic luminosity and the flux observed on earth.

Redshift In order to derive the expression for distances in cosmology, we must first derive the relation between the scale factor and time by considering two pulses of light. The first pulse is emitted at time t_e and observed after travelling a null geodesic t_o . The distance travelled by the photon a radial geodesic ($\theta = \phi =$ constant) is given according to the FLRW line element

$$ds^2 = -dt^2 + a^2(t)dr^2 = 0 \tag{1.18}$$

$$dt^2 = a^2(t)dr^2 \tag{1.19}$$

$$r = \int_{t_e}^{t_o} \frac{dt}{a(t)} \tag{1.20}$$

A second pulse is emitted at $t_e + \delta t_e$ and observed at $t_o + \delta t_o$ which travels the same comoving distance such that

$$r = \int_{t_e+\delta t_e}^{t_o+\delta t_o} \frac{dt}{a(t)} \tag{1.21}$$

Equations 1.20 and 1.21 can be combined to show

$$\int_{t_e}^{t_e+\delta t_e} \frac{dt}{a(t)} = \int_{t_o}^{t_o+\delta t_o} \frac{dt}{a(t)} \tag{1.22}$$

which means that the integral of dt/a(t) is the same between the emitted and observed pulses. If we look at the first order perturbation that the universe has not expanded appreciably between the emission of the two pulses, we can simplify Equation 1.22

$$\frac{\delta t_o}{a(t_o)} = \frac{\delta t_e}{a(t_e)} \tag{1.23}$$

If the time between the pulses defines the period of the wave then 1.23 can be re-written in terms of the wavelength as

$$\frac{\lambda_o}{a(t_o)} = \frac{\lambda_e}{a(t_e)} \tag{1.24}$$

Rearranging 1.24 in terms of the expression for the redshift, we obtain

$$1 + z = \frac{\lambda_o}{\lambda_e} = \frac{a(t_o)}{a(t_e)} \tag{1.25}$$

1.2.3. Luminosity Distance and the accelerating universe

The luminosity distance, d_L, in its Euclidean definition, relates the *intrinsic* and *observed* luminosities of an astrophysical source as:

$$L = \mathcal{F} \cdot 4\pi d_L^2 \tag{1.26}$$

hence, the definition of d_L is

$$d_L = \sqrt{\frac{L}{4\pi\mathcal{F}}} \tag{1.27}$$

In the FLRW metric, the luminosity distance can be written as an integral equation, as a function of redshift, z and the dimensionless density parameters (see [43]; Equation 25.)

$$d_L = \frac{1+z}{H_0\sqrt{\Omega_k}} sinn \left\{ \sqrt{\Omega_k} \times \int_0^z \frac{dz'}{\sqrt{(1+z')^2(1+\Omega_m z') - z'(2+z')\Omega_\Lambda}} \right\} \tag{1.28}$$

Where sinn= { sin, n , sinh } for Ω_k <, = , >0, respectively.

In astronomy, we do not directly measure d_L, but instead, we infer a *distance modulus*, μ, corrected for extinction from material in the line-of-sight between the source and the observer. μ is defined to be the difference between the

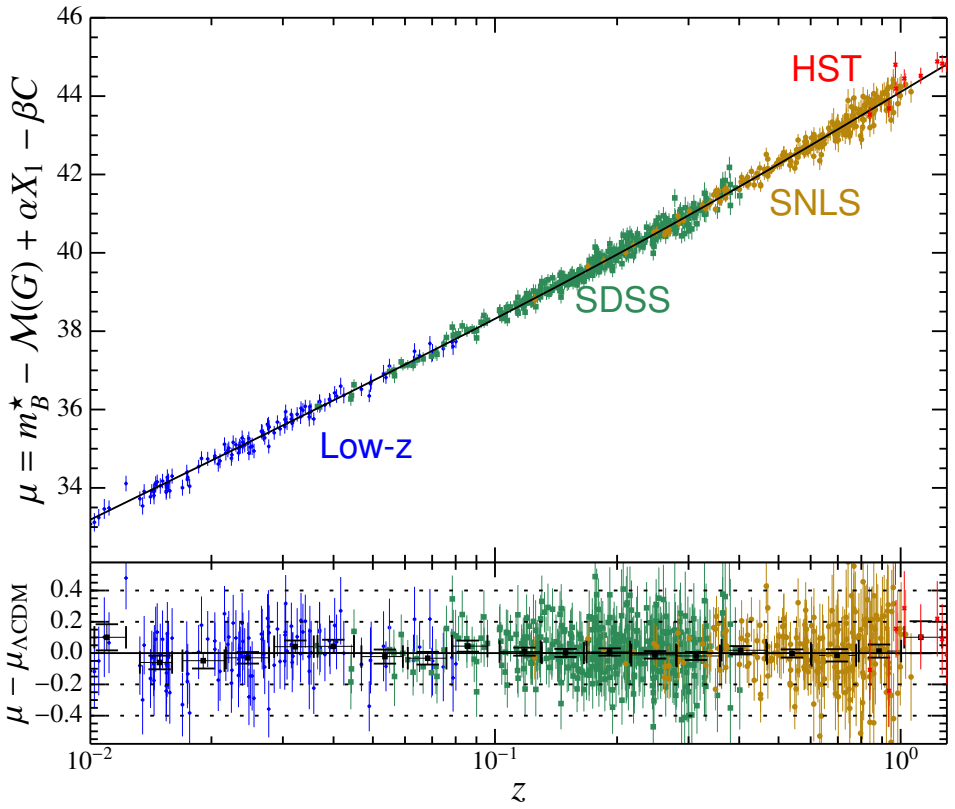

Figure 1.6.: **Top**: The distance versus redshift (Hubble diagram) for a sample of 740 SN Ia. The different sub-samples in varying redshift ranges are labelled in different colours. **Bottom**: The residuals with respect to the ΛCDM model distance modulus. Credits [21]

apparent magnitude, $m = -2.5 \cdot \log\mathcal{F} +$ constant and the absolute magnitude $M = m - 2.5 \cdot \log(d_L/10pc)$ (i.e. the apparent magnitude that an object would have at a distance of 10 parsecs - or $\sim$ 33 light years - from the Earth):

$$\mu = m - M = 5 \log_{10} d_L + 25 \tag{1.29}$$

where d_L is in units of megaparsecs (Mpc) and M is the absolute magnitude of the source. For SN Ia this is the *calibrated* absolute magnitude after corrections for light curve width, observed colour and host galaxy properties have been applied.

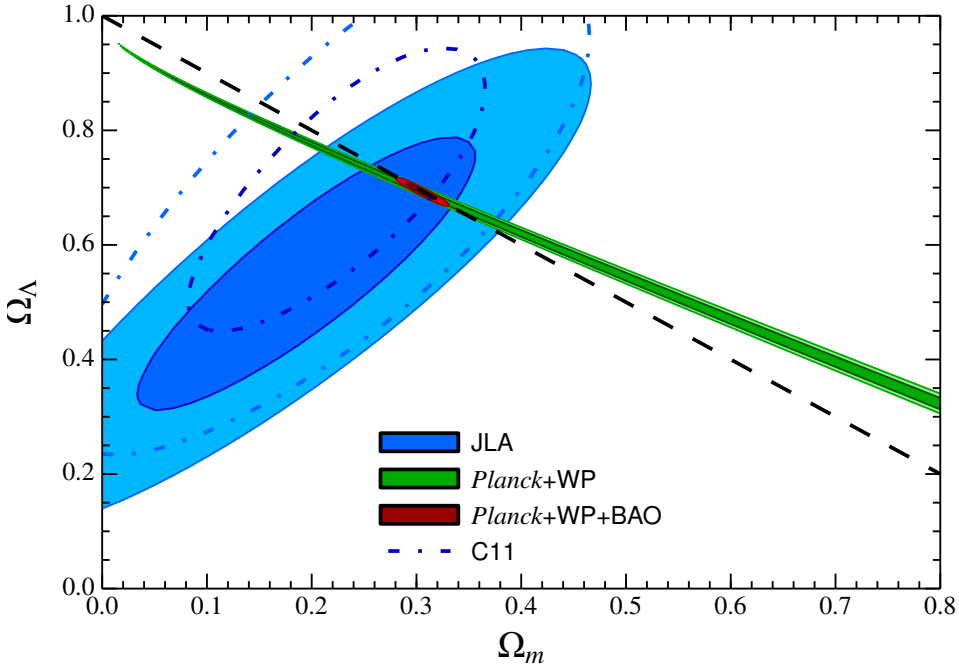

Figure 1.7.: 68% and 95% on Ω_m and Ω_Λ from a combination of different cosmological probes, namely SN Ia, BAO and CMB. JLA refers to the Joint Light Curve Analysis of the SDSS and SNLS samples, C11 is the SNLS3 year sample presented in Conley et al. [50]. *Planck*+WP refers to a combination of the *Planck* temperature and *WMAP* polarisation measurements of the cosmic microwave background fluctuation and BAO refers to the combination of measurements of the baryon acoustic oscillation scale. The black dashed line corresponds to a flat universe. Credits: [21]

1.2.4. Measuring the equation-of-state parameter of dark energy

A cosmological constant with an associated equation of state $w = -1$ fits the SN Ia data well. In this cosmological model, termed as wCDM, the expression for the luminosity distance is expressed as a function of Ω_m and w (assuming $\Omega_k = 0$, i.e. flat universe, hence $\Omega_\Lambda = 1 - \Omega_m$)

$$d_L = \frac{(1+z)}{H_0} \int_0^z \frac{dz'}{\sqrt{(1+z')^3\Omega_m + (1-\Omega_m)(1+z)^{3(1+w)}}} \tag{1.30}$$

Thus, one can construct a likelihood contour in the (Ω_m, w) plane. The constraints from SN Ia can be combined with complementary cosmological probes, e.g. the Cosmic Microwave Background (CMB) and Baryon Acoustic Oscillations (BAO). Current, the most precise measurements of w (assuming flat universe and a cosmological constant) are -1.027 ± 0.055 (statistical and systematic uncertainties) from the Joint Analysis of the light curves from SNLS and SDSS presented in [21].

In Equation 1.30, w is assumed to be a constant equation of state for 'dark energy'. The equation of state parameter for 'dark energy' can also be parametrized as a function of redshift to test the time-variability of the acceleration (as shown in [182]). It is represented as

$$w(a) = w_0 + w_a(1-a) \tag{1.31}$$

where w_0 is the constant term and w_a is the coefficient for the linear relation with the scale factor a. Current constraints from a combination of different probes yield an estimate of $w_0 = -0.957 \pm 0.124$ and $w_a = -0.336 \pm 0.552$ [21].

Table 1.2.: Estimates for Ω_m and w from various supernova surveys. Adapted from [104], Details on the light curve fitters can be found in section 1.3.1. Note that the Freedman et al. 2009 study provides constraints on the wCDM model from both optical and i-band data for the *same* SN Ia. The estimates from the Betoule et al. study are mentioned for both the case with and without BAO constraints. Credits: Bruno Leibundgut.

N_{SN}	Ω_m (flat)	w	Light Curve Fitter	Reference
115	0.263($\pm$ 0.042 $\pm$ 0.032)	-1.023 $\pm$ 0.090 $\pm$ 0.054	SALT	Astier et al. 2006
162	$0.267^{+0.028}_{-0.018}$	$-1.069^{+0.091+0.13}_{-0.083-0.13}$	MLCS2k2	Wood-Vasey et al. 2007
178	$0.288^{+0.029}_{-0.019}$	$-1.069^{+0.091+0.13}_{-0.083-0.13}$	SALT2	...
288	0.307 ($\pm$ 0.019 $\pm$ 0.023)	-0.76 ($\pm$ 0.07 $\pm$ 0.11)	MLCS2k2	Kessler et al. 2009
288	...	...	SALT2	...
56	0.27 ($\pm$ 0.02)	-1.05 $\pm$ 0.13 (i-band)	SN(oo)Py	Freedman et al. 2009
56	0.27 ($\pm$ 0.02)	-1.08 $\pm$ 0.14 (B-band)	SN(oo)Py	...
472	...	$-0.91^{+0.16+0.07}_{-0.054-0.13}$		Conley et al. 2011
472	0.269 ($\pm$ 0.015)	$-1.061^{+0.069}_{-0.068}$	SALT2	Sullivan et al. 2011
580	0.271 ($\pm$ 0.014)	$-1.013^{+0.077}_{-0.073}$	SALT2	Suzuki et al. 2012
740	0.307 ($\pm$ 0.017)	-1.018 $\pm$ 0.057 (CMB)	SALT2	Betoule et al. 2014
740	0.303 ($\pm$ 0.012)	-1.027 $\pm$ 0.055 (CMB+BAO)	SALT2	...

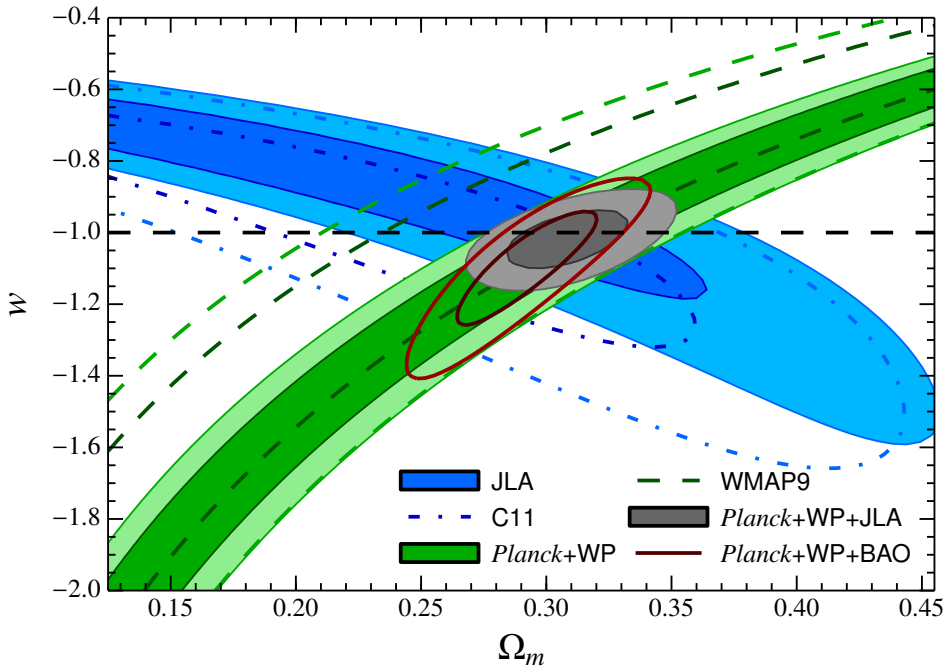

Figure 1.8.: 68% and 95% on Ω_m and w from a combination of different cosmological probes, namely SN Ia, BAO and CMB. Labels are the same as in Figure 1.7 The black dashed line corresponds to a flat universe. Credits: [21]

1.3. Current Status and Recent Developments in Supernova cosmology

With the advent of dedicated large programs to gather multi-band data of SN Ia, the ability of SN Ia to constrain cosmological parameters is limited by systematic uncertainties as opposed to statistical uncertainties [21, 50]. A summary of current constraints from different SN Ia surveys is presented in Table 1.2.

With future transient facilities designed to increase this number by at least 2 orders of magnitude, it is important to understand the systematic effects in SN Ia datasets.

In this section we provide a (non-exhaustive) list of possible sources of sys-

tematic uncertainty and the benefits of expanding the wavelength window for observing SN Ia. See [104] for a comprehensive review.

1.3.1. Sources of Systematic Uncertainties

- **Calibration**: Precise distance measurements with SN Ia require very accurate relative photometry ($\Delta w \sim 2\Delta m$). While future surveys are likely to measure most if not all their SNe with a single, well-calibrated system, current cosmological bounds are derived from a compilation of surveys. [22] present an improved photometric cross-calibration for the SNLS and SDSS SN Ia samples, which has been used to create the "JLA" sample by [21], demonstrating the importance of photometric calibration to overall systematic uncertainty budget.

- **Reddening and absorption**: Intervening material between the SN and the observer can absorb photons from the explosion or scatter them to redder wavelengths. Thus, in order to obtain an intrinsic magnitude, a reddening correction needs to be applied. There are several sources for material for light from the SN to interact with, namely, the circumstellar medium around the SN, the interstellar medium in the host galaxy of the SN, the intergalactic medium and the local dust in the Milky Way. Although, the Milky Way dust correction is fairly well known, there are significant problems pertaining to the correction for extinction from host galaxy dust, which is significantly larger than the other sources of extinction. Several recent studies [36, 161, 165, 216] have shown that the total to selective absorption ratio (R_V), which captures the dust-size distribution, is significantly smaller for SN hosts (~ 2) than the Milky Way value of 3.1, especially for SNe with a high colour excess ($E(B-V)$). Moreover, low R_V values lead to a smaller scatter in the Hubble diagram and better global parameter fitting of SN Ia across a wide range of redshifts, indicating that the properties of dust are not fully understood.

- **Brightness Evolution**: The SN brightness has been shown to depend on host-galaxy environment. E.g. Hamuy et al. [113, 116] found that on average the B and V-band light curve width differs between host galaxy

types. Elliptical galaxies host a larger fraction of SN Ia with narrow light curves. Furthermore, studies of nearby [153] and distant [289] SNe suggest evidence for varying SN Ia properties with host galaxy that are not entirely corrected for with the standard width-luminosity and colour-luminosity relations. Splitting the sample by host galaxy mass is seen to decrease the scatter in the Hubble residuals and hence, improve cosmological constraints [21, 290]. More recent studies have demonstrated correlations of SN Ia Hubble residuals with other host galaxy properties, e.g. star formation rate [259], metallicity [39]. Given the time-evolution of the metallicity and stellar mass of galaxies, the possibility of the evolution in brightness of SN Ia with redshift is a source of uncertainty for cosmological parameters.

- **Light Curve Fitters**; Historically, several different consortia used different fitting software to analyse SN Ia light curves. Currently, there are two main light curve fitters used for low- and high-z SN analysis, namely, SALT2 [107] and MLCS2k2 [142], next generation versions of SALT [108] and MLCS [256]. Differences in these light curve fitters arise from different treatment of host galaxy reddening and different reference spectral templates in the blue and UV regions. Another key difference is the color-brightness relation. MLCS assumes that SN Ia reddening comes from host galaxy dust, therefore allowing for only positive corrections, whereas SALT2 combines intrinsic and extrinsic contributions to the observed colour, and hence, negative corrections are permitted. More recently, other light curve fitters have been developed, e.g. SifTO [52] used by the SNLS collaboration and for low-z studies. SN(oo)Py has been used by the CSP [37, 38], and is unique in its capability to fit NIR light curves as well.

- **Inhomogenous Cosmology**: Equations 1.28, 1.30 assume that the universe is homogenous and isotropic. It has been claimed that the average expansion in a locally inhomogenous universe behaves different than expected in a FLRW model, due to the non-linearity of Einstein equations, which means that spatial averaging and solving the Einstein equations do not commute [72]. This is known as the "back-reaction" problem. Since it is difficult to compute these effects from non-linear back-reaction in general relativity, it remains unclear whether this is a limitation for precision tests of w.

- **Peculiar Velocities**: Local density perturbations induce peculiar velocities in galaxies of the order of ~ 300 kms^{-1}. Additionally, the exploding SN could have a comparable motion in the host galaxy. The error in the peculiar velocity $\sigma_\mu \sim \frac{v}{c} \cdot \frac{5}{ln(10)}[\frac{1+z}{z(1+z/2)}]$ dominates over the error from intrinsic brightness for SNe for z<0.015. Davis et al. [57] concluded that including SNe as nearby as $z = 0.02$, the systematic uncertainty will be about $\Delta w \sim 0.01$.

- **Gravitational Lensing**: The light from distant SN Ia is deflected by massive objects in its path to us. This effect, known as gravitational lensing is used to measure the masses of galaxy halos and galaxy clusters. These foreground objects introduce a "scatter" in the observed SN Ia flux that increases with redshift. Since the number of photons are conserved under lensing (some objects are magnified, some de-magnified), the luminosity distance over a large number of SN Ia is expected to converge to Equation 1.28. However, for small number statistics, or magnitude-limited samples, gravitational lensing can be a source of selection bias. Jonsson et al. [143] studied the weak-lensing perturbations in the SNLS three-year data. The distributions of lensing perturbations as a function of redshifts matches the expectation and no significant bias is seen in the current high-z sample.

Errors pertaining to the intrinsic diversity of SN Ia and dust extinction can be overcome by expanding the wavelength window in which the SN Ia are observed. We discuss this below.

1.3.2. Expanding the Wavelength Window

As detailed above, the ability of SN Ia to constrain cosmological parameters is limited by different sources of systematic uncertainties. Understanding the properties of dust extinction and the progenitors of SN Ia are crucial to reducing these systematic uncertainties. One possible pathway to circumvent these systematic uncertainties is by expanding the studied wavelength window. For sizeable samples of nearby SN Ia, it has been found that the scatter in the luminosity in the NIR ($YJHK$) filters *without* any correction is comparable to the scatter in the optical *after* applying corrections for the light curve width,

colour and host-galaxy properties, essentially forwarding the case that SN Ia are close to *standard* candles in the NIR. Moreover, theoretical arguments have been put forward to suggest that the intrinsic dispersion of peak magnitudes is significantly lower in the NIR ($YJHK$) filters [27, 147].

Ground-based NIR observations of SN Ia are severely limited by the Earth's atmosphere. Vibrational bands of H_2O and CO_2 and thermal emission from narrow OH-lines reduce the observational windows and the obtainable signal-to-noise ratio. This is made more challenging by the fact that SN Ia are fainter in the NIR ($YJHK$ filters) than in the optical. However, the benefit of the narrow intrinsic scatter can be exploited at high redshifts with existing (e.g. Hubble Space Telescope) and future space based facilities (e.g. Euclid, Wide-Field Infrared Space Telescope, James Webb Space Telescope).

The i-band Hubble diagram of SN Ia has been shown to be consistent with a flat ΛCDM universe [214, 215]. Freedman et al. [89] use a sample of 56 SN Ia (21 nearby and 35 in the range 0.1 <z <0.7) and find precise constraints on w. These high-z observations also favour an atypical R_V of 1.7 over the canonical Milky Way value of 3.1.

1.4. Organisation of the thesis

The uniform behaviour of SN Ia in the Near Infrared makes them an excellent possibility to be used as distance indicators in this wavelength region. In this thesis, we assess the use of SN Ia in the NIR and bolometric properties of SN Ia to understand the properties of the explosion and the use of SN Ia for cosmological parameter estimation. In Chapter 2 we analyse a large sample of SN Ia with NIR light curves presented in the literature. In Chapter 3 we present a method to measure the ^{56}Ni mass for a sample of SNe using only their Near Infrared light curves, in order to circumvent systematic uncertainties from host galaxy reddening correction. In Chapter 4 we analyse the Near Infrared and bolometric properties of fast-declining SN Ia to shed light on their progenitor properties. In Chapter 6, we measure the ejecta masses for SN Ia using the measured contribution in the Near Infrared. In Chapter 5, we analyse Near Infrared properties of SN Ia at over 1 year after explosion to measure global properties e.g. ^{56}Ni mass and to use NIR spectra in the

nebular phase as an independent method to constrain properties of the dust around SN Ia. Finally, in Chapter 7 we present constraints on cosmological models from future experiments that can observe SN Ia in the NIR and hence, exploit their uniform nature at longer wavelengths.

2. Near Infrared Light Curves of Type Ia supernovae: Studying the properties of the Secondary Maximum [1]

2.1. Introduction

The uniformity of Type Ia supernovae (SNe Ia) has led to their use, after calibration, as distance indicators (reviewed in [104]) and they provided the first evidence for the accelerated expansion of the Universe [234, 251].

Observations of large SN Ia samples show that the peak luminosity in the optical is not uniform but can be normalised following a variety of calibration techniques, most notably the correlation between light curve shape and peak luminosity, and between light curve colour and peak luminosity (e.g. [107–109, 142, 237, 256]). The variation in bolometric luminosity for the objects [53] implies variations in the physical parameters of the explosion, in particular the synthesised Ni mass and the total ejected mass [267, 285].

At near-infrared (NIR) wavelengths (900nm $> \lambda >$ 2000nm), SNe Ia have a very uniform brightness distribution without any prior normalisation [69, 161, 166, 207]. The scatter in the peak luminosity in these studies is $\sim$0.2 mag, which when combined with the lower sensitivity of the NIR to extinction by dust, has sparked interest in the use of this wavelength region. Following large observational campaigns, statistically significant samples of SN Ia light curves

[1] This Chapter is already published in [61]

have been made public [15, 54, 288, 324], and have been used to construct the first rest-frame NIR Hubble diagrams [89, 151, 214, 318].

Dust extinction in the NIR is significantly reduced compared to the optical leading to smaller corrections and uncertainties. In addition to the photometric calibration systematics (see [50]), the dust extinction for SNe Ia is one of the major sources of systematics in SN Ia cosmology measurements (e.g [104,231]). In particular, extinction law measurements for galaxies remains uncertain (see discussions in [243, 270]). The recent SN 2014J is a case in point with derived dust properties very different from local interstellar dust [2,86]. Strongly reddened SNe Ia may also exhibit variations in their light curve shapes [2,173].

The light-curve morphology in the NIR is markedly different from that in the optical with a pronounced second maximum in $IYJHK$ filters for 'normal' SNe Ia [69, 70, 84, 173, 174, 207, 324]. The formation of the NIR spectrum in SNe Ia is highly sensitive to the opacity variations [281,320] as the spectrum is dominated by line blanketing opacity making the evolution of the NIR light a sensitive probe of the structure of the ejecta. [147] in a detailed study suggested that the second maximum is a result of a decrease in opacity due to the ionisation change of Fe group elements from doubly to singly ionised atoms, which preferentially radiate the energy at near-IR wavelengths. A direct prediction of [147] is that a larger iron mass leads to a later NIR second maximum.

Studies of the i band light curve find a relation between the phase of the second maximum and the optical light curve shape (e.g. $\Delta m_{15}(B)$; [84, 115]). The strength of the second maximum in i does not show such a correlation.

In this paper, we investigate the properties of SN Ia NIR light curves (YJH) and establish correlations with other observational characteristics. Connections to possible physical properties in the explosions are explored. The structure of this paper is as follows: after a presentation of the input data in Section 2.2, we analyse the NIR light curve properties (Section 2.3) along with a description of NIR colours. Correlations with optical light curve parameters and their interpretations are given in §2.4 followed by a discussion in §2.5. The conclusions are presented in Section 4.4.

Table 2.1.: SN sample

SN name	Phase range (days)	N_i	N_Y	N_J	N_H	N_K	Reference
SN1980N	5.7 ··· 99.7	...	...	11	13	...	M00
SN1981B	2.7 ··· 120.5	...	...	17	17	...	M00
SN1986G	−6.1 ··· 101.0	...	...	28	29	...	M00
SN1998bu	−8.5 ··· 31.5	...	...	23	23	...	M00
SN1999ac	−13.1 ··· 63.8	...	...	30	30	...	Ph06
SN1999ee	−7.5 ··· 27.5	...	17	18	20	...	K04a
SN1999ek	−8.0 ··· 23.0	...	...	14	15	...	K04a
SN2000E	−7.7 ··· 126.6	...	...	18	18	...	V03
SN2000bh	−5.5 ··· 39.0	...	6	21	22	...	K04a
SN2001ba	−6.0 ··· 34.9	...	...	14	15	...	K04a
SN2001bt	−1.6 ··· 65.3	...	...	21	21	...	K04a
SN2001cn	4.2 ··· 59.1	...	...	19	19	...	K04b
SN2001cz	−2.4 ··· 47.6	...	...	12	12	...	K04b
SN2001el	−10.6 ··· 64.3	...	...	33	32	...	K03
SN2002bo	−11.0 ··· 44.0	...	...	17	17	17	K04b, ESC
SN2002dj	−11.0 ··· 67.0	...	...	21	21	...	P08, ESC
SN2002fk	−12.2 ··· 102.1	...	...	24	23	23	C13
SN2003cg	−6.4 ··· 413.5	...	...	13	13	...	ER06, ESC
SN2003hv	1.2 ··· 62.0	...	16	16	16	...	L09, ESC
SN2004ef	−8.7 ··· 65.2	46	4	3	4	3	CSP
SN2004eo	−12.0 ··· 63.0	39	8	9	9	8	CSP, P07, ESC
SN2004ey	−8.9 ··· 48.1	32	7	9	9	8	CSP
SN2004gs	−3.6 ··· 99.1	50	12	11	10	...	CSP
SN2004gu	−0.4 ··· 48.6	27	8	7	7	...	CSP
SN2005A	−3.5 ··· 30.4	35	10	10	10	...	CSP
SN2005M	−8.0 ··· 74.7	56	17	17	14	12	CSP
SN2005ag	−1.7 ··· 66.3	44	9	9	9	...	CSP
SN2005al	−1.0 ··· 82.0	35	7	8	8	7	CSP
SN2005am	−4.6 ··· 75.3	36	6	6	6	6	CSP
SN2005el	−7.3 ··· 83.6	25	21	22	15	3	CSP
SN2005eq	−3.6 ··· 97.3	27	15	15	10	1	CSP
SN2005hc	−4.5 ··· 84.4	22	13	11	9	...	CSP
SN2005hj	−2.3 ··· 87.6	16	11	12	10	1	CSP
SN2005iq	−5.3 ··· 67.7	19	11	11	11	1	CSP
SN2005kc	−10.4 ··· 30.6	13	9	9	8	...	CSP
SN2005ki	−9.9 ··· 155.8	47	12	11	10	...	CSP
SN2005na	−1.8 ··· 94.0	27	14	11	12	...	CSP
SN2006D	−6.0 ··· 112.8	42	17	16	16	6	CSP
SN2006X	−11.0 ··· 119.8	39	32	33	32	9	CSP, ESC
SN2006ax	−11.7 ··· 71.2	26	19	18	16	3	CSP
SN2006bh	−4.9 ··· 60.0	24	12	11	10	...	CSP
SN2006br	5.8 ··· 37.7	9	5	5	5	...	CSP
SN2006ej	4.4 ··· 69.4	13	3	3	3	...	CSP
SN2006eq	0.2 ··· 43.0	18	10	7	8	...	CSP
SN2006et	−7.2 ··· 105.7	23	18	12	13	...	CSP
SN2006ev	4.2 ··· 48.1	12	10	8	8	...	CSP
SN2006gj	−1.8 ··· 96.0	19	13	10	4	...	CSP
SN2006gt	−2.1 ··· 62.8	13	10	8	6	...	CSP
SN2006hb	7.2 ··· 136.9	25	10	10	9	...	CSP
SN2006hx	−9.3 ··· 30.7	8	7	6	5	...	CSP
SN2006is	6.4 ··· 118.2	24	8	8	7	...	CSP
SN2006kf	−4.8 ··· 86.0	20	17	14	11	3	CSP
SN2006lu	5.1 ··· 90.1	21	6	4	3	...	CSP
SN2006ob	−2.6 ··· 58.3	13	12	9	5	...	CSP
SN2006os	2.4 ··· 57.3	14	10	6	5	...	CSP
SN2007A	−4.7 ··· 18.3	9	9	5	3	...	CSP
SN2007S	−10.5 ··· 102.2	19	12	17	18	7	CSP
SN2007af	−8.8 ··· 82.1	28	26	25	24	5	CSP
SN2007ai	−0.4 ··· 86.4	17	7	7	6	3	CSP
SN2007as	−0.0 ··· 77.7	19	11	10	10	...	CSP
SN2007bc	−3.0 ··· 58.8	10	11	8	6	...	CSP
SN2007bd	−9.5 ··· 215.8	14	12	9	7	...	CSP
SN2007bm	−0.2 ··· 34.7	10	10	9	7	...	CSP
SN2007ca	−8.8 ··· 32.1	12	10	8	7	2	CSP
SN2007if	14.4 ··· 100.2	16	8	7	5	...	CSP
SN2007jg	−3.1 ··· 58.8	18	8	6	5	...	CSP
SN2007le	−11.5 ··· 71.2	26	17	17	16	...	CSP
SN2007nq	−1.4 ··· 77.5	25	19	10	4	...	CSP
SN2007on	−8.6 ··· 88.2	38	29	28	25	7	CSP
SN2008C	2.9 ··· 85.6	19	15	13	18	1	CSP
SN2008R	−1.3 ··· 32.6	12	8	7	5	...	CSP
SN2008bc	−9.3 ··· 96.6	32	7	12	11	...	CSP
SN2008bq	−0.8 ··· 43.1	16	4	4	4	...	CSP
SN2008fp	−6.0 ··· 89.9	28	22	20	20	7	CSP
SN2008gp	−10.5 ··· 34.4	19	10	11	9	...	CSP
SN2008hv	−10.5 ··· 78.3	25	18	16	16	...	CSP
SN2008ia	−3.5 ··· 43.5	15	16	15	14	...	CSP
PTF09dlc	−5.56 ··· 19.5	...	...	4	4	...	BN12
PTF10hdv	−3.9 ··· 10.3	...	...	4	4	...	BN12
PTF10hmv	−10.1 ··· 7.9	...	...	...	5	...	BN12
PTF10mwb	−12.3 ··· 5.7	...	...	5	5	...	BN12
PTF10ndc	−3.9 ··· 5.1	...	...	4	4	...	BN12
PTF10nlg	−5.1 ··· 3.9	...	...	3	5	...	BN12
PTF10qyx	−3.5 ··· 7.5	...	...	4	4	...	BN12
PTF10tce	−6.6 ··· 6.5	...	...	4	4	...	BN12
PTF10ufj	−9.0 ··· 4.1	...	...	4	4	...	BN12
PTF10wnm	−7.1 ··· 4.8	...	...	4	4	...	BN12
PTF10wof	−3.9 ··· 9.1	...	...	4	4	...	BN12
PTF10xyt	−4.6 ··· 7.3	...	...	2	5	...	BN12
SN2011fe	−16.0 ··· 45.9	...	...	32	35	32	M12
SN2014J	−10.0 ··· 72.4	...	...	24	24	24	F14

References: M00 - [207]; Ph06 - [239]; K04a - [164]; V03 - [310]; K04b - [166]; P08 - [245]; C13 - [44]; ER06 - [71]; K09 - [162]; P07 - [225]; CSP - Carnegie Supernova Project [54, 288]; M12 - [201]; F14 - [86]

2.2. Data

We investigate a large sample of nearby objects with well-sampled optical and NIR data (Table 2.1). The main data source of NIR SN Ia photometry is the Carnegie SN Project (CSP; [36,37,54,238,288]). The low-redshift CSP provides a sample of SNe Ia with optical and NIR light curves in a homogeneous and well-defined photometric system (in Vega magnitude system) and thus forms an ideal basis for the evaluation of light curve properties. CSP relies primarily on SN discoveries from the Lick Observatory SN Search (LOSS; [172]). The CSP has published light curves on a total of 82 SNe Ia of which 70 have photometry in $YJHK$ bands.

From the CSP NIR dataset, we removed spectroscopically peculiar objects such as SN2006bt and SN2006ot. We also rejected SNe Ia with spectra similar to the peculiar SN 1991bg [78,175] and objects that do not exhibit a second maximum (SNe 2005bl, 2005ke, 2005ku, 2006bd, 2006mr, 2007N, 2007ax, 2007ba, 2009F).

We have included in our sample near-IR SN Ia photometry from [207] and several SNe Ia observed by the European SN Consortium (ESC; [16, 71, 162, 225, 245]). Twelve SNe Ia have been discussed by [15] and have data only near the first maximum. We also included NIR photometry from two recent nearby explosions, SN2011fe [201] and SN2014J [86].

The 91 objects used in this work are listed in Table 2.1, where the phase range of observations (first and last observation), total number of observations in each filter and the reference for each data set are tabulated. The sample is dominated by SNe Ia from the CSP and we show the results separately for the CSP and non-CSP objects. It is worth noting that there are 15 SNe Ia with observed NIR light curves beyond 100 days.

As can be seen in Table 2.1 and displayed in Fig. 2.1, the K-band light curves are sparsely sampled and not enough objects are available for detailed analysis. Therefore, we exclude the K-band light curves from further analysis.

2.3. NIR Light Curve Morphology

In parameterising the NIR light curves we follow the nomenclature introduced by [24]. The first maximum in filter X, $M_1(X)$ is reached at a phase, $t_1(X)$ relative to the phase of the B maximum (t_B^{max}=0 d). The light curves dip to a minimum $M_0(X)$ at $t_0(X)$ before reaching a second maximum, $M_2(X)$ at time, $t_2(X)$. These three prominent features are shown in Fig. 2.1. The light curves are plotted without normalisation for phase or corrections for possible differences in photometric systems or absorption.

2.3.1. Light curve fitting

We fit the optical light curves using the programme SNooPy [37] to determine the peak of the B-band light curve through cubic-spline fitting and determine the phase, t_B^{max} used throughout this work and the peak brightness m_B^{max}. SNooPY also determines the Δm_{15} parameter[1] commonly used to characterise the SN light curve shape and provides an estimate of the extinction in the host galaxy. The SNooPy light curve fit parameters and distance moduli for the SNe Ia in our sample are given in Table 2.2. We used the published values of the distance modulus, μ, for non-CSP objects, (references in Table 2.2). The distance moduli for CSP SNe Ia not in the Hubble flow are taken from [54] and [288], and the individual references are listed in Table 2.2. The distance moduli for the rest of the SNe are based on the host galaxy redshift from the NASA/IPAC Extragalactic Database adopting a Hubble constant of H_0=70 km s^{-1} Mpc^{-1}.

While the extinction is much reduced in the NIR it is not entirely negligible. Using the Cardelli extinction law [41], the extinction in the H-band is $\sim$18% of that in V-band. We have also included some heavily-extinguished SNe Ia like SNe 1986G, 2005A, 2006X, 2006br and 2014J without an extinction correction in our sample. Therefore, the observed scatter is larger than the intrinsic variation among SNe Ia. We have chosen not to apply a correction for the host galaxy extinction as the reddening law remains under debate (e.g. [243]).

[1] The Δm_{15} is calculated by SNooPy from all available filters. It is linearly related to $\Delta m_{15}(B)$ (see [37])

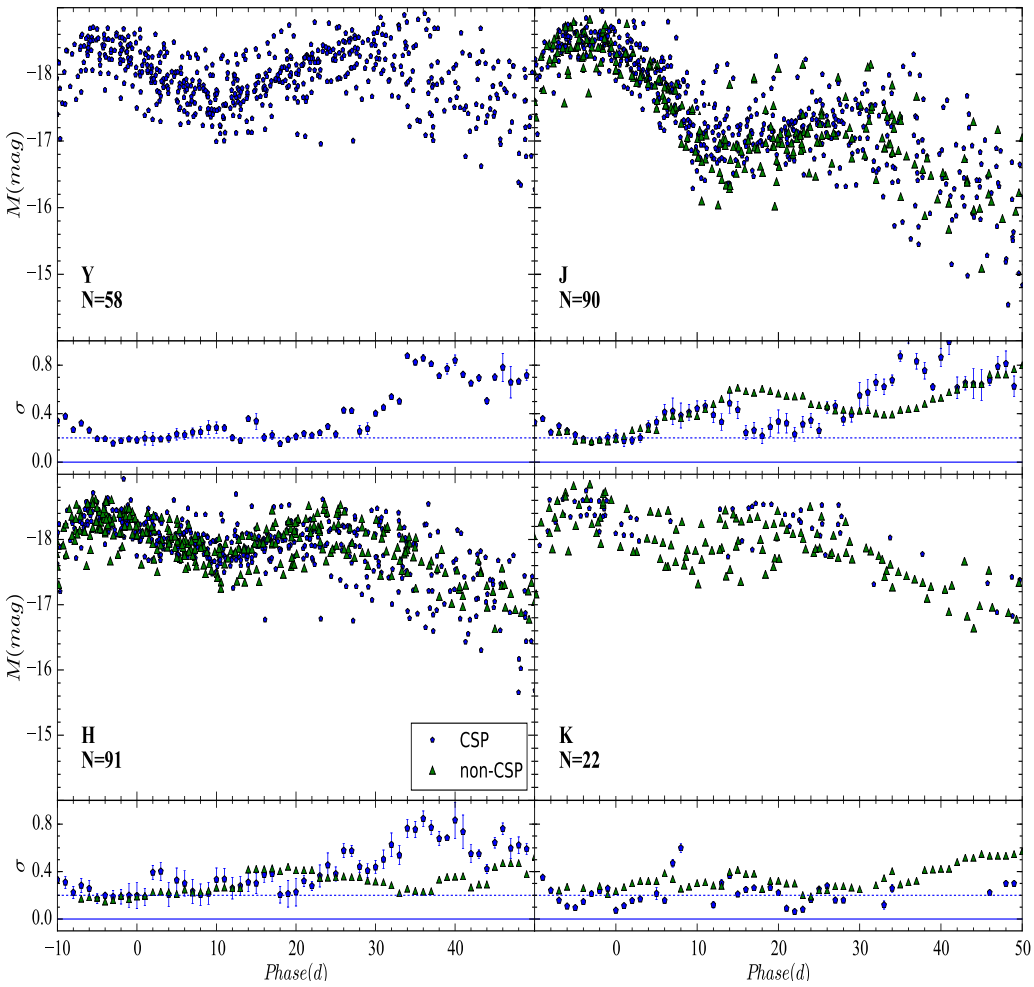

Figure 2.1.: The Y, J, H and K absolute magnitude light curves of SNe Ia. The CSP sample is shown as blue pentagons. The green triangles indicate the non-CSP sample (see Table 2.1 for the references). The root-mean-square (RMS) scatter for each day is shown in the lower panels. For guidance a line at a scatter of 0.2 magnitudes is drawn in each panel. The luminosities are based on the literature distances (cf. Table 2.2) and no correction has been applied. The steady increase of the scatter after the first maximum is evident.

Table 2.2.: Timing of B_{max}, Δm_{15}, distance modulus for the SN in our sample. References for the published distance moduli are provided in the footnote.

SN Name	$t(B_{max})$ (MJD)	err	Δm_{15} (mag)	err	μ (mag)	err
SN1980N	44585.8	0.5	1.28	0.04	31.59	0.10
SN1981B	44672.0	0.2	1.10	0.04	30.95	0.07
SN1986G	46561.0	0.1	1.76	0.10	28.01	0.12
SN1998bu	50953.3	0.5	1.01	0.02	30.20	0.10
SN1999ac	51251.0	0.5	1.34	0.02	33.50	0.30
SN1999ee	51469.1	0.5	1.09	0.02	33.20	0.20
SN1999ek	51481.8	0.1	1.17	0.03	34.40	0.30
SN2000E	51557.0	0.5	0.99	0.02	31.90	0.40
SN2000bh	51635.2	0.5	1.16	0.01	34.60	0.30
SN2001ba	52034.5	0.5	0.97	0.05	35.40	0.50
SN2001bt	52063.4	0.5	1.18	0.02	34.10	0.40
SN2001cn	52071.6	0.2	1.15	0.02	34.10	0.30
SN2001cz	52103.9	0.1	1.05	0.07	33.50	0.10
SN2001el	52182.5	0.5	1.13	0.04	31.30	0.20
SN2002bo	52356.5	0.2	1.12	0.02	31.80	0.20
SN2002dj	52450.0	0.7	1.08	0.02	32.90	0.30
SN2002fk	52547.9	0.3	1.02	0.04	32.59	0.15
SN2003cg	52729.4	0.5	1.12	0.04	31.28	0.20
SN2003hv	52891.2	0.3	1.63	0.02	31.40	0.30
SN2004ef	53264.4	0.1	1.45	0.01	35.57	0.07
SN2004eo	53278.4	0.1	1.32	0.01	34.03	0.10
SN2004ey	53304.3	0.1	1.02	0.01	34.01	0.12
SN2004gs	53356.2	0.1	1.53	0.01	35.40	0.08
SN2004gu	53362.2	0.2	0.80	0.01	36.59	0.04
SN2005A	53379.7	0.2	1.08	0.02	34.51	0.11
SN2005M	53405.4	0.1	0.80	0.04	35.01	0.09
SN2005ag	53413.7	0.2	0.87	0.01	37.80	0.03
SN2005al	53430.5	0.1	1.30	0.01	33.79	0.15
SN2005am	53436.9	0.1	1.48	0.01	32.85	0.20
SN2005el	53647.0	0.1	1.40	0.01	34.04	0.14
SN2005eq	53654.4	0.1	0.82	0.01	35.46	0.07
SN2005hc	53666.7	0.1	0.80	0.01	36.50	0.05
SN2005hj	53673.8	0.2	0.80	0.02	37.03	0.04
SN2005iq	53687.7	0.1	1.28	0.01	35.80	0.15
SN2005kc	53697.7	0.1	1.12	0.02	33.89	0.15
SN2005ki	53705.5	0.1	1.36	0.01	34.73	0.10
SN2005na	53740.2	0.1	1.03	0.01	35.34	0.08
SN2006D	53757.7	0.1	1.47	0.01	33.00	0.15
SN2006X	53786.3	0.1	1.09	0.03	30.91	0.08
SN2006ax	53827.2	0.1	1.04	0.01	34.46	0.11
SN2006bh	53833.6	0.1	1.42	0.01	33.28	0.20
SN2006br	53853.7	0.6	1.45	0.05	35.23	0.08
SN2006ej	53976.4	0.2	1.37	0.01	34.62	0.11
SN2006eq	53975.9	0.4	1.88	0.04	36.66	0.04
SN2006et	53993.7	0.1	0.88	0.01	34.82	0.10
SN2006ev	53990.1	0.3	1.34	0.01	35.40	0.08
SN2006gj	54000.3	0.2	1.56	0.04	35.42	0.08
SN2006gt	54003.1	0.3	1.71	0.03	36.43	0.05
SN2006hb	54006.0	0.3	1.69	0.02	34.11	0.13
SN2006hx	54021.9	0.2	1.07	0.05	36.47	0.05
SN2006is	54007.5	0.4	0.80	0.01	35.69	0.07
SN2006kf	54041.3	0.1	1.51	0.01	34.78	0.10
SN2006lu	54034.4	0.2	0.92	0.01	36.92	0.04
SN2006ob	54063.4	0.1	1.51	0.01	37.08	0.04
SN2006os	54063.9	0.2	1.08	0.02	35.70	0.07
SN2007A	54113.1	0.2	1.06	0.04	34.26	0.13
SN2007S	54143.8	0.1	0.81	0.01	34.06	0.14
SN2007af	54174.4	0.1	1.11	0.01	32.10	0.10
SN2007ai	54173.5	0.3	0.84	0.02	35.73	0.07
SN2007as	54181.3	0.4	1.27	0.03	34.45	0.12
SN2007bc	54200.3	0.2	1.27	0.02	34.89	0.10
SN2007bd	54206.9	0.1	1.27	0.01	35.73	0.07
SN2007bm	54224.1	0.2	1.11	0.02	32.30	0.07
SN2007ca	54227.7	0.2	1.05	0.03	34.04	0.14
SN2007if	54343.1	0.6	1.07	0.03	37.59	0.03
SN2007jg	54366.1	0.3	1.09	0.04	36.03	0.06
SN2007le	54399.3	0.1	1.03	0.02	32.34	0.08
SN2007nq	54398.8	0.1	1.49	0.01	36.44	0.05
SN2007on	54419.8	0.4	1.65	0.04	31.45	0.08
SN2008C	54466.1	0.2	1.08	0.02	34.34	0.12
SN2008R	54494.5	0.1	1.77	0.04	33.73	0.16
SN2008bc	54550.0	0.1	1.04	0.02	34.16	0.13
SN2008bq	54562.1	0.2	0.78	0.02	35.79	0.06
SN2008fp	54730.9	0.1	1.05	0.01	31.79	0.05
SN2008gp	54779.1	0.1	1.01	0.01	35.79	0.06
SN2008hv	54817.1	0.1	1.30	0.01	33.84	0.15
SN2008ia	54813.2	0.1	1.34	0.01	34.96	0.09
SN2011fe	55815.0	0.3	1.20	0.02	28.91	0.20
SN2014J	56689.7	0.3	1.10	0.02	27.64	0.10

References: SN1980N, SN1981B, SN1986G, SN1998bu [207]; SN1999ac, SN1999ee, SN2002dj [323]; SN2000E, SN2002bo [307]; SN2001el [1]; SN2003hv, SN2007on [302]; 2006X [91] (note: we add the correction to μ's from [302] and [1] using the values provided in [140])

We fit a spline interpolation to the data to derive the phase and magnitude at maximum, the minimum and the second maximum in each filter. In order for a measurement of the minimum and second maximum to be made, we require $\geq$4 observations at late phases (>7 d for the minimum and >15 d for the second maximum). We also require that observations at least 4 d before t_{max} were available. The uncertainties for each derived parameter were calculated by repeating the fits to 1000 Monte Carlo realisations of light curves generated using the errors on the photometry.

The NIR light curves are very uniform up to the time of the B-band maximum, $\sim$3–4 d after the maximum is reached in the NIR light curves. In the lower panels in Fig. 2.1, we show the RMS scatter for each epoch.

The scatter remains small for $\sim$1 week around maximum in the different bands independent of the sample (CSP or non-CSP). The two samples show very consistent scatter out to a phase of $\sim$10 d in J and $\sim$25 d in H, after which they start to deviate. With only 14 objects in the non-CSP sample in this phase range compared to 25 from the CSP, we consider the differences not statistically significant. The scatter continues to increase beyond 35 d, which we attribute to the colour evolution (see §2.3.6 below).

2.3.2. The first maximum

[69] showed, in a small sample of SNe Ia, that the JHK light curves of SNe Ia peak earlier than the optical light curves. We confirm this for our sample (Fig. 2.2).

The NIR light curves peak within -2 to -7 d of the B-band peak confirming the result of [84] for SNe Ia with $\Delta m_{15}(B)$ <1.8. There is no obvious difference between our full sample and the CSP sample as seen in the scatter. The distribution of t_1 is remarkably tight (less than one day dispersion) for all filters. This indicates a close relationship between t_B^{max} and the NIR t_1 values for the SNe Ia in our sample.

Table 2.3 gives the phase of lowest scatter measured in each filter. Without any attempt to normalise the light curves, we find the smallest scatter in all NIR light curves near t_1. The dispersion remains very low for $\sim$1 week, before increasing to >0.2 mag at later phases.

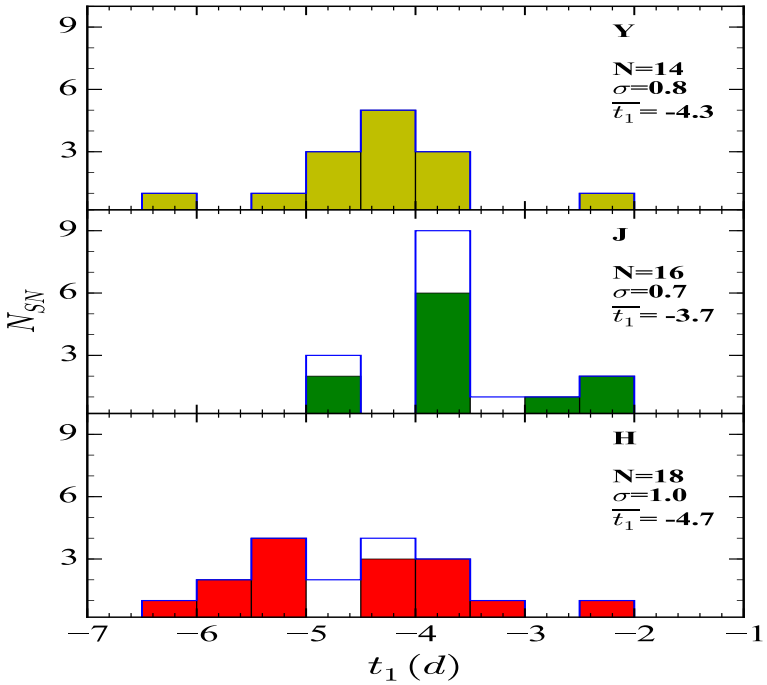

Figure 2.2.: Distribution of t_1 for the Y, J, and H light curves relative to the B-band maximum. The filled histograms are for SNe Ia from the CSP sample while the open histograms show the combined CSP and non-CSP sample. In the Y band, we only use the objects observed by the CSP. The NIR light curves peak at within -2 to -7 d relative to the B maximum.

2.3.3. The minimum

The minimum in J occurs $\sim$2 weeks after t_B^{max} (Fig. 2.3). The Y light curves dip about 3 d earlier at $t_0 = +11$ d. The minimum in H is reached on average about 2 d before J at $t_0 = +12$ d. The phase range is still relatively narrow with the minima all occurring within roughly ± 2 d. While Y and H display a tight distribution of t_0, the J distribution exhibits a tail of late minima.

No significant difference between the CSP and the literature samples can be seen in the distributions. The scatter among M_0 is fairly small for the three

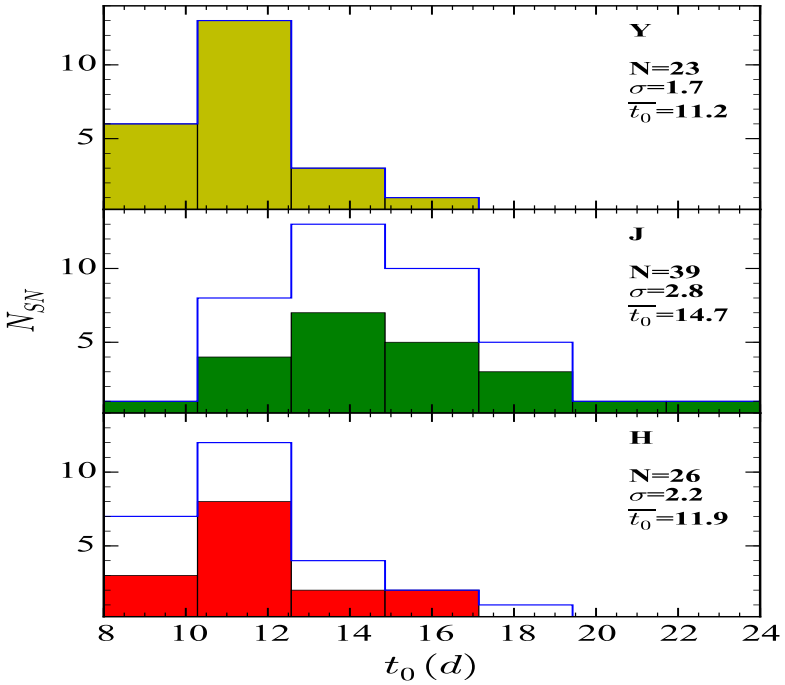

Figure 2.3.: Distribution of t_0 in Y, J, and H light curves. The Y and H minimum is reached a few days before the J light curve dips, which occurs ∼2 weeks after B-band maximum.

Table 2.3.: Magnitude scatter in NIR light curves. The second column indicates the time of minimum magnitude scatter in each filter, while the third column gives the scatter at this phase. The fourth column gives the phase range for which the scatter stays below 0.2 mag.

Filter	t (days)	$\sigma(M)$ (mag)	Phase range ($\sigma(M) < 0.2$ mag)	SN sample
Y	−4.4	0.15	[−4 , +1]	CSP
J	−3.6	0.16	[−4 , +3]	CSP
J	−3.8	0.17	[−6 , +1]	non-CSP
H	−5.1	0.17	[−5 , +1]	CSP
H	−4.7	0.14	[−7 , +2]	non-CSP

NIR bands although about 2 to 3 times larger than at t_1. In the Y-band, the scatter is low (<0.2 mag) immediately after t_0, while the J and H light curves display a larger dispersion at this point.

2.3.4. The second maximum

Figure 2.4 shows that t_2 occurs over a wide range of phases and can vary by as much as 20 d from one SN Ia to another. This diversity had been observed before for the i light curves (e.g. [84]) and for JHK [24]. In Figure 2.4, we show that the mean t_2 is later in Y- and J-bands, with the H-band light curves reaching t_2, on average, a few days earlier. The scatter in the luminosity starts to increase slowly after t_0, and is seen to increase significantly (>0.5 mag) around the time of t_2 (Fig. 2.1).

2.3.5. The late decline

After the second maximum, the light curves steadily decline. In Fig. 2.5 we show the distribution of slopes calculated for SNe Ia with at least three observations in phases $40<t<90$ d. This choice of phase range ensures that the measurements are not influenced by the second maximum. All the SNe Ia in our sample with data at these late phases come from the CSP.

There is a tight distribution of decline rates in the Y- and H-bands, with the notable exception of SN 2005M in H, which declined twice as fast as the other SNe Ia. The scatter in the H-band decline rate, when excluding SN 2005M, is only 0.004 mag per day, similar to the scatter in the Y filter. The same SN is also one of the two fast declining objects in J (in the fastest bin, *middle panel*), where the scatter in the decline rates is significantly larger than for the other two bands.

2.3.6. NIR colours

[70] showed that the early $J-H$ colour evolution is rather uniform for SNe Ia. In Fig. 2.6, we show the colour curves ($Y-J$ and $J-H$) for the CSP and

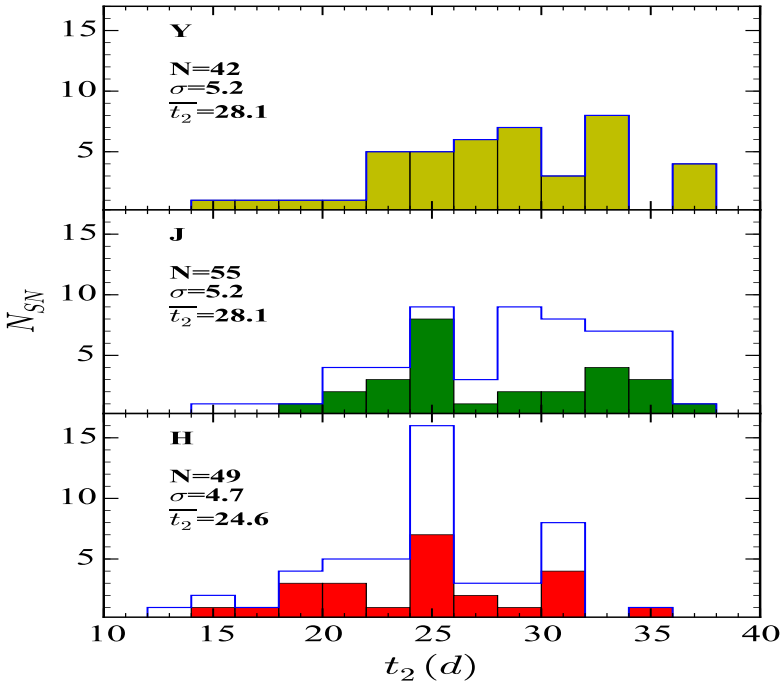

Figure 2.4.: Distribution of t_2 in the Y, J and H light curves. Note the expanded scale on the abscissa compared to the phase ranges in Figs. 2.2 and 2.3.

non-CSP objects. The scatter at each epoch is plotted in the lower panels. Similar to the light curves, the early colour evolution is similar for most SNe Ia in our sample.

At the first maximum the scatter is minimal in $Y-J$ ($\sigma(Y-J)=0.07$ mag) and in $J-H$ ($\sigma(J-H)=0.05$ mag). The scatter stays <0.1 mag between -7 and -3 d for $Y-J$ and between -10 and -3 d for $J-H$. At early times, we find that the samples display the same scatter. Immediately after the first maximum, the colour curves start to deviate like the light curves. By the time of the minimum the colours display a wide spread which continues to increase into the late decline.

The $Y-J$ colour remains fairly constant until about one week after maximum when the $Y-J$ colour starts a monotonic evolution towards bluer colours.

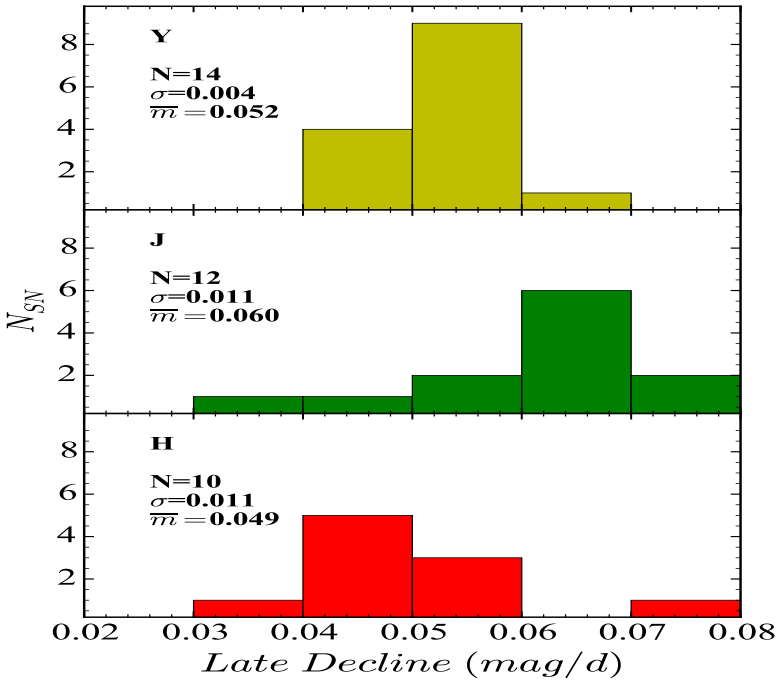

Figure 2.5.: Distribution of decline rates after t_2.

For the $J - H$ colour, SNe Ia evolve to redder colours after maximum. Then after the light curve minimum, the $J - H$ colour tends towards slightly bluer colours until ∼30 d.

2.4. Correlations

The uniformity of the NIR light curves at maximum light suggests that the size of the surface of last scattering at these wavelengths is independent of the details of the explosion and progenitor.

A diversity in the NIR only becomes visible at later phases as the lines contributing to the line blanketing opacity arise from deeper in the ejecta. The phase and magnitude the minimum and in particular the second maximum of the NIR light curves display large variations. Correlating these changes with

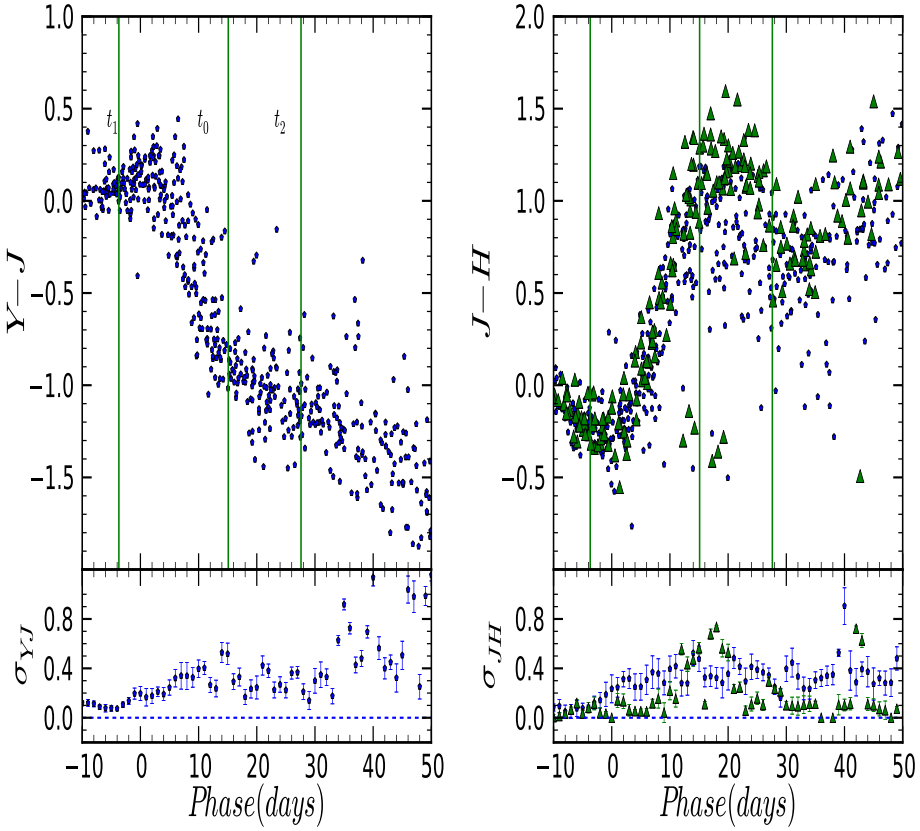

Figure 2.6.: *Left*: $Y - J$ colour curve. The mean t_1, t_0 and t_2 in the Y filter are plotted as green lines. The scatter plot in the lower panel only contains information from the CSP objects since the non-CSP sample does not have Y-filter observations. The blue points are the objects in the CSP sample, whereas the green points are the non-CSP objects. *Right*: $J - H$ colour curve. The epoch of minimum scatter in J, the average value of t_0 and t_2 in J are overplotted in green. The lower panel shows the evolution of the scatter around the mean in the colour curve.

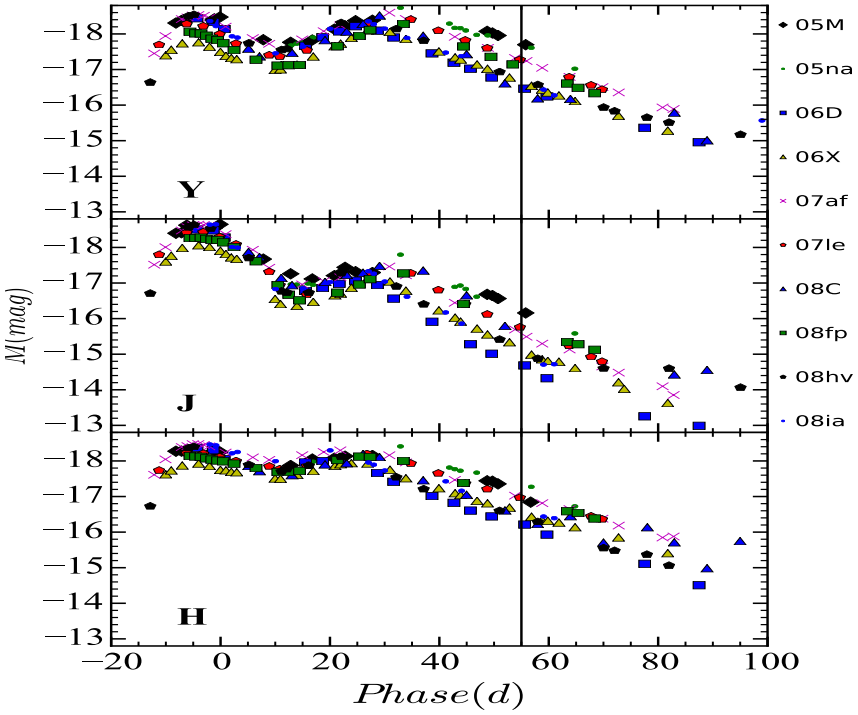

Figure 2.7.: Complete absolute magnitude light curves in YJH for the 10 objects for which a late decline is measured in all three filters. The figure illustrates that the decline rates at late times are uniform, whereas there is a large scatter in the absolute magnitude at +55 d indicated by the vertical line.

other SN parameters should shed light on the physical processes underlying the explosions and the release of the radiation.

In Fig. 2.7 we show example NIR light curves extending to late times for 10 SNe Ia in our sample. It should be noted that among these 10 SNe are two where the extinction has been determined to be high (SN 2006X and SN 2008fp). Therefore, some of the scatter can be attributed to uncorrected host galaxy extinction.

In the following sections, we note that correlations reported with $r > 0.4$ are significant, and those with $r > 0.65$ are termed as strong.

2.4.1. NIR light curve properties

In the previous section, we found a large diversity in the NIR light curve properties at post-maximum epochs. In this section, we investigate correlations between these properties in more detail. We find a correlation between t_0 and t_2 in JH filters (Pearson parameter $r \sim 0.5$) suggesting that a later minimum is followed by a later second maximum. We also find a correlation between M_2 and M_0 in Y and J filters, with $r = 0.59$ and $r = 0.50$ respectively. This implies that SNe Ia with a more luminous minimum also display a more luminous second maximum.

Interestingly, the M_2 and t_2 do not correlate ($r < 0.4$) in any filter. However, there we do find a significant correlation across different filters between M_2 and t_2 (e.g. M_2 in Y band correlates with t_2 in J band with $r = 0.61$). [193] found that the rate of luminosity increase (rise rate r/β in the [193] nomenclature) to the second maximum correlated with the luminosity of the first peak. We cannot confirm this at any significance with our data.

Comparison of Figs. 2.3 and 2.4 reveals that the light curve evolution in the Y-band is slowest amongst the NIR filters. SNe Ia on average reach t_0 in Y earlier than in J and H, but reach t_2 later in the Y compared to the other filters. The rise time in Y is nearly 4 d longer than in J and nearly 7 d longer than in H.

The phase and luminosity of the second maximum strongly correlate between the NIR filters (Fig. 2.8). SNe Ia with a later t_2 display a higher luminosity during the late decline. The luminosity at 55 d past the B maximum, hereafter referred to as $M|_{55}$ was chosen to ensure all SNe Ia have entered the late decline well past t_2. A choice of a later phase may be more representative of the decline but would result in a smaller SN sample as not many objects are observed at these epochs and the decreasing flux results in larger uncertainties.

In Figure 2.9 we plot $M|_{55}$ against t_2 and M_2. A clear trend between $M|_{55}$ and t_2 is present in all filters (Pearson coefficients r of 0.78, 0.92, 0.68 in the YJH, respectively; Fig. 2.9, left panels). At this phase SNe Ia are on average most luminous in Y followed by H and J, a trend that is already present at M_2. This is also reflected in the NIR colour evolution (see section §2.3.6).

The dispersion in $M|_{55}$ is large with $\sigma(M|_{55}) = 0.48$ mag, 0.51 mag and

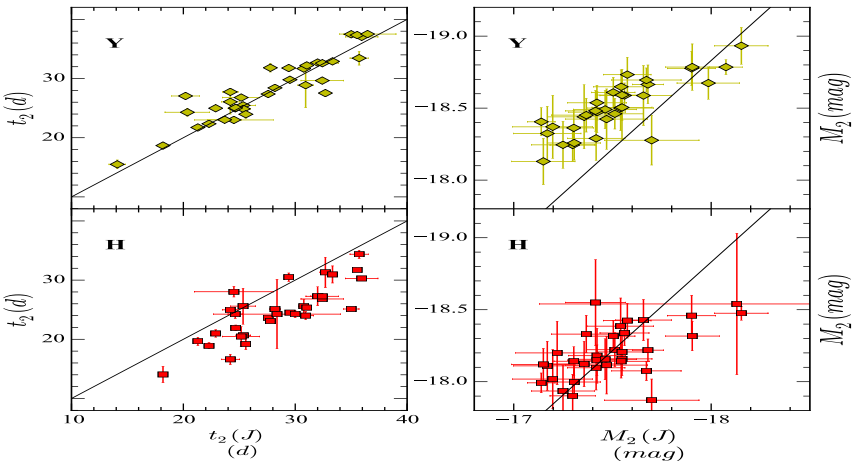

Figure 2.8.: Phases (*left*) and luminosity (*right*) of the second maximum in NIR filters. There are clear correlations between the filters with the weakest trend in the H versus J luminosities. The black line is a one-to-one relation.

0.30 mag in Y, J and H, respectively. This is not unexpected as it continues the trend to larger (luminosity) differences in the NIR light curves with increasing phase.

2.4.2. Correlations with optical light curve shape parameters

It is interesting to see whether the NIR light curve parameters correlate with some of the well known optical light curve shape features (Δm_{15}; [37]).

[84] have shown that the value of t_2 in i correlated with $\Delta m_{15}(B)$. Since the dispersion increases with phase we concentrate on the second maximum and explore whether the timing and the strength correlate with the optical light curve shape.

The second maximum in the NIR is a result of an ionization transition of the Fe-group elements from doubly to singly ionized states. Models predict that t_2 depends on the amount of Ni (M_{Ni}) synthesized in the explosion [147]. Since M_{Ni} is known to correlate with m_B^{max}, which itself is a function of the light

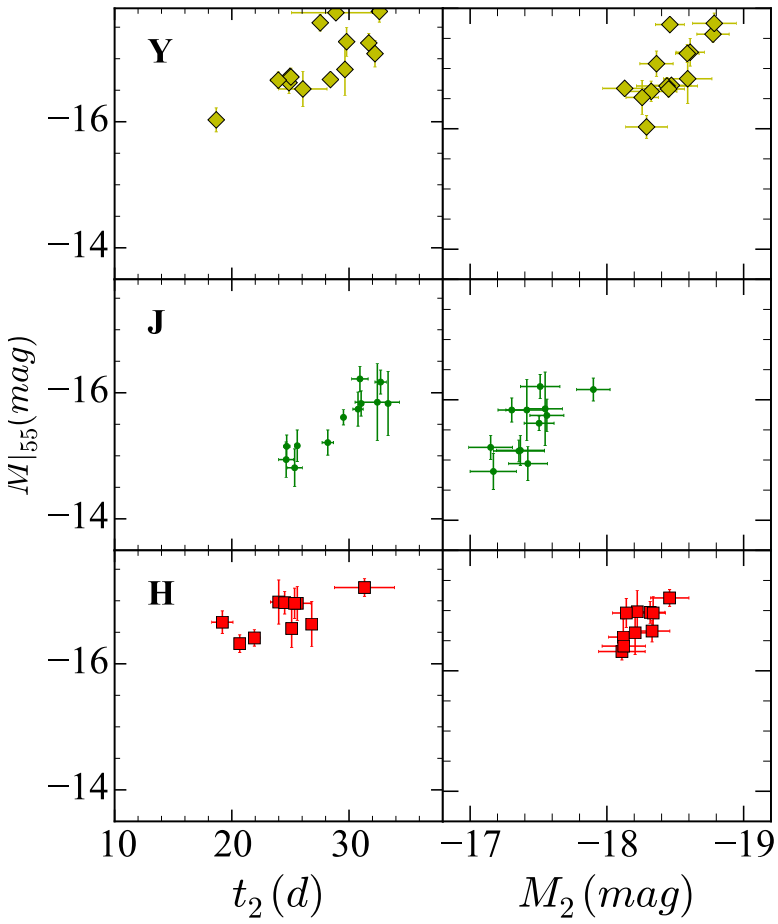

Figure 2.9.: (*Left:*) Absolute magnitude at $t = 55$ d in YJH *vs.* t_2. (*Right:*) $M|_{55}$ compared to the absolute magnitude of the second maximum M_2.

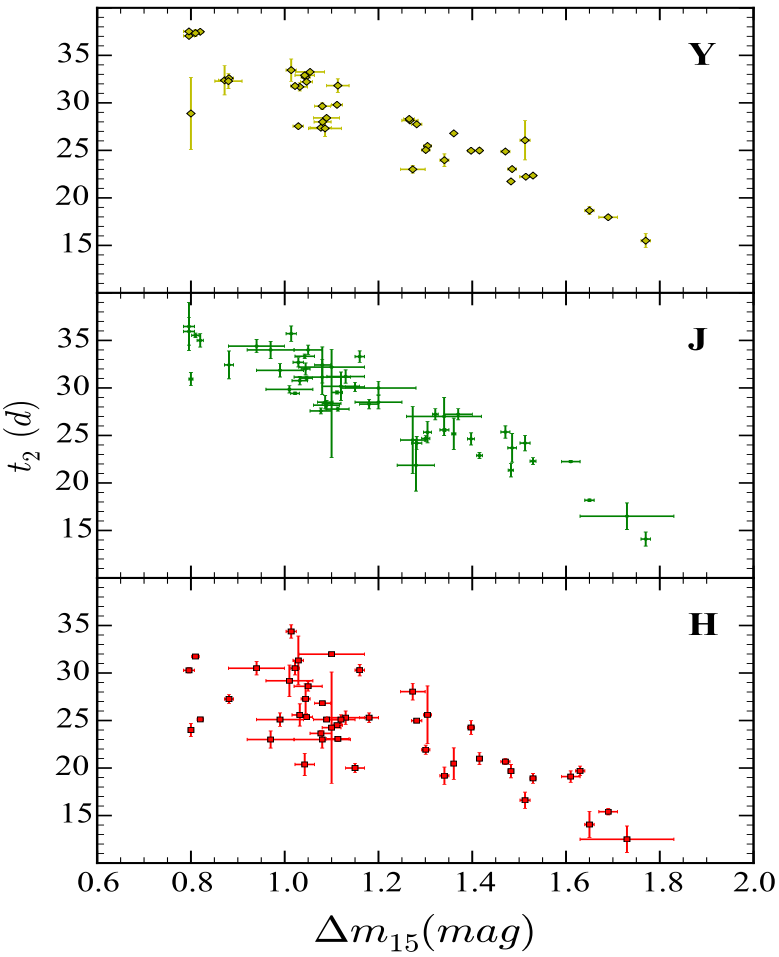

Figure 2.10.: Comparison of t_2 in the NIR light curves with $\Delta m_{15}(B)$.

curve shape [5, 204, 269, 285], we explored the relation between t_2 and Δm_{15} (Tab. 2.2).

Figure 2.10 confirms a strong correlation between t_2 and Δm_{15}. The Pearson coefficients are 0.91, 0.93 and 0.75 for the Y, J, and H-bands, respectively. The weaker correlation in H may be due to a low dependency on t_2 for objects with $\Delta m_{15} < 1.2$, where t_2 appears independent of Δm_{15}. This applies only to SNe Ia with a slow optical decline. For higher Δm_{15}, the trend is as strong

as in the other filters.

A linear regression yields equation 2.1 for each filter. The RMS scatter is 2.1 d, 1.8 d and 3.0 d in the YJH filters.

$$t_2(Y) = (-20.6 \pm 1.0)\Delta m_{15} + (53.6 \pm 1.2) \tag{2.1a}$$

$$t_2(J) = (-20.3 \pm 0.9)\Delta m_{15} + (51.7 \pm 1.1) \tag{2.1b}$$

$$t_2(H) = (-16.0 \pm 2.7)\Delta m_{15} + (42.3 \pm 2.8) \tag{2.1c}$$

Since the phase of the second maximum (t_2) in NIR bands is strongly correlated with Δm_{15} and thereby the optical maximum luminosity, t_2 could also serve as an indicator of the luminosity of SNe Ia. It is noteworthy that even extreme cases, like SN 2007if, which have been associated with super-Chandrasekhar mass progenitors [266, 268] are fully consistent with the derived relations.

There is a weak correlation between M_2 and Δm_{15} as shown in Fig. 2.11, with very little difference between objects. We find r values of 0.59, 0.50 and 0.63 for the Y, J, and H filters, respectively.

2.5. Discussion

As has been shown earlier in this paper and in a number of other publications [15, 207, 318, 324], SN Ia NIR light curves show remarkable uniformity around maximum light, compared to at optical wavelengths. This uniformity, combined with reduced effects of extinction, holds great promise for the use of SNe Ia as distance indicators in the NIR. [151] proposed to further reduce the scatter in the luminosity of the first maximum in the NIR by a decline rate correction similar to the procedure in the optical.

The spread in optical luminosity is attributed to different masses, or distributions, of ^{56}Ni within the ejecta [5, 269, 285]. The indifference of the NIR maximum light to the nickel mass suggests that it is intermediate-mass elements that dominate the opacity in these bands at maximum light.

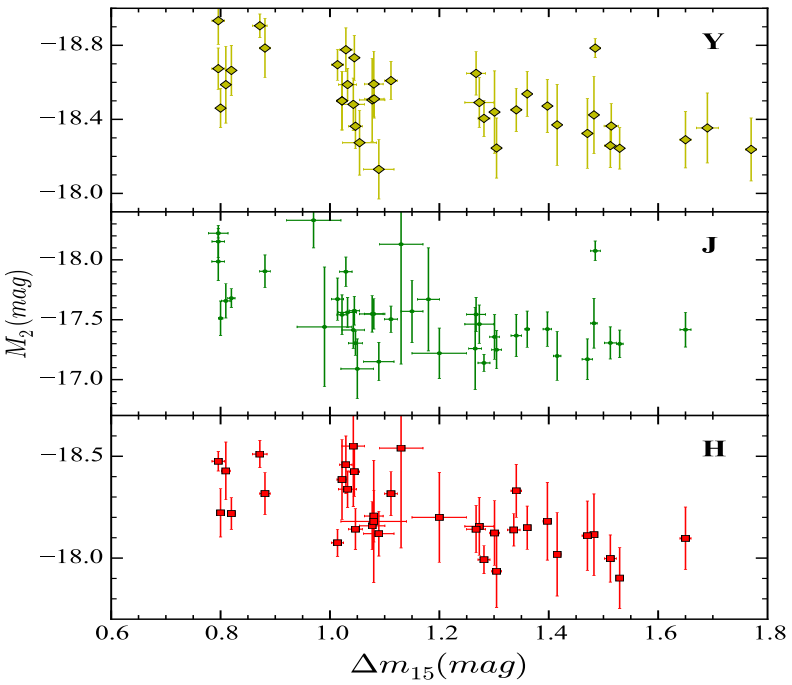

Figure 2.11.: M_2 versus Δm_{15} is shown and a weak correlation is observed.

The NIR light curves showed an increased dispersion at later times. We attribute this increased scatter to differences in the speed of the evolution of the SNe Ia. The phase of the second maximum depends on the mass and distribution of ^{56}Ni, the change in opacity, the ionisation and the dominant species setting the emission.

Not all SNe Ia display a second maximum (e.g. [162]) and we restricted our analysis only to objects in which the second maximum is defined well enough to be fit. This translates into a sample including only SNe Ia with $\Delta m_{15}(B) < 1.8$ mag. Events without a second maximum tend to be of low luminosity, often similar to SN 1991bg, and with large $\Delta m_{15}(B)$.

The strength of the second peak in the $iJHK$ light curves does not correlate with Δm_{15}, but the phase does [24, 84].

As presented in the previous section, we confirm this relation between t_2 and

Δm_{15} for the YJH filters. The correlation of M_2 with Δm_{15} is rather weak (Fig. 2.11) although it appears somewhat stronger than in [24] (the Pearson coefficients in our data are 0.5 and 0.63 for J and H compared to 0.12 and 0.08 in [24]).

2.5.1. A possible physical picture

The various features of the NIR light curves can be assembled into a physical picture of the explosions. The striking similarities of the late decline rates, when the SN becomes increasingly transparent to the $\gamma-$rays generated by the radioactive decays, indicate that the internal structure of the explosions is probably similar for all SNe Ia considered here. The uniform decline rates are consistent with the predictions of [328] for a range of Chandrasekhar-mass models, with different M_{Ni} but similar radial distribution of iron-group elements. We find that the late-time decline rate in J is faster than in Y and H, a trend also seen between the simulated J and H light curves in [59]. The NIR light curves depend very little on the explosion geometry [168]. The DDC15 models of [28] show that the YHK decline rates are similar to the pseudo-bolometric decline rate (S. Blondin, private communication). The J band shows a faster decline due to a lack of emission features [281]. This also explains the evolution of the $J-H$ colour curve to redder colours at late times.

At the these late times $M|_{55}$ shows a large scatter (cf. Fig. 2.9). If the similar late decline rates (cf. Fig. 2.5) indicate a similarity in the evolution of the γ-ray escape fraction for different SNe Ia,then, a higher luminosity would translate into a higher energy input at late phases, i.e. a larger mass of Fe-group elements.

[147] predicted that the second maximum should be delayed for larger Fe masses, which is exactly what is observed in the NIR (see also [137]). According to [149], the faster decline in the B-band light curve is mostly due to line blanketing through Fe and Co lines, which shifts the emission into the NIR and shapes the NIR light curves after maximum. The optical colour evolution post B-maximum is suggested to be more rapid for explosions with lower Ni masses. If this is true then the onset of the uniform $B-V$ colour evolution (referred to as the 'Lira law' and originally defined as the uniformity of the

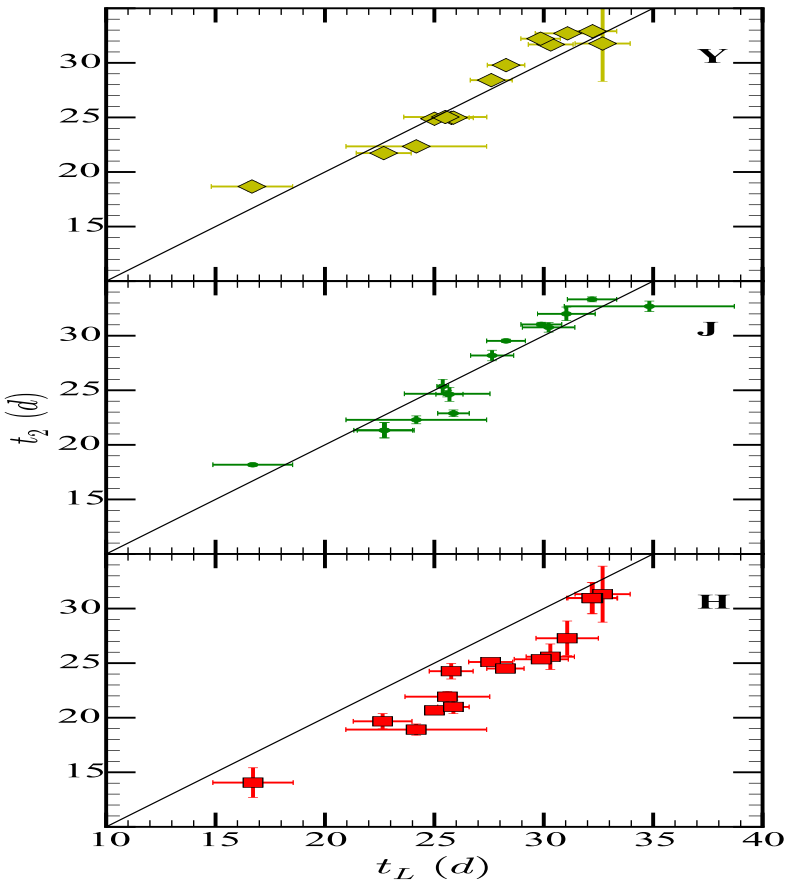

Figure 2.12.: The phase of the second maximum versus t_L. The black line is the one-to-one relation.

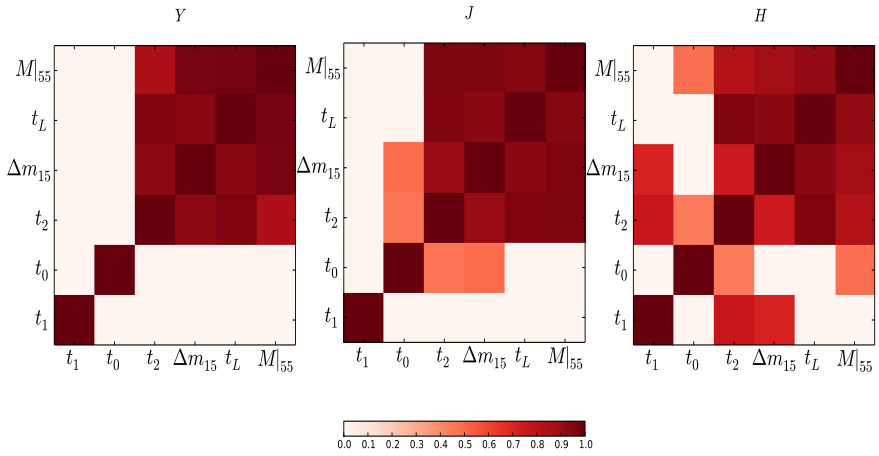

Figure 2.13.: A summary of the correlations between the timing parameters (t_1, t_0 and t_2), Δm_{15} , t_L and the late time luminosity ($M|_{55}$), in each filter There is a strong correlation amongst the t_2, Δm_{15}, t_L and $M|_{55}$ ($r > 0.65$). The colorbar scales from white to red in ascending order of correlation strength. Correlations with $r < 0.4$ have been set to white

slope of the colour curve from 30 to 90 days, although the onset is generally at earlier phase; [241]) marks the beginning of the nebular phase. At these epochs, the SN Ia spectrum is dominated by emission lines from Fe-group elements and the emission line strength depends on the Fe mass in the explosion. We measure the time at which the SN enters the Lira law, hereafter t_L, as the epoch of inflection in the $(B - V)$ colour curve, at late times. The procedure for measuring t_L is identical to the measurement of t_2 described in §2.3.4.

Figure 2.12 shows that t_2 coincides nearly exactly with t_L for the Y and J bands. While the H light curve peaks 3–4 d earlier. The reason for this is not entirely clear, but both Y and J-bands are expected to be strongly influenced by Fe lines, while H is dominated by Co lines (e.g. [137, 198]). The striking coincidence of t_2 and t_L in the NIR light curves is further evidence that t_2

directly depends on the Ni mass in the explosion.

[267] found that the Ni mass depends on $\Delta m_{15}(B)$ and the bolometric peak luminosity. All these parameters (m_B^{max}, $\Delta m_{15}(B)$, t_2 and t_L, and NIR late-phase luminosity) can be tied to the Ni (and/or Fe) mass in the explosion. We provide a summary of the important correlations analysed in this work for the three NIR filters in Figure 2.13, where we correlate the timing parameters (t_1, t_0, t_2), Δm_{15}, t_L and NIR late phase luminosity ($M|_{55}$). With most of the Fe synthesised in the explosion, we propose that all light curve parameters point to the Ni as the dominant factor in shaping the light curves. We find a consistent picture that the properties of second maximum in the NIR light curves are strongly influenced by the amount of Ni produced in the explosion followed by a more luminous decline.

The NIR colours show a pronounced evolution after t_1, the flux in the J band decreases significantly with respect to both Y and H shortly after t_1 (Fig. 2.6). The reason for this depression is most likely the lack of transitions providing the required channel for radiation to emerge around 1.2 μm [122, 281, 320]. This persists until t_2 when the [Fe II] (1.25 μm) emission line forms and the J-band magnitude recovers relative to H, although not compared with Y, which is also dominated by Fe lines [198]. The H filter is dominated by Co II lines (e.g. [137, 147]). After the second maximum $J - H$ turns redder again due to the faster decline rate in the J filter.

We investigated whether the (optically) fast-declining SNe Ia can be grouped within our analysis. These SNe have very low ^{56}Ni mass which is almost certainly centrally located (low velocities of Fe III in the optical at late times in SN 1991bg; [203]) and transition so rapidly that a second maximum barely has time to form. Thus, we could not include them directly in our study. However, a comparison of $M|_{55}$ with $\Delta m_{15}(B)$ can be made for four objects of this class (SNe 2005ke, 2006mr, 2007N and 2007ax). The trend of these objects showing a fainter $M|_{55}$ luminosity with larger $\Delta m_{15}(B)$ is followed, but it is unclear whether these SN 1991bg-like SNe Ia follow the same relation as their brighter counterparts. The result remains inconclusive as the scatter remains currently too large. We note that the decline rates in the NIR at late times for these objects do not differ significantly from our sample. They follow the same distribution as in Fig 2.5.

2.5.2. Improved Distance Measurements?

The uniformity of the NIR light curves is in use for cosmological projects [15, 318]. [162] finds no correlation of the maximum luminosity with other light curve parameters, but identified the (optically) fast-declining SNe Ia as subluminous in the NIR compared to the other SNe Ia in their sample. In [151], the authors find a weak trend between the NIR first maximum luminosity and Δm_{15}.

We looked for NIR light curve properties to further improve SNe Ia as distance indicators. In Fig. 2.14 we find no significant evidence for a correlation between M_1 and t_2 for objects in our sample. The faintness of SN 2006X in this diagram is probably due to the strong absorption towards this SN.

The scatter in Fig. 2.1 falls to around 0.2 mag at later NIR phases. Between t_0 and t_2 all NIR light curves reach comparable luminosities. These phases are between 10 and 20 d in Y, near 15 and 20 d in J and H when SNe Ia are only about 1 (0.5) magnitude fainter than at the first maximum in Y (H). The decline in the J light curves is quite steep after the first maximum and the SNe have already faded by nearly 2 magnitudes. At least for Y and H, it might be worthwhile to investigate whether good distances can be determined at later phases (between +10 and +15 days). The advantage would be a distance measurement with a reduced extinction component, i.e. mostly independent of the exact reddening law, and the possibility of targeted NIR observations even when the first maximum had been missed.

2.6. Conclusions

The cosmological interest in SNe Ia in the NIR stems from the small observed scatter in the peak magnitudes. We confirm this with our extended literature sample despite our simple assumptions on distances and neglect of host galaxy absorption. The phase of the first maximum in the YJH light curves shows a narrow distribution. The uniformity of the SNe Ia in the NIR lasts until about one week past B maximum. The NIR light curves diverge showing a large scatter by the time of the second maximum and thereafter. The IR colour curves are uniform at early phases with increasing scatter after 20 days.

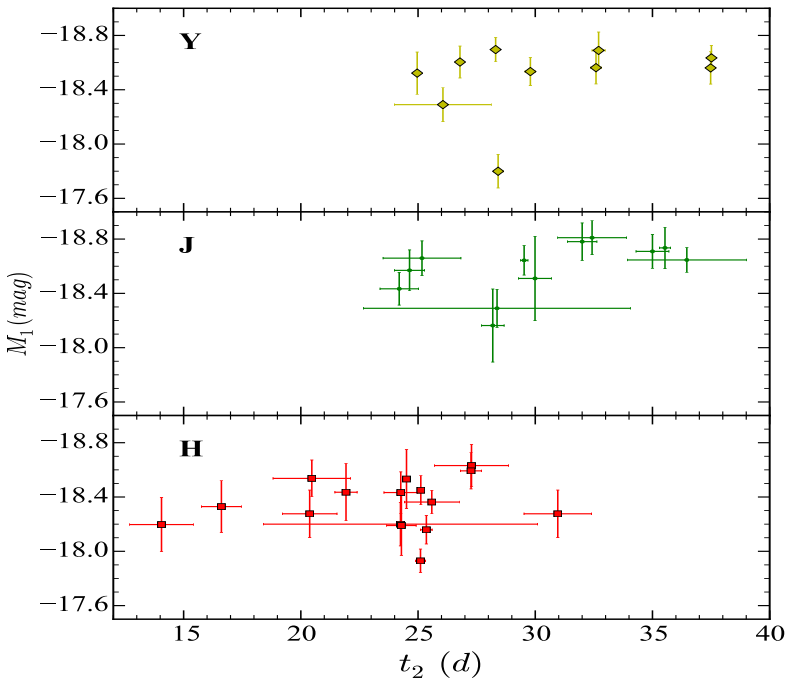

Figure 2.14.: The magnitude of the first maximum in the YJH bands is plotted against the phase of the second maximum in J band. The underluminous object in Y and J bands is the heavily extinguished SN 2006X. In the J band SN 2014J also appears fainter.

These findings corroborate the use of only few IR observations near the first maximum to obtain good cosmological distances [15, 318]. The small scatter prevails for nearly a week around the first maximum and potentially another window opens near the second maximum, where the scatter again appears rather small. A condition for these measurements is accurate phase information to be able to use sparse NIR observations to derive the distances. The phase information could come from accurate optical light curves, as used here, or through spectra. The latter are needed for redshifts and classification in any case.

The information contained in the NIR light curves points towards the nickel/iron mass as the reason for the variations. The absolute magnitude 55 d past max-

imum together with the very uniform decline rate of the light curves in all bands, including the optical [14, 174, 241], points towards differences of the energy input into the ejecta with a rather uniform density structure. This is also found in theoretical studies [59, 149, 168], although most of these models employ Chandrasekhar-mass explosions and a wider range of ejecta mass models may need to be explored to confirm the similarities in the structure of the ejecta. A higher luminosity at a fixed phase in the nebular phase points towards a larger iron core and hence a higher nickel production in the explosion. A corollary is the phase of the second maximum which also occurs later for larger iron cores [147].

The strong correlation of the phase of the second IR maximum with the optical light curve shape parameter Δm_{15} and the onset of the uniform $(B-V)$ colour evolution ('Lira law') point towards SNe Ia as an ordered family and nickel mass as the dominating factor in shaping the appearance of SNe Ia. With a higher nickel mass a larger Fe core is expected. This would result in higher expansion velocities observed at late phases [203]. It is worth checking whether this prediction holds true in future observations.

The phase of the second maximum should provide a handle to determining the nickel masses in SN Ia explosions, in particular for SNe Ia where absorption is significant. In cases like SN 2014J the NIR light curve can yield an independent check on the nickel mass and a direct comparison to the direct measurements of the $\gamma-$rays from the nickel decay [49, 63]. A calibration of a fair set of (preferably bolometric) peak luminosities and the derived nickel masses with our parameter t_2 should lead to the corresponding relation.

We attempted to improve the IR first maximum for distance measurements and looked for a possible correlation of M_1 with the phase of the second maximum. There is a slight improvement in the J band and none in Y and H. The resulting scatter after correction in J band is 0.16 mag. This is comparable to the observed value from previous studies [151, 193, 318]. It remains to be seen whether larger samples will provide a better handle in the future.

Since we specifically studied the second maximum in the NIR light curves, we excluded SNe Ia, which do not display this feature. These are objects similar to either SN 1991bg, SN 2000cx or SN 2002cx and are typically faint and peculiar SNe [78, 85, 175, 179, 180]. They appear to also display a fainter

first maximum in the NIR [162]. It would be interesting to check whether the uniform decline rate observed in the near-IR also applies to SNe Ia which do not show the second maximum. This could be used to check whether these explosions share some physical characteristics with the ones discussed here. There are only very few SNe Ia of this type and we do not find a conclusive answer. Increasing the number of SNe Ia with this information is important to assess the physical differences among the different SN Ia groups. The recent CFAIR2 catalogue [92] will provide some of these data.

The NIR light curves display a decline rate after the second maximum, which is significantly larger than the optical light curves at the same phase (e.g. [174]). At very late phases ($\geq$ 200 days) the near-IR light curves become nearly flat as observed for SN 2001el, while there is no observable change in the optical decline rates [287]. It would be interesting to observe the change in decline rate between 100 and 300 days. Presumably, the internal structure of the explosions sets the transition towards the positron decays as the dominant energy source, when the ejecta have thinned enough that the $\gamma-$rays escape freely. This phase might be correlated with other physical parameters, like the nickel and ejecta mass, determined through early light curves.

A possible extension of this photometric study with detailed spectroscopic observations and theoretical spectral synthesis calculations might be worthwhile to check on the emergence of the various emission lines, trace the exact transition to the flatter IR light curves and determine whether it indicates any differences in the structure of the SNe, e.g. transition to positron channel.

Finally, Euclid will discover many SNe at near-NIR wavelengths out to cosmologically interesting redshifts (e.g. [8]). With the small scatter of the peak luminosity, these observations will provide distances with largely reduced uncertainties due to reddening. Our study confirms the promise the NIR observations of SNe Ia offer.

Acknowledgements

This research was supported by the DFG Cluster of Excellence 'Origin and Structure of the Universe'. We would like to thank Chris Burns for his help

with template fitting using SNooPy, Richard Scalzo for discussion on the nickel masses and Saraubh Jha on the nature of Type Ia SNe. We thank Stéphane Blondin for his comments on the manuscript. B.L. acknowledges support for this work by the Deutsche Forschungsgemeinschaft through the TransRegio project TRR33 'The Dark Universe' and the Mount Stromlo Observatory for a Distinguished Visitorship during which most of this publication was prepared. S.D. acknowledges the use of University College London computers Starlink and splinter. K.M. acknowledges support from a Marie Curie Intra-European Fellowship, within the 7th European Community Framework Programme (FP7). This research has made use of the NASA/IPAC Extragalactic Database (NED) which is operated by the Jet Propulsion Laboratory, California Institute of Technology, under contract with the National Aeronautics and Space Administration.

3. A reddening-free method to estimate the ^{56}Ni mass of Type Ia supernovae [1]

3.1. Introduction

Type Ia supernovae (SNe Ia) exhibit diverse observable properties. In addition to the spectral and colour differences, the peak luminosity of SNe Ia range over several factors [181,292,293]. The amount of ^{56}Ni, derived from the bolometric luminosity, [53] and the total ejecta mass [267,285] also show a wide dispersion. The $M_{^{56}Ni}$ distribution provides insight into the possible progenitor channels and explosion mechanisms for SNe Ia [121, 185, 306].

The uncertainty in the reddening correction directly impacts the ability to derive accurate bolometric luminosities and ^{56}Ni masses derived from the peak luminosity. The total to selective absorption (R_V) appears systematically and significantly lower in the SN hosts than the canonical Milky Way R_V value of 3.1. [216] use a large sample of nearby SNe Ia to derive an average R_V which is significantly lower than 3.1. Taking into account spectroscopic features that correlate with luminosity, [47] found an R_V of 2.8 ± 0.3 which is consistent with the Milky Way value. However, objects with high extinction are seen to have an unusually low R_V [230, 243]. Due to interstellar dust a correction for reddening in the Milky Way and the host galaxy needs to be applied. Our goal is to establish a relation between the bolometric peak luminosity and the ^{56}Ni mass independent of reddening.

The Near Infrared (NIR) light curve morphology of SNe Ia is markedly different from that in the optical. In particular, the light curves start to rebrighten

[1] This Chapter is already published in [60]

about 2 weeks after the first maximum, resulting in a second peak. Recent studies [24, 61] found that more luminous SNe Ia reach the second maximum in NIR filters at a later phase. This was predicted by [147] who also indicated that the phase of the second maximum (designated in the following as t_2 and measured relative to the B-band light curve maximum) should be a function of the ^{56}Ni mass in the explosion. We expect that the phase of the second NIR maximum can be used to determine bolometric peak luminosity L_{max} and the amount of ^{56}Ni synthesized in the explosion.

In the following, we investigate the link between the peak bolometric luminosity (L_{max}) and the phase of the second maximum in the NIR light curves (t_2). We use a sample of nearby SNe Ia with low host-galaxy extinction (described in Section 4.1) to determine L_{max} and then employ different methods to derive $M_{^{56}Ni}$ (Section 4.2). This relation can then be used to derive L_{max} and $M_{^{56}Ni}$ for all SNe Ia with a measured t_2, since the timing parameter is free of reddening corrections and allows us to include heavily reddened objects. We check our derivation against independent measurements of $M_{^{56}Ni}$ with the nearby SN 2014J in M82 and SN 2006X (Section 3.4). With the reddening independent method we can establish the luminosity function of SNe Ia at maximum and also derive the distribution of nickel masses among SN Ia explosions (Section 3.5). We finish by discussing the implications of this determination of the $M_{^{56}Ni}$ distribution in the conclusions (Section 3.6).

3.2. Data

Our SN Ia sample is constrained to objects, which have NIR observations at late times ($t > 50$ days after B maximum) with well-sampled optical and NIR light curves to construct a (pseudo-)bolometric light curve and measure t_2. The main source of near-infrared photometry of SNe Ia is the Carnegie Supernova Project (CSP; [36, 37, 54, 238, 288]). We add to this sample objects from the literature. We only included SNe Ia with observations near maximum from U to H filters. The full description of the selected SNe Ia can be found in [61].

The sample of low-reddening SNe Ia is defined to circumvent the uncertainties of host galaxy extinction. The 18 objects are presented in Table 3.1. We use $E(B-V)_{host}$ values from the literature. Only objects with $E(B-V)_{host} < 0.1$

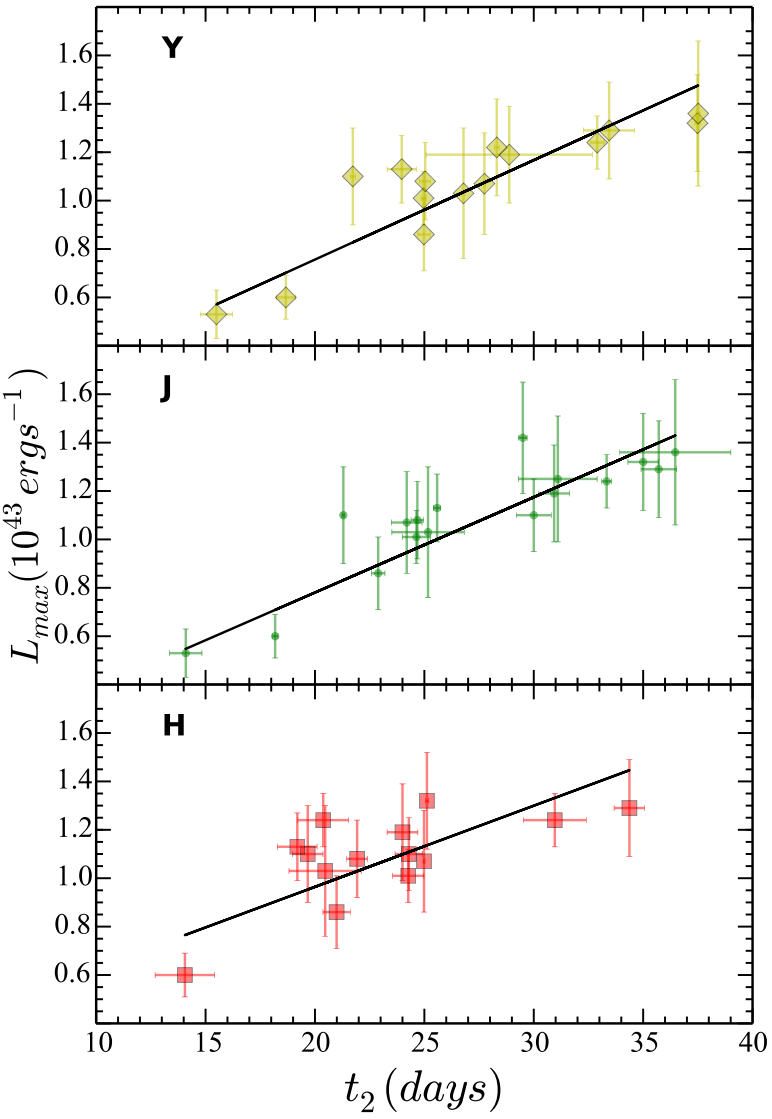

Figure 3.1.: The bolometric maximum luminosity L_{max} is plotted against the phase of the second maximum t_2 in YJH filter light curves. A strong correlation is observed in Y and J, whereas a weaker correlation is seen in the H band. Best fit lines are overplotted in black. The fit includes errors on both axes.

mag were included. Since we consider only objects, which display the second maximum in their NIR light curves this implies that most low-luminosity SNe Ia, especially SN 1991bg-like objects were excluded.

At maximum light the UV-optical-IR integrated luminosity represents >90% of the true bolometric luminosity [27]. We constructed $UBVRIJH$ bolometric light curves for objects with sufficient photometry near maximum light in the optical and the NIR. The K filter data was excluded since only few SN Ia have well-sampled K light curves. We calculated the fraction of the flux emitted in K for a few well-observed SNe Ia with sufficient data and determined it to be around $1-3\%$ of the UVOIR luminosity at maximum. The exclusion of the K-flux results in only a minor uncertainty in the final UVOIR luminosity.

Prior to the derivation of a bolometric flux for the low extinction sample (see Table 3.3) we apply a correction for the measured extinction following [41]. The assumed distances and their references can be found in Table 3.1.

3.3. Results

Based on our previous work [61], where we found strong correlations between various derived parameters of SNe Ia with t_2 in the Y and J filters, we argued that the bolometric maximum luminosity should also correlate with t_2. The sample of low-reddening SNe Ia described in Section 4.1 is used to establish the relation between t_2 and L_{max}. The t_2 parameter has the advantage that is is essentially independent of reddening and distance (relative to the calibration sample). With such a relation we will be in a position to derive the luminosity function of SNe Ia at maximum.

3.3.1. Correlation between L_{max} and t_2

Figure 3.1 displays a strong correlation between t_2 for the Y and J filter light curves and the bolometric (UVOIR) luminosity L_{max} (determined by fitting a spline interpolation to the UVOIR light curve) with Pearson coefficients $r = 0.88$ and $r = 0.86$, respectively for the low-reddening sample. A much weaker trend is observed in the H filter light curve with $r\approx0.60$.

Table 3.1.: The sample of SNe Ia with low reddening $E(B-V)_{host} < 0.1$. The references for the SNe Ia are presented along with the extinction values and the distances employed for calculation of the (pseudo-) bolometric luminosity at maximum.

SN	μ	$E(B-V)_{host}$	$E(B-V)_{MW}$	Reference	$t_2(Y)$ (d)	$t_2(J)$ (d)	$t_2(H)$ (d)	L_{max} (10^{43} erg/s)
SN2002dj	32.93 ± 0.30	0.096 ± 0.030	0.010 ± 0.003	P08	...	31.1 ± 1.8	23.0 ± 0.9	1.25 ± 0.26
SN2002fk	32.59 ± 0.15	0.009 ± 0.044	0.035 ± 0.003	C14	...	29.5 ± 0.2	25.8 ± 0.3	1.42 ± 0.23
SN2005M	35.01 ± 0.09	0.060 ± 0.021	0.027 ± 0.002	B14	28.9 ± 3.8	30.9 ± 0.7	...	1.19 ± 0.20
SN2005am	32.85 ± 0.20	0.053 ± 0.017	0.043 ± 0.002	B14	21.7 ± 0.1	21.3 ± 0.7	19.7 ± 0.7	1.10 ± 0.20
SN2005el	34.04 ± 0.14	0.015 ± 0.012	0.098 ± 0.001	B14	25.0 ± 0.1	24.6 ± 0.6	24.3 ± 0.7	1.01 ± 0.11
SN2005eq	35.46 ± 0.07	0.044 ± 0.024	0.063 ± 0.003	B14	37.5 ± 0.1	35.0 ± 0.7	25.1 ± 0.1	1.32 ± 0.20
SN2005hc	36.50 ± 0.05	0.049 ± 0.019	0.028 ± 0.001	B14	37.5 ± 0.1	36.5 ± 2.5	...	1.36 ± 0.30
SN2005iq	35.80 ± 0.15	0.040 ± 0.015	0.019 ± 0.001	B14	27.7 ± 0.1	24.2 ± 0.7	25.0 ± 0.1	1.07 ± 0.21
SN2005ki	34.73 ± 0.10	0.016 ± 0.013	0.027 ± 0.001	B14	26.8 ± 0.1	25.2 ± 1.7	20.5 ± 1.7	1.03 ± 0.27
SN2006bh	33.28 ± 0.20	0.037 ± 0.013	0.023 ± 0.001	B14	25.0 ± 0.3	22.9 ± 0.3	21.0 ± 0.6	0.86 ± 0.15
SN2007bd	35.73 ± 0.07	0.058 ± 0.022	0.029 ± 0.001	B14	28.3 ± 0.1	...	...	1.22 ± 0.13
SN2007on	31.45 ± 0.08	< 0.007	0.010 ± 0.001	B14	18.7 ± 0.4	18.2 ± 0.1	14.1 ± 1.4	0.60 ± 0.09
SN2008R	33.73 ± 0.16	0.009 ± 0.013	0.062 ± 0.001	B14	15.5 ± 0.7	14.1 ± 0.7	...	0.53 ± 0.10
SN2008bc	34.16 ± 0.13	< 0.019	0.225 ± 0.004	B14	32.9 ± 0.3	33.3 ± 0.2	31.0 ± 1.4	1.24 ± 0.19
SN2008gp	35.79 ± 0.06	0.098 ± 0.022	0.104 ± 0.005	B14	33.5 ± 1.2	35.7 ± 0.8	34.4 ± 0.7	1.29 ± 0.14
SN2008hv	33.84 ± 0.15	0.074 ± 0.023	0.028 ± 0.001	B14	25.0 ± 0.3	24.7 ± 0.3	21.9 ± 0.5	1.08 ± 0.16
SN2008ia	34.96 ± 0.09	0.066 ± 0.016	0.195 ± 0.005	B14	24.0 ± 0.7	25.6 ± 0.2	19.2 ± 0.9	1.13 ± 0.14
SN2011fe	28.91 ± 0.20	0.014 ± 0.010	0.021 ± 0.001	P13	...	30.0 ± 0.8	24.3 ± 0.6	1.10 ± 0.15

E(B-V) references: P08: [245]; C14: [44] B14: [36];P13: [228]

Table 3.2.: Values of the coefficients for correlations between L_{max} and t_2 in the individual filters

Filter	a_i	b_i
Y	0.041 ± 0.005	-0.065 ± 0.122
J	0.039 ± 0.004	0.013 ± 0.106
H	0.032 ± 0.008	0.282 ± 0.174

The slope of the L_{max} vs. t_2 relation appears to flatten for objects with $t_2 \gtrsim 27$ d. This is most prominent in the Y band. However, we would require a larger sample to confirm this trend amongst the most luminous objects.

We fit a simple linear relation to the data

$$L_{max} = a_i \cdot t_{2,i} + b_i \tag{3.1}$$

which leads to the entries in Table 3.2 (for YJH filters). The corresponding fits are shown in Figure 3.1. We compare our observed values to the L_{max} and t_2 from the DDC models of [28]. Model spectra and light curves published in [28] based on delayed detonation explosions show similar correlations to those described herein.

In the interest of a clean low extinction sample, we have removed 7 objects with $E(B-V)_{host} < 0.1$ but total $E(B-V) \geq 0.1$. Interestingly, several of the excluded objects are amongst the most luminous SNe Ia in the sample. Even after the removal of these 7 objects we do not derive a significant correlation for the H band light curves from our sample. It will have to be seen, whether future data will reveal a correlation or whether the H light curves are not as sensitive to the nickel mass as the other NIR filters. The relations are identical for the full and restricted sample within the uncertainties listed in Table 3.2. We combine the relations from the two bands for extrapolating the values of L_{max} in the following analysis. We assume the Y band estimate to be equivalent to the value in the J band and calculate the slope and intercept with the photometry of both filters, which leads to improved statistics.

3.3.2. Deriving $M_{^{56}Ni}$ from L_{max}

We present three different methods to derive $M_{^{56}Ni}$ from L_{max}, namely using Arnett's rule with an individual rise time for each SN Ia, using Arnett's rule with an assumed constant rise time applied to all SNe Ia and by calculating L_{max} from delayed detonation models with different $M_{^{56}Ni}$ yields [28]. Arnett's rule states that at maximum light the bolometric luminosity equals the instantaneous rate of energy input from the radioactive decays. Any deviations from this assumption are encapsulated in a parameter α below. It is quite possible that α depends on the explosion mechanism and shows some variation between explosions [31, 155]. These early papers found rather large ranges with $0.75 < \alpha < 1.4$ depending on the exact explosion model and the amount of assumed mixing [31, 155]. More recently [28] found a range of α within 10% of 1 for delayed detonation models. These models are not applicable for low-luminosity SNe Ia. Should α systematically depend on explosion characteristics then the derived nickel masses may suffer from a systematic drift not captured in our treatment. These uncertainties must be taken into account for the interpretation of the derived ^{56}Ni mass.

Arnett's rule with individual rise times

Arnett's rule states that the luminosity of the SN at peak is given by the instantaneous rate of energy deposition from radioactive decays inside the expanding ejecta [5, 6].

This is summarized as [285]:

$$L_{max}(t_R) = \alpha E_{^{56}Ni}(t_R), \tag{3.2}$$

where $E_{^{56}Ni}$ is the rate of energy input from ^{56}Ni and ^{56}Co decays at maximum, t_R is the rise time to bolometric maximum and α accounts for deviations from Arnett's Rule. The energy output from 1 $M_\odot$of ^{56}Ni is ($\alpha = 1$):

$$\epsilon_{Ni}(t_R, 1\ M_\odot) = (6.45 \cdot 10^{43} e^{-t_R/8.8} + 1.45 \cdot 10^{43} e^{-t_R/111.3}) \text{ergs}^{-1} \tag{3.3}$$

Table 3.3.: $M_{^{56}Ni}$ measurements for low reddening SNe Ia. The components of the error from L_{max} and rise time are given along with the total error.

SN	$M_{Ni} - Arn$ ($M_\odot$)	err (L_{max}) ($M_\odot$)	err (rise time) ($M_\odot$)	$M_{Ni} - Arn$ (fixed rise) ($M_\odot$)	err (L_{max}) ($M_\odot$)	err (rise time) ($M_\odot$)	$M_{Ni} - DDC$ ($M_\odot$)
SN2002dj	0.59 ± 0.16	0.12	0.10	0.63 ± 0.16	0.13	0.10	0.61 ± 0.13
SN2002fk	0.68 ± 0.16	0.11	0.12	0.71 ± 0.17	0.12	0.12	0.76 ± 0.13
SN2005M	0.59 ± 0.14	0.10	0.10	0.60 ± 0.14	0.10	0.10	0.59 ± 0.11
SN2005am	0.47 ± 0.13	0.08	0.10	0.55 ± 0.14	0.10	0.10	0.52 ± 0.11
SN2005el	0.45 ± 0.10	0.05	0.09	0.51 ± 0.11	0.06	0.09	0.48 ± 0.07
SN2005eq	0.67 ± 0.15	0.10	0.11	0.66 ± 0.15	0.10	0.11	0.67 ± 0.11
SN2005hc	0.69 ± 0.19	0.15	0.12	0.68 ± 0.19	0.15	0.12	0.71 ± 0.16
SN2005iq	0.48 ± 0.13	0.09	0.09	0.54 ± 0.14	0.11	0.09	0.51 ± 0.10
SN2005ki	0.45 ± 0.14	0.11	0.09	0.51 ± 0.17	0.14	0.09	0.49 ± 0.14
SN2006bh	0.37 ± 0.10	0.06	0.08	0.43 ± 0.11	0.08	0.07	0.40 ± 0.07
SN2007bd	0.55 ± 0.13	0.06	0.11	0.61 ± 0.12	0.07	0.10	0.59 ± 0.10
SN2007on	0.23 ± 0.06	0.03	0.05	0.30 ± 0.07	0.05	0.05	0.28 ± 0.05
SN2008R	0.20 ± 0.06	0.04	0.05	0.27 ± 0.07	0.05	0.05	0.25 ± 0.06
SN2008bc	0.60 ± 0.14	0.09	0.11	0.62 ± 0.15	0.10	0.11	0.63 ± 0.11
SN2008gp	0.62 ± 0.13	0.06	0.11	0.65 ± 0.11	0.07	0.09	0.64 ± 0.09
SN2008hv	0.48 ± 0.11	0.07	0.09	0.54 ± 0.12	0.08	0.09	0.52 ± 0.09
SN2008ia	0.50 ± 0.12	0.06	0.10	0.57 ± 0.11	0.07	0.09	0.55 ± 0.09
SN2011fe	0.50 ± 0.12	0.07	0.10	0.55 ± 0.12	0.08	0.09	0.52 ± 0.10

We use the relation for estimates using different rise times in the B filter for each SN following,

$$t_{R,B} = 17.5 - 5 \cdot (\Delta m_{15} - 1.1) \tag{3.4}$$

from [267] which covers the $t_{R,B}$–Δm_{15} parameter space of [96]. Like [267] we apply a conservative uncertainty estimate of ± 2 days. The bolometric maximum occurs on average 1 day before B_{max} [267].

Arnett's rule with a fixed rise time

Originally $M_{^{56}Ni}$ was determined from L_{max} for a fixed rise time of 19 days for all SNe Ia [285]. Similar to these analyses we propagate an uncertainty of ± 3 days to account for the diversity in the rise times.

The peak luminosity then becomes [285]

$$L_{max} = (2.0 \pm 0.3) \cdot 10^{43} (M_{^{56}Ni}/M_{\odot}) \mathrm{ergs}^{-1}. \tag{3.5}$$

As described above, we assumed $\alpha = 1$ (see [204, 285]), which is the analytical approximation of [5]. For the DDC models of [28] α is within 10 % of 1 for all but the least luminous model.

Interpolating using delayed detonation models

We interpolate the relation between L_{max} (in a given filter set, u $\rightarrow$ H in this case) and $M_{^{56}\mathrm{Ni}}$ found from a grid of Chandrasekhar mass delayed detonation models of [28] to derive a ^{56}Ni mass from the observed peak luminosity for the sample presented in Table 3.1. The resulting ^{56}Ni mass estimates are presented in the bottom panel of Figure 3.2. For all but the least luminous of these models, α is within 10 % of 1 [28].

3.3.3. Comparison of different methods

In Figure 3.2, we plot the distributions of the $M_{^{56}Ni}$, inferred for the low-reddening sample, from the different methods.

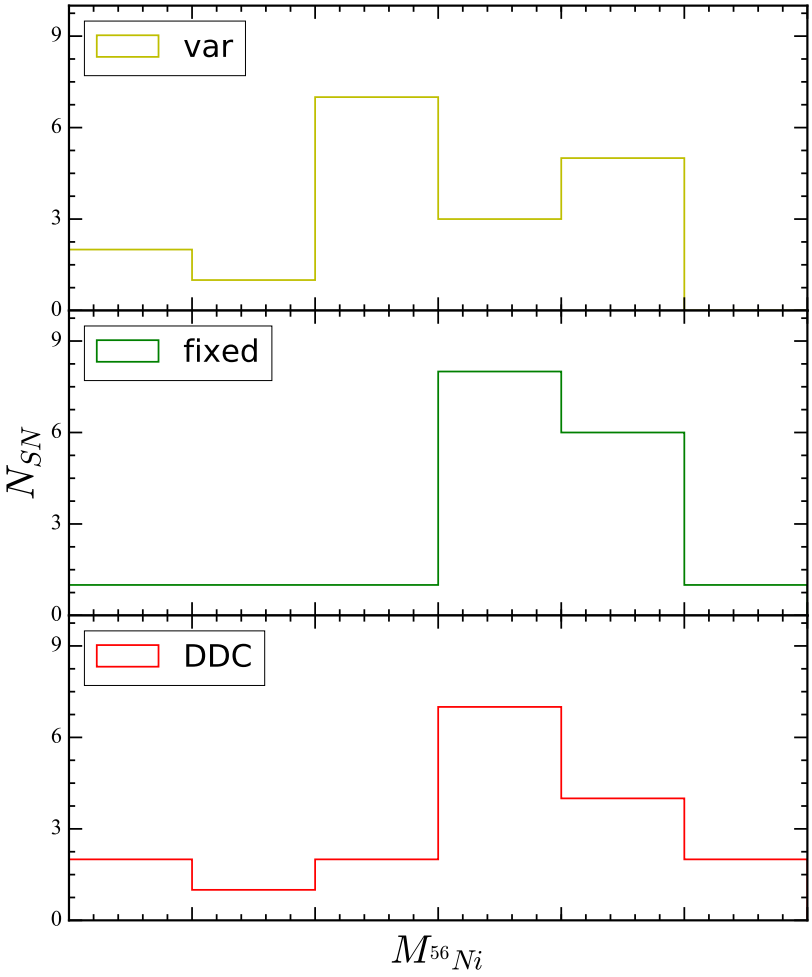

Figure 3.2.: The histograms show the different methods to estimate the $M_{^{56}Ni}$ from the L_{max}. The values found from Arnett's rule with fixed and individual rise times are plotted in the *top* and *middle* panels. The *bottom* panel displays the values estimated by using the relation between L_{max} and $M_{^{56}Ni}$ found from the DDC models.

Similar to previous studies we find that there is a large distribution in the $M_{^{56}Ni}$ values for the sample in Table 3.1. We note a over a factor of 2 difference between the lowest and highest $M_{^{56}Ni}$ values (a factor of ~ 3 for the variable rise time formalism). Unlike previous studies, this sample doesn't include faint, 91bg-like objects, since their NIR light curves do not display a second maximum. These objects are found to have a much lower $M_{^{56}Ni}$ $\sim$0.1 $M_\odot$ [267, 285] from their peak luminosities. There is clearly a majority of objects with nickel masses between 0.4 and 0.7 $M_\odot$ with extensions to higher and lower masses. A further difference can be seen in Fig. 3.2 where the mass distribution between the case of individual and the fixed rise times is slightly different due to the fact that observed rise times often are shorter than the assumed 19 days.

The individual errors clearly dominate over the differences between the methods and the results are not influenced by the chosen method. There appears a small systematic offset between the ^{56}Ni masses derived from DDC models and the ones with Arnett's rule and fixed rise time. The ^{56}Ni masses from the DDC models are about 0.05 $M_\odot$ smaller, however, well within the overall uncertainties, which are typically around 0.15 $M_\odot$ (Tab. 3.3).

For SN2011fe [233] report a rise time of 16.58 days. Using this rise time, we obtain an $M_{^{56}Ni}$ of 0.49 $M_\odot$which is a 0.06 $M_\odot$shift from the value using a 19 d rise. This shift is smaller than the uncertainty on the ^{56}Ni mass. For the low-reddening sample we note that the average difference between the fixed rise and variable rise formalisms is 0.04 $M_\odot$.

For the following analysis, we calculate the $M_{^{56}Ni}$ using t_2. By substituting the relation derived between L_{max} and t_2 (equation (3.1) **and** equation (3.3)), we obtain

$$\frac{M_{^{56}Ni}}{M_\odot} = \frac{a_i \cdot t_2(i) + b_i}{\alpha \cdot \epsilon_{Ni}(t_R, M_\odot)}. \tag{3.6}$$

We mostly will use the fixed rise time formalism in the following analysis, although in special cases, we will also make use of the more accurately known rise time.

3.4. Test with well observed SNe Ia

Dust in the host galaxy and the Milky Way makes the determination of the peak luminosity uncertain. Many nearby SNe Ia have shown marked deviations in the host galaxy dust properties from those observed in the Milky Way mostly favouring a smaller R_V value [102, 243]. The extinction corrections are notoriously uncertain and directly affect our ability to measure peak bolometric luminosities of SNe Ia. Since t_2 is independent of reddening, we can use the derived correlation to determine the peak luminosity and estimate the ^{56}Ni mass for heavily reddened SNe Ia.

We test this relation on SN 2014J, which has a direct $\gamma-$ray detection from the $^{56}\mathrm{Ni} \rightarrow {}^{56}\mathrm{Co}$ decay chain [49,64]. Using the best fit relation for the reddening-free sample, we obtain $M_{^{56}Ni} = 0.64 \pm 0.15 M_{\odot}$ for a $t_2 = 31.99 \pm 1.15$ days and a rise time of 19 days. Since the error on the rise time is taken as ± 3 days, we expect the error on $M_{^{56}Ni}$ to decrease with a less conservative error estimate on t_R. [103] used Palomar Transient Factory (PTF) and Kilodegree Extremely Little Telescope (KELT) data to measure the rise time of SN 2014J. They find $t_R = 17.25$ days. We place a conservative error estimate of 1 day and evaluate the $M_{^{56}Ni} = 0.60 \pm 0.10 M_{\odot}$ which has a lower error bar than from the fixed rise time formalism.

The direct measurement of $M_{^{56}Ni}$ for SN 2014J through the $\gamma-$ray detection gives an independent and fairly secure estimate of the nickel mass. [49] derive $^{56}Ni = 0.62 \pm 0.13 M_{\odot}$. [64] find a slightly lower mass of $M_{^{56}Ni} = 0.56 \pm 0.10 M_{\odot}$.

A detailed comparison of the derived ^{56}Ni masses is given in Table 3.4. The difficulty of the extinction correction and the advantage of the method presented here are obvious. The uncertainty in the $\gamma-$ray determination is due to the weakness of the signal and leads to slightly different interpretations. The very good correspondence between the direct $\mathrm{M}_{^{56}\mathrm{Ni}}$ measurement and our relation of the second maximum in the NIR light curves is encouraging.

As a second case, we determine the bolometric peak luminosity L_{max} and the nickel mass $M_{^{56}Ni}$ based on t_2 to the heavily extinguished SN 2006X. [313] derived a peak luminosity for this SN from multi-band photometry and a correction for dust absorption in the host galaxy. They determined a bolometric peak luminosity for SN 2006X of $(1.02 \pm 0.1) \cdot 10^{43}$ erg s^{-1}, which compares

Table 3.4.: Comparison of different methods to estimate $M_{^{56}Ni}$ for SN 2014J. All measurements assume a distance modulus of 27.64 ± 0.10.

M_{Ni} (inferred)	σ	Method	Reference
0.62	0.13	γ ray lines	[49]
0.56	0.10	γ ray lines	[64]
0.37	...	Bolometric light curve A_V=1.7 mag	[49, 195]
0.77	...	Bolometric light curve A_V=2.5 mag	[49, 103]
0.64	0.13	NIR second maximum	this work (combined fit)
0.60	0.10	NIR second maximum + measured rise	this work

well with our measurement of $(1.14 \pm 0.16) \cdot 10^{43}$ erg s^{-1}. [313] determined $M_{^{56}Ni} = 0.50 \pm 0.05 M_{\odot}$, which should be compared to $M_{^{56}Ni} = 0.57 \pm 0.11$ $M_{\odot}$ found from t_2 using the fixed rise time formalism. The measured rise time for SN 2006X is $t_R(B) = 18.2 \pm 0.9$ d, which leads to $M_{^{56}Ni} = 0.55 \pm 0.10$ M$_{\odot}$.

Table 3.5 presents several additional highly reddened SNe Ia, which had a previous determination of the nickel mass. The $M_{^{56}Ni}$ for these objects were calculated in the same way as for SN 2014J and SN 2006X.

From Table 3.5, we can see that 1986G has a lower value of $M_{^{56}Ni}$ than the other heavily reddened objects. This is consistent with the observed optical decline rate and lower B band luminosity [242]. Using nebular spectra, [264] calculate the M$_{^{56}\mathrm{Ni}}$ for SN 1986G and find a value of 0.38 ± 0.03 $M_{\odot}$. This is fully consistent with the estimate from t_2.

[267] give M$_{^{56}Ni}$ for SN 2005el and SN 2011fe. The comparison for SN 2011fe shows $M_{^{56}Ni} = 0.52 \pm 0.15$ $M_{\odot}$from the NIR light curves, whereas [267] find $M_{^{56}Ni} = 0.42 \pm 0.08$ $M_{\odot}$. The difference is mostly in the adopted value of α, 1.2 in [267] compared to 1 in this study. Rescaling the value from [267] to α=1, we obtain M$_{^{56}\mathrm{Ni}} = 0.50 \pm 0.08$ $M_{\odot}$, which is fully consistent with our value. [233] report nickel masses for SN 2011fe for different values of α. Their nickel mass for α=1 is $M_{^{56}Ni} = 0.53 \pm 0.11$ $M_{\odot}$, nearly identical to our determination. For SN 2005el, [267] obtain an M$_{^{56}\mathrm{Ni}}$ of 0.52 ± 0.12 M$_{\odot}$. Scaled to an $\alpha = 1$, this gives M$_{^{56}\mathrm{Ni}} = 0.62$. We find M$_{^{56}\mathrm{Ni}} = 0.51 \pm 0.11$ M$_{\odot}$, which is broadly consistent with the value found in [267].

From the comparisons in Table 3.5, we conclude that there is good agreement between our values and those published in the literature. For SN 2001el we see that the error in the estimate from t_2 is substantially smaller than from the bolometric light curve.

One significant outlier is SN 2007if. This was presented as a super-Chandrasekhar-mass explosion [268] with a total luminosity of $3.2 \cdot 10^{43}$ erg s^{-1}. The reddening from the host galaxy is somewhat unclear. There is no indication of Na foreground absorption, while the colour evolution and the Lira law would indicate some reddening. Any reddening would only increase the luminosity and the derived nickel mass based on Arnett's rule. The M$_{^{56}\mathrm{Ni}}$ estimate from t_2 for SN 2007if is significantly lower than the mass estimate through the bolometric peak luminosity by [268]. If we recalculate the M$_{^{56}\mathrm{Ni}}$ from the bolometric light

Table 3.5.: $M_{^{56}Ni}$ estimates for objects with high values of $E(B-V)_{host}$. Comparison with independent estimates from the literature are given where available.

SN	t_2 (d)	$M_{^{56}Ni}$ (inferred) ($M_\odot$)	$M_{^{56}Ni}$ (Lit. Val.) ($M_\odot$)	Percent Difference	Reference [a]
SN 1986G	16.4 ± 1.4	0.33 ± 0.08	0.38 ± 0.03	15.15	RL92
SN 1998bu	29.9 ± 0.4	0.58 ± 0.12	0.57	1.7	S06b
SN 1999ac	27.0 ± 2.0	0.53 ± 0.12	0.67 ± 0.29	26.4	S06a
SN 2001el	31.2 ± 0.7	0.62 ± 0.12	0.40 ± 0.38	33.8	S06a
SN 2002bo	28.9 ± 0.7	0.56 ± 0.12	0.52	7.1	St05
SN 2003cg	30.2 ± 1.5	0.59 ± 0.13	0.53	10.1	ER06
SN 2003hv	22.3 ± 0.1	0.43 ± 0.11	0.40 ± 0.11	6.9	L09
SN 2006X	28.2 ± 0.5	0.57 ± 0.11	0.50 ± 0.05	12.2	W08
SN 2007if	32.3 ± 0.8	0.65 ± 0.16	1.6 ± 0.1	158.3	S10

[a]The references for the $M_{^{56}Ni}$ measurements are RL92: [264], S06a: [285], S06b: [286], St05: [283], ER06: [71], L09: [177], W08: [313], S10: [268]

curve presuming no extinction from the host galaxy, we obtain $M_{^{56}Ni} = 1.6\,M_\odot$. This is a factor of ~ 2 larger than our estimate. We discuss this supernova in Section 3.6.

3.5. The luminosity function of SNe Ia at maximum

We are now in a position to derive L_{max} for all SNe Ia with a reliably measured t_2 (as given in Tables 3.1 and 3.6) and establish the bolometric luminosity function of SNe Ia at maximum light. For objects in the low-reddening sample, we use the L_{max} determined from t_2 and the best-fit linear relation (green histogram in Figure 3.3). Since the phase of the second maximum in the near infrared is independent from the reddening we can derive the reddening-free distribution of the luminosity function of SNe Ia (Fig. 3.3). We show here the histogram of 58 SNe Ia as derived from the Y and J light curves. The luminosity scale is based on the calibration sample of low-reddening objects (Section 4.2).

The luminosity function of SNe Ia is clearly not symmetric. The luminosity range spans slightly over a factor of 2. We find no obvious difference between the full sample and the low-reddening sample used to calibrate the relation between t_2 and L_{max}. If anything the calibration sample has a flatter distribution with most SNe around $0.9 \cdot 10^{43}$ erg s^{-1}, while the full sample includes more luminous objects. This could be an effect of the magnitude limit of the searches. The exact biases in our sample are difficult to define as it is not volume limited.

The bolometric luminosity function can be compared to the R filter luminosity function derived by [181] based on 74 SNe Ia including the low-luminosity objects missing in our sample. The [181] magnitude-limited luminosity function (their Fig. 10) peaks at an absolute magnitude of ≈ -19 with a few objects above -19.5 and a tail to fainter objects down to -17. This is also reflected in our luminosity function (Fig.3.3), where we observe a clear peak at $L_{max} = 1.3 \cdot 10^{43}$ergs^{-1} with some more luminous objects and a tail to fainter objects. The range is also comparable to the one found by [181].

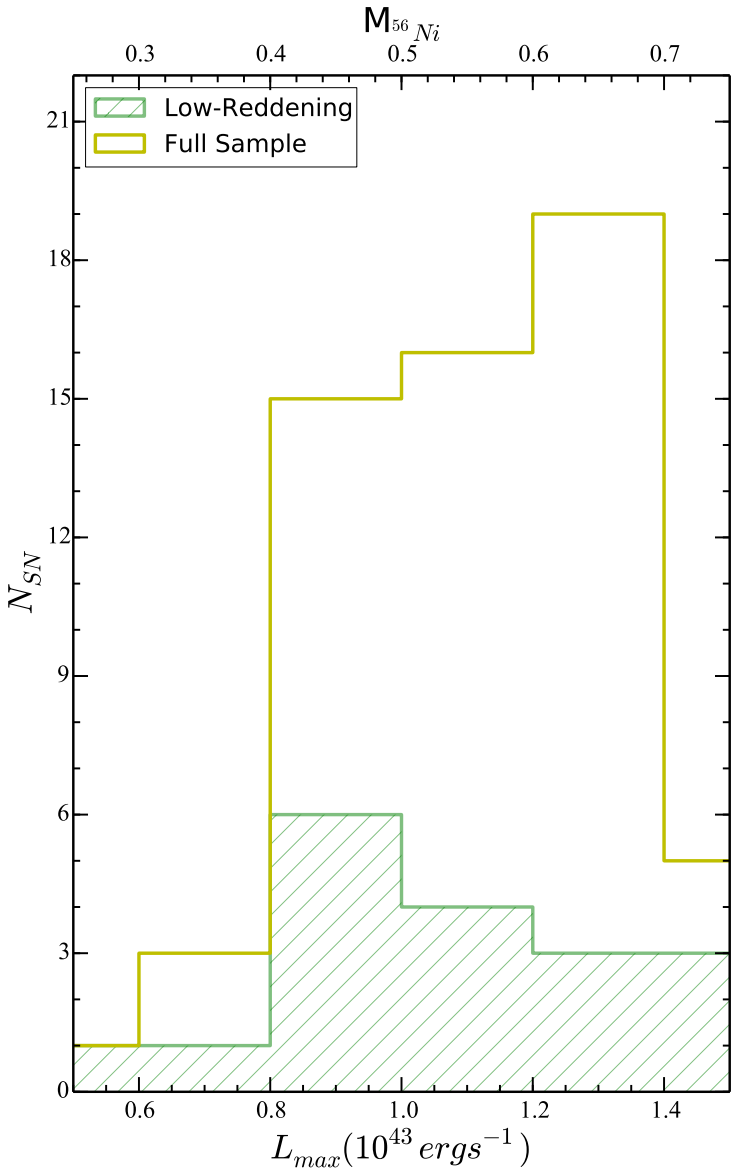

Figure 3.3.: Histogram distribution of L_{max} derived from the relations for the full sample of objects. *Green:* Estimates of L_{max} for the low-reddening, calibration sample. *Yellow:* Estimates for all objects with a t_2 measurement in the full sample. The axis labels on top correspond to the $M_{^{56}Ni}$ estimate. We use the combined fit to obtain the final values.

.

In the next step we derive the distribution of $M_{^{56}Ni}$ for all SNe Ia with sufficient infrared light curve data using equation 3.6 and a fixed rise time and $\alpha = 1$. Table 3.6 and Fig. 3.3 present the SN Ia nickel mass function.

3.6. Discussion and Conclusion

Using the relation derived from the low-reddening sample we extrapolate an L_{max} value for 58 SNe Ia objects having a measured t_2. The estimate of t_2, along with this relation, provides a method to deduce the bolometric peak luminosity, independent of a reddening estimate, distance measurement (relative to the calibration of our low-absorption sample) and without requiring multi-band photometry. We hence have established a reddening-free luminosity function of SNe Ia at peak (Fig. 3.3).

We established an intrinsic luminosity function and ^{56}Ni mass distribution for all SNe Ia with a t_2 measurement (Tab. 3.5). The distribution of L_{max} has a standard deviation of $0.2 \cdot 10^{43}$ erg s^{-1} and $M_{^{56}Ni}$ has a standard deviation of $0.11\,M_\odot$. [267] find a similar distribution of $M_{^{56}Ni}$ with a σ of $0.16\,M_\odot$. We test our method on SN 2014J, a heavily reddened SN Ia in the nearby galaxy M82 and find good agreement between the estimates from the $\gamma-$ray observations (see Table 3.4 [49, 64]). Faint, 91bg-like SNe Ia, which show typically lower luminosities [78, 175], do not display a second maximum in their NIR light curves and are not in our sample. Therefore, the true dispersion, in peak luminosity and $M_{^{56}Ni}$, for SN Ia will likely be larger than what is derived here. [285] find a dispersion of a factor of ~ 10, since their sample included peculiar SNe Ia like SN 1991bg and SN 1991T.

Our reddening-free estimate of the $M_{^{56}Ni}$ can be compared to independent ^{56}Ni mass estimates, e.g. from the late-time (≥ 200 d) pseudo-bolometric light curve. It should also be possible to determine the amount of radiation emitted outside the UVOIR region of the spectrum at late phases and a bolometric correction (e.g. [177]). There are very few objects for which both NIR data to measure t_2 and nebular phase pseudo-bolometric observations are present, making a quantitative comparison for a sample of objects extremely difficult. Thus, we strongly encourage more late-time observations of SN Ia.

Table 3.6.: $M_{^{56}Ni}$ and L_{max} measurements for the complete sample of objects with t_2 measurements

SN	$M_{^{56}Ni}$ ($M_\odot$)	σ	L_{max} (10^{43} erg/s)	σ
1980N	0.42	0.10	0.84	0.21
1981B	0.63	0.13	1.26	0.21
1986G	0.33	0.07	0.66	0.18
1998bu	0.58	0.12	1.16	0.20
1999ac	0.53	0.12	1.05	0.20
1999ee	0.68	0.15	1.36	0.21
2000E	0.62	0.14	1.24	0.22
2000bh	0.65	0.14	1.30	0.22
2001bt	0.55	0.12	1.10	0.20
2001cn	0.58	0.13	1.19	0.20
2001cz	0.67	0.14	1.33	0.22
2001el	0.61	0.13	1.22	0.21
2002bo	0.56	0.11	1.12	0.21
2003cg	0.64	0.13	1.19	0.22
2003hv	0.43	0.10	0.84	0.17
2004ey	0.57	0.14	1.14	0.20
2004gs	0.43	0.11	0.85	0.18
2004gu	0.71	0.17	1.42	0.23
2005A	0.56	0.13	1.12	0.18
2005al	0.49	0.13	0.97	0.21
2005na	0.64	0.15	1.28	0.22
2006D	0.49	0.13	0.98	0.19
2006X	0.57	0.11	1.13	0.19
2006ax	0.62	0.15	1.24	0.21
2006et	0.64	0.16	1.27	0.22
2006gt	0.39	0.09	0.77	0.18
2006hb	0.41	0.11	0.81	0.19
2006kf	0.47	0.12	0.94	0.19
2007S	0.71	0.16	1.41	0.22
2007af	0.57	0.14	1.16	0.20
2007as	0.47	0.14	0.94	0.25
2007bc	0.55	0.14	1.09	0.20
2007bm	0.54	0.13	1.08	0.20
2007ca	0.66	0.16	1.29	0.22
2007if	0.65	0.16	1.30	0.22
2007jg	0.53	0.14	1.06	0.20
2007le	0.61	0.15	1.21	0.20
2007nq	0.46	0.13	0.92	0.20
2008C	0.63	0.16	1.26	0.23
2008fp	0.62	0.13	1.24	0.21
2014J	0.64	0.13	1.28	0.22

The observed L_{max} and $M_{^{56}Ni}$ distributions directly connect to the physical origin of the diversity amongst SNe Ia. A possible explanation is the difference in the explosion mechanism. Pure detonations of M_{ch} WDs [4] were seen to be unfeasible since they burn the entire star to iron group elements and do not produce the intermediate mass elements (IMEs) observed in SN Ia spectra. Pure deflagrations (e.g. [304]) can reproduce observed properties of SNe with $M_{^{56}Ni} \leq 0.4\,M_{\odot}$. Deflagration models however, cannot account for SNe with higher $M_{^{56}Ni}$ and hence, cannot explain the entire distribution in Figure 3.3.

Delayed-detonation models (e.g. [156, 326]) are more successful in producing higher $M_{^{56}Ni}$. In this explosion model a subsonic deflagration expands the white dwarf to create low densities for IMEs to be produced in a supersonic detonation phase which is triggered at a deflagration-to-detonation transition density (ρ_{tr}).

Recent 1D studies by [28] confront a suite of Chandrasekhar mass (M_{Ch}) delayed detonation models with observations for SNe with a range of peak luminosities. They find a very good agreement of their models with photometric and spectroscopic observations at maximum. The range of $M_{^{56}Ni}$ produced by their models corresponds well with the observations in Figure 3.3, making these models a strong candidate to explain the observed diversity.

M_{Ch} explosion models can possibly account for the observed distribution in $M_{^{56}Ni}$. Recent studies (e.g. [311]) on the other hand posit sub-Chandrasekhar mass explosions as a progenitor scenario for SNe Ia (for e.g. see [330]). This scenario is attractive since it can account for the progenitor statistics from population synthesis (see [185,263]) . Moreover, studies like [285] and [267] find a significant fraction of SNe Ia to have $M_{ej} < 1.4\,M_{\odot}$, providing observational evidence for the sub-M_{Ch} progenitor scenario. We compare the luminosity function in Figure 3.3 to the one obtained by [263], using their violent merger models. They present a relation between primary white dwarf mass (M_{WD}) and peak brightness for a grid of sub-M_{Ch} models. For objects in the lowest two bins of our luminosity distribution, the M_{WD} corresponds to 1 to 1.1 $_{\odot}$. For the highest luminosity objects, the models indicate an M_{WD} of $1.28\,M_{\odot}$. Thus, the luminosity function corresponds to a range of sub-Chandrasekhar M_{WD}, which provides further evidence for the plausibility of sub-M_{Ch} explosions as a progenitor scenario. The ^{56}Ni mass distribution (Fig. 3.3) is comparable to the yields from the models of [275]. Our L_{max} and $M_{^{56}Ni}$ distributions do

not allow us to distinguish which explosion mechanism is responsible for the observed variety.

We note that our sample includes one peculiar, super-M_{Ch} event, SN 2007if [268], with an estimated $M_{^{56}Ni} = 0.65\pm 0.16\ M_{\odot}$using our technique. This is significantly lower than the value estimated in [268] of $1.6 \pm 0.1\,M_{\odot}$. The t_2 estimate for this object is not exceptionally high, indicating a substantial but not exceptional amount of ^{56}Ni (similar to 91T-like SNe). One of the possible reasons for this discrepancy could be that the peak luminosity is not just a product of ^{56}Ni decay. This idea has been entertained in theoretical models for these super-M_{Ch} SN Ia. The models advocate a scenario of ejecta interaction with circumstellar material (CSM; [56, 110]). There is also an indication of a shell interaction in this supernova [268] and if this interaction results in increased peak luminosity then the ^{56}Ni mass through Arnett's rule would be overestimated. It could well be that additional energy is emitted in these super-M_{Ch} objects. A significant, but not extreme, amount of ^{56}Ni produced in the explosion along with interaction with the CSM could then explain the observed properties, e.g. lower ejecta velocities ($\sim$ 9000 km s^{-1}) and high peak luminosity. In [110], the lower limit on $M_{^{56}Ni}$ is $\sim 0.6\ M_{\odot}$which agrees well with our estimate.

The literature for such super-M_{Ch} objects with NIR light curves is still limited. Using the data in [297] for SN 2009dc, we obtain a t_2(J) of 31.7 ± 6.2 d which corresponds to an $M_{^{56}Ni}$ of $0.65 \pm 0.18\,M_{\odot}$. [300] also argue for less extreme $M_{^{56}Ni}$ based on late phase photometry and spectroscopy, although they prefer a comparatively higher $M_{^{56}Ni}$ ($\sim$1 $M_{\odot}$) than our inferred value. One possible reason could be that the high ejecta densities lead to an earlier onset of the recombination wave than expected for normal Ia's and hence an earlier t_2 than is expected for a given ^{56}Ni mass. This would lead to an inference of lower $M_{^{56}Ni}$ from t_2 for super-M_{Ch} SNe.

We note that the above derived $M_{^{56}Ni}$ estimates for the super-M_{Ch} SN Ia presume a "normal" rise time of 19 d. It was noted for both SN 2007if and SN 2009dc that the light curves were slowly-rising compared to normal SN Ia with $t_R \sim 20 - 22\,d$. Using this value of the rise time, the $M_{^{56}Ni}$ for SN 2009dc is $0.85 \pm 0.16\ M_{\odot}$, which is within errors of the estimate of 1 $M_{\odot}$presented by Taubenberger et al. [300]

If we assume that the inferred ^{56}Ni mass from t_2 indicate the core ^{56}Ni for

all SNe Ia the peak luminosity of super–M_{Ch} SNe Ia would be boosted by an additional energy source, like shell interaction within the explosion. A good indicator could be the late bolometric decline phase and luminosity. This comparison would be much closer to the ^{56}Ni determitation of the second peak than the peak bolometric luminosity.

Larger samples of well-observed SNe (e.g. [92]) will help in improving the statistics of such a study. Future investigations with a detailed comparison between observations and a suite of sub-M_{Ch} detonation models will help shed more light on the nature of the progenitor scenario and explosion mechanism of SN Ia. Moreover, future theoretical studies of peculiar, super-M_{Ch} SNe will help in deciphering the nature of these extreme explosions.

Acknowledgements This research was supported by the DFG Cluster of Excellence Origin and Structure of the Universe'. B.L. acknowledges support for this work by the Deutsche Forschungsgemeinschaft through TRR33, The Dark Universe. We all are grateful to the ESO Visitor Programme to support the visit of S. B. to Garching. We would like to thank Rahman Amanullah for providing published photometry of SN2014J in the near infrared.

4. Near Infrared and bolometric properties of fast-declining SN Ia indicate sub-Chandra explosions

Type Ia supernovae (SN Ia) are thermonuclear explosions of a C/O white dwarf in a binary system [121,130]. They exhibit diverse observable properties in the optical and the near infrared (NIR). In [61], we analysed NIR light curves of SN Ia at early and late phases to deduce that the diversity at late times was caused by the differences in ^{56}Ni mass (e.g. [27, 147]). We followed this up in [60] by correlating the peak bolometric luminosity (L_{max}) with the timing of the second maximum (hereafter, t_2), and estimating the ^{56}Ni mass independently of host galaxy reddening. In the above mentioned studies, however, SN Ia without a second maximum had to be excluded. Here, we analyse the NIR and bolometric properties of fast-declining SN Ia with two main aims; firstly, to characterise the diversity in fast-declining SN Ia and secondly, to determine whether they are a continuation of normal SN Ia to lower luminosities or if they arise from different explosions.

Dedicated supernova searches have discovered several SN Ia with unusual photometric and spectroscopic properties. One sub-class of peculiar SN Ia is characterized by high-luminosity at peak, slow post-peak decline rates and a spectrum dominated by strong Fe III absorption up to maximum light, similar to the prototypical SN 1991T [79, 244]. At the other extreme end, peculiar SN Ia show faint peak magnitudes, fast optical post-peak decline and a deep trough-like feature at $\sim$ 4200 Å in their maximum light spectra, attributed to TiII. These observables are similar to the prototypical SN 1991bg [78, 175]. [181] showed that SN 1991T-like objects constitute $\sim$ 9% of all SN Ia and fall on

the high-luminosity end of the width-luminosity relationship where they appear to merge with the bright end of normal SN Ia. However, SN 1991bg-like events comprise a larger fraction (15-20%) of the SN Ia population and appear distinct from normal SN Ia in their width-luminosity relationship. Unlike normal SN Ia, 91bg-like events show a preference to occur in elliptical and lenticular galaxies [127].

Based on multi-epoch spectra and multi-band optical light curves of a sample of fast-declining, 91bg-like SN Ia, [299] postulate that this class of SN Ia may have a different physical origin to normal SN Ia, but the possibility that they are a low-luminosity, fast-declining extension of normal SN Ia cannot be excluded. These SNe show markedly different optical colour evolution and low ^{56}Ni mass values, as calculated from UBVRI (pseudo-) bolometric light curves. SNe with intermediate properties between normal and subluminous SN Ia would lend support to the latter hypothesis [100].

The optical width-luminosity relation (WLR) for SN Ia [237, 241] shows a notable break for fast-declining objects ($\Delta m_{15}(B) > 1.6$). Fast declining SN Ia are fainter given their $\Delta m_{15}(B)$ assuming a linear WLR, possibly due to the inability of $\Delta m_{15}(B)$ to properly characterise fast-declining SNe since their light curves settle onto the linear decline earlier than +15 d. [36] propose a different ordering parameter, s_{BV} , to improve the treatment of fast-declining objects. s_{BV} is defined as the epoch at which the $(B-V)$ colour curve is at its maximum value, divided by 30 d. Using s_{BV} the fast declining SNe appear less as a distinct population and more as a continuous tail of normal SN Ia.

[100], reported that the 91bg-like SN 1999by was fainter in the NIR (JHK filters) than the average peak magnitudes derived for normal SN Ia in [163]. Subsequent studies found a bimodality in the NIR light curve properties of fast-declining SNe (e.g. [84,151,162,238]). Events whose NIR primary maxima occur after B-band maximum (t_{max}(B)) are subluminous in all bands compared to normal SN Ia. These subluminous SN Ia also tend to lack or have very weak second maxima in their NIR light curves. However, objects that peak in the NIR *before* t_{max}(B) have NIR absolute magnitudes comparable to normal SN Ia and show prominent (albeit, early) second maxima. Following these results, [131] propose the definition of 'transitional' SNe as fast-declining SN Ia with an NIR maximum before t_{max}(B).

Several theoretical models have been invoked to explain the origin of 91bg-like

SNe. [28] compare a suite of Chandrasekhar mass (M_{Ch}) delayed detonation models to observed properties of normal and fast-declining SN Ia at maximum light and find a good agreement at this epoch between the models and the observations for both normal and fast-declining SN Ia.

Recent studies (e.g. [275]) have shown that the detonation of a sub-M_{Ch} WD can also explain the observed properties of fast-declining SN Ia. A possible mechanism to detonate a sub-M_{Ch} WD is by the detonation of a surface layer of He, accreted from a companion (e.g. [23]), which triggers a secondary carbon detonation in the WD core (known as the *double detonation* scenario [80,330]). [222] showed that the violent merger of two equal mass, sub-M_{Ch} WD's also shows a good agreement with the observations of subluminous SN Ia. [224] explain both normal and rapidly declining SN Ia as helium-ignited violent mergers, thus, suggesting a common progenitor scenario for normal and fast-declining SN Ia.

From current observational and theoretical studies, it is still unclear whether fast declining SN Ia are a physically distinct population of SNe, arising from a different progenitor scenario. Our goal here is to analyse the NIR and bolometric properties for a sample of fast declining SN Ia and measure global parameters, e.g. ^{56}Ni mass and total ejecta mass, in order to characterise the diversity in the sample of fast declining SNe and see whether they appear separate from normal SN Ia.

The structure of the paper is as follows. In section 4.1 we describe our sample. We present our results in section 4.2, discuss them in section 4.3 and conclude in section 4.4.

4.1. Data

Our sample includes fast-declining SN Ia (Δm_{15} >1.6, corresponding to s_{BV} <0.65) from the literature with observations in the NIR (YJH) filters. Most of our data is compiled from the Carnegie Supernova Project [54, 288] as well as the CfA supernova survey on PAIRITEL [92, 324]. To these objects we add SN1999by [100] and iPTF13ebh [131]. The objects in our sample along with the source of the data are presented in Table 4.1

Our sample has 15 SNe. Ten of these SNe are spectroscopically classified as 1991bg-like [83,100]. Seven SNe in our sample show a pronounced NIR second maximum, three of which are spectroscopically 91bg-like (2006gt, 2007ba and 2008R). We discuss these cases in section 4.2. Since s_{BV} is shown to be a better ordering parameter than $\Delta m_{15}(B)$ for fast-declining SN Ia [36], we adopt this parameter for our analysis.

4.2. Results

NIR (YJH) light curves of some fast-declining SN Ia appear distinct from those of normal SN Ia [151,162]. In this section, we analyse the NIR (YJH) and bolometric properties of fast-declining SN Ia and compare them to normal SN Ia. We calculate the absolute magnitude and epoch of the NIR light curve peak as well as the light curve width and luminosity at late phases. The bolometric peak and late decline rate are calculated for fast-declining SNe and used to infer physical parameters, e.g. ^{56}Ni mass and total ejecta mass.

4.2.1. NIR light curve morphology near maximum

Some fast-declining SNe do not show a second maximum in the NIR, hence we look at the timing and strength of the first maximum and the width of the NIR light curve for objects in our sample.

Primary Maximum

Normal SN Ia peak in the NIR (YJH) bands *before* t_{max}(B) [61, 84, 151]. The magnitude and epoch of the NIR maximum for our sample is reported in Table 4.2.

Similar to [162] we find that some fast declining SNe peak after t_{max}(B) in the NIR. Most of these objects are also subluminous in the NIR filters, whereas SNe which peak before t_{max}(B) were *not subluminous*. The luminosity and epoch of the NIR maximum is correlated for fast-declining SN Ia, however, no such correlation is seen for normal SN Ia (Figure 4.1). SN 2007ba is that only SN that is bright in the Y-band but peaks ~ 1 d after t_{max}(B).

Table 4.1.: SN sample used in this analysis

SN	$t_B(max)$ (MJD; d)	Δm_{15} (mag)	s_{BV}	t_2(Y)[a] (d)	t_2(J) (d)	μ (mag)	Ref [b]
SN1999by*[c]	51308.3	1.93	0.46	N/A	N/A	30.82 (± 0.15)	H02,G04
SN2003gs	52848.3	1.83	0.49	···	15.3 (± 0.7)	31.65 (± 0.28)	K09
SN2005bl*	53481.6	1.80	0.39	N/A	N/A	35.14 (± 0.09)	WV08, F14
SN2005ke*	53698.6	1.78	0.41	N/A	···	31.84 (± 0.08)	WV08, C10, F14
SN2006gt*	54003.1	1.66	0.56	···	20.2 (± 1.2)	36.43 (± 0.05)	C10
SN2006mr*	54050.2	1.84	0.26	N/A	N/A	31.15 (± 0.23)	C10
SN2007N*	54124.3	1.79	0.29	N/A	N/A	33.91 (± 0.16)	S11
SN2007ax*	54187.5	1.86	0.36	N/A	N/A	32.20 (± 0.14)	S11
SN2007ba*	54196.2	1.88	0.54	20.0 (± 0.4)	···	36.18 (± 0.05)	S11
SN2007on	54421.1	1.90	0.57	18.7 (± 0.4)	18.2 (± 0.1)	31.45 (± 0.08)	S11
SN2008R*	54494.3	1.85	0.59	15.5 (± 0.7)	14.1 (± 0.7)	33.73 (± 0.16)	S11
SN2008hs	54812.1	1.83	0.60	···	14.0 (± 1.0)	34.28 (± 0.13)	F14
SN2009F*	54841.8	1.97	0.33	N/A	N/A	33.73 (± 0.16)	S11
SN2010Y	55247.5	1.73	0.61	···	···	33.44 (± 0.20)	F14
iPTF13ebh	56622.9	1.79	0.63	19.4 (± 0.2)	17.2 (± 1.5)	33.63 (± 0.16)	H15

[a]SN Ia with only one maximum are marked as 'N/A'. Ellipses indicates insufficient data to determine a second maximum
[b]References H02: [123], G04: [100], WV08: [324], C10: [54], S11: [288], F14: [92], H15: [131]
[c]*: Spectroscopically classified as SN 1991bg-like

Table 4.2.: Peak magnitude and epoch of maximum (with respect to t_{max}(B)) in $YJHK$ filters for the objects in our sample

SN	t_Y (d)	t_J (d)	t_H (d)	m_Y (mag)	m_J (mag)	m_H (mag)
1999by	...	...	2.98 (± 0.63)	...	...	-18.33 (± 0.19)
2005bl	...	1.12 (± 1.09)	...	...	-17.96 (± 0.13)	...
2005ke	1.88 (± 0.52)	1.33 (± 0.23)	2.05 (± 0.28)	-17.42 (± 0.08)	-17.45 (± 0.08)	-17.50 (± 0.08)
2006mr	5.46 (± 0.41)	3.26 (± 0.12)	5.11 (± 0.47)	-17.17 (± 0.23)	-17.17 (± 0.23)	-17.27 (± 0.23)
2007N	6.62 (± 1.03)	4.92 (± 2.00)	5.96 (± 1.30)	-17.48 (± 0.16)	-17.48 (± 0.18)	-17.65 (± 0.21)
2007ax	5.56 (± 0.24)	...	4.41 (± 1.63)	-17.01 (± 0.14)	...	-17.00 (± 0.15)
2007ba	1.12 (± 0.63)	-1.05 (± 1.9)	-0.42 (± 1.40)	-18.65 (± 0.06)	-18.56 (± 0.31)	-18.64 (± 0.11)
2007on	-2.88 (± 0.10)	-2.67 (± 0.10)	-3.49 (± 0.10)	-18.28 (± 0.19)	-18.37 (± 0.19)	-18.18 (± 0.19)
2008hs	...	-2.77 (± 0.63)	-3.21 (± 1.69)	...	-17.92 (± 0.15)	-17.82 (± 0.15)
2009F	5.14 (± 0.90)	1.80 (± 1.00)	...	-17.64 (± 0.19)	-17.57 (± 0.17)	...
2010Y	...	-1.88 (± 1.70)	...	...	-18.21 (± 0.26)	...
iPTF13ebh	-2.02 (± 0.10)	-0.48 (± 0.09)	-2.62 (± 0.91)	-18.57 (± 0.16)	-18.58 (± 0.16)	-18.46 (± 0.16)

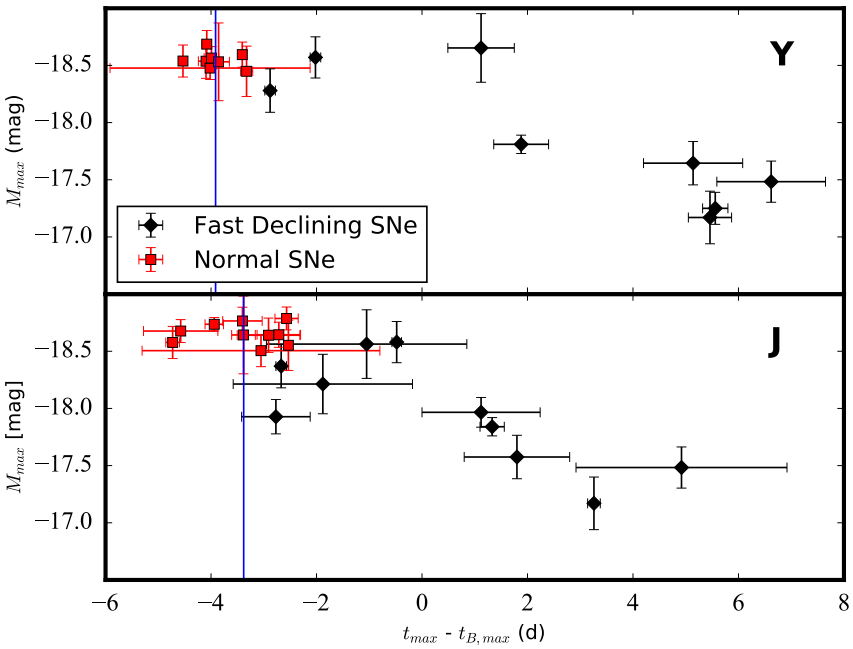

Figure 4.1.: The absolute magnitude versus epoch of the first maximum in the Y and J bands for normal SN Ia (red) and fast-declining SN Ia (black). The solid blue line is the mean value for the normal sample [61].

NIR Light curve width

SN Ia without an NIR second maximum are characterised, in this study, by the width of the NIR light curve (hereafter, $t_{0.5}$, defined as time between peak and the epoch when the SN has declined by 0.5 mag).

There is a correlation between $t_{0.5}$ in the Y-band and s_{BV} (Figure 4.2) for the single peaked SNe, suggesting that SNe with higher s_{BV} have wider NIR light curves. The relation is similar to the one between t_2 and $\Delta m_{15}(B)$ for normal SN Ia, however, the $t_{0.5}$ values are on average smaller than the t_2 for normal SNe [24, 61].

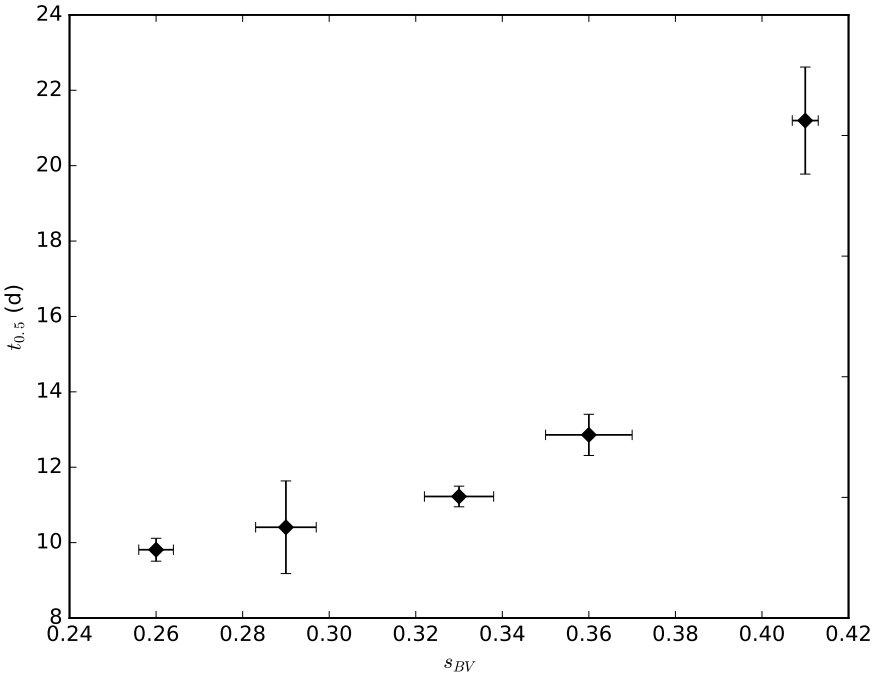

Figure 4.2.: Y-band light curve width versus s_{BV} for fast-declining SNe with a single peak.

Table 4.3.: Peak width of the low-luminosity SNe (in the Y filter)

SN	$t_{0.5}$ (d)
SN2005ke	21.2 ($\pm$ 1.4)
SN2006mr	9.8 ($\pm$ 0.3)
SN2007N	10.4 ($\pm$ 1.2)
SN2007ax	12.9 ($\pm$ 0.5)
SN2009F	11.2 ($\pm$ 0.3)

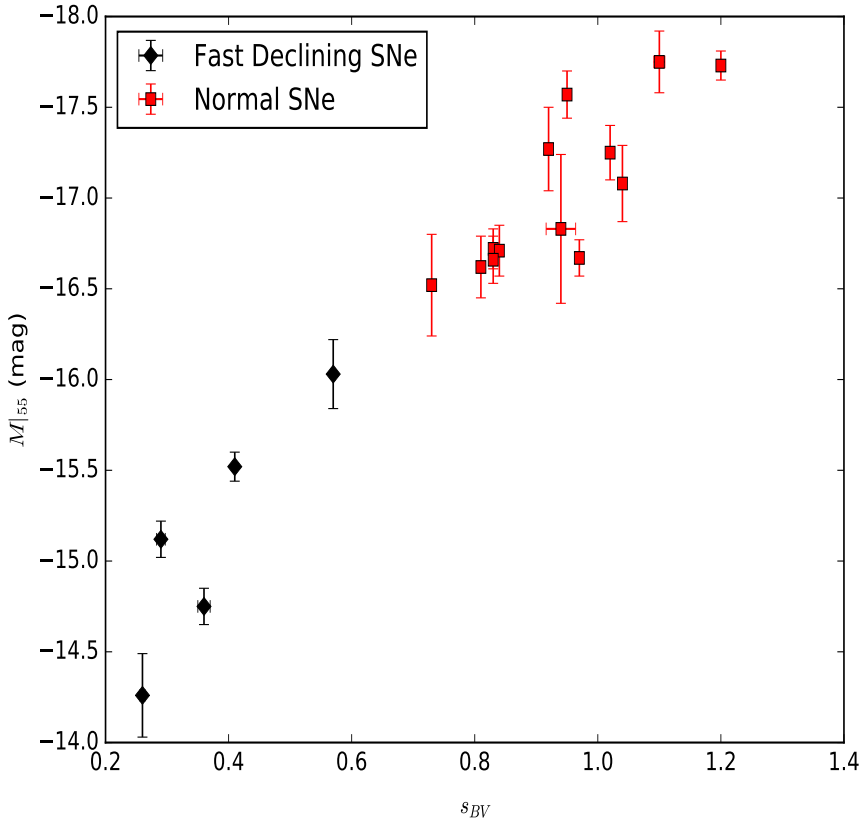

Figure 4.3.: $M|_{55}$ in the Y-band versus s_{BV} Red squares are normal SN Ia whereas black diamonds are the fast-declining objects in our sample.

4.2.2. Late phase properties

At phases >+40 d, the light curves settle onto a period of linear decline. The NIR absolute magnitude at +55 d ($M|_{55}$) is measured for SNe with at least 3 observations between +40 and +90 d after t_{max}(B). In [61], we showed that the decline rate after the second maximum is very similar for all SN Ia and that the absolute magnitude at +55 d ($M|_{55}$) is correlated with the intrinsic brightness. Here, we compare the $M|_{55}$ values of fast-declining and normal SN Ia.

Fast-declining SN Ia smoothly extend the relation between $M|_{55}$ and s_{BV} found for normal SN Ia to fainter luminosities (Figure 4.3). The average $M|_{55}$ value for fast-declining SN Ia is clearly lower (-15.13 mag) than the average for normal SN Ia (-17.02 mag), as can be seen in Figure 4.3. Similar to normal SN Ia, there is a large spread in the $M|_{55}$ values for fast-declining SN Ia

UBVRIJH (hereafter, UVOIR) pseudo-bolometric light curves are constructed for fast-declining SN Ia as described in [60]. The bolometric decline rate in the late phase was measured for fast-declining and normal SN Ia. Normal and fast-declining SN Ia have very similar and narrow distribution of their decline rates. Normal SN Ia have a mean decline rate of 0.034 ($\pm$ 0.004) mag d^{-1} whereas fast-declining SN Ia have a mean value of 0.033 ($\pm$ 0.004) mag d^{-1}. We note, however, that the sample of fast-declining SN Ia has only three SNe.

[53] also found that SN Ia in their sample have similar decline rates. The average value derived here of 0.033 ($\pm$ 0.004) mag d^{-1} is higher than the rate of 0.026 ($\pm$ 0.002) mag d^{-1} reported for their sample. This is because we include the NIR filters when constructing the bolometric light curve, which have significantly faster decline rates than the optical [61].

4.2.3. ^{56}Ni and Ejecta mass

Bolometric light curves are an important tool to measure physical parameters of SN Ia, e.g. ^{56}Ni mass, total ejecta mass. The UVOIR peak luminosity (L_{max}) is determined by fitting a cubic spline to the bolometric light curve.

The distribution of L_{max} for fast-declining and normal SN Ia is shown in Figure 4.4. Although the sample is small, there appear to be two subgroups amongst the fast-declining SNe, one with L_{max} $<0.3 \cdot 10^{43}$ erg s^{-1}and another with L_{max} $>0.5 \cdot 10^{43}$ erg s^{-1}. The faint sub-group appears distinct from the distribution for normal SN Ia, whereas the brighter sub-group extends the normal SN Ia distribution to fainter luminosities.

L_{max} is correlated with s_{BV} for both normal and fast-declining SNe (Figure 4.5). The relation for the faint subgroup of fast-declining SN Ia is different from the relation for SNe at the $\sim 2\ \sigma$ level (Table 4.4).

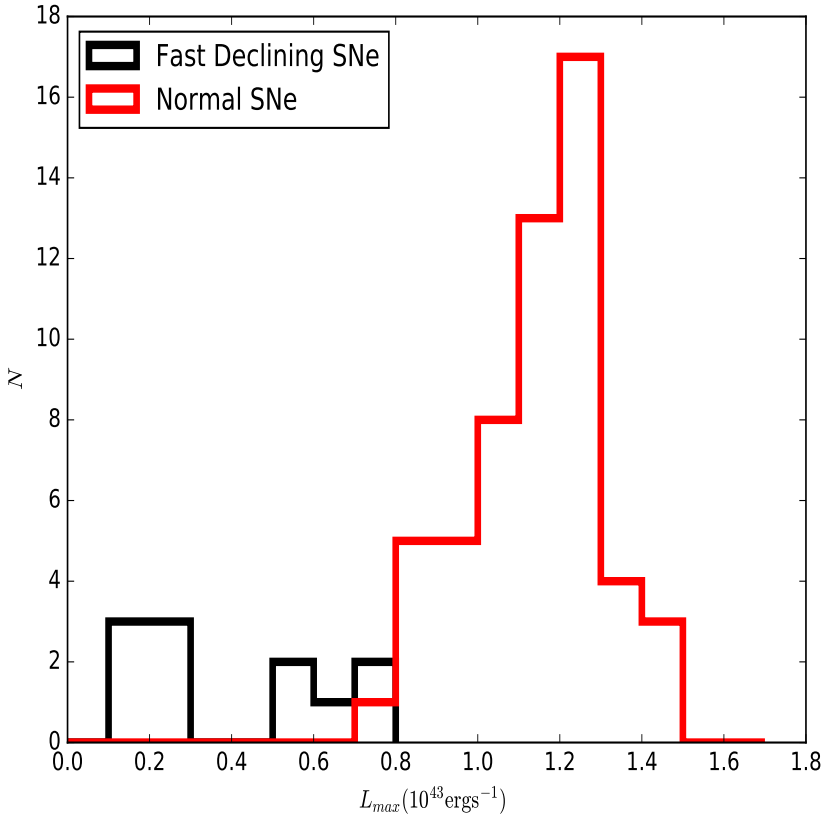

Figure 4.4.: Distribution of peak bolometric luminosity for fast-declining (black) and normal SN Ia (red). Fast-declining SNe are in two sub-groups based on their L_{max} , a faint group that is distinct from the normal SN Ia and a bright sub-group that is an extension of normal SN Ia.

Table 4.4.: Slope and intercept for the L_{max} -s_{BV} for the faint subgroup of fast-declining SN Ia.

Sample	Slope	Intercept
Fast-declining (faint sub-group)	0.76 (± 0.17)	-0.08 (± 0.06)
Others	1.24 (± 0.14)	-0.05 (± 0.11)

Arnett's rule states that the luminosity of the SN at peak is given by the instantaneous rate of energy deposition from radioactive decays inside the expanding ejecta [5,6]. For a rise time of 19($\pm$ 3) d and $\alpha = 1$ (the α parameter accounts for deviations from Arnett's rule), the relation between L_{max} and $M_{^{56}Ni}$ is shown in equation 4.1 (see [60] for a discussion).

$$L_{max} = 2.0(\pm 0.3) \times 10^{43} \frac{M_{^{56}Ni}}{M_{\odot}} \mathrm{ergs}^{-1} \tag{4.1}$$

The resulting ^{56}Ni masses for objects in our sample are reported in Table 4.5.

It has been noted that rise times of fast-declining SN Ia are shorter than for normal SN Ia (typically $\sim$ 13-16 d, see [96, 150, 299]). Shorter rise times of 13-16 d imply a larger coefficient relating the L_{max} and $M_{^{56}Ni}$ by 40 -15 % (and hence, smaller inferred ^{56}Ni mass) . Moreover, [28] find that the value of α for their least luminous model is 1.2. Therefore, using a more appropriate rise time and α would result in even lower ^{56}Ni masses. The values in Table 4.5 should, therefore, be treated as upper limits for fast declining objects.

The values of ^{56}Ni mass in Table 4.5 are significantly lower than the average amount of ^{56}Ni produced by a normal SN Ia (0.5 -0.6 $M_{\odot}$, e.g. see [60,267,285]). The ^{56}Ni mass values range from 0.05 - 0.38 $M_{\odot}$ indicating significant diversity in the sample of fast-declining SNe.

Fitting a radioactive deposition function to the quasi-exponential tail of the bolometric light curve (+40 to +90 d), we evaluate the fiducial timescale, the epoch at which the ejecta transition from optically thick to optically thin to γ rays (known as the fiducial timescale; see [295]).

The deposition function is given by the following equation

$$E_{dep} = E_{Ni} + E_{Co,e^+} + [1 - exp(-\tau)] \cdot E_{Co,\gamma} \tag{4.2}$$

The rise time (t_R) is an important parameter to infer ^{56}Ni mass and hence, the fiducial timescale and M_{ej} . To estimate its effect on the resulting t_0 values, we calculate t_0 for two different values of t_R (13 d and 19 d respectively) and discuss the resulting effect on M_{ej} in section 4.3.3.

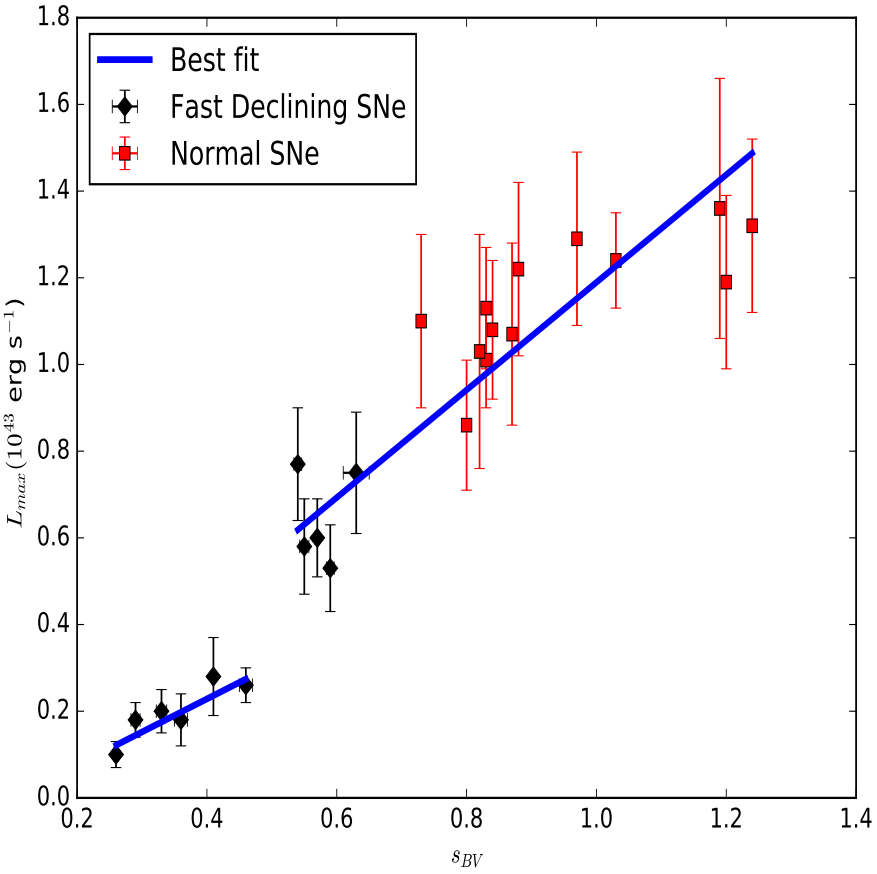

Figure 4.5.: L_{max} versus s_{BV} for normal SN Ia (red) and objects in our sample (black). Th best fit linear relations for the faint sub-group of the fast-declining SN Ia and the rest are plotted as blue solid lines.

Table 4.5.: ^{56}Ni masses for fast declining SNe with sufficient early and late time coverage to get a peak luminosity and a late time slope

SN	L_{max} (10^{43} erg s^{-1})	$M_{^{56}Ni}$ t_R=19 d; $M_\odot$	$M_{^{56}Ni}$ t_R=13 d; $M_\odot$
1999by	0.26 (± 0.04)	0.13 (± 0.03)	0.10 (± 0.02)
2005ke	0.28 (± 0.09)	0.14 (± 0.04)	0.10 (± 0.04)
2006gt	0.58 (± 0.11)	0.29 (± 0.07)	0.21 (± 0.05)
2006mr	0.10 (± 0.03)	0.05 (± 0.02)	0.04 (± 0.01)
2007N	0.18 (± 0.04)	0.09 (± 0.03)	0.07 (± 0.02)
2007ax	0.17 (± 0.06)	0.09 (± 0.03)	0.07 (± 0.02)
2007ba	0.77 (± 0.13)	0.38 (± 0.09)	0.28 (± 0.06)
2007on	0.60 (± 0.09)	0.30 (± 0.07)	0.22 (± 0.05)
2008R	0.53 (± 0.10)	0.27 (± 0.07)	0.20 (± 0.05)
2009F	0.20 (± 0.05)	0.10 (± 0.03)	0.07 (± 0.02)
iPTF13ebh	0.75 (± 0.14)	0.38 (± 0.10)	0.28 (± 0.07)

The total ejecta mass is calculated using Equation 4.3 (see [139] for a detailed derivation).

$$M_{ej} = 1.38 \cdot (\frac{v_e}{3000\,\mathrm{kms}^{-1}})^2 \cdot \frac{1/3}{q} \cdot \frac{0.025\,\mathrm{cm}^2\mathrm{g}^{-1}}{\kappa} \cdot (\frac{t_0}{36.80\,d})^2 \mathrm{M}_\odot \qquad (4.3)$$

where q is a form factor that describes the distribution of ^{56}Ni in the ejecta, κ is the mean γ-ray opacity, and v_e is the e-folding velocity of an exponential model's density profile. During the optically thin phase for an all-metal (μ_e = 2) ejecta κ is expected to be between 0.025 and 0.033 cm^{2}g^{-1} (see [139, 295]). Following previous studies, (e.g. [267, 285]), we adopted 0.025 cm^{2}g^{-1} as our fiducial mean γ-ray opacity.

For the e-folding velocity, we use a value of 3000 kms^{-1}, as adopted in [285] from 1-D Chandrasekhar mass models. We note, however, that the least luminous Chandrasekhar mass models of [28] as well as the least luminous sub-Chandrasekhar mass models (Blondin et al. in prep) v_e is $\sim$ 2700 kms^{-1}. We report ejecta mass values using both these values of v_e in Table 4.6.

We adopt a q parameter value of 1/3 as in [285] which implies that the ^{56}Ni is distributed uniformly in the ejecta. We note, however, that there is evidence

from nebular phase (>+100 d) spectra of fast declining SNe that the ^{56}Ni is concentrated more towards the center of the ejecta (e.g. [29, 203]). This would imply a higher q value and hence, a lower M_{ej}. Therefore, the values in Table 4.6 should be treated as upper limits for the ejecta masses.

Two SNe in our sample (SN 2007ax, SN 2009F) have sufficient late time coverage in the UBVRI filters, but not J and H filters. Using the optical-only (pseudo)-bolometric light curve, we calculate the t_0 and M_{ej} estimates for these two SNe (also reported in Table 4.6) .

4.3. Discussion

There is significant diversity in the NIR and bolometric properties of fast-declining SN Ia. Both the NIR and bolometric properties analyse here point towards a dichotomy in fast-declining SN Ia. We discuss our findings in context of the progenitor scenario and explosion mechanism for fast-declining SN Ia.

4.3.1. NIR properties

The peak luminosity and epoch of maximum in the Y and J-bands are correlated (Pearson coefficient $r \sim 0.7$) for fast-declining SN Ia (Figure 4.1, black diamonds;see also [36]). No such correlation is seen for normal SNe, indicating a difference between the normal and fast-declining SN Ia. Most objects with an NIR maximum *before* $t_{max}(B)$ are as bright as normal SN Ia in the NIR filters, whereas objects with late NIR maxima are faint in all filters (as seen in [162]).

For SNe with a single NIR peak, the diversity in the NIR is characterised by a light curve width parameter, $t_{0.5}$, the time between peak and when the SN has declined by 0.5 magnitudes. $t_{0.5}$ is correlated with the ordering parameter, s_{BV} , similar to the relation between t_2 and $\Delta m_{15}(B)$ for normal SN Ia [24,61]. [162] suggest that for faint explosions, t_2 occurs soon after t_1 and hence, the two peaks 'merge' into a single peak. This would be consistent with our result that the $t_{0.5}$ parameter for single peaked SN Ia is analogous to the t_2 for normal SN Ia.

Table 4.6.: Fiducial timescales (t_0), ejecta masses (M_{ej}) and bolometric decline rate for the low-luminosity SNe with sufficient early and late time coverage to get a peak luminosity and a late time slope (see text for assumptions about v_e, κ, and the form factor q).

SN	t_0 ($t_R = 13$ d) (d)	t_0 ($t_R = 19$ d) (d)	M_{ej} (t_R=13 d) ($M_\odot$; v_e=3000 kms^{-1})	M_{ej} (t_R=13 d) ($M_\odot$; v_e=2700 kms^{-1})	M_{ej} (t_R=19 d) ($M_\odot$; v_e=3000 kms^{-1})	M_{ej} (t_R=19 d) ($M_\odot$; v_e=2700 kms^{-1})	Decline rate (mag d^{-1})
2005ke	31.69 (± 0.83)	28.49 (± 0.60)	1.03 (± 0.24)	0.84 (± 0.20)	0.83 (± 0.20)	0.67 (± 0.16)	0.030 (± 0.0004)
2006mr	26.72 (± 0.47)	24.67 (± 0.40)	0.73 (± 0.19)	0.61 (± 0.17)	0.62 (± 0.17)	0.51 (± 0.16)	0.039 (± 0.0013)
2007ax*[a]	28.27 (± 0.69)	26.07 (± 0.50)	0.81 (± 0.21)	0.70 (± 0.18)	0.70 (± 0.18)	0.56 (± 0.16)	...
2007on	29.70 (± 0.77)	26.89 (± 0.16)	0.90 (± 0.21)	0.72 (± 0.19)	0.74 (± 0.19)	0.60 (± 0.16)	0.033 (± 0.0003)
2009F*	26.49 (± 0.60)	24.69 (± 0.40)	0.72 (± 0.19)	0.60 (± 0.16)	0.62 (± 0.16)	0.51 (± 0.14)	...

[a]*:Only using UBVRI data

The late phase NIR luminosity ($M|_{55}$) is also correlated with s_{BV} , extending the relation for normal SNe to fainter luminosities and smaller s_{BV} values. $M|_{55}$ estimates for fast-declining SNe span a large range of values, similar to the spread for normal SN Ia [61].

4.3.2. Bolometric properties and ^{56}Ni mass

The peak bolometric luminosities for fast-declining SNe span a large range from ~ 0.1 - $0.8 \cdot 10^{43}$ erg s^{-1}. There are two sub-groups, one with L_{max} <0.3 $\cdot 10^{43}$ erg s^{-1}and another with L_{max} >0.5 $\cdot 10^{43}$ erg s^{-1}. SNe in the faint sub-group have single-peaked NIR light curves whereas those in the bright sub-group show a double peak, similar to normal SN Ia. L_{max} is correlated with s_{BV} for fast declining and normal SN Ia as shown in Figure 4.5.

The late bolometric decline (between 40 - 90 d) for fast-declining SN Ia has a narrow distribution. This implies that the fraction of energy converted to the (pseudo-)bolometric flux at late phases appears to change in an identical manner for the majority of SNe. Although normal SN Ia are brighter in the late phase than the fast-declining SN Ia, the distribution of the decline rate is very similar to that for fast-declining SNe implying that the inner ejecta structure for normal and fast-declining SNe is similar [328]. We caution, however, that there are only 3 fast-declining SNe with enough data to measure the UVOIR late decline rate. A larger sample of SN Ia with multi-band data at late epochs will be useful to confirm this result.

4.3.3. Ejecta mass

By fitting a radioactive energy deposition function to the quasi-exponential part of the bolometric light curve, we derive fiducial timescale values and ejecta masses for SN Ia that have sufficient coverage in the specified range of epochs. From the resulting values in Table 4.6, we find that the ejecta masses are significantly below 1.4 $M_{\odot}$, pointing towards a sub-Chandrasekhar mass progenitor for these SNe. The two SNe 2007ax and 2009F for which we measured t_0 from the UBVRI (pseudo)-bolometric light curve also show significantly sub-M_{Ch} ejecta masses.

Table 4.6 shows the fiducial timescale (t_0) estimates for two different values of the rise time (13 d and 19 d). A shorter rise time (t_R) implies a smaller inferred ^{56}Ni mass estimate for the same L_{max} and hence, yields a larger t_0. A longer t_R of 19 d would yield a smaller t_0 and hence, a lower ejecta mass (M_{ej}). Therefore, a t_R of longer than 13 d, assumed here, would imply smaller M_{ej} values, further strengthening the argument for a sub-M_{Ch} progenitor.

Several theoretical studies have invoked the sub-M_{Ch} scenario to explain SN Ia. The C/O fuel can be ignited indirectly through the surface detonation of a thin He-rich accreted layer leading to carbon detonation from compressional heating (known as the "double detonation" scenario [80,330]). [169] find that the double detonation scenario can reproduce the single-peak light curve morphology of faint SN Ia. An alternate mechanism to ignite the C/O fuel is through a merger of two sub-M_{Ch} WDs with the total system mass (M_{tot}) that is sub- [311] or super- [222] M_{Ch} . [222] show that the prompt explosion of the primary during the dynamical merger process (known as a 'violent merger') can reproduce the low-luminosity, red colours, Ti II features in the spectra and the single-peak NIR light curves of SN Ia spectroscopically similar to SN 1991bg. However, the violent merger scenario produces light curves that are too broad compared to the observations. [275] find a good agreement between the width-luminosity relation for their models and the observed relation from [118]. The lower ejecta densities in sub-M_{Ch} models favour γ ray escape and leakage of optical photons leading to narrower light curves for the same ^{56}Ni mass (and hence, peak luminosity; [25], Blondin et al. in preparation).

Two fast-declining SN Ia (SN 1999by, SN 2005ke) have spectropolarimetric observations presented in the literature [127, 229]. The SNe display similar continuum polarisation values, which are significant larger than the values found for normal SN Ia [226, 312] indicating asymmetries in the ejecta arising from the explosion mechanism.

Detailed modeling of the polarisation spectra led to the conclusion that these fast-declining SNe could result from one of three scenarios; a WD rotating at close to break-up velocity, a M_{Ch} delayed detonation or a merger of two WDs. For SN 2005ke , a significantly sub-M_{Ch} ejecta mass (Table 4.6) combined with the conclusions from the polarimetry would suggest that a merger of two WDs (with total mass $M_{tot} < M_{Ch}$) would be the most favourable scenario for this SN.

Combining Tables 4.5 and 4.6 (for a rise time of 13 d), we calculate the ratio of the M_{ej} to $M_{^{56}Ni}$ (hereafter, R_M) for fast-declining SNe. Fast-declining SN Ia in the faint sub-group have significantly larger R_M values compare to normal SNe (red squares, Figure 4.6 [267]).

Figure 4.6 shows the comparison between R_M and $M_{^{56}Ni}$ estimates from observations of SNe and the values from different model scenarios. The solid green curve shows the values for a M_{Ch} ejecta whereas the yellow squares are the values from the sub-M_{Ch} detonations of [275]. The blue squares are the values for violent mergers of two WDs leading to subluminous [222] and normal [223] SN Ia. The observed ratios agree better with sub-M_{Ch} model values than with the M_{Ch} values, although the errors are large due to large uncertainties in the individual M_{ej} and $M_{^{56}Ni}$ values.

4.4. Conclusion

Based on their NIR and bolometric properties, fast-declining SN Ia appear to be in two distinct sub-groups. The first sub-group is characterised by single peaked NIR light curves that peak *after* t_{max}(B), whereas the second sub-group shows a double peak morphology in the NIR and a first maximum occuring *before* t_{max}(B), similar to normal SN Ia [162,238]. SNe with a single peak also show fainter bolometric peak luminosities ($<0.3 \cdot 10^{43}$ erg s^{-1}) compared to double peaked SNe ($>0.5 \cdot 10^{43}$ erg s^{-1}).

Fast-declining SN Ia display a range of L_{max} values, implying a range of ^{56}Ni masses for these SNe. Single peaked SNe have $M_{^{56}Ni}$ values $\lesssim 0.15\ M_{\odot}$whereas double peaked fast-declining SNe have ^{56}Ni masses in the range $\sim$ 0.25 - 0.4 $M_{\odot}$, closer to the low end of the normal SN Ia ^{56}Ni mass distribution [60, 267, 285].

M_{ej} estimates for fast-declining SN Ia, including the 'transitional' SN 2007on, are significantly sub-M_{Ch} , even for conservative assumptions on the e-folding velocity and the distribution of ^{56}Ni .

Faint, single peaked, fast-declining SN Ia have extremely high R_M values (Figure 4.6) compared to the estimates for normal SN Ia [267]. SN 2007on, the only 'transitional' SN in this study with enough data for an M_{ej} estimate, has an

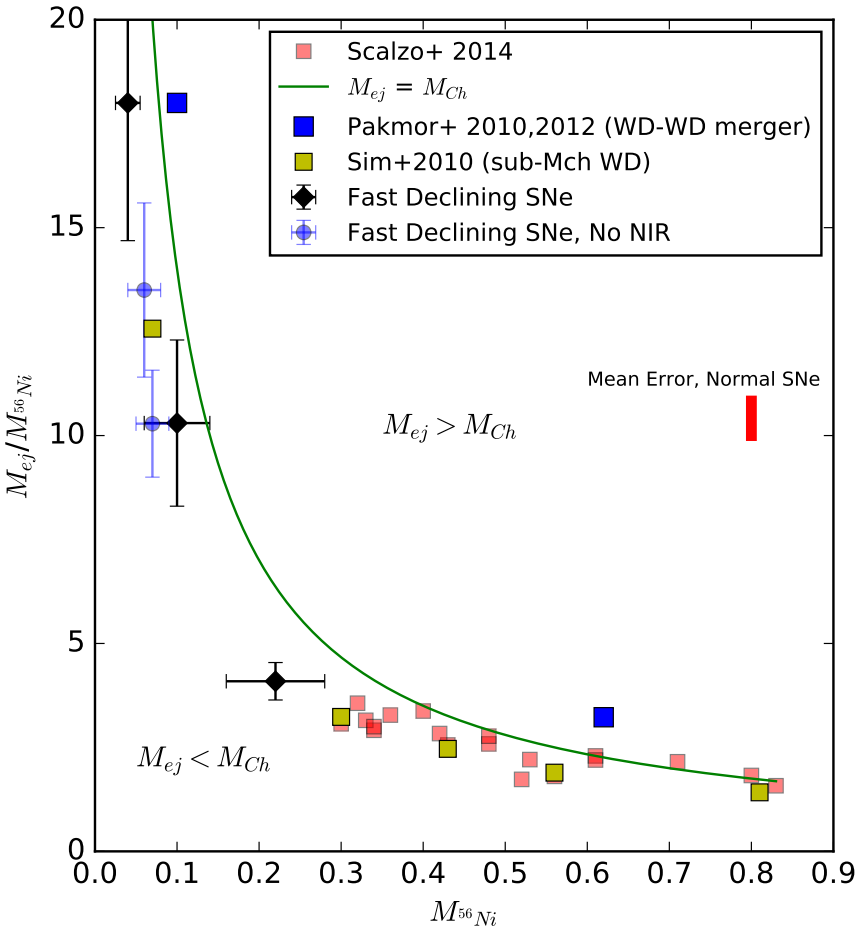

Figure 4.6.: The ratio of the ejecta mass to ^{56}Ni mass is plotted against the ^{56}Ni mass. The black points are SNe with NIR coverage in the late phase (+40 to +90 d) whereas the blue points are the two SNe without NIR coverage (SN2007ax, SN2009F). The red points are normal SN Ia taken from [267]. We also plot the values from different model scenarios. The yellow squares are from [275], blue squares from violent merger models for normal and subluminous SNe from [222, 223] and the green curve is the ratio for a M_{Ch} explosion. We plot the typical error bar for the observed SNe in red.

Table 4.7.: Comparison of parameters for SNe in our sample with typical values for normal SN Ia

SN	s_{BV}	L_{max} ($\cdot 10^{43}$erg s^{-1})	NIR second maximum	$t_{0.5}$ (d)	t_{max}(J) (d)	$M\|_{55}$ (mag)	$M_{^{56}Ni}$ ($M_\odot$)	M_{ej} ($M_\odot$)	R_M
SN2006mr*[a]	0.26	0.10 (± 0.03)	N	9.8 (± 0.3)	3.26 (± 0.12)	-14.26 (± 0.23)	0.10 (± 0.03)	0.72 (± 0.15)	18.0
SN2007N*	0.29	0.18 (± 0.04)	N	10.4 (± 1.2)	4.92 (± 2.00)	-15.12 (± 0.10)	...	...	...
SN2009F*	0.33	0.20 (± 0.04)	N	11.2 (± 0.3)	1.80 (± 1.00)	...	0.10 (± 0.04)	0.72 (± 0.15)[b]	10.3
SN2007ax*	0.36	0.17 (± 0.06)	N	12.9 (± 0.5)	...	-14.75 (± 0.10)	0.09 (± 0.03)	0.81 (± 0.15)[a]	13.5
SN2005bl*	0.39	...	N	...	1.12 (± 1.09)	...	...	...	...
SN2005ke*	0.41	0.28 (± 0.09)	N	21.2 (± 1.4)	1.33 (± 0.23)	-15.52 (± 0.08)	0.14 (± 0.04)	1.03 (± 0.19)	10.3
SN1999by*	0.46	0.26 (± 0.04)	N	...	...	...	0.13 (± 0.03)	...	...
SN2007ba*	0.54	0.77 (± 0.11)	Y	...	-1.05 (± 1.9)	...	0.38 (± 0.10)	...	...
SN2006gt*	0.56	0.58 (± 0.10)	Y	...	...	...	0.29 (± 0.07)	...	...
SN2007on	0.57	0.60 (± 0.09)	Y	...	-2.67(± 0.10)	-16.03 (± 0.19)	0.30 (± 0.07)	0.90 (± 0.17)	4.1
SN2008R*	0.59	0.53 (± 0.10)	Y	...	...	...	0.27 (± 0.07)	...	...
SN2008hs	0.60	...	Y	...	-2.77 (± 0.63)	...	...	...	...
SN2010Y	0.61	...	Y	...	-1.88 (± 1.70)	...	...	...	...
iPTF13ebh	0.63	0.75 (± 0.10)	Y	...	-0.48 (± 0.09)	...	0.37 (± 0.08)	...	...
Normal SN Ia	$\gtrsim 0.55$	$\sim$ 0.6 - 1.4	Y	N/A	$\sim$ -3.5	$\sim$ -17	$\sim$ 0.25 - 0.75	$\sim$ 0.9 - 1.4	$\sim$ 1.5 - 3.5

[a]*:Spectroscopically classified as SN 1991bg-like

[b]Calculated from UBVRI (pseudo-)bolometric light curve

R_M values that is similar to normal SNe from [267]. This would indicate that single peaked fast-declining SNe may arise from a different explosion mechanism to normal SN Ia, however, the 'transitional', fast-declining SNe might arise from the same explosion mechanism as normal SNe. A larger sample of these 'transitional' SNe would be required to test this hypothesis.

The evidence from the NIR and bolometric properties suggests that there are two sub-groups of fast-declining SN Ia, the fainter of which may arise from a different explosion mechanism to normal SN Ia, whereas the bright subgroup appears to be a extension of the normal SN Ia population to fainter luminosities (and hence, lower ^{56}Ni masses). The evaluated ejecta masses for SNe in the fast-declining sample would point towards a sub-M_{Ch} progenitor for these explosions.

Larger samples of fast-declining SN Ia with optical and NIR observations at late phases will help in creating a distribution of M_{ej} values for these SNe. Future investigations with a detailed comparison between observations and a suite of sub-M_{Ch} models will help shed more light on the progenitor scenario and explosion mechanism for fast-declining SN Ia.

Acknowledgements We all are grateful to the ESO Visitor Programme to support the visit of S. B. to Garching when this work was started. We thank Andrew Friedman for providing CfAIR2 light curves in machine-readable form.

5. Nebular Phase Observations of Type Ia supernovae

5.1. Introduction

At early times (upto a few months post maximum), SN Ia light curves are powered by the γ- rays from the radioactive decay of ^{56}Ni . As the ejecta expands, the γ-ray escape fraction increases and the light curve is mostly dominated by the contribution from e^+ that result from the decay of ^{56}Ni and its daughter nuclide ^{56}Co. Hence, observations in the nebular phase offer complementary information to the near-maximum light observations.

Spectroscopy in the nebular phase (>100 days past maximum light) has provided key insights into the physical properties of the SN explosion. Measurements of the 7380 Å line, attributed to stable ^{58}Ni (since only a negligible amount of ^{56}Ni would be leftover at such late epochs) were used to infer a common explosion mechanism for SN Ia [204]. The line velocity for this feature was used to infer the presence of asymmetries in the inner core of SN Ia [189], which was also found to correlate with optical colour and the SiII 6355 Å velocity gradient during the photospheric phase [189]. These shifts have been found to also correlate with photospheric phase spectropolarimetry indicating a general correlated asymmetric geometry of SN Ia [202]. Liu et al. [184] find that sub-Chandra "double-detonations" fit that late time spectra of SN 1994D better than Chandrasekhar mass delayed detonations. Hence, the nebular phase spectra are a key tool to distinguish the explosion mechanism and progenitor mass.

Taubenberger et al. 2015 [298] presented a spectrum for SN 2011fe at >1000 d after maximum and found two puzzling effects. Firstly, the spectra were dominated by [Fe I] lines at $\sim$ 1000 d, as opposed to [Fe II] lines in the spectra

at $\sim$ 300 d indicating a lower ionisation state of the ejecta. Secondly, there was a collective redshift of the features by $\sim$ 4000 km/s. Apart from the ionisation evolution of the ejecta, observations at such late phases are also crucial to test the presence of less abundant radioactive isotopes, e.g. ^{57}Ni, ^{55}Fe and ^{44}Ti. Nebular spectra of SN Ia have also been used to place limits on the amount of stripped/ablated hydrogen from a non-degenerate companion and hence, present constraints on the progenitor scenario for SN Ia (for e.g. see [192, 273]).

Most studies of SN Ia at nebular phases mentioned above focus on data in the optical wavelength regime. Profiles of spectral lines in the NIR offer key information about the temperature, ionisation state and geometry of the ejecta. Unlike in the optical where the spectral features are produced by a number of overlapping lines, making the intrinsic emission profile difficult to untangle, the NIR contains lines that are much more isolated (for e.g. see [205]). Early efforts by Spyromilio et al. [280] used NIR spectra to obtain limits on the total Fe mass in the ejecta and to constrain the physical conditions e.g. electron density and temperature. Modelling the optical + NIR spectra, the authors were able to calculate the ionisation fraction for the iron in the ejecta. Moreover, the late-time evolution of the [Fe II] and [Co II] lines in the optical [170] and NIR [279] have been used to explore the radioactive element abundances in the SN ejecta.

NIR spectra in the nebular phase have also been used to deduce asymmetries in the ejecta of SN Ia [210]. The profile of the [Fe II] 1.644 μm line is important to constrain the presence of stable iron-group elements in the core of the SN ejecta. For SN 2003du, Hoeflich et al. [124] find a signature of electron capture elements, indicating burning under high density conditions. Diamond et al. [62] present three NIR spectra of SN 2005df. They use the width of the [Fe II] 1.644 μm line to determine the central density (ρ_c) of the exploding WD, finding the mass to be close to the Chandrasekhar limit ($1.31 \pm 0.03\ M_\odot$) and find high initial magnetic fields of 10^6G, although they cannot rule out 0G due to noisy spectra. This motivates the need for higher signal-to-noise spectra to distinguish between different magnetic field strengths in SN Ia ejecta.

In this chapter we present observations of SN Ia in the nebular phase to understand the physical properties of the ejecta as well as constrain parameters for the reddening from host galaxy dust. The NIR spectra in the nebular phase

provide complementary constraints on the dust properties to maximum light observations and are particularly important for highly-reddened supernovae in order to understand the behaviour of dust around SN Ia compared to dust in the Milky Way. We present three Near Infrared spectra about between $\sim$ 400 and 500 days from maximum light for SN 2014J. We analyse these spectra to constrain the ^{56}Ni mass, R_V and A_V for the host galaxy dust. We also discuss ongoing and future work on multi-band photometry in the nebular phase to derive transparency timescales, ^{56}Ni masses and to constrain the strength and configuration of the magnetic field.

5.2. Near Infrared Spectroscopy in the Nebular Phase

5.2.1. Observations and data reduction

SN 2014J is the nearest SN Ia observed in $\sim$ 40 years. It was discovered serendipitiously in the nearby edge-on irregular galaxy M82 by Fossey et al. [88]. Although the early time photometry indicates a high extinction from host galaxy dust (see for e.g. [2]), a visual peak magnitude of 10.61 ($\pm$ 0.05) mag [86] and a distance of 3.5 Mpc [146] make it an ideal candidate for follow-up observations in the nebular phase.

In this study we present Near Infrared (NIR) spectra of SN2014J, obtained using GNIRS, a Near Infrared spectrograph on Gemini-North telescope. The spectra were obtained on March 15, April 26, and May 24, 2015, between 400 and 500 days after explosion on January 14.75, 2014 (Zheng et al. 2014 [332]). The observations were made as part of the Gemini Fast Turnaround program [200] under proposal GN-2015A-FT-3 (P.I. M. Van-Kerkwijk). The spectrum was obtained in cross-dispersed (XD) mode with a central wavelength of 1.65 μm. The spectrum has wavelength coverage from 0.825 to 2.5 μm.

The spectra were reduced using the standard Gemini IRAF [1] package. The final spectra were extracted using the IRAF task *apall*. For the first night we

[1] IRAF is distributed by the National Optical Astronomy Observatories, which are operated by the Association of Universities for Research in Astronomy, Inc., under cooperative agreement with the National Science Foundation

Table 5.1.: Observing log for the NIR spectra of SN 2014J taken with the GNIRS Spectrograph on Gemini-North Telescope

UT Date	Phase	Wavelength coverage (μm)
Mar 15, 2015	+408	0.825 - 2.5
Apr 26, 2015	+450	0.825 - 2.5
May 24, 2015	+478	0.825 - 2.5

used the A0 star HIP 32549 as our standard star for telluric correction. For the second and third night , we use the A7 star HIP 50685.

5.2.2. Analysis

The NIR spectrum of SN 2014J is dominated by forbidden lines of singly ionised iron and singly ionised cobalt. In particular the prominent features at the long end of the J window (around 1.26 μm) and almost the entirety of the H band emission arise from multiplets a^6D–a^4D and a^4F–a^4D of [Fe II] respectively while the feature around 0.9 μm is dominated by the a^4F–a^4P multiplet. Additional contributions at these wavelengths arise from [Co II] transitions from the a^3F–b^3F and a^5F–b^3F multiplets in the J (around 1 μm) and H (around 1.5 μm) bands respectively. The line identification is provided in Table 5.2.

The two strongest lines in the spectrum are the [Fe II] 1.257 μm $a^6D_{9/2}$–$a^4D_{7/2}$ and the 1.644-μm [Fe II] $a^4F_{9/2}$–$a^4D_{7/2}$ which arise from the same upper level. In the absence of additional contributions to the features at these wavelengths the observed line ratio can be used to determine the extinction between the J and H bands is it solely dependent on the Einstein A-values and the statistical weights of these transitions. Similarly the [Co II] 1.547 μm a^5F_5–b^3F_4 and 1.019 μm a^3F_4–b^3F_4 transitions also share an upper level.

Fitting the J and H band spectra is relatively straightforward either using LTE or non-LTE prescriptions as all the lines arise from the same upper energy levels. In the case of [Fe II] the a^4D and in the case of the [Co II] b^3F. The free parameters are the ratio of iron to cobalt, the line width, the offset from the systemic velocity of the supernova that the singly ionised transitions of

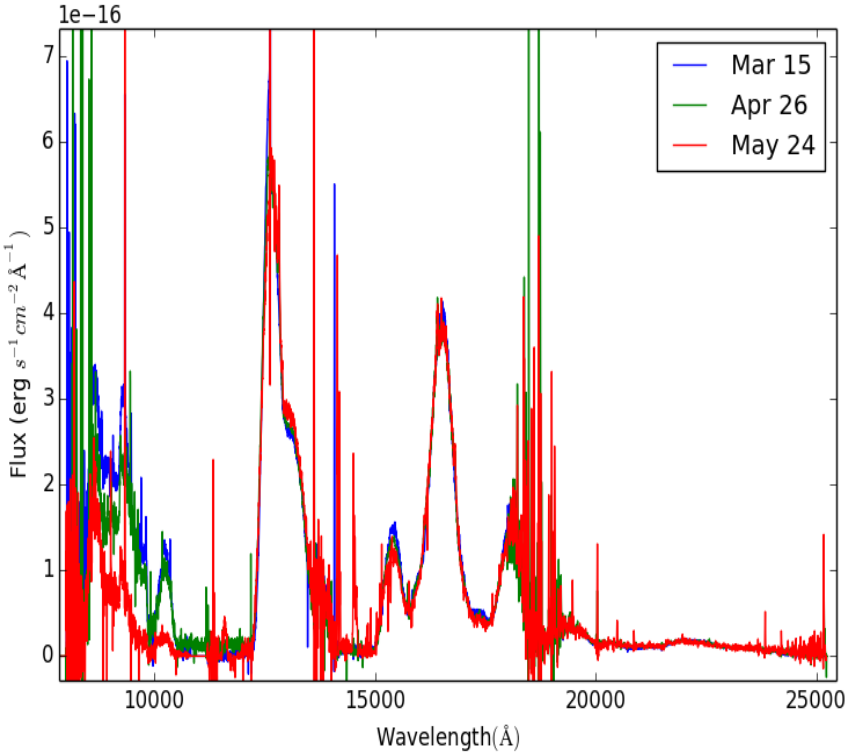

Figure 5.1.: NIR spectra of SN 2014J for the three nights it was observed with the GNIRS spectrograph. The first spectrum was corrected for tellurics using the A0 standard star HIP32549, whereas the second and third spectra were corrected with the A7 star HIP 50685.

the iron group elements may exhibit (for e.g. see [189]) and the extinction. In Fig. 5.2 the fit to the spectrum is shown using solely singly ionised cobalt and iron. Only the prominent feature at 0.98 μm remains unaccounted for. The cobalt lines are fit using an LTE population of the energy levels while for the iron we use a non-LTE distribution as described in Spyromilio et al. [280]. The Einstein A values used in that model are from Nussbaumer & Storey [220].

The contribution of the [Co II] to the spectrum can be easily determined by the strength of the 1.019 μm, feature which then determines (modulo the extinction) all the other lines.

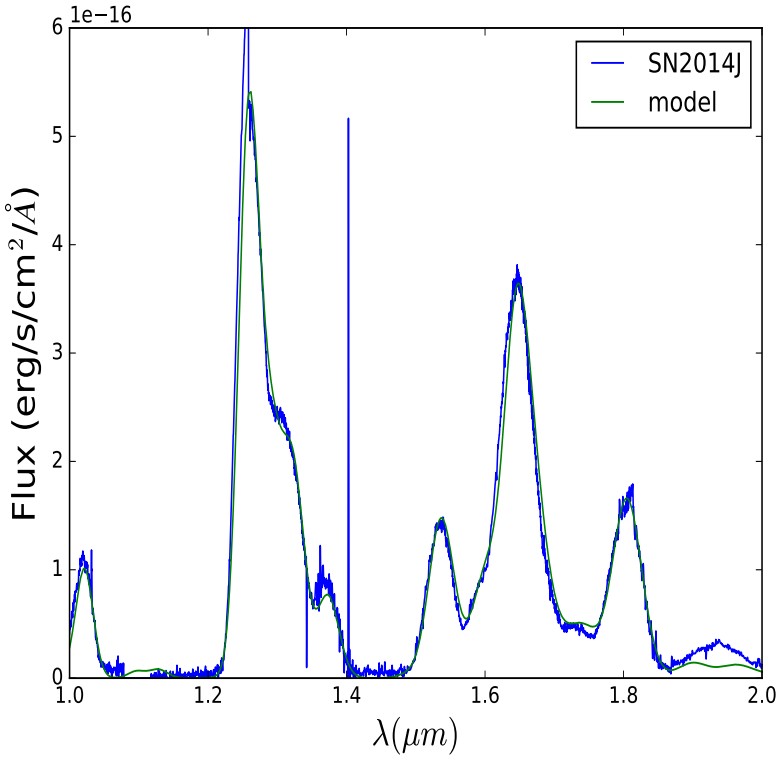

Figure 5.2.: The NIR spectrum taken on March 15, 2015 (+408 d; *blue*) is fit with a forbidden line spectrum for [Fe II] and [Co II] reddened with a CCM reddening law with $R_V = 3.1$ and $A_V = 2.2$ (*green*). The model spectrum is seen to fit the observed line ratios well.

Table 5.2.: Line Identification for SN 2014J

$\lambda(\mu m)$	Species	Term	J
0.8619	[Fe II]	a^4F - a^4P	9/2 - 5/2
1.0191	[Co II]	a^3F - b^3F	4 - 4
1.2570	[Fe II]	a^6D - a^4D	9/2 - 7/2
1.5339	[Fe II]	a^4F - a^4D	9/2 - 5/2
1.5474	[Co II]	a^5F - b^3F	5 - 4
1.6440	[Fe II]	a^4F - a^4D	9/2 - 7/2

Excluding contaminants

A strong line at 1.644 μm arises from [Si I] and can be expected to be contributing to the H band spectrum as Si is present in the early spectra of supernovae. The high quality data presented here for 2014J show a clear 'knee' on the blue side of the 1.6440 μm feature. This 'knee' at 1.600 μm is clearly reproduced in our model spectra and is identified as arising from the 1.600 μm [Fe II] $a^4F_{7/2}$–$a^4D_{3/2}$ transition. Any contribution by [Si I] to this feature would reduce the relative contribution of the 1.600 μm line and underproduce the 'knee' in the profile (see Fig. 5.2).

Extinction

With the absence of contaminants established and the scale of the contributions of [Fe II] and [Co II] determined by the flux of the 1.644 μm and the 1.019 μm features the remaining free parameter is the extinction.

Requiring the ratio of the 1.257 to 1.644 lines as well as the 1.547 and 1.019 lines to fit the data we derive $A_{1.257}$–$A_{1.644}$=0.21 and $A_{1.019}$–$A_{1.547}$=0.42 which fits well within the errors of the derivation of the Cardelli, Clayton, Mathis reddening law [41] (hereafter CCM) assuming an R_V of 3.1 and A_V of 2.2. These values of the differential absorption are at odds with the derived R_V of 1.40 ± 0.10 and A_V of 1.85 ± 0.11 [230] which using the CCM prescription would give $A_{1.257}$–$A_{1.644}$= 0.09 and $A_{1.019}$–$A_{1.547}$=0.17.

Observations of SN 2014J near maximum light support an R_V that is lower than the Milky Way value. Kawabata et al. 2014 [152] confirm this observation from broad-band imaging polarimetry in the optical and NIR. The authors, however, note that there is a systematic difference between the polarisation law fitted and the observations at $\lambda > 1$ μm. Here, we fit the polarisation law to the NIR data only and derive the R_V. Below we describe the polarisation law and the derivation of R_V.

Serkowski Law: The empirical wavelength dependence of the optical/NIR polarisation follows the "Serkowski Law" given as follows

$$\frac{P(\lambda)}{P(\lambda_{max})} = \exp[\mathrm{K} \ln^2(\lambda/\lambda_{\max})] \tag{5.1}$$

where λ_{max} is the maximum wavelength for polarisation $P(\lambda_{max})$ and K is a linear function of λ_{max}. Although the Serkowski law describes the dust properties well in the optical/NIR regime at $\lambda > 2$ μm the polarisation departs from the Serkowski law and has a power law behaviour.

λ_{max} is related to the total to selective absorption ratio R_V as follows (see Serkowski et al. 1975 [272], Whittet 2003 [322] for more details)

$$R_V = 5.6(\pm 0.3) \cdot \lambda_{max} \tag{5.2}$$

We fit Equation 5.1 to the imaging polarimetry data presented in Kawabata et al. 2014 [152]. In line with the analysis presented by the authors, we fix the K parameter to 1.15, typical for Galactic Interstellar Polarisation (ISP) [272]. For the optical + NIR case we reproduce the maximum polarisation and λ_{max} noted in the study. For the NIR only case we find that λ_{max} is 0.54 ($\pm$ 0.05) μm, which is higher than the optical+NIR value of 0.23 μm. Using Equation 5.2 and the derived λ_{max} we obtain R_V of 3.02 $\pm$ 0.32, which is consistent with the Milky Way value of 3.1.

Mass of Fe^+

We use the flux in the 1.644μm line to derive the mass of Fe in the ejecta. We correct the spectrum for R_V = 3.1 and A_V =2.2 as mentioned above, using the CCM law to obtain the unextinguished flux in the line.

The emissivity of the 1.644 μm transition is 8.56×10^{-17} ergs/s/atom [280]. Assuming a distance of 3.5 Mpc for M82 and an unextinguished flux of 3.15 $\times 10^{-13}$erg/s/Åfor the 1.644 line we derive a mass of 0.25 $M_\odot$ for [Fe II] for the supernova at the epoch of the spectrum.

The infrared spectrum provides little evidence for doubly ionised iron but it is well known from combined optical and infrared spectra (e.g. Spyromilio et al. [280]) that strong transitions of [Fe III] are present in the blue (4700-Å). Typical ionisation fractions of Fe^{++} to Fe^+ of 8:5 or higher have been derived by Axelrod 1980 [11] as well as other authors for this phase. Our derived mass of Fe^+ is compatible with the earlier determinations of the mass of ^{56}Ni .

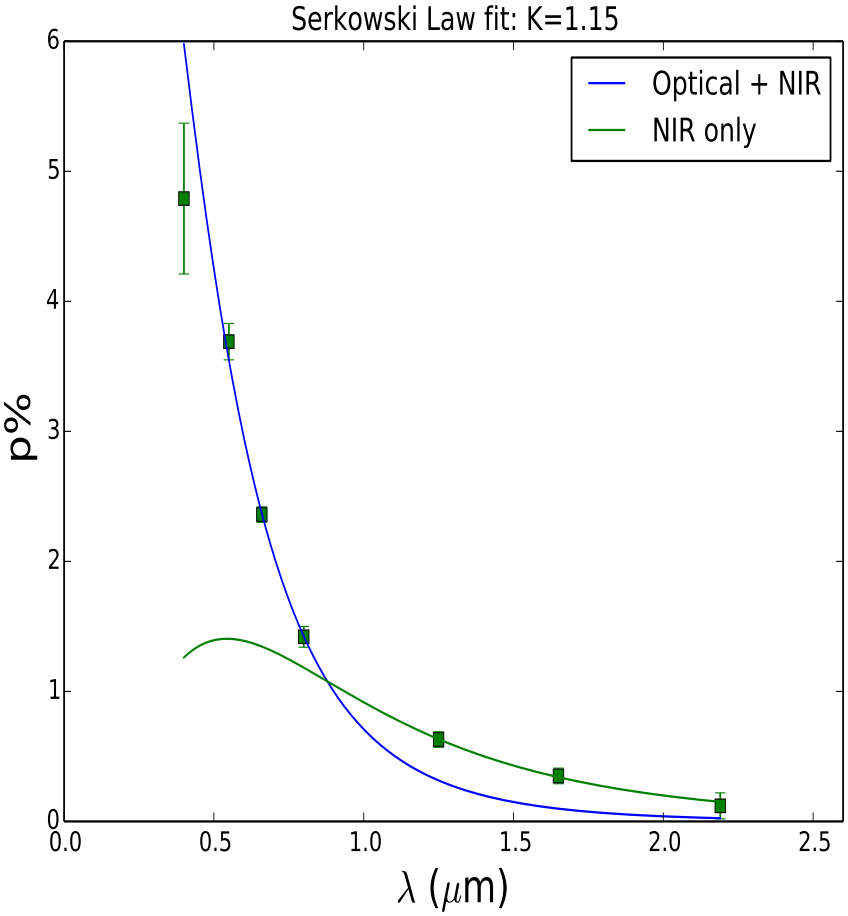

Figure 5.3.: The polarisation percentage as a function for wavelength in the optical and the NIR (data from Kawabata et al. 2014, green points). The solid blue line is the fit to all the presented data whereas the solid green line is the fit to only the NIR points (λ >1 μm). The λ_{max} shifts to a higher value for the NIR only fit.

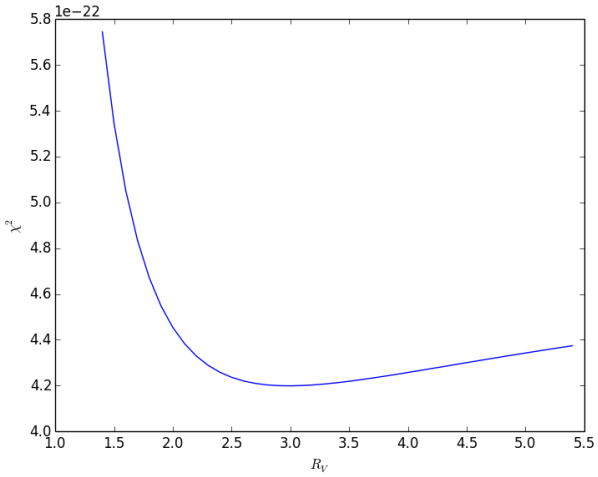

Figure 5.4.: The χ^2 distribution for R_V values by fitting the [Fe II] and [Co II] lines (see text for details). From the plot we can see that an R_v of 3.1 is preferred over lower values.

Line shifts

As noted by [189] some type Ia supernovae exhibit a shift of the line centres of the singly ionised iron group lines relative to the systemic velocity of the supernova and also with respect to the doubly ionised features. In the absence of doubly ionised features in our data we cannot identify a differential velocity shift. However, the lines in our data exhibit a 1300 kms^{-1} redshift which is 1100 kms^{-1} in excess of the M82 recession velocity.

5.2.3. Discussion

Extinction by host galaxy dust

The $E(B-V)$ and R_V of SN 2014J is a subject of significant debate. Measurements from maximum light photometry prefer a high colour excess (~ 1.2 mag, see [7, 103]). Fitting a CCM reddening law to colour excesses near maximum light, [2] find a preference for low R_V (~ 1.4). This is confirmed by spectropolarimetry present in Patat et al. 2015 [230], who also demonstrate

the preference for low R_V in other highly reddened SN Ia, a trend that has been observed with large samples in [216] and [243].

[2] conclude that the near maximum colour excesses prefer a peculiar extinction law. This indicates 'non-standard' reddening and hence, significantly different properties of the dust in M82 compared to that in our galaxy (Gao et al. [98]). Such anomalous behaviour motivated two-component dust models, wherein light is scattered by two different kinds of dust, one more typical of the Milky Way and another with smaller grain sizes in the circumstellar environment (see [86]]). [33], using UV spectrophotometry, prove that the dust is interstellar in origin, a conclusion that is supported by the wavelength independence of the polarisation angle [230].

The Near Infrared spectra of SN 2014J prefer an R_V value closer to the canonical Milky Way value of 3.1 with an $A_V \sim 2$ mag. This implies an $E(B-V) \sim 0.67$ mag which is consistent with the reported value from the DIBs in Welty et al. [315]. [152] present multi-band optical and NIR imaging polarimetry from which they deduce a low R_V. However, by fitting only the NIR data ($\lambda > 1\mu m$), we find that the data is consistent with an R_V of 3.1. This trend can also be seen in the near maximum colour excess. The NIR observations supporting a higher R_V is further evidence that the dust in M*2 has anomalous behaviour.

Iron Mass in the ejecta

We use the NIR spectra to obtain an estimate of the Fe^+ mass. We find a total Fe mass (using the ionisation fraction from [11]) of $\sim 0.6\ M_\odot$ which is consistent with findings from the γ-ray line detections [49].

[2] conclude that, after accounting for the reddening (using a power law behaviour which is similar to a CCM reddening law with a low $R_V \sim 1.4$), there is a striking similarity between SN 2014J and SN 2011fe, which was a normal, unreddened SN Ia in M101. Since typical SN Ia produce $\sim 0.6\ M_\odot$ of ^{56}Ni , the ^{56}Ni mass estimate from the [Fe II] 1.644 μm line supports this conclusion.

Stable Iron-Group Elements

The presence of stable Iron-group elements (IGEs) is associated with burning at high density conditions and can distinguish whether the progenitor WD exploded at or below the Chandrasekhar mass limit. A recent study of NIR spectra in the transitional phase ($\sim$ +50 - +90 d) by Friesen et al. [95] found that the spectra show [Ni II] forbidden lines at an observed wavelength of 1.98 μm, about 0.5 μm redwards of the laboratory wavelength of 1.939 μm calculated for this transition. The authors suggest that this redshift could be due to an asymmetric explosion.

We find an emission line at 1.94 μm in our nebular phase spectra, which would correspond to the rest wavelength of the forbidden [Ni II] transition. Since at such late phases, the amount of ^{56}Ni is negligible, this line would indicate the presence of the stable ^{58}Ni isotope in the ejecta. Complementary observations near maximum light find that SN 2014J could be well explained by a Chandrasekhar mass delayed-detonation model (for e.g. see Marion et al. 2015 [199]). Since sub-Chandrasekhar mass models do not have high enough burning densities to create ^{58}Ni, the detection of stable IGEs is a useful diagnostic to determine whether the explosion occurred at the Chandrasekhar mass [271]. If both the spectral line at 1.98 μm in the transitional phase spectra presented by Friesen et al. and the 1.94μm line in the spectra presented here are arising from the [Ni II] transition then we would require detailed modeling to explain why the observed wavelength of this transition changes at a function of phase.

5.3. Conclusions and Current Work

In this Chapter we presented and analysed three Near Infrared spectra of the nearby SN 2014J, an SN Ia in M82 at $\sim$ 400 days after maximum light.

The NIR spectra are dominated by singly ionised forbidden lines of iron and cobalt. We use these observations, for the first time to determine the properties of the dust in the environment of the SN. After excluding contaminants, esp. the presence of a neutral silicon line in the H-band, we redden the model spec-

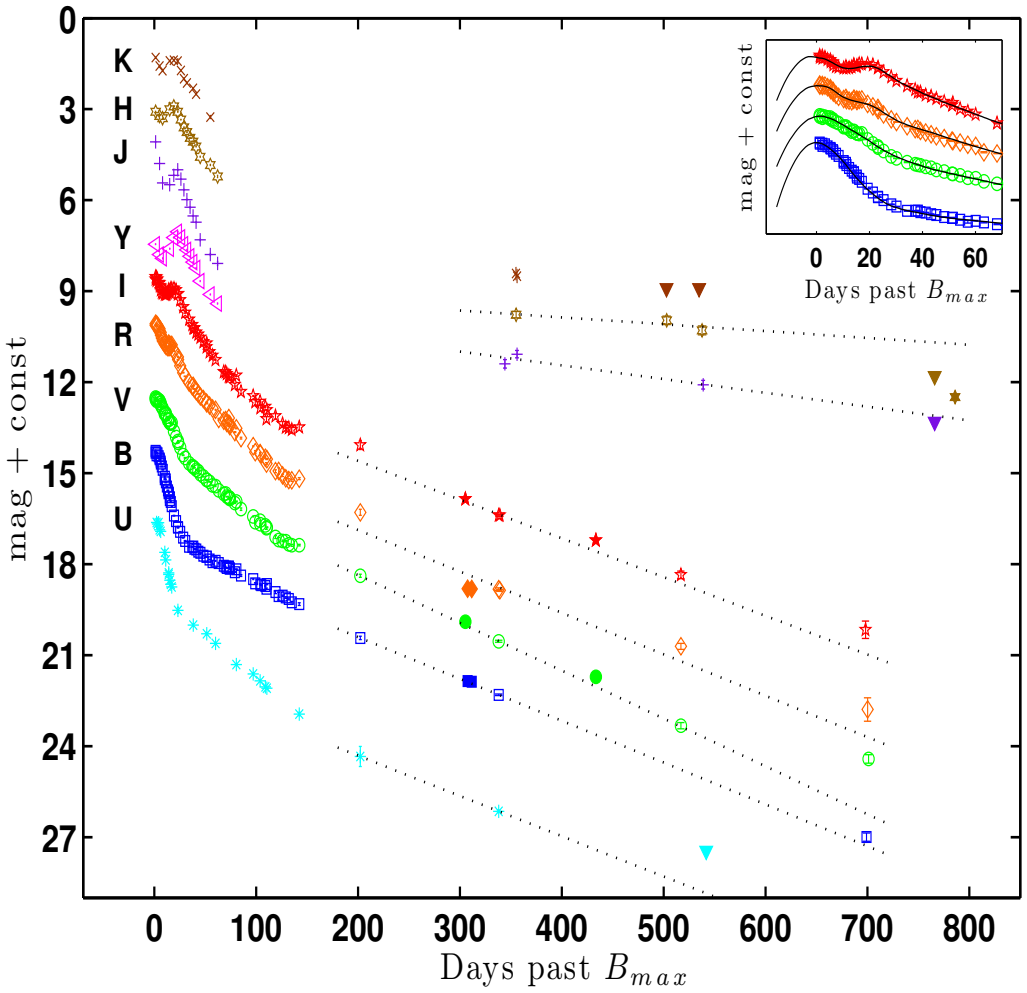

Figure 5.5.: Multi-band light curves (u to K) band for SN 2003hv, a spectroscopically normal, fast-declining SN Ia. The JHK light curves are seen to "flatten" at $\sim$ 200 days after maximum light. The H band starts to decline again after +700 d. Figure from [177]

trum using a CCM reddening law to evaluate the total to selective absorption ratio, R_V.

We find that the NIR spectrum prefers a Galactic reddening law with R_V of 3.1 and an $A_V = 2.2$. This is significantly different from the R_V evaluated using maximum light photometry (in the optical and Near Infrared). However, NIR imaging polarimetry is consistent with a Milky Way type reddening law, indicating a difference in the behaviour of the dust between the optical and NIR. This lends further credence to a peculiar extinction law of SN 2014J.

We use the [Fe II] 1.644 μm line to estimate the ^{56}Ni mass and find that the estimate from the nebular phase NIR spectra are consistent with ^{56}Ni mass measurements from γ ray line detections and the timing of the J-band second maximum [60]. Hence, we conclude that nebular phase NIR spectroscopy is a powerful tool to deduce physical parameters of SN Ia as well as extinction from host galaxy dust. We also find evidence for a [Ni II] line at 1.94 μm, which would indicate burning at high densities and suggest a Chandrasekhar mass explosion for SN 2014J. The width of [Fe II] 1.644 μm in the NIR spectra can be used to determine the central density of the exploding WD and the mass of the progenitor of SN 2014J [62]. Moreover, the line morphology is also crucial to differentiate between magnetic field strengths and the extent of positron trapping in the ejecta.

Multi-band photometry of SN Ia in the nebular phase is an extremely informative tool that, in comparison with spectroscopy, is observationally inexpensive. There are a handful of SN Ia in the literature with optical and NIR band photometry out to phases of $\sim$ 1 year or later. Sollerman et al. [277] for SN 2000cx and Spyromilio et al. [279] for SN 1998bu found that the NIR light curve at $\sim$ 1 year post-maximum "flattens", implying that the NIR contribution to the UVOIR (pseudo-)bolometric light curve is significantly increased compare to at maximum light (multi-band photometry out into the nebular phase for the nearby SN 2003hv is presented by Leloudas et al. in [177]; see Figure 5.5). The late time bolometric decline rate is sensitive to the magnetic field strength and configuration. For a strong, tangled magnetic field, a large fraction of the positrons are trapped in the ejecta and the bolometric light curve follows the ^{56}Co decay rate ($\sim$ 1 mag/100 d), whereas a weak, radially combed magnetic field would lead to a larger positron escape fraction. This observation can also help constrain the contribution of positrons escaping the ejecta to the Galactic

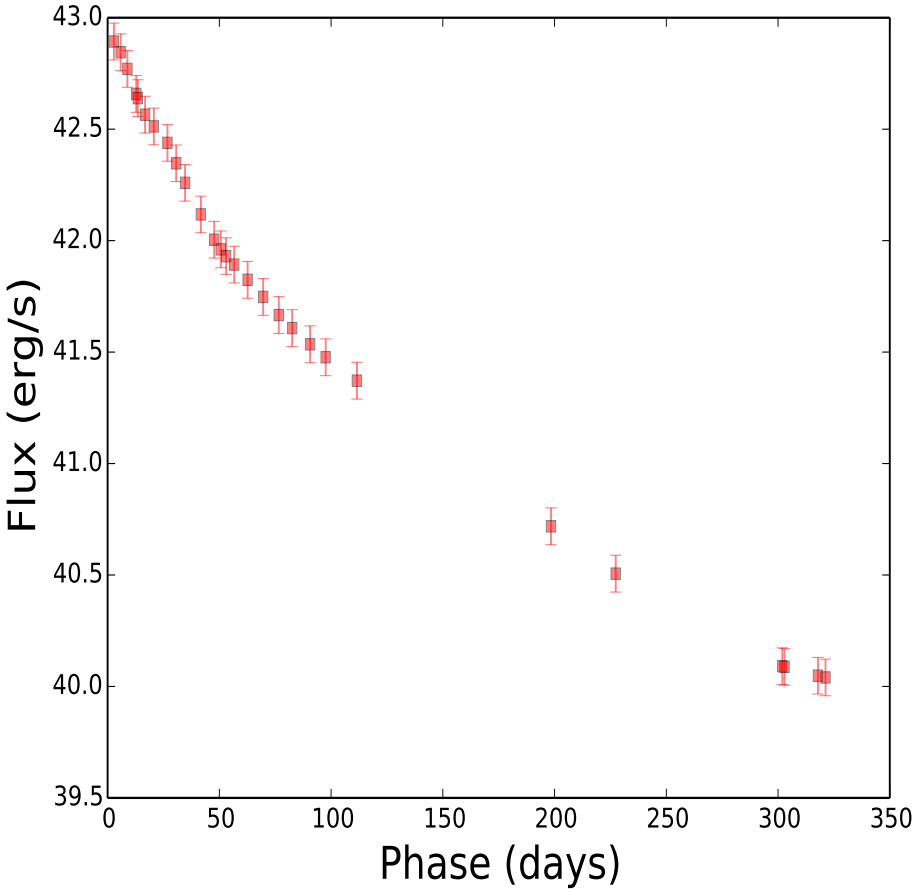

Figure 5.6.: (Pseudo-) bolometric light curve for SN 2004S constructed from the B to H filters using data presented in Krisciunas et al. 2007 [161].

511 KeV line.

In Figure 5.6, we constructed the bolometric light curve for SN 2004S, as an example, from multi-band data presented in [161]. The NIR light filters for SN 2004S show a "flattening" after $\sim +200$ days, consistent with the increased NIR contribution seen for other SN Ia. SN 2004S also displays a possible "third maximum" in the J and H filters which could be due to an ionisation transition of Fe-group elements from singly ionised to neutral (as shown in the models of Kasen 2006 [147]), which makes this object interesting to study at late phases.

The current sample of SN Ia with optical and NIR observations in the nebular phase is very small. We have an ongoing program (P97.D-0279(A); P.I. S. Dhawan) with the VLT to follow-up SNe observed as part of the Carnegie Supernova Project-II (CSP-II). Such a sample will allow us to test correlations between the nebular phase and maximum light properties of SN Ia to uncover important physical properties like the γ-ray escape timescale as well as the magnetic field in the ejecta.

Acknowledgements We would like to thank the staff at Gemini-North, especially Tom Geballe and Rachel Mason for their help during the observations and data reduction.

6. Ejecta Masses of Type Ia supernovae

6.1. Introduction

SN Ia exhibit a diverse range of photometric and spectroscopic properties. No single self-consistent explosion model has been proposed to explain the observed range of properties of SN Ia. One possible pathway to place constraints on the progenitor scenarios that would produce the observed diversity is to reconstruct the total ejecta mass (M_{ej}) from the bolometric light curves.

The mass of the progenitor is a fundamental physical variable with the power to differentiate between progentior scenarios. While Chandrasekhar-mass delayed detonations have been historically favoured, viable super-Chandrasekhar-mass evolution pathways and explosion models have been proposed, within both the *single-degenerate* [144] and *double-degenerate* [222] degenerate scenarios. Moreover, a good agreement between observations from sub-Chandrasekhar mass models (e.g. [80, 275]) have made them a viable candidate to describe at least some of the observed SN Ia explosions. Since the white dwarf is completed disrupted in normal SN Ia (see [59] for exceptions in the case of peculiar events similar to the underluminous SN 2002cx) the problem of estimating the progenitor mass essentially reduces to measuring ejecta mass.

In this chapter, we present calculations of the ejecta mass for SN Ia with sufficient late time (+40 d - +90 d) data in the UVOIR filters. As mentioned in Chapter 3 (and shown in recent studies e.g. [27]) a significant fraction of the total bolometric flux is emitted in the UV to NIR region of the spectrum and hence the UVOIR (pseudo-) bolometric light curve can be used to estimate global parameters like M_{ej} , $M_{^{56}Ni}$.

The method to determine ejecta masses is described in section 6.2, the results are presented in section 6.3. A discussion of the findings in context of recent explosions is presented in section 6.4 and finally, a conclusion in section 6.5.

6.2. Measurement of ejecta masses

To measure the ejecta mass, we perform a least square fit of a radioactive beta decay energy (RDE) deposition function to the post-maximum phase UVOIR light curve, which has been discussed in Jeffrey [139].

The fraction of the UVOIR flux emitted in the NIR increases from $\sim$ 5 - 10 % at maximum light to >25% at $\sim$ a few weeks after maximum. Hence, it is important to use the measured NIR fluxes to determine the UVOIR light curve. Previously, [285] and [267] have reconstructed the ejecta masses from bolometric light curves of SN Ia. These studies use optical ($UBVRI$) quasi-bolometric light curves with different prescriptions for correcting for the flux emitted in the NIR (JHK) filters. In our study we construct UVOIR light curves from observed uv to NIR light curves which has not previously been done to measure the ejecta masses.

The energy deposition function for ^{56}Ni atoms in the optically thin limit (i.e. where τ<<1) is given by:

$$\begin{aligned} E_{\rm dep} &= E_{\rm Ni} + E_{\rm Co\ e^+} + [1-\exp(-\tau)]E_{\rm Co\ \gamma} \\ &= \lambda_{\rm Ni} {\rm N_{Ni0}}\ \exp(-\lambda_{\rm Ni} {\rm t}) {\rm Q_{Ni\ \gamma}} \\ &+ \lambda_{\rm Co} {\rm N_{Ni0}} \frac{\lambda_{\rm Ni}}{\lambda_{\rm Ni}-\lambda_{\rm Co}} [\exp(-\lambda_{\rm Co} {\rm t}) - \exp(-\lambda_{\rm Ni} {\rm t})] \\ &\times \{Q_{\rm Co\ e^+} + Q_{\rm Co\ \gamma}[1-\exp(-\tau)]\}\ . \end{aligned} \quad (6.1)$$

where λ_{Ni} and λ_{Co} are the e-folding decay times of 8.8 days and 111.3 days for ^{56}Ni and ^{56}Co respectively. $Q_{{\rm Ni}\,\gamma}$ (1.75 MeV) is the energy release per ^{56}Ni $\rightarrow$ ^{56}Co decay. $Q_{{\rm Co}\,\gamma}$ (3.61 MeV) and $Q_{{\rm Co}\,e^+}$ (0.12 MeV) are the γ-ray and

positron energies, respectively, released per ^{56}Co $\rightarrow$ ^{56}Fe decay (a detailed discussion of the ^{56}Ni $\rightarrow$ ^{56}Co $\rightarrow$ ^{56}Fe decay chain is presented in [213]) and τ is the optical depth.

The Jeffrey Model The fiducial timescale (t_0) defines the epoch at which the optical depth is unity and is calculated from the quasi-exponential tail of the bolometric light curve. In this section we examine the comprehensive derivations of the expression relating the fiducial timescale to the total ejecta mass.

Homologous expansion implies that the mean radius of the expanding ejecta scales with the velocity as $\vec{v} \propto \vec{r}$. For homologous expansion the density profile is given by

$$\rho(v,t) = \rho_{ce,0}\,(\frac{t_0}{t})^3 \exp(-v/v_e) = \rho_{ce,0}\,(\frac{t_0}{t})^3 \exp(-z) \tag{6.2}$$

where $\rho_{ce,0}$ is the central density at t_0, v_e is the e-folding velocity and z is the radial velocity

The optical depth of the beam paths in the homologously expanding medium is given by

$$\tau = \int_0^\infty ds\kappa\rho[\vec{v}(s),t] \tag{6.3}$$

substituting the expression for the density from Equation 6.2

$$\tau = \tau_{ce,0}\,(\frac{t_0}{t})^2 \int_0^\infty dz_s exp(-z^{'}) \tag{6.4}$$

where $\tau_{ce,0}$ is the radial optical depth at the fiducial time, t_0, expressed as $\tau_{ce,0} = \kappa v_e t_0 \rho_{ce,0}$ and z_s is the beam path velocity (in units of the e-folding velocity, v_e)

$$z^{'} = \sqrt{z^2 + 2zz_s\mu + z_s^2} \tag{6.5}$$

Table 6.1.: List of Supernovae for which ejecta masses were calculated along with the morphologies of the host galaxies. References for the SN data and host morphology are also given.

SN	Host Morphology	Reference
SN2002bo	SA(s)a	B04, K04
SN2002dj	S	P08
SN2003cg	SAa pec	ER06
SN2004ey	SB(rs)c	CSP
SN2005M	S?	CSP
SN2005ke	Sa	CSP
SN2005ki	(R)SA0	CSP
SN2006D	SAB(s)abpec?HII	CSP
SN2006X	SAB(s)bc	CSP
SN2006et	SB(r)a?pec	CSP
SN2006mr	E	CSP
SN2007S	Sb	CSP
SN2007af	SAB(rs)cd	CSP
SN2007as	SB(rs)c	CSP
SN2007le	SA(s)c	CSP
SN2007on	E1	CSP
SN2008bc	S	CSP
SN2008fp	SAB(r)0 pec	CSP
SN2008hv	S0	CSP
SN2014J	I0	F14, A14

B04- [16]; K04- [166]; P08- [245]; ER06- [71]; CSP- [54, 288], F14- [86]; A14- [2]

μ is the cosine of the angle at the emission point between the outward radial direction and the beam propagation direction. For a beam in the outward radial direction, $\mu = 1$ and the optical depth expression reduces to

$$\tau_r = \tau_{ce,0}(\frac{t_0}{t})^2 exp(-z) \tag{6.6}$$

During the optically thin regime, when the energy deposition is powered only by ^{56}Co (the daughter nucleus of ^{56}Ni), we can rewrite Equation 6.6 from a radial optical depth to a mean optical depth as

$$\overline{\tau} = \tau_{ce,0}(\frac{t_0}{t})^2 q \tag{6.7}$$

where q is the general form factor describing the distribution of ^{56}Co in the ejecta. The expression for the total mass above a velocity v is given as

$$M(z) = 4\pi t^3 \int_v^\infty dv v^2 \rho(v,t) \tag{6.8}$$

To solve the expression for M(z) in 6.8, we use the following integral solution

$$I_n(z) = \int_z^\infty dz^{'}(z^{'})^n \exp(-z^{'}) = \exp(-z) \sum_{k=0}^{n} \frac{n!}{k!} z^k \tag{6.9}$$

to evaluate the expression for the mass as a function of the radial velocity co-ordinate (6.8), we obtain

$$M(z) = M\, exp(-z)(1 + z + \frac{1}{2}z^2) \tag{6.10}$$

where $M = 8\pi\rho_{ce,0}(v_e t_0)^3$. Relating M to $\tau_{ce,0}$

$$\tau_{ce,0} = \frac{\kappa M}{8\pi v_e^2 t_0^2} \tag{6.11}$$

Substituting Equation 6.11 in Equation 6.7 and then evaluating 6.7 at $t = t_0$ and a fiducial characteristic optical depth $\tau_{ch,0}$, we get (for the case of SN Ia studied here, the quantity M corresponds to the total ejecta mass, M_{ej})

$$t_0 = (\frac{M_{ej}\kappa q}{8\pi\tau_{ch,0}})^{\frac{1}{2}}\frac{1}{v_e} \tag{6.12}$$

where $\tau_{ch,0}$ is the characteristic optical depth. At fiducial time t_0, $\tau_{ch,0}$ becomes the optically thin $\overline{\tau}$. By definition of the fiducial timescale at $t = t_0$; $\tau_{ch,0} = 1$

$$t_0 = (\frac{M_{ej}\kappa q}{8\pi})^{\frac{1}{2}}\frac{1}{v_e} \tag{6.13}$$

where M_{ej} is the total ejected mass, κ is the mean γ-ray opacity, v_e is the e-folding velocity of an exponential model's density profile and q describes the ^{56}Ni mass distribution.

6.3. Results

As defined above, we fit a radioactive decay energy (RDE) deposition function to the late-time UVOIR light curve for a sample of SN Ia. We find that there is a factor of 1.5 range in the t_0 estimates We use equation 6.13 to derive the M_{ej} from the calculated t_0. Calculating the total ejected mass from the fiducial timescale requires knowing the form factor describing the ^{56}Ni mass distribution, the mean γ-ray opacity and the e-folding velocity.

The expression for the form factor, q, given in [139], is

$$q = \frac{\int_a^b dzz^2 exp(-z)\int_{-1}^{1}\frac{d\mu}{2}\int_0^\infty dz_s exp(z^{'})}{\int_a^b dzz^2 exp(-z)} \tag{6.14}$$

where a and b are velocity limits within which the ^{56}Ni mass is concentrated. The integral in the numerator of Equation 6.14 cannot be solved analytically, unless crude approximations are made. Solving the expression numerically,

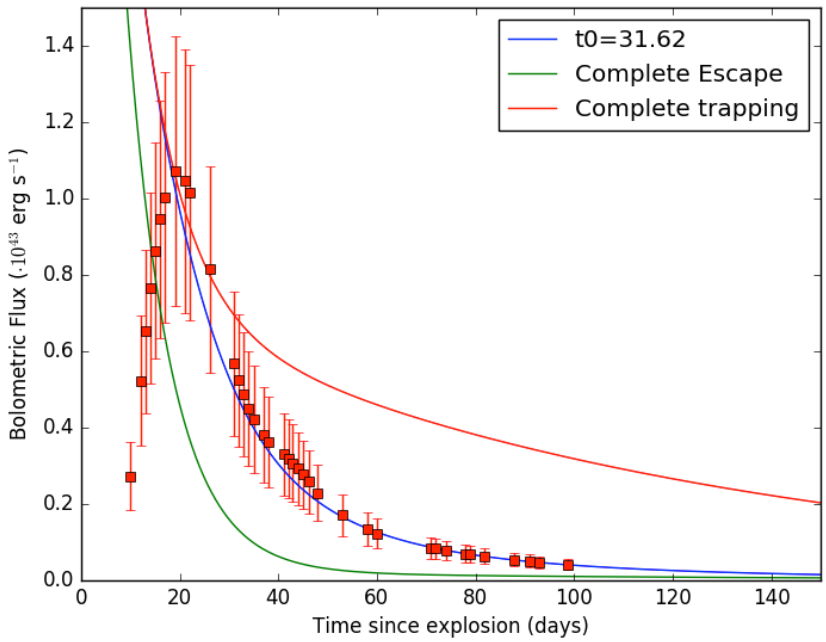

Figure 6.1.: The least squares fit of the radioactive decay energy deposition function to the quasi-exponential tail (+50 - +100 d) of the bolometric light curve of SN 2008hv is shown. The three deposition curves are for complete γ-ray trapping (i.e $\tau >> 1$; *red*), complete escape (i.e. $\tau << ; 1 green$), and the best fit t_0 value.

for evenly mixed ^{56}Ni (i.e. $a = 0, b = \infty$), we obtain a q value of 0.33 (note that the dz_s variable in the numerator is dependent on z and hence the first term in the numerator is not the same as the term in the denominator). We note, however, that some delayed detonation models (e.g. [124]) predict a ^{56}Ni 'hole', due to electron capture elements being present in the innermost layers (up to $\sim$ 1500 kms^{-1}) of the SN ejecta. Using this as a lower limit for the velocity range doesn't change the value of q by more than $\sim$ 10 %.

The mean γ-ray opacity (κ_γ) for supernovae, calculated in [295] ranges between 0.025 to 0.033 cm^{2}g^{-1}. The authors demonstrate that the constant asymptotic $\kappa_\gamma$value of $0.050 Y_e$ cm^{2}g^{-1}reproduces the SN light curve to within 10% from maximum light to $\sim$ 1200 d after, where Y_e is the electron to nucleon ratio.

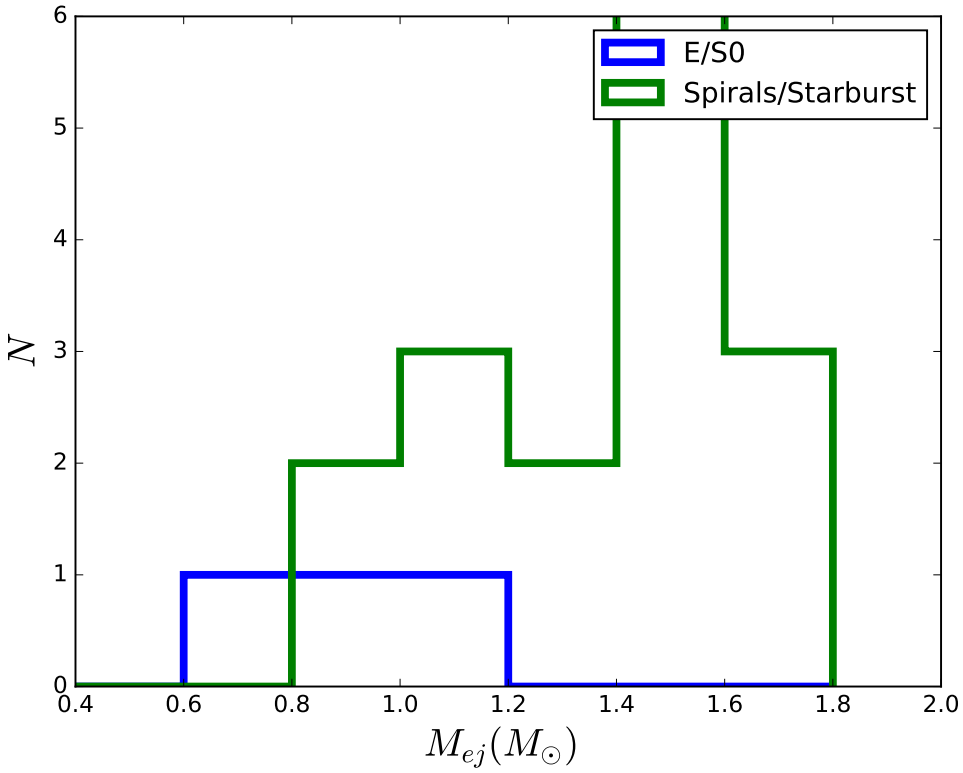

Figure 6.2.: Ejecta mass distribution for the sample of SN Ia. Assumptions for the e-folding velocity, ^{56}Ni distribution and the mean γ ray opacity are discussed in the text

For an ejecta with $Y_e = 0.5$, the $\kappa_\gamma$value is 0.025 cm^{2}g^{-1}, which is what we adopt for our analysis.

In line with previous studies (e.g. [285]), we adopt an e-folding velocity value of 3000 kms^{-1}. For the 1-D delayed detonation models of [28], the mean value for v_e is 2925 kms^{-1}, which is close to the value adopted here.

We calculate the error in the ejecta mass by propagating a 15% error in the value of q and using a 1-σ spread in the v_e values from the DDC models of [28] (corresponding to $\sigma(v_e)$ of 179 kms^{-1}). The spread in these models is comparable to other models, e.g. the sub-M$_{\rm Ch}$ models of [275, 327]

Table 6.2.: Transparency timescale estimates and the resulting calculations for the ejecta masses for SNe with sufficient late time data in the optical and Near Infrared. The reddening-free ^{56}Ni mass estimates are also presented. Note, however, that two fast-declining SNe (2005ke and 2006mr) do not show a second maximum and hence, the ^{56}Ni masses are calculated from the bolometric peak luminosity using Arnett's rule.

SN	t_0 (d)	error (d)	M_{ej} ($M_\odot$)	error ($M_\odot$)	$M_{^{56}Ni}$ ($M_\odot$)	error ($M_\odot$)
SN2002bo	37.58	0.10	1.44	0.28	0.51	0.11
SN2002dj	34.53	0.12	1.22	0.23	0.71	0.11
SN2003cg	32.98	0.21	1.11	0.21	0.53	0.10
SN2004ey	37.45	0.08	1.43	0.28	0.57	0.14
SN2005M	41.31	0.07	1.74	0.33	0.60	0.15
SN2005ke	31.69	0.30	1.03	0.20	0.14	0.04
SN2005ki	31.19	0.09	1.00	0.21	0.51	0.15
SN2006D	29.08	0.11	0.87	0.19	0.49	0.13
SN2006X	39.41	0.10	1.59	0.33	0.57	0.11
SN2006et	40.80	0.12	1.70	0.33	0.64	0.16
SN2006mr	26.71	0.10	0.73	0.15	0.05	0.02
SN2007S	41.31	0.11	1.75	0.33	0.71	0.16
SN2007af	35.38	0.05	1.28	0.27	0.57	0.14
SN2007as	33.08	0.07	1.12	0.23	0.47	0.14
SN2007le	38.89	0.08	1.54	0.32	0.61	0.15
SN2007on	29.63	0.06	0.90	0.17	0.30	0.09
SN2008bc	37.54	0.04	1.44	0.30	0.62	0.15
SN2008fp	38.94	0.10	1.55	0.30	0.62	0.13
SN2008hv	31.62	0.12	1.04	0.21	0.54	0.11
SN2014J	38.80	0.09	1.53	0.30	0.62	0.13

6.3.1. Host Galaxy Properties

SN Ia luminosities have been shown to be dependent on the properties of their host galaxies [116]. Brighter SNe with broader light curves preferrentially occur in younger stellar populations whereas faint SNe occur in older stellar populations [116, 291]. This environmental dependency of the SN luminosity has also been used to reduce the errors on the cosmological parameter estimation by using SN Ia as distance indicators.

In this section, we analyse the ejecta mass distribution in context of the host galaxy properties of the SNe in our sample. In Figure 6.2 we plot a histogram of the M_{ej} values as a function of the host galaxy morphology. We find that the SNe with lowest ejecta mass occur in elliptical galaxies. Moreover, in Figure 6.3 we also see that SNe in E/S0 galaxies have a lower ^{56}Ni mass which is consistent with the relation found in the literature with the SN luminosity and decline rate (e.g. [116, 291]). We note, however, that our sample only has 3 SNe in E/S0 host galaxies and hence a larger sample would help to confirm/refute this result.

6.4. Discussion

Calculations of the total ejecta mass using the prescription in [139] indicate a range of estimates from 0.7 - 1.7 $M_{\odot}$, slightly over a factor of 2 difference. We note that the absolute value of the ejecta mass is dependent on the assumptions for the e-folding velocity, the ^{56}Ni mass distribution and the mean γ-ray opacity. However, the variation in the M_{ej} values is due to the variation in the fiducial timescales and hence, increasing or decreasing the values of the other parameters in Equation 6.13

We compare the γ-ray transparency timescale (t_c) estimates from the bolometric light curves to the estimates from the flux evolution of the [Co III] λ5893 line at >200 d. The γ-ray timescale is defined at the epoch at which the energy deposited from the γ-ray photons equals the energy deposited from the positrons.

We find that there is only one object (SN 2007af) in our sample that also has a t_c estimate given in [46]. For SN 2007af, the late time bolometric light curves

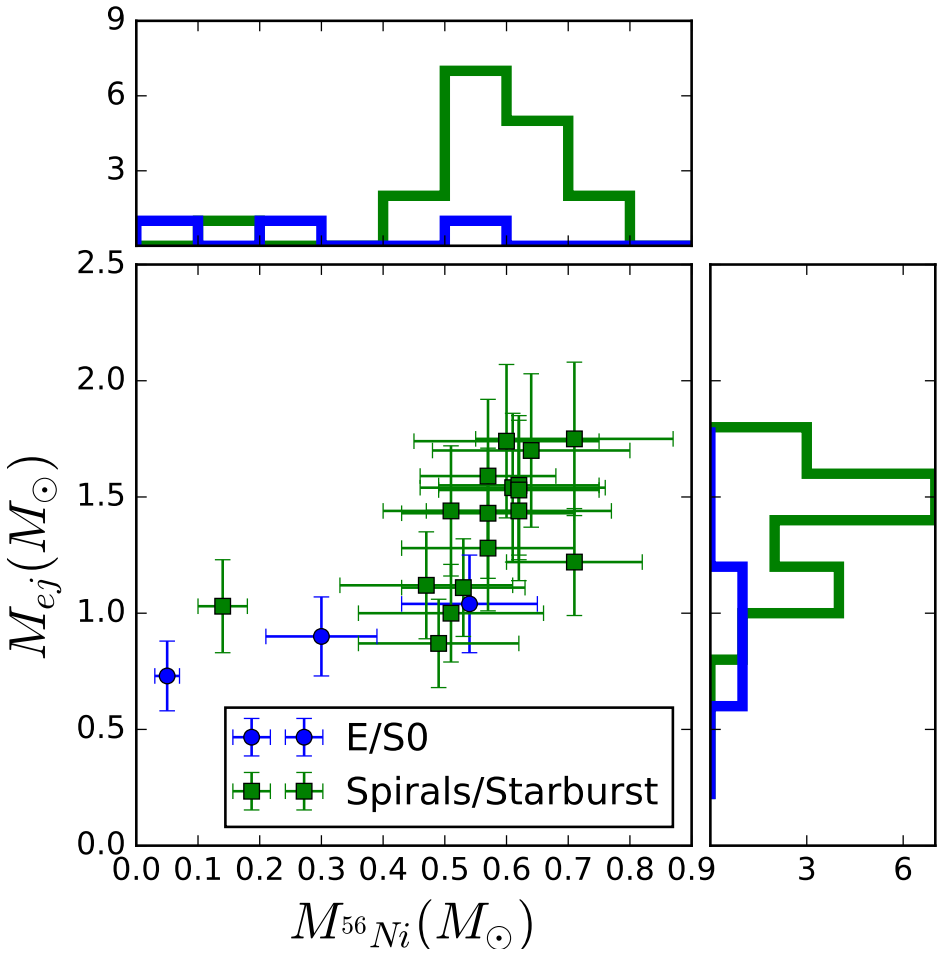

Figure 6.3.: M_{ej} versus $M_{^{56}Ni}$ for the SNe in our sample presented here. The histogram panels on either side have been split by host galaxy morphology in two categories, one with SNe occurring in E/S0 hosts (*blue*) and another with SNe occurring in spiral galaxies (*green*). It is clear from the ^{56}Ni mass histograms that the SNe in elliptical galaxies on average produce less ^{56}Ni than those in spiral galaxies. Note, however, that there are only 3 SNe with host morphologies report as E/S0 and hence, a larger sample is required to derive more firm conclusions.

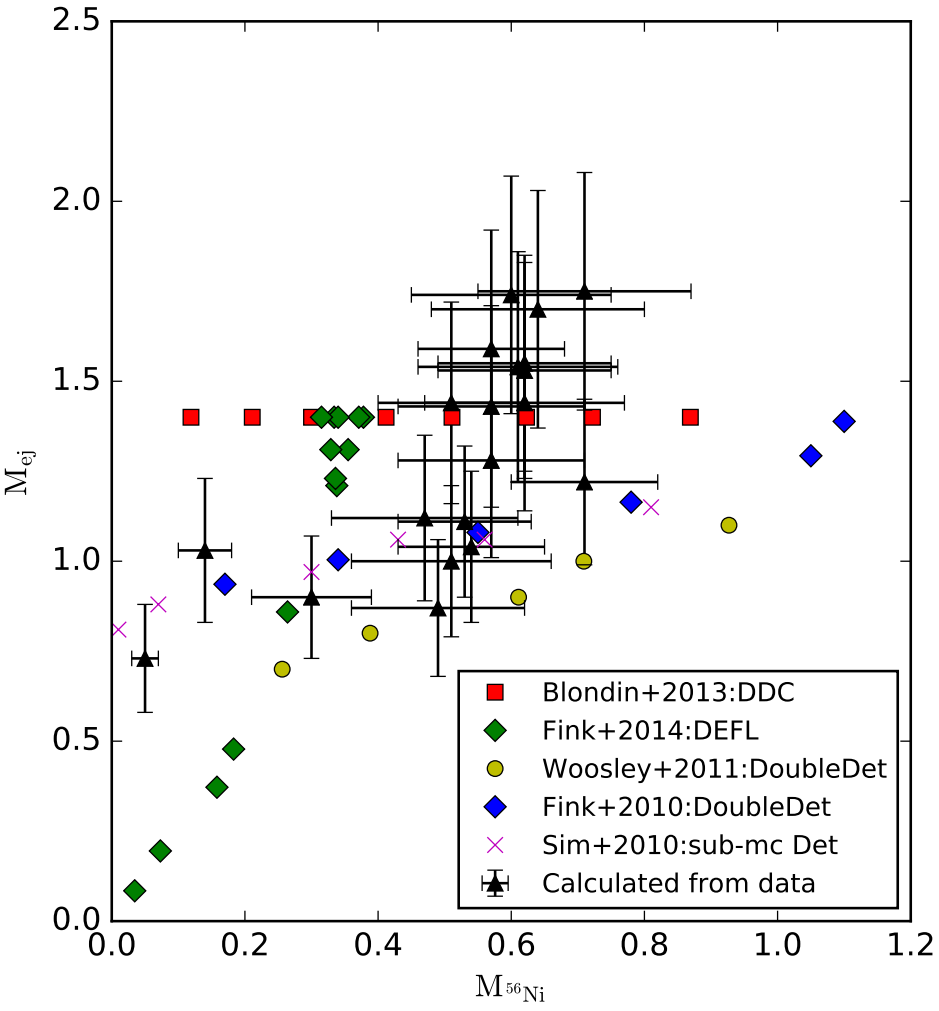

Figure 6.4.: Calculated M_{ej} values are plotted against the ^{56}Ni masses from the reddening free estimation (except for SN 2005ke and SN 2006mr, the two lowest ^{56}Ni masses; see text for discussion). For comparison, the M_{ej} - $M_{^{56}Ni}$ loci for different M_{Ch} and sub-M_{Ch} models are also plotted. We plot the double detonation models from Fink et al. 2010 [80] and Woosley et al. 2011 [327] (for He accretion rates of 10^{-5} $M_{\odot}$yr^{-1}). We also plot the deflagration models of Fink et al. 2014, the M_{Ch} delayed detonation models of Blondin et al. 2013 [28] and the sub-M_{Ch} detonations of Sim et al. 2010 [275].

Table 6.3.: Assumed values for the e-folding velocity and form factor describing the ^{56}Ni distribution, used for calculating the M_{ej} from the t_0

Case	v_e kms^{-1}	q	κ_γ cm^2g^{-1}
1	3000	0.33	0.025
2	2700	0.33	0.025
3	3000	0.45	0.025
4	2700	0.45	0.025

imply a t_c of 211 $\pm$ 12 d. This is similar to the theoretical expectation for t_c for a Chandrasekhar-mass delayed detonation model (DDC10 model of [28]; see Sections 4.1 and 4.3 of [46] for more details). The t_c for SN 2007af is also comparable to the estimate for other SNe namely 2000cx and 2001el which have t_c values of $\sim$ 170 days [277] and $\sim$ 188 days [287] respectively.

[46], using the [Co III] line evolution in the nebular phase, report a significantly smaller t_c value for SN 2007af of 71 $\pm$ 21 d, although they find that the other SNe in their sample have longer transparency timescales ($t_c \sim$ 180 days). The discrepancy between the two methods for estimating t_c for SN 2007af is possibly because the bolometric light curve is sensitive to the entire ejecta whereas the flux of the [Co III] line is sensitive only to the IGE core.

We test the difference in the estimated M_{ej} for the different assumptions on the fixed parameters v_e, q and κ_γ. The difference in the estimated M_{ej} values for different assumptions on the e-folding velocity and the form factor, q in Figure 6.5 . The assumed values for the parameters are given in Table 6.3.

[46] present estimates of the M_{ej} using the light curve width parameter and the relation between the light curve width and M_{ej} . For SN 2007af [46] report an M_{ej} of 1.3($\pm$ 0.1 $M_\odot$, including systematic errors) and for SN 2002dj, they report a value of 1.3 ($\pm$ 0.1$M_\odot$). These values are within the errors of the estimates presented in Table 6.2.

We measure an M_{ej} of 1.53 ($\pm$ 0.3) $M_\odot$for SN 2014J, which is in good agreement with the value of 1.44 $\pm$ 0.1 $M_\odot$reported in [46]. [48] compare the synthetic

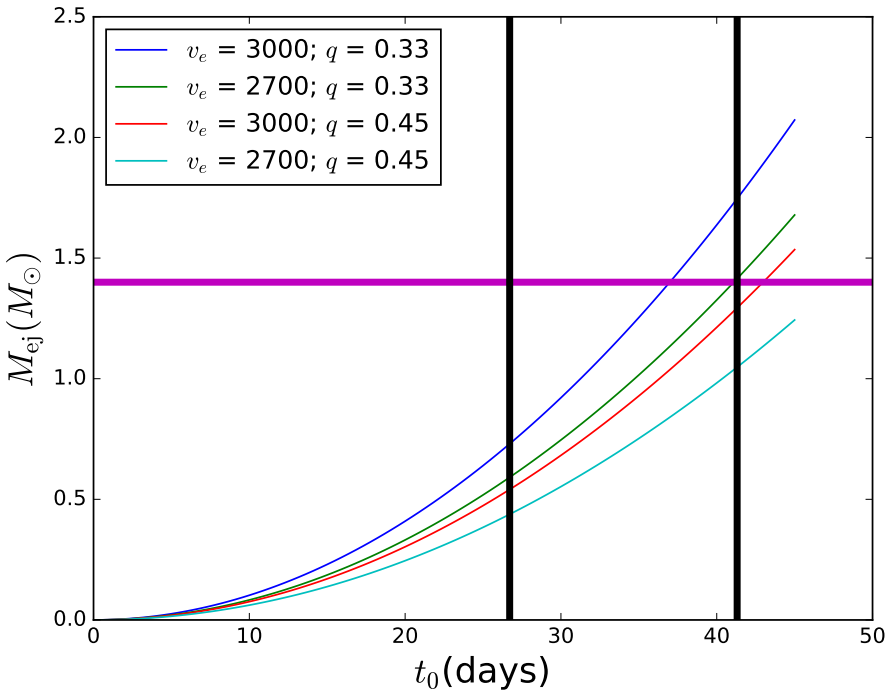

Figure 6.5.: Total ejecta mass estimates versus t_0 for different assumptions on the e-folding velocity (v_e) and the form factor describing the ^{56}Ni distribution (q). The solid horizontal blue line is the Chandrasekhar mass limit. The vertical black lines are the lowest and highest measured values of t_0 for SNe in our sample.

γ-ray observables to data from the *INTEGRAL* satellite and find that a M_{Ch} delayed detonation model is the best fit to the γ ray spectrum post-maximum. IR spectra of SN 2014J a few months after explosion show stable ^{58}Ni lines [95, 301] which would indicate burning at high densities and hence, the explosion of a near-Chandrasekhar mass WD (note that the presence of ^{58}Ni lines is also seen in the late phase NIR spectra presented in Chapter 5). Moreover, [309] find an excellent agreement between NIR spectra (1.1-3.4μm) and the M_{Ch} delayed detonation models of [59] in the wavelength range of 1.5 - 2.7 μm. We find that our result for the M_{ej} value is consistent with a M_{Ch} progenitor, which agrees well with independent conclusions presented in the literature.

In Figure 6.4, we plot the calculated M_{ej} for our sample of SNe against the estimated ^{56}Ni mass. For all SNe that display an NIR second maximum,

we use the reddening-free estimate using the method described in Chapter 3 (only two SNe 2005ke and 2006mr do not show a second maximum and their ^{56}Ni masses are calculated using "Arnett's rule", see [5] and Chapter 3 for more details). We note that there appear to be two populations. Dividing into two sub-samples with M_{ej} <and $\geq$ 1.4 $M_{\odot}$, we perform a Kolmogorov-Smirnov test on the ^{56}Ni mass distribution and find that a probability both the ^{56}Ni distributions arising from the same parent distribution of 0.6 % which is evidence for two populations within the family SN Ia.

SNe with significanty sub-M_{Ch} ejecta masses (0.9 - 1.1 $M_{\odot}$) show a wide range of ^{56}Ni masses, 0.05 - 0.7 $M_{\odot}$. On the other hand, SNe with M_{ej} values near the canonical Chandrasekhar limit have ^{56}Ni masses that are in a narrower range of 0.4 - 0.7$M_{\odot}$. Recently [82] have shown that M_{Ch} SN Ia progenitors preferentially lack a vigorous deflagration phase after the initial ignition, leading to an almost pure detonation and hence, over luminous SNe. The finding that M_{Ch} ejecta mass SNe produce more ^{56}Ni (Figure 6.4) would lend support to this theory.

We also study the ejecta and ^{56}Ni masses of SNe in our sample in the context of their host galaxy morphology. We find that the SNe in elliptical/lenticular galaxies are on average fast-declining and have lower ^{56}Ni mass values than the SNe in spiral/starburst galaxies. Recently, [269] calculated the M_{ej} for 337 SNe out to a redshift z<0.7 and found that fast-declining SNe preferentially occur in more massive host galaxies. [128] also reported that faint, fast-declining SNe happen almost exclusively in high-metallicity galaxies, which would be consistent with our finding that the faint, low-M_{ej} SNe prefer elliptical/lenticular hosts. We note, however, that our sample has very few objects in "E/S0" hosts and expanding this study to a larger sample of SNe will be very useful to study the M_{ej} in context of host-galaxy properties.

Comparing the observed M_{ej} - $M_{^{56}Ni}$ distribution with a suite of explosion models, we find that no single explosion mechanism can explain the entire observed diversity in the population of SN Ia. We consider sub-M_{Ch} detonations of [275] where the detonations are artificially induced in WDs of varying initial masses. The increase in $M_{^{56}Ni}$ for increase in WD mass in the models agrees well with the observations. We also examine the double detonation models from [80], which are qualitatively similar to the models of [275], but the ignition naturally arises from the accretion of a thin shell of helium from

the companion, which detonates and triggers a secondary carbon-detonation in the centre, known as the "double-detonation" scenario. As a comparative, we also plot the double-detonation models of [327] for the He accretion rate of 10^{-5} $M_{\odot}\mathrm{yr}^{-1}$. The slope of sub-$M_{Ch}$ models matches well with the observed M_{ej} -$M_{^{56}Ni}$ slope up to $M_{^{56}Ni}$ values of ~ 0.6 $M_{\odot}$.

6.5. Conclusion

For a sample of 20 SN Ia with sufficient late time (+40 d - +90 d) coverage in the u to H filters, we construct (pseudo-)bolometric light curves amd estimate the fiducial timescales i.e. the epoch at which the ejecta transition from being optically thick to optically thin (see Figure 6.1). The estimated values of the fiducial timescales range between $\sim$ 26 to $\sim$ 42 d. The values of the fiducial timescales are lower than the phase range of the bolometric light curve used to derive t_0.

The derived values of the ejecta masses differ by a factor of $\sim$ 2 between 0.7 and 1.7 $M_{\odot}$. However, we note that in our analysis, we assume the same q, v_e and κ_{γ} for all SNe (unlike in [267]) and hence, this factor maybe different if we assume different q, v_e and κ_{γ} for each SN in our sample.

We calculate the γ-ray transparency timescale, defined as the time at which the contribution of the γ-rays and positrons to the energy deposition is equal. For SN 2007af, we calculate the γ transparency timescale from the bolometric light curve and find the estimate to be much longer than that derived from nebular phase spectra by [46]. Having a larger sample of SNe with both late time multi-band photometry (at +40-+90 days) and spectra at $\sim$ 1 year past maximum will be crucial to understand the physical cause of this discrepancy.

We find that SNe with lower M_{ej} preferentially occur in "E/S0" host galaxies. This finding corroborates previous results that show that fast-declining SNe occur in more massive, high metallicity host galaxies [128, 267]. We note, however, that there are only 3 SNe in "E/S0" hosts and hence, a larger sample is required to confirm this finding.

We also find that M_{ej} is correlated with the ^{56}Ni mass (Figure 6.4). Comparing our observed relation to model predictions from a suite of sub-M_{Ch}

and Chandrasekhar mass models, we find that no single model can produce the observed M_{ej} - $M_{^{56}Ni}$ relation. From this comparison we conclude that at least 2 explosion mechanisms are necessary to explain the observed diversity in the population of SN Ia (possibly an M_{Ch} delayed-detonation to explain the bright SNe and one or more sub-M_{Ch} explosion mechanism to explain the low-^{56}Ni mass end of the distribution). We note that our sample has only 20 SNe. We would like to further expand upon this sample with SNe observed as part of the CfA SN program [92, 119]. Moreover, using a template for the contribution in the NIR (as done by Scalzo et al. in [267]) would include SNe with detailed optical light curves but no NIR measurements, significantly increase the sample size and allowing a better comparison of the model and observed M_{ej} - $M_{^{56}Ni}$ trends.

7. Forecasts of cosmological constraints with future observatories in the rest-frame Near Infrared

7.1. Introduction

Observations of Type Ia supernovae present the strongest evidence for an accelerating universe [21, 290, 294]. Independently, measurements of fluctuation in the cosmic microwave background (CMB) from the *Wilkinson Microwave Anisotropy Probe (WMAP)* [17] and *Planck* [246] satellites, acoustic oscillations in the matter density spectrum [67] as well as the comparison of Hubble expansion ages from the Hubble Key Project (HKP; [91]) have led to a growing body of evidence for a dark-energy component dominating the overall matter-energy density budget of the universe (Frieman et al. [94] and Weinberg et al. 2013 [314] present a review of the different probes of dark energy). A physical understanding of dark energy at present remains elusive, and there are a wide variety of possible explanations ranging from the cosmological constant, as originally proposed by Einstein in 1917, a decaying scalar field or perhaps even a modification of general relativity. A convenient measure is w, the ratio of pressure (P) to density (ρ) , known as the equation of state of dark energy, which equals -1 for the cosmological constant scenario. Currently, the evolution of w as a function of redshift is not precisely known, hence, further observational data are required in order to constrain and characterise the properties of dark energy. Recently concluded surveys of SN Ia have presented data for $\mathcal{O}(10^3)$ SN Ia out to $z \sim 1.4$ (e.g. 740 SN Ia in the Joint Light Analysis

(hereafter JLA) presented in [21]). Due to such large sample sizes, the statistical uncertainties have been reduced to a level such that they are comparable to, or even smaller than the systematic uncertainties. Hence, the reduction of systematic uncertainties is critical to obtain more precise estimates on cosmological parameters , as argued in [50, 290]. One of the well-known sources of systematics arises from the reddening and extinction due to host galaxy dust. It has been demonstrated for a large sample of nearby SN Ia that the total to selective absorption ratio (R_V) for SN hosts is significantly smaller than that of the Milky Way [36, 89, 216], hence, using a Milky Way reddening law to correct the SNe for host galaxy reddening can introduce systematic errors. An exciting pathway to circumvent the systematic errors from reddening is by observing SN Ia at longer rest-frame wavelengths where the contribution from reddening is significantly reduced.

In this Chapter, we forecast constraints on cosmological parameters from a *rest-frame* Near Infrared survey of Type Ia supernovae with future observatories (Hook 2013 [125] present a review of future facilities for supernovae and cosmology). Apart from the smaller contribution from host-galaxy reddening, SN Ia are also more uniform in the NIR near maximum light, with the intrinsic magnitude scatter into YJH *without* any corrections being similar to or smaller than the scatter in the B-band *after* applying corrections for light curve shape and colour (e.g. see [151] and Chapter **??**). The NIR peak magnitudes are nearly completely standard, with no or a weak dependence on the optical light curve shape and hence, nearly independent of the ^{56}Ni mass, which also makes the NIR less susceptible to evolutionary effects as a function of redshift. Hence, the systematic effects from the lack of knowledge of the SN Ia progenitor system and host galaxy reddening are significantly reduced by observing in the Near Infrared. Moreover, measuring a distance to *same* SN in the optical and NIR is an appealing test of the methods using the different wavelength regimes and possible biases.

7.2. Euclid Deep Drilling Fields

Euclid is a 1.2m optical-NIR space telescope within ESA's Cosmic Vision 2015-2025 programme [171]. The primary science goals of the mission are to im-

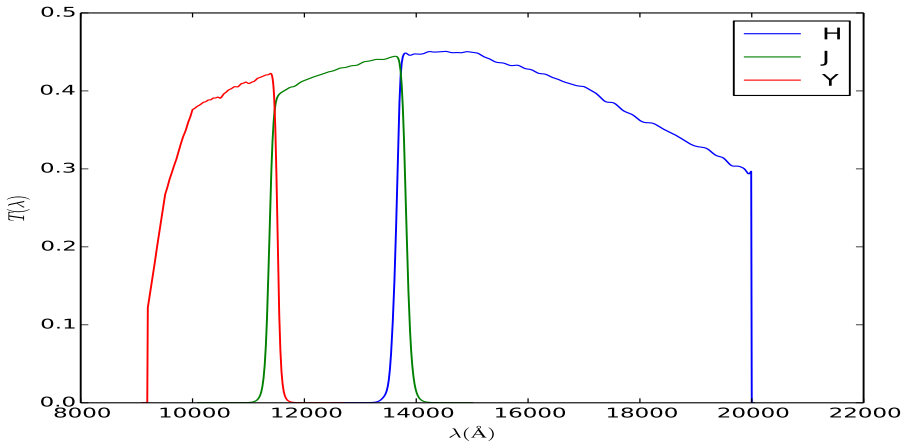

Figure 7.1.: Transmission Curves for the Y,J,H filters on board the proposed Euclid mission

prove the Figure of Merit (FoM) for determining cosmological parameters using galaxy clustering and weak lensing probes.

Euclid's Wide Survey will cover $\geq$ 15000 sq. def. with imaging in a single broad optical band (R+I+Z), three Near Infrared bands (y,J,H) and NIR slit less spectroscopy. Additional Deep Fields will cover $\geq$ 40 sq. deg., reaching 2 magnitudes deeper than the Wide Survey in both optical and NIR imaging and NIR spectroscopy. Although the deep fields are primarily for calibration purposes, they can be used for additional science like the study of transients. Moreover, ideas for specialised dedicated surveys are being considered.

Recently, a dedicated survey for observing high redshift supernovae (z >1) from space with the Euclid satellite has been proposed by Astier et al. [8]. At such high redshifts, the rest frame optical bands shift into the NIR, requiring observations from space. The survey, named "Dark Energy Supernova Infrared Experiment" or "DESIRE" in short involves a "three-pronged" approach with a low-z anchor of $\sim$ 8000 SNe in the redshift range z <0.35, an intermediate sample in the deep fields of the Large Synoptic Survey Telescope (LSST) in the redshift range 0.2 <z <0.95 and a high-z sample with Euclid in the redshift range 0.75 <z <1.55, requiring 6 months of Euclid observing time.

In our investigation, we focus on the repeat observations of the Euclid Deep Fields during the main survey as a source for discovering and obtaining sparsely

sampled light curves of SN Ia in the *rest-frame* Near Infrared. We emphasise, hence, that the constraints on dark energy from such a dataset would come at no additional cost to the survey.

In order to simulate the SN survey using the Euclid Deep Drilling Fields, we first create a mean template for the NIR light curves and use it to generate mock realisations of SNe observed in the Euclid filters

7.3. Creating Mock SN Ia data

7.3.1. Redshift Distribution

In order to calculate the expected redshift distribution for SN Ia in a given range $[z_{min},\ z_{max}]$, we need to use a function form for the SN Ia rates as a function of redshift. In this section, we look at generating the mock data as seen in the Euclid Deep Drilling Fields (DDF). First, we calculate the redshift distribution as seen with the yJH filters aboard Euclid. We then create a template light curve from which we generate the SN absolute magnitudes. Perrett et al. [235] present the parametrize SN Ia rate function from the sample of SNLS supernovae. The parametric formula is given as follows

$$SNR_{Ia}(z) = r_0(1+z)^{\alpha} \tag{7.1}$$

For the SNLS data alone, the authors find $\alpha = 2.11 \pm 0.28$ and $r_0 = (0.17 \pm 0.03) \times 10^{-4} SNeyr^{-1}Mpc^{-3}$. Since the SNLS data alone doesn't constrain the relation at z<0.3, the authors combine the SNLS data with lower redshift SDSS SNe from Dilday et al. [65] yielding the final value of $\alpha = 1.70 \pm 0.12$ and $r_0 = (0.21 \pm 0.01) \times 10^{-4} SNeyr^{-1}Mpc^{-3}$. Note that this function for the SN rates has a redshift cutoff at z $\sim$ 1.0.

We calculate the redshift distribution for a survey area of 20 sq. degrees and a duration of 100 days. The resulting distribution is plotted in Figure 7.2.

For the SNLS survey, the contamination from non-Ia SNe that survive the culling criteria to the measured rates is at most $\sim$ 2 % out to $z \sim 1$ and is negligible at $z \sim 0.5$

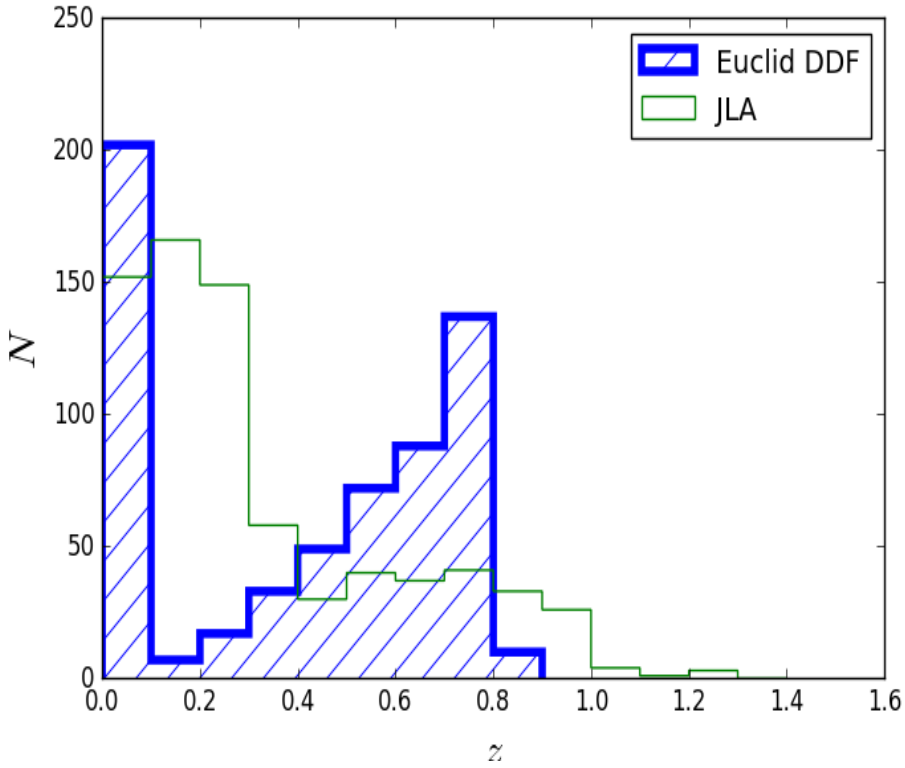

Figure 7.2.: Redshift distribution for the mock sample of SN Ia in the NIR, which includes 200 SNe observed at low-z (z <0.1) from the grounds (blue) compared with the redshift distribution for the JLA sample (green). The maximum redshift for the Euclid survey is determined by the cutoff for the Euclid H-band filter. For the expected redshift distribution the errors on the distance moduli for the SNe in the last two bins (i.e. z >0.6) are extremely high due to the large error in the photometry. This can be resolved with longer exposure times for the visits to the Deep Drilling Fields. We note that both samples presented in this Figure are of comparable size. The JLA sample has a total of 740 SNe, whereas the NIR mock sample has 615 SNe (200 low-z SNe along with 415 SNe at intermediate redshifts).

Errors on the photometry for faint objects are calculated using

$$\sigma(mag) = 0.2 \cdot 10^{0.4*(mag - m_{AB,5sig})} \tag{7.2}$$

where "mag" is the observed magnitude and $m_{AB,5sig}$ is the 5 σ limit for the given filter.

7.3.2. Creating the Mean Curve

As an input to our simulations, we create a mean Y-band light curve from observations of low-z SN Ia. We use the best observed SNe from the Carnegie Supernova Project (CSP) [54, 288], which has compiled an atlas of SN light curves in the optical and the Near Infrared. We correct the low-z sample for K-correction, time dilation and Galactic reddening. We note that these effects are very small in the NIR for the low-z sample. No host galaxy correction is applied to the data before creating the mean curve.

We create a mean curve with a binning of 1 day. For each SN event in the distribution, we draw a phase at random and magnitude for each phase value in the light curve using the spread at the given phase from the mean curve. We fit the resulting light curve with an NIR template using the software SN(oo)Py [37]. The sparse sampling for long cadence observations with the Euclid Deep Fields Survey Strategy doesn't allow us to derive phase information from the NIR light curves alone. Hence, we assume an independent estimate of the timing of the B-band maximum from an optical light curve.

Since we want to probe the same restframe wavelength region at every redshift, we fit the light curves for all mock catalogs in the restframe. We assume that the redshift is known precisely to correct the observed magnitudes to the rest frame. We discuss the impact of the errors in estimating the K-corrections to map the observed filters to the restframe in Section 7.7.1

The final output of the light curve fitting is a three column file with the redshift, fitted peak magnitude and the error on the peak.

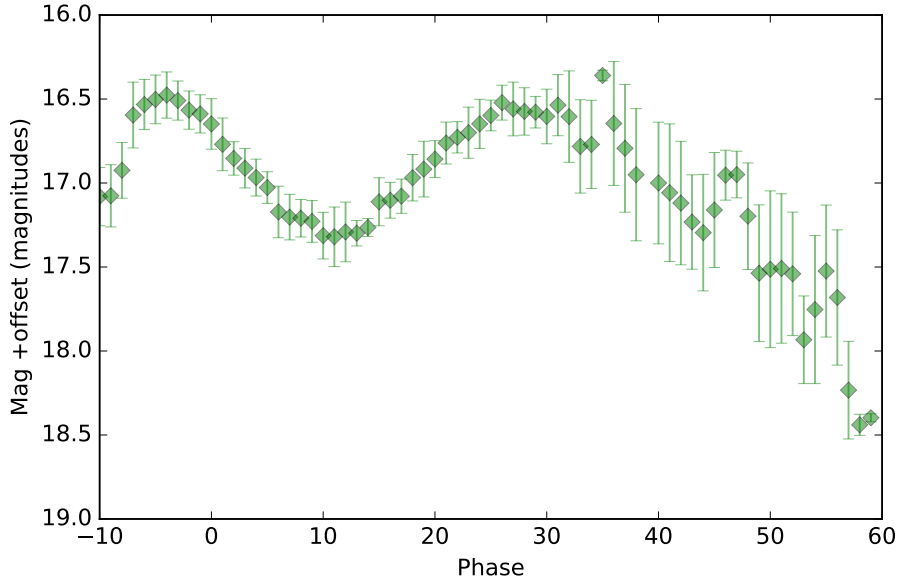

Figure 7.3.: The mean light curve in the Y filter. Details of how the mean curve was generated are discussed in the text.

7.4. Advantages of Sparse Sampling in the NIR

The uniform behaviour of SN Ia in the NIR led to increased interest in obtaining sparsely sampled light curves in the J and H filters in order to measure distances precisely in an observationally inexpensive way. Recently, there have been a few studies demonstrating the power of light curves with 1 -3 points along with prior information from the optical to measure precise distances to nearby SN Ia. The pilot study of the SweetSpot program on the WIYN telescope [318] demonstrated that with only a few NIR observations per SN in the J and H bands (for SNe out to a maximum redshift of 0.09), one can obtain an rms scatter of 0.164 mag. More recently, Stanishev et al. [282] presented NIR light curves for intermediate redshift SN Ia ($z_{max} \sim 0.18$) to extend the NIR Hubble diagram out to $z \sim 0.2$. Moreover, Barone-Nugent et al. presented J and H light curves for 12 SN Ia in the Hubble flow (z>0.03) and evaluated a residual scatter of 0.085 mag in the H band. Although the stretch range for these SNe was narrow compared to the total distribution (0.8 -1.15), this demonstrated the excellent ability of SN Ia to be used as distance indicators in the NIR. The authors also showed that with only a single point per SN in

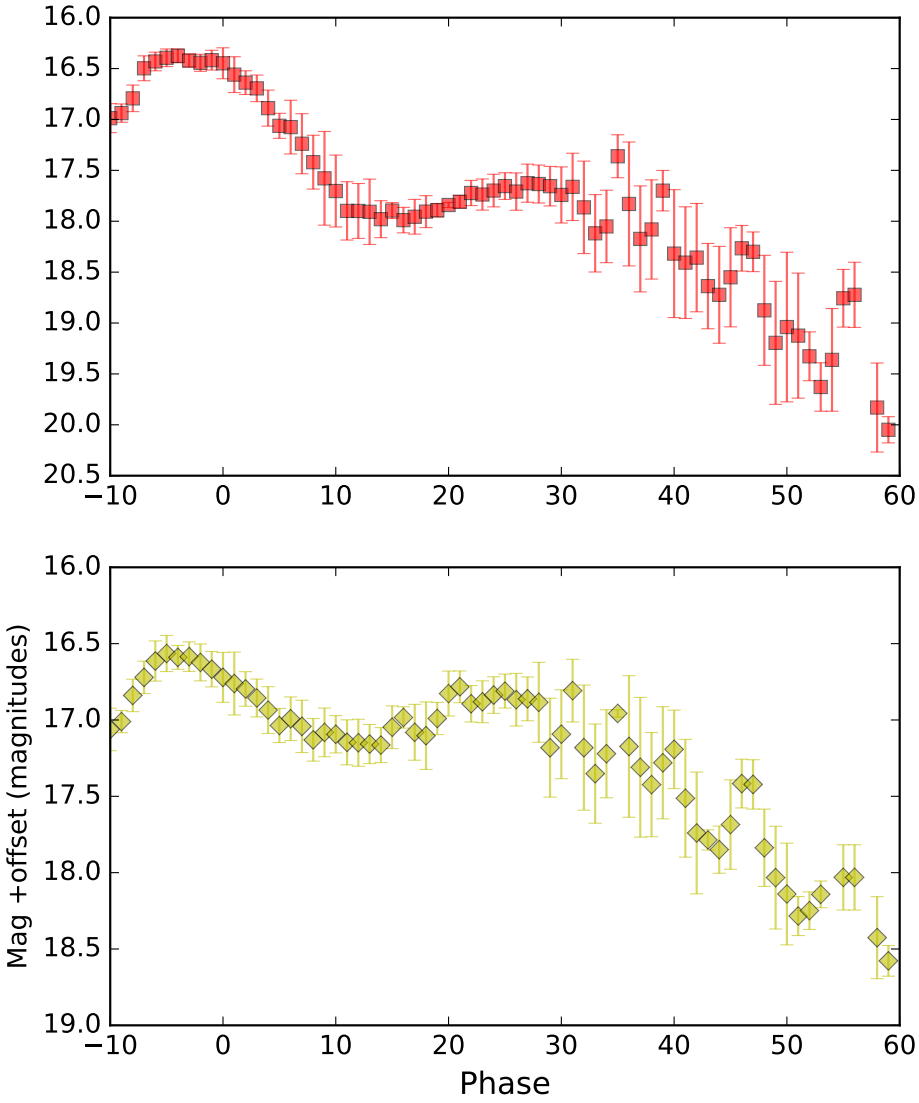

Figure 7.4.: The mean light curve in the J (top) and H (bottom) filter. Details of how the mean curve was generated are discussed in the text.

their sample, they still get scatter values of ~ 0.12 mag in the H band and 0.15 mag in the J band.

Since sparsely sampled light curves have been demonstrated as a rich, potential source to increase the sample size of SN Ia studies (without requiring more observing time) and still obtain precise distances, we aim to quantify whether it is more beneficial to use larger sample sizes or to have more densely sampled light curves. In other words, we would like to know whether observing a larger sample of SNe is more beneficial or if having densely sampled light curves yields the most promising results.

In this investigation, we generate mock realisations of SN Ia with a total of N_{obs} observations. We alter N_{SN}, the number of supernovae, each with $\frac{N_{obs}}{N_{SN}}$. As a test case we take 1000 observations and distribute them amongst 125, 250, 500, 1000 SNe and evaluate the standard error on the mean for each case using Equation 7.3.

$$\sigma_{SEM} = \frac{\sigma_{rms}}{\sqrt{N}} \tag{7.3}$$

We report the resulting values for σ_{rms} and σ_{SEM} in Table 7.2. From Table 7.2 we find that, as expected , the rms scatter reduces for a sample with better sampling per SN (i.e. higher $\frac{N_{obs}}{N_{SN}}$), however, the standard error on the mean, given by Equation 7.3, is smallest in the case for $N_{SN} = 1000$, suggesting that the most profitable strategy is to observe more SNe with fewer observations per object. We find that this corresponds well with the tests demonstrated in [15], although the authors in that study use a small sample of 12 SNe (see Table 4 of [15]) .

7.4.1. Precision on $\mathrm{t_{max}(B)}$

We note that in the absence of complementary optical data (either spectra or well-sampled B or V band light curves), it is not possible to constrain $\mathrm{t_{max}(B)}$ from only sparsely sampled NIR light curves. In our simulations, we have assumed that $\mathrm{t_{max}(B)}$ is known with high accuracy and hence, do not account for large errors in $\mathrm{t_{max}(B)}$.

Table 7.1.: The filter definitions and sensitivity limits (5σ point source) for the Euclid mission. Credits: Euclid Definition Study Report and Astier et al. [8].

Filter	λ_{min}(nm)	λ_{max}(nm)	Sensitivity (mag)
y	920	1146	24.02
J	1146	1372	24.03
H	1372	2000	23.98

However, as was demonstrated for the pilot study of the SweetSpot survey, in many cases the SNe did not have well-sampled optical light curves [318]. For the pilot sample of the SweetSpot survey, the authors report an t_{max}(B) from an optical spectrum. Measuring t_{max}(B) from an optical spectrum has an associated uncertainty of $\pm$ 2 d. [318] coherently shift the t_{max}(B) by 2 d for their NIR fits and find a shift in the peak magnitude of 0.06 mag, corresponding to an error of 0.017 mag for their sample of 12 SNe, which is significantly smaller than the rms scatter of their sample or the individual measured uncertainties on the peak magnitude.

We test the effect of a coherent shift in t_{max}(B) on the mean peak absolute magnitude for 1000 realisations. We find a similar shift of 0.07 mag, corresponding to a smaller error of mag owing to a larger sample size than the SweetSpot pilot study. Hence, we find, similar to [318] that a coherent shift in t_{max}(B) doesn't contribute significantly to the error in the mean.

Table 7.2.: The standard error on the mean as a function of the number of SNe for a fixed total number of observationsi. For this investigation we assume that accurate phase information is available from complementary optical photometry.

N_{SN}	N_{obs}/SN	σ	σ_{SEM}
1000	1	0.134	0.0043
500	2	0.126	0.0056
250	4	0.091	0.0057
125	8	0.075	0.0067

Moreover, we also look at the effect of t_{max}(B) being drawn randomly from a normal distribution from a $\mathcal{N}(0,1)$ distribution and use this value as the prior for the phase information in the NIR template fit.

We generate 1000 SN events as in the first case of Table 7.2 and propagate the uncertainty in t_{max}(B) as described above. The resulting σ_{rms} increases to 0.15 mag (from 0.134 mag in Table 7.2), however, the shift in the mean value is 0.003 mag hence, it has a minimal contribution to the error on the mean magnitude.

7.5. Constraints on Cosmology

In order to use apparent magnitudes for the cosmological fitting, we add a distance modulus μ(z; θ). For testing constraints on wCDM cosmology, we use $\theta \in \{H_0, \Omega_m, w\} = \{70, 0.27, -1\}$ for a flat universe.

$$\mu = 5\log_{10}(\frac{D_L}{Mpc}) + 25 \tag{7.4}$$

The luminosity distance is a function of the redshift (z) and the cosmological parameters for the input model (in this case wCDM)

$$D_L(z, \mathcal{C}) = \frac{c}{H_0}\frac{(1+z)}{\sqrt{\Omega_{k,0}}} S(\sqrt{\Omega_{k,0}} I(z)) \tag{7.5}$$

where

$$I(z) = \int_0^z \frac{dz'}{\sqrt{(1+z')^3\Omega_{m,0} + (1+z')^{3(1+w)}\Omega_{\Lambda,0} + (1+z')^2\Omega_{k,0}}} \tag{7.6}$$

and $S(x) = x$, $\sin(x)$ or $\sinh(x)$ for flat ($\Omega_{k,0} = 0$) , closed ($\Omega_{k,0}$<0)and open ($\Omega_{k,0}$>0) universe, respectively.

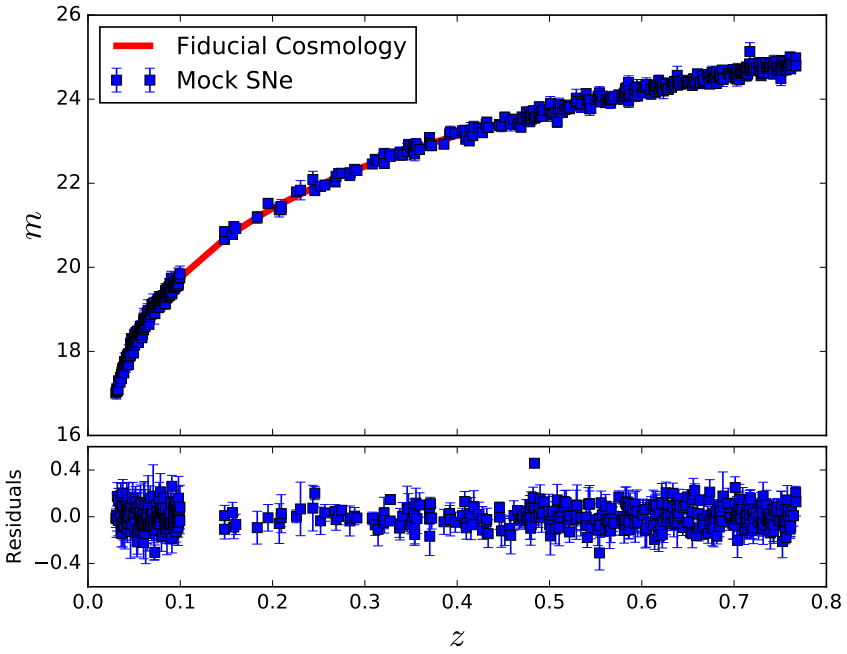

Figure 7.5.: The simulated, rest-frame Y-band Hubble diagram for the SN Ia surveys with the Euclid Deep Drilling Fields (DDFs; *blue*) and the fiducial cosmology (*red*). The Hubble residuals are plotted in the lower panel.

Table 7.3.: "Uninformative" prior values for the cosmological parameter estimation with MCMC fitting. The parameters given here are for the w_zCDM model, however, we note that we use the same prior on constant w as we do for w_0 in w_zCDM

Parameter	Prior range
Ω_m	[0, 2]
w_0	[-5, 0]
w_a	[-5, 5]

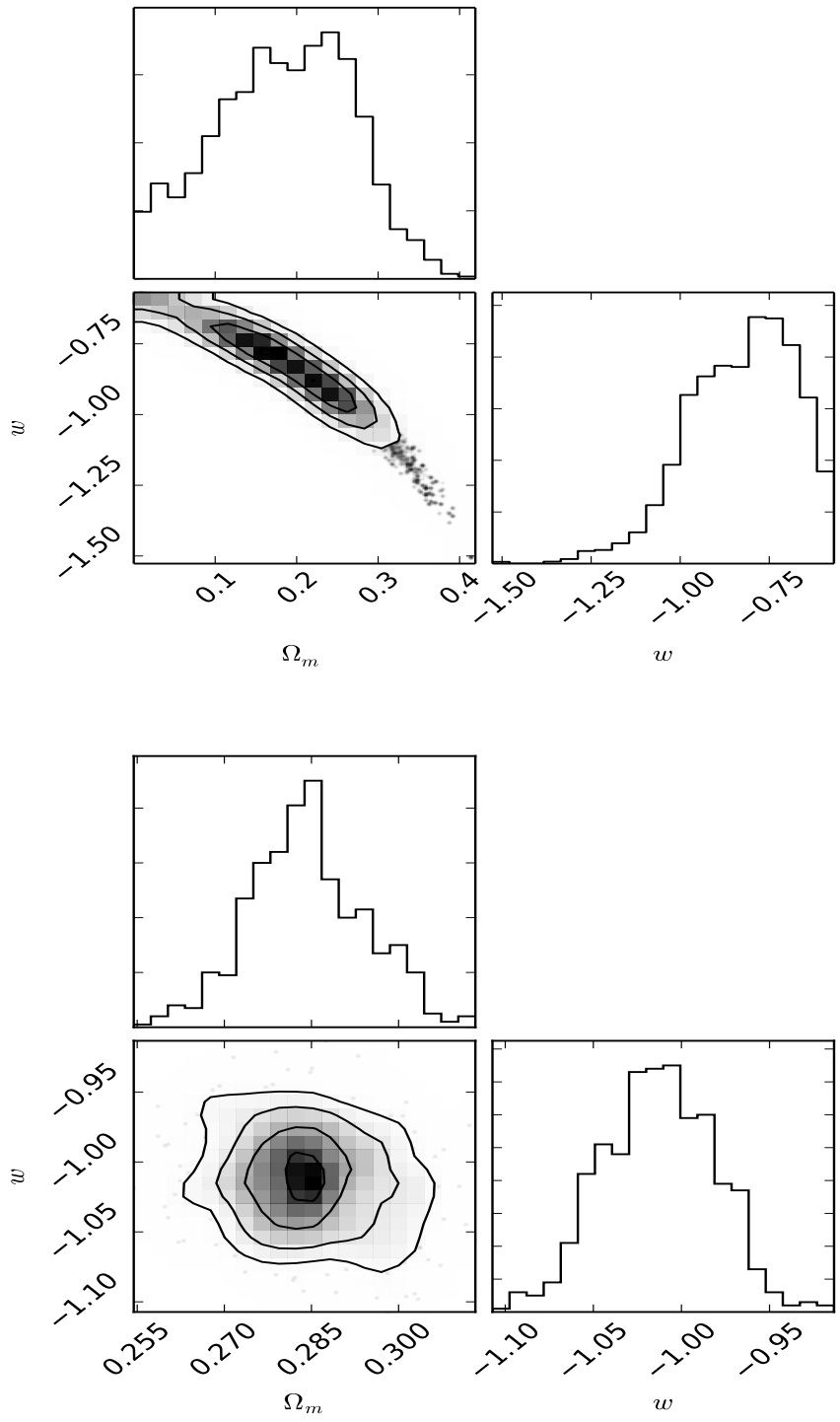

Figure 7.6.: *Top*: Ω_{m} -w contours for the NIR mock sample of SN Ia from the Euclid Deep Drilling Fields. *Bottom*: Ω_{m} - w contours along with a distance prior from the CMB. As expected, the constraints on w improve significantly with the addition of the CMB data, which is complementary to the constraints from the SNe. The error contours are 0.5 σ.

$$\chi^2_{SN\ Ia} = \sum_{I=0}^{N} \frac{(\mu_i - \mu_{mod})^2}{\sigma^2_{\mu,i}} \tag{7.7}$$

where $\sigma^2_{\mu,i}$ is

$$\sigma^2_{\mu,i} = \sigma^2_{fit,i} + \sigma^2_{int} + \sigma^2_{phot} \tag{7.8}$$

$$\sigma^2_{phot} = \sigma_m * (z/z_{max})^2 \tag{7.9}$$

$\sigma_{fit,i}$ is the error on the light curve fit, σ_{int} is the intrinsic scatter and σ_m encapsulates the photometric accuracy, which was conservatively taken as 0.02 mag by [42]. We adopt the same value here.

Hence, the likelihood is given by

$$\mathcal{L}_{SNIa} = \exp(\frac{-\chi^2}{2}) \tag{7.10}$$

We evaluate the posterior distribution for the parameters of interest using a Markov Chain Monte Carlo algorithm (nested sampling, see Appendix A and [75] for details on the algorithm). The likelihood is given in Equation 7.10 and we use "un-informative" priors on the parameters, summarised in Table 7.3.

7.5.1. Variable w

The expression for luminosity distance given in Equation 7.5 and the integral $I(z)$ assume that the equation of state of dark energy, w is a constant with redshift. A more general expression for the integral can be given as

$$I(z) = \int_0^z \frac{dz'}{\sqrt{(1+z')^3\Omega_{m,0} + \Omega_{DE}(z') + (1+z')^2\Omega_{k,0}}} \tag{7.11}$$

Table 7.4.: Comparison of the constraints on the wCDM and w_zCDM model from the NIR mock SNe and the most recent constraints from the JLA sample in the optical. The parameter estimates are presented both for the SNe only case and the SNe + CMB case.

Sample	$\frac{\Delta w}{w}$	$\frac{\Delta w_0}{w_0}$	Δw_a
NIR mock	0.18	0.24	1.74
JLA	0.27	0.30	1.83
with CMB prior			
NIR mock	0.04	0.20	0.87
JLA	0.04	0.23	0.94

$$\Omega_{DE}(z) = \Omega_\Lambda \exp[3 \int_0^z \frac{1 + w(z^{'})}{1 + z^{'}} dz^{'}] \tag{7.12}$$

We implement the most commonly used parametrisation for $w(z)$ in the literature $w(z) = w_0 + w^{'} z + \ldots$, is ill-behaved at high z, and hence a more useful two parameter model is proposed by Chevallier & Polarski in 2001 [45] and Linder in 2003 [182] (hereafter CPL) is expression as follows

$$w(a) = w_0 + w_a(1 - a) \tag{7.13}$$

where $a = 1/(1 + z)$. This parametrisation is referred to as w_zCDM hereafter. Note, for our analysis we assume flatness, i.e. $\Omega_k = 0$ and $\Omega_m = 1 - \Omega_\Lambda$. For the mock catalogs the input (w_0, w_a) is (-1., 0.)

7.5.2. Comparison with the Optical

The most competitive constraints on the equation of state of dark energy have been presented by Betoule et al. [21] using a combination of SN Ia, CMB and BAO measurements. The sample of SN Ia includes 740 objects in the redshift range 0.01 <z <1.3 (see Figure 7.2 for the complete redshift distribution).

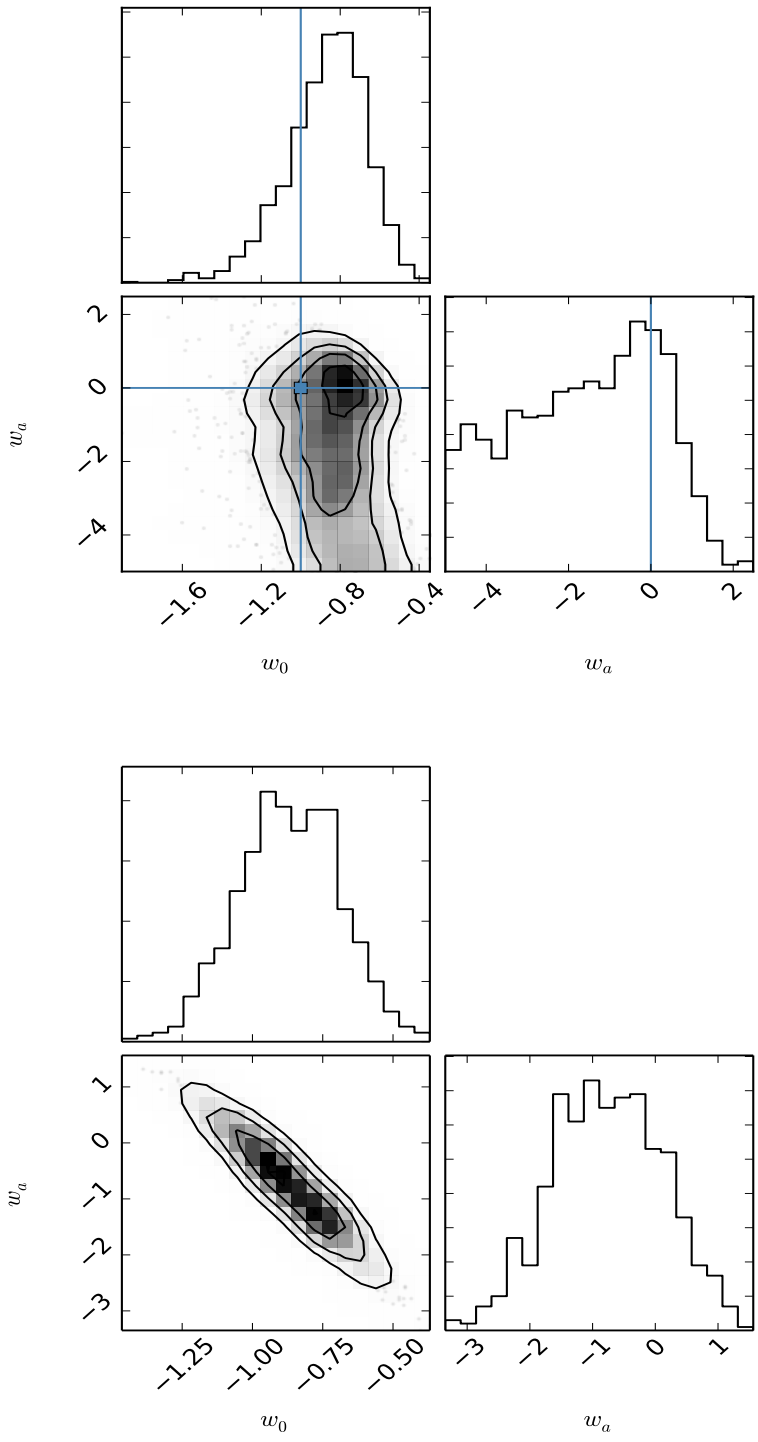

Figure 7.7.: *Top*: Constraints on w_zCDM from the NIR mock SN catalog (SN-only constraints). There is a strong degeneracy between the two parameters. The error on w_a is ~ 1.8, which makes it difficult to constrain the time-varying equation of state. *Bottom*: w_zCDM constraints from the NIR mock SNe combined with the CMB prior (see text for discussion of CMB constraints). The errors improve significantly with $\sigma(w_a) \sim 0.9$, similar to the constraints from the optical SNe data + CMB.

For this, we derive constraints on the cosmological model from the binned distance moduli from the JLA sample presented in Appendix E of Betoule et al. [21].

The resulting w-Ω_{m} contours for the JLA sample are plotted in Figure 7.8 For the SN only fits, the median and 68% credible regions for w and Ω_m are $-0.90^{+0.333}_{-0.170}$ and $0.267^{+0.133}_{-0.113}$ which is in good agreement with the results from [274].

7.5.3. Combined Constraints with Complementary Probes

As seen above (e.g. top panel Figure 7.8), Type Ia supernova are excellent distance indicators to estimate cosmological parameters. However, especially for testing time-varying equation of state of dark energy, the constraints on the cosmological parameters can be improved significantly (e.g. top panel Figure 7.9). For this purpose, SN Ia data has often been combined with complementary probes, e.g. the Cosmic Microwave Background [17] and Baryon Acoustic Oscillations (BAOs) [10] (some studies also combine the likelihood with a prior on H_0 from local measurements, e.g. Cepheids [254, 255]).

For our study, we focus on the distance prior from the Cosmic Microwave Background (CMB) compressed likelihood, using the CMB shift parameter calculated by the Planck Collaboration (similar to the procedure implemented by Astier et al. for the DESIRE survey [8], although the authors in that study use the forecasts for the *Planck* satellite [211]). Ongoing and future missions (e.g. DES, Euclid) are designed to significantly improve upon the current cosmological constraints from complementary probes like BAOs and Weak Lensing (WL), hence, we defer the discussion for a combinations of all four probes to a later study.

Cosmic Microwave Background The CMB is a rich source of information regarding the physical conditions in the early universe ($z \sim 1100$). It also provides a complementary high-redshift distance prior that, when combined with SN Ia, or other probes (e.g. Baryon Acoustic Oscillations) at later stages in the evolution of the universe, can provide extremely precise constraints on

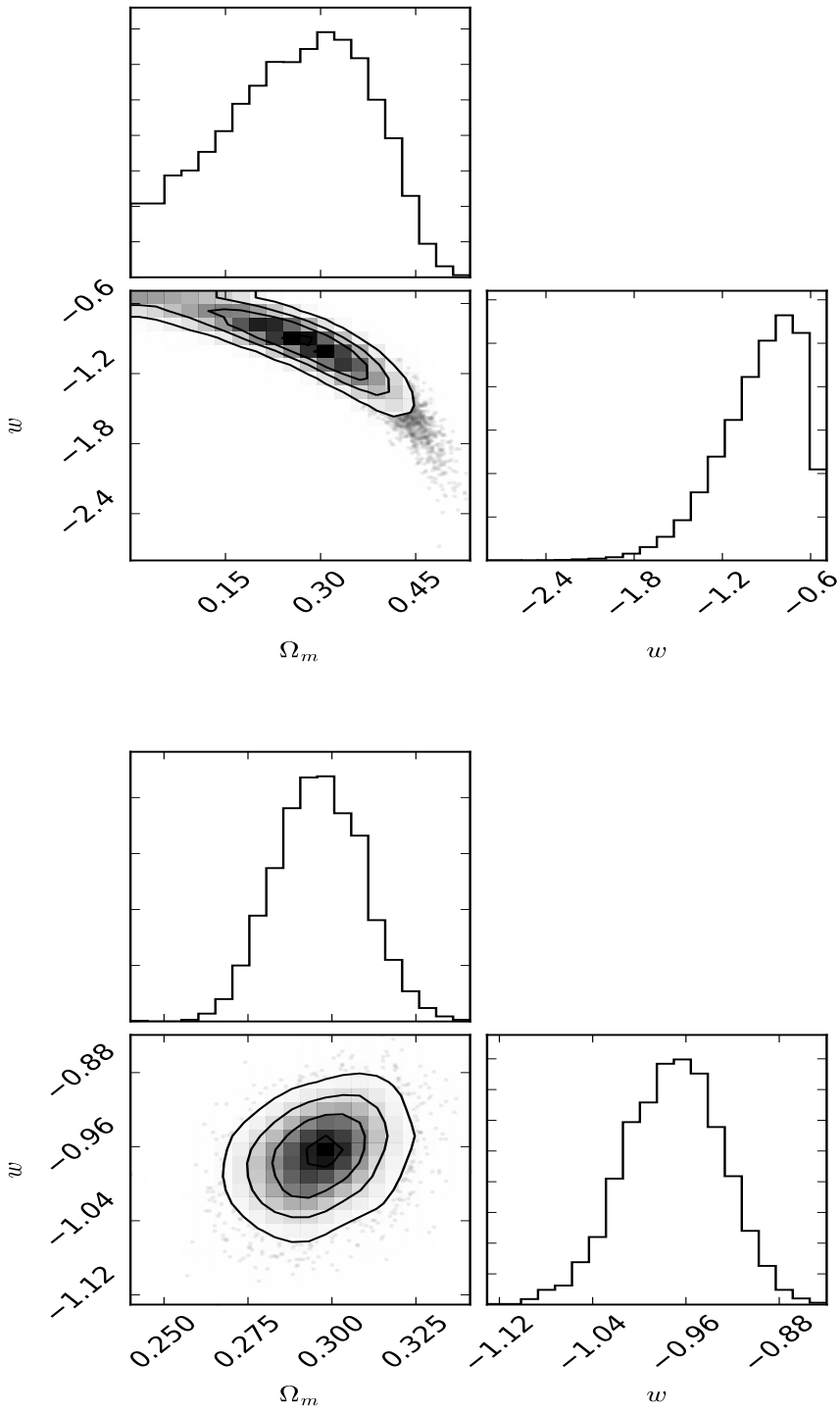

Figure 7.8.: Constraints on wCDM from the Joint Light Curve analysis of SDSS and SNLS SN Ia sample. *Top*: The constraints on w - $\Omega_{\rm m}$ from SNe only. *Bottom*: Constraints from SNe + CMB. For the SN only constraints we use the binned distances and the covariance matrix provided in Appendix E of [21].

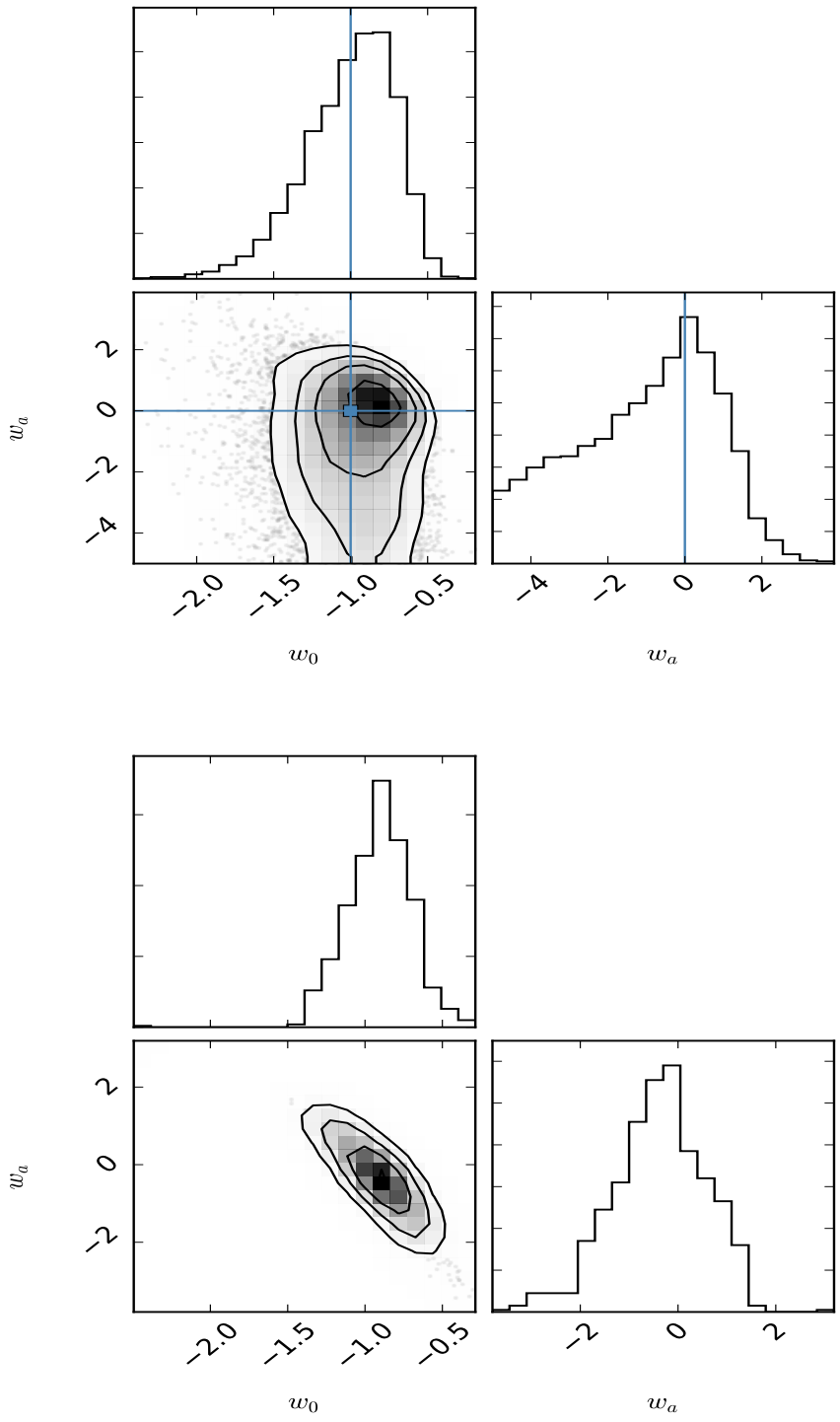

Figure 7.9.: w_0-w_a contours from the JLA binned distance moduli. The blue lines show the point for the cosmological constant (-1, 0). The data are consistent with the cosmological constant hypothesis, although the errors on w_a are large. *Bottom*: The constraints on (w_0 - w_a) from the JLA SN sample combined with a CMB distance prior. The errors on w_0 and w_a are significantly reduced.

dark energy. Constraints on standard cosmological parameters can be calculated from the CMB observations without needing to compute the complete likelihood from fitting the power spectrum. A compressed likelihood has been derived from observations conducted by recently concluded CMB experiments, e.g. *WMAP* and *Planck* teams to place constraints on w, Ω_Λ and Ω_k. For the *WMAP* five-year data, Komatsu et al. 200,9 [157] demonstrate that there is a good agreement between the parameter estimates from the complete CMB likelihood calculation and the compressed likelihood (Figures 12 and 13 in [157]). An important caveat presented in the study and in previous analyses of cosmological models (e.g. [55, 68]) is that the compressed likelihood parameters are *derived* parameters from the fitting of the CMB power spectrum, and hence, they must be used carefully when testing alternative cosmological models.

The CMB shift parameter. R measures the size of the apparent sound horizon at recombination [68] and is related to the position of the first acoustic peak in the CMB temperature power spectrum. The value of the shift parameter is not directly measured from the CMB temperature maps, but rather, requires assumptions on the background cosmology. This provides a computationally less intensive approach to derive CMB priors on cosmology. Comparing to the different MCMC chains, the Planck collaboration finds that the compressed likelihood is stable for ΛCDM, wCDM and w_zCDM models [246, 248]. For a spatially flat universe, the CMB shift parameter is defined as

$$R = \sqrt{\Omega_m \cdot H_0^2}(1+z^*)\frac{D_A(z^*)}{c} \tag{7.14}$$

where Ω_m is the dimensionless matter density, $D_A(z^*)$ is the angular diameter distance at the redshift of decoupling, z^*. The expression for redshift of decoupling is given by the fitting formula of Hu & Sugiyama 1996 [133]

$$z^* = 1048 \cdot [1 + 0.00124(\Omega_b h^2)^{-0.738}][1 + g_1(\Omega_m h^2)^{g_2}] \tag{7.15}$$

where

$$g_1 = \frac{0.0783(\Omega_b h^2)^{-0.238}}{1 + 39.5(\Omega_b h^2)^{0.763}} \tag{7.16}$$

$$g_2 = \frac{0.560}{1 + 21.1(\Omega_b h^2)^{1.81}} \tag{7.17}$$

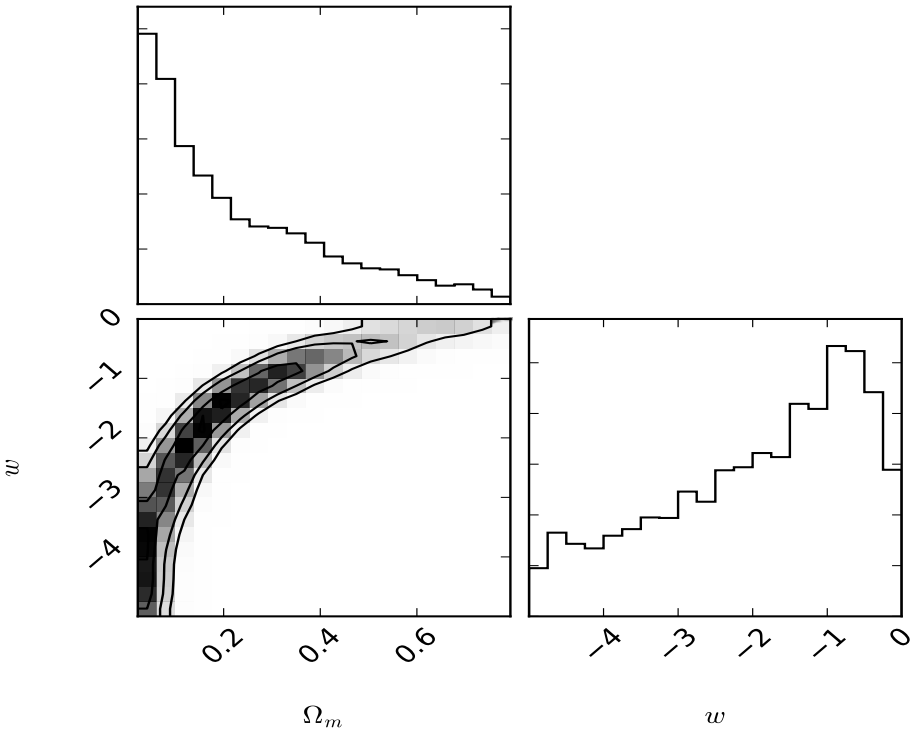

Figure 7.10.: The $\Omega_{\rm m}$ -w constraints from the CMB shift parameter alone using the χ^2 expression from Equation 7.18. Although the constraints from the CMB alone are not very precise, the contours are orthogonal to those from the SNe and hence, combined with SNe provide extremely precise constraints on w

For our calculation, we fix the $\Omega_b h^2$value to 0.022 [246]. Keeping $\Omega_b h^2$ as a free parameter doesn't significantly change the CMB constraints on $\Omega_{\rm m}$ -w . Thus, the constraints on cosmology are obtained by minimising the χ^2 given by

$$\chi^2_{CMB} = (\frac{R - R_{pl}}{\sigma_{pl}})^2 \tag{7.18}$$

where the subscript pl denotes the best estimate and error on R from the *Planck* satellite [248]. Since the SN Ia and the CMB provide independent constraints, for the combined χ^2 we can simply add the χ^2 from the two

Table 7.5.: The effect of the cadence at which the Deep Drilling Fields are visited on the final error on w_a

Cadence (days)	$\sigma(w_a)$
10	0.75
15	0.87
30	1.02

probes from Equations 7.7 and 7.18

$$\chi^2_{tot} = \chi^2_{SN\ Ia} + \chi^2_{CMB} \tag{7.19}$$

7.5.4. Impact of Deep Drilling Fields Cadence

For our analysis of the Euclid NIR SN survey, we assumed a cadence of 2 weeks. In this section we look at the impact of faster and slower cadences on the cosmological estimates. We find that the change in the scatter in the peak magnitude as a result of the cadence does not significantly change the final error on constant w , however, a faster cadence does improve the errors on w_a. The results are summarised in Table 7.5. We find that a 10 day cadence yields $\sim$ 10 % better errors on w_a and likewise, a 30 day cadence yields $\sim$ 10 % larger errors on w_a. For further analysis, we use the baseline case of a 2 week cadence.

7.6. $z>$ 1 constraints with James Webb Space Telescope

The constraints on w from the Euclid DDF are comparable to the most precise constraints from recently concluded optical surveys (see Table 7.5). Since the forecast survey only extends out to a maximum redshift of $\sim$ 0.8, the survey does not precisely constrain any possible time variation in the dark energy

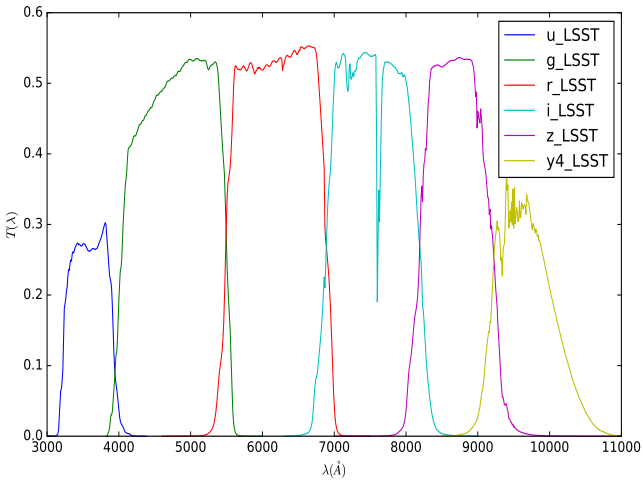

Figure 7.11.: The proposed filter set for the Large Synoptic Survey Telescope (LSST).

equation of state. Therefore, in order to obtain more precise constraints on $w(z)$ from restframe NIR observations, we need to extend the high redshift lever of the YJH band Hubble diagram, to z>1. This would involve observations in a wavelength region that is redder than the NIR (λ>2μm). Since the Euclid satellite has a filter cutoff at $\sim$ 2 μm, such a high-z study cannot be conducted using the Euclid deep fields.

The James Webb Space Telescope (JWST) is a joint mission of NASA, the European Space Agency and the Canadian Space Agency consisting of a 6.5 m space observatory which is optimised for Near- and mid- Infrared observations. The NIRCam aboard JWST has a filter set that extends out to $\sim$ 5 μm, making it an ideal instrument for such a high-z follow-up program.

In this section, we present a simulated survey of rest-frame YJH observations at z>1. For this high-z arm the SNe will be discovered in the optical with future facilities (e.g. LSST) and followed up with NIRCam on JWST. We analyse the constraints on constant w and $w(z)$ with $\sim \mathcal{O}(10^2)$ in the redshift range z >0.8.

Table 7.6.: Simulated depths for the LSST deep-drilling fields. The depths shown here were calculated by [8] for the intermediate-redshift part of their three-pronged SN survey

Filter	Magnitude	Exp. Time
g	26.47	300
r	26.35	600
i	25.96	600
z	25.50	780
$y4$	24.51	600

LSST Deep Drilling Fields The Large Synoptic Survey Telescope (LSST) [1] is a 8.4m survey telescope equipped with a very wide-field camera (9.6 sq. deg.) with u,g,r,i,z,y filters (see Figure 7.11). The science for SN Ia from LSST alone is described in Chapter 11 of the LSST science book, concentrating on the key gain for SN cosmology of having large number statistics (of order 50000 SN Ia). Such statistics would also improve systematics by allowing the sample to be split into subsamples, e.g. by host galaxy type. This SN survey would also be critical to measuring rates for all types of supernovae and to test isotropy and homogeneity as well as SN Ia evolution.

In this investigation, we primarily look at an optical SN discovery telescope like LSST to find suitable targets for NIR follow-up with JWST. We emphasize that the prior information along with the NIR observations is the supernova classification and phase information alone and hence, it is not sensitive to the LSST mission configuration. The DDFs are scheduled to be visited with a 4-day cadence with exposure times listed in Table 7.6.

Since the SN rates are very uncertain at $z \sim 1$ (see [8] for a discussion), for the high-z arm we draw a a uniform redshift distribution in the range [0.8, 1.4]. For each SN we only draw a single observation in the NIR in the phase range [-6, +5] days from t_{max}(B). Since we only have single point instead of 4-5 points in the NIR we can observe of order few hundred SNe without requesting for a large amount of observing time.

[1] http://lsst.org/

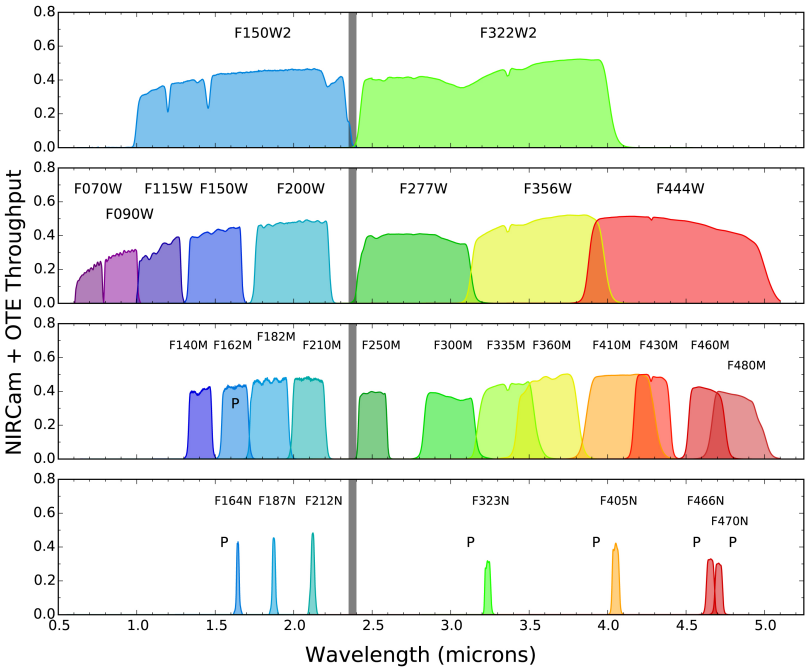

Figure 7.12.: Short-Wavelength and Long-Wavelength filter passbands for the narrow, medium and wide filters available with NIRcam on JWST. The wavelength range covered is from 0.6 - 5 μm making it possible to observe the rest frame NIR at z >1. Figure credits: http://www.stsci.edu/jwst/instruments/nircam/instrumentdesign/filters

7.6.1. Constraints on cosmology

As with the Euclid DDF survey, we evaluate the constraints for the different cosmological parametrisations

Constant w

We test the wCDM model constraints with the addition of the high-z NIR observations from JWST to the SNe from the Euclid DDF survey. The resulting contours for Euclid + JWST SNe (for SNe alone and SNe + CMB) are presented in Figure 7.15. For SNe only, we get constraints on constant w

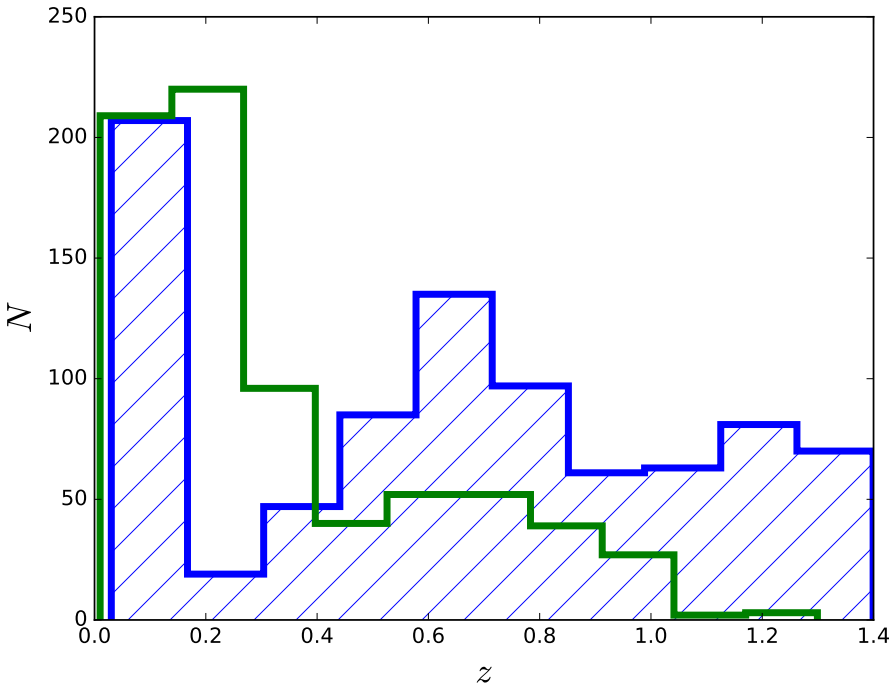

Figure 7.13.: The redshift distribution for the NIR survey with the Euclid DDF combined with 300 SNe measured with JWST (*blue*) compared with the redshift distribution of the JLA sample of Betoule et al.(*green*) The NIR sample has roughly the same number of SNe spanning a similar redshift range to the latest sample in the optical.

(flat universe) of order $\sim 10\%$ (see Table 7.7, a significant improvement on constant w compared to the Euclid-only forecasts and the current constraints from JLA (see top two rows of Table 7.5 for a comparison). This demonstrates the power of the high-z to improve the SN only constraints on w.

Combined with the CMB distance prior, the JWST constraints are ~ 3 % which is slightly better than the estimate from the Euclid DDF SNe + CMB estimates.

‘

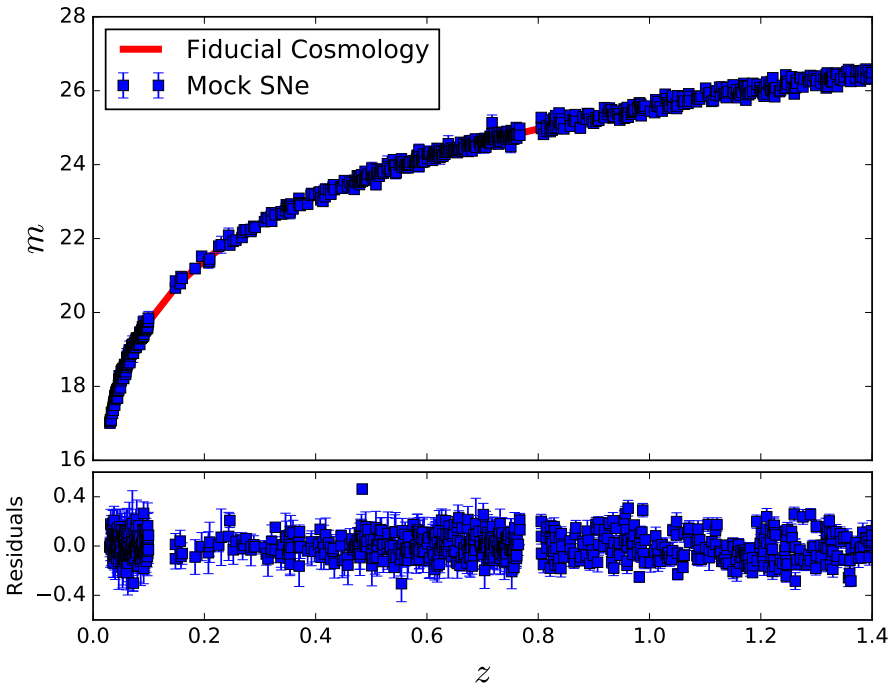

Figure 7.14.: The Hubble diagram for the SNe forecast to be observed with Euclid and JWST combined with a low-z anchor (see text for details). The red line is the fiducial cosmology input to derive the apparent magnitudes. *bottom*: Hubble residuals for the mock catalog of SNe.

Variable w

The high-redshift lever provided by observations from JWST at > 2 μm are critical to constrain the time evolution of dark energy. Using the same parametrisation for variable w as for the Euclid DDF, we present the constraints on (w_0, w_a) using a combination of Euclid DDF SN Ia and the JWST high-z arm.

We estimate the improvement in the uncertainties on w_0 and w_a by increasing the sample size for the the high-z lever. We find that there is a $\sim$ 10 % improvement in the errors on both w_0 and w_a by increasing the total number of SNe from 200 to 500. We discuss these estimates of $\sigma(w_a)$ and $\sigma(w_0)$ in context of forecasts from other surveys in the literature in section 7.7.

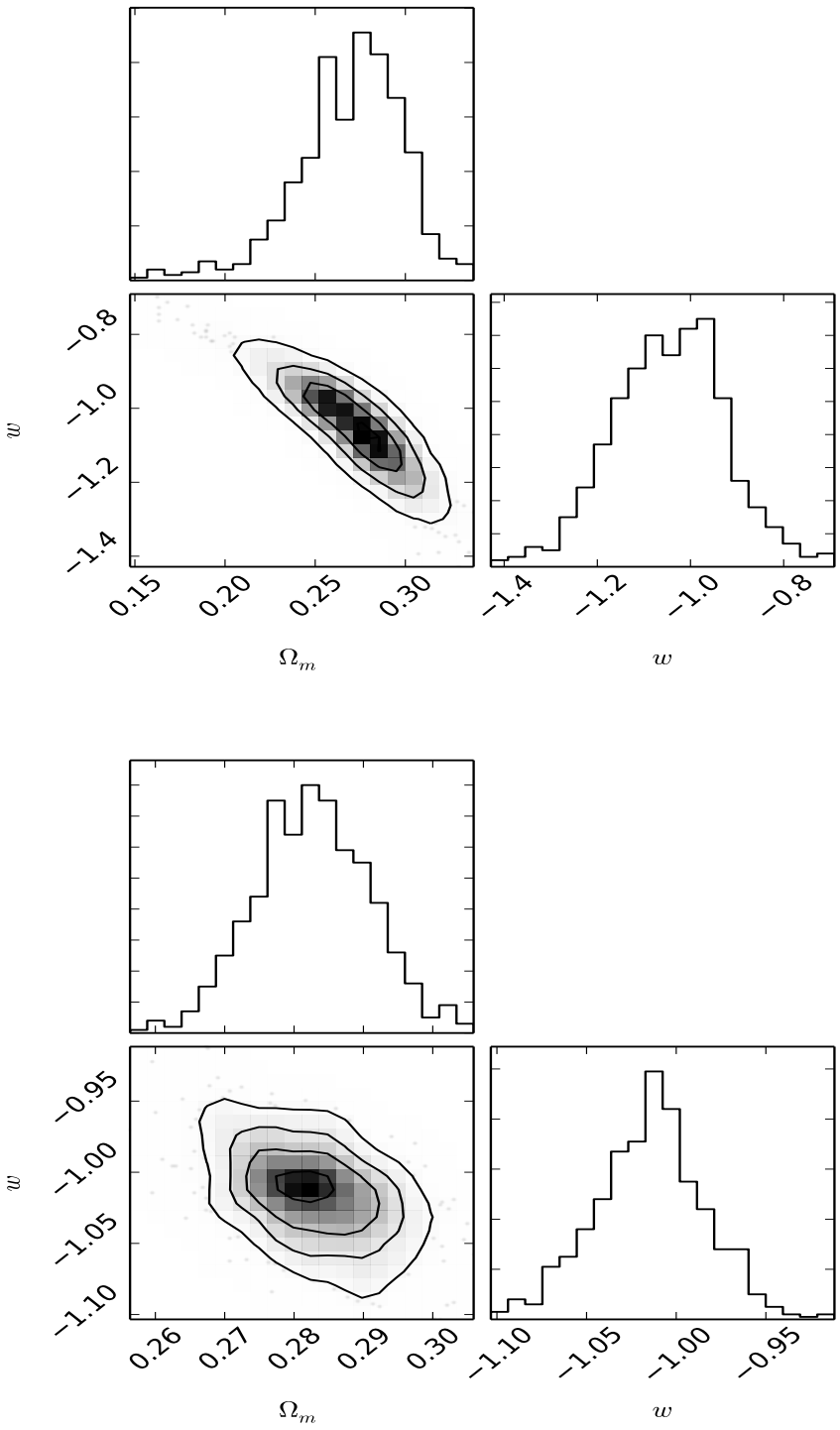

Figure 7.15.: *Top*:Constraints on wCDM model from Euclid DDF + JWST high-z SNe only. The 1-σ errors are of the order of 10%, which is a significant improvement over the current constraints from the JLA sample. *Bottom*: Constraints for the same model with a distance prior from CMB observations. As expected, the CMB prior shrinks the errors on w. The errors are reduced to ~ 3 % for constant w, assuming a flat universe.

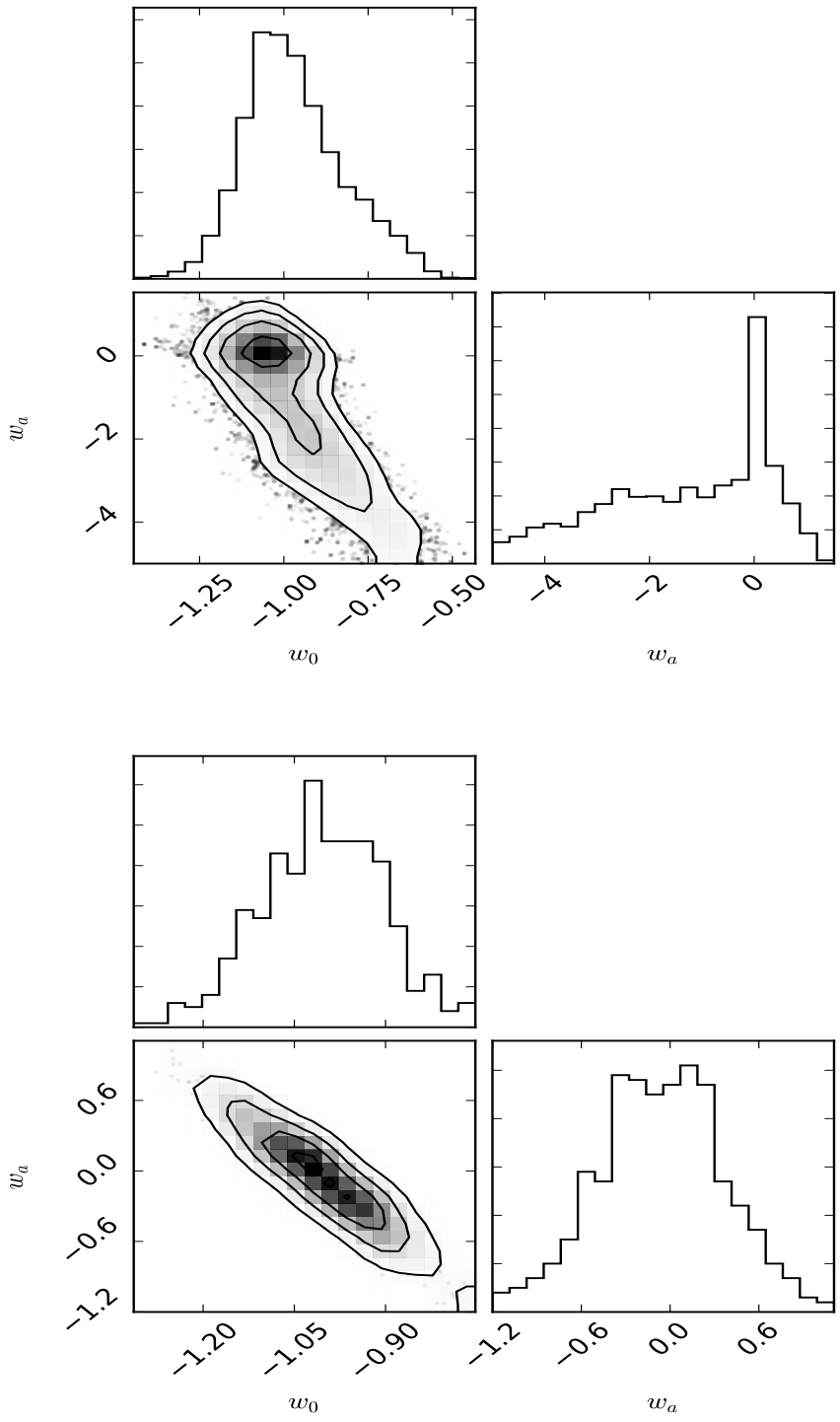

Figure 7.16.: *Top*: Constraints on the w_zCDM model from a combination of the Euclid DDF survey and single point observations of high-z SN Ia with JWST. The w_a contours have large 1 σ errors ($\sim$ 1.5) with a long tailed distribution. This is expected since the SNe alone cannot precisely constrain the dark energy equation of state as a function of redshift. *Bottom*: The SN constraints for the w_zCDM are combined with a distance prior from CMB observations. The errors on w_a shrink significantly with the 1 σ error on $w_a \sim 0.45$.

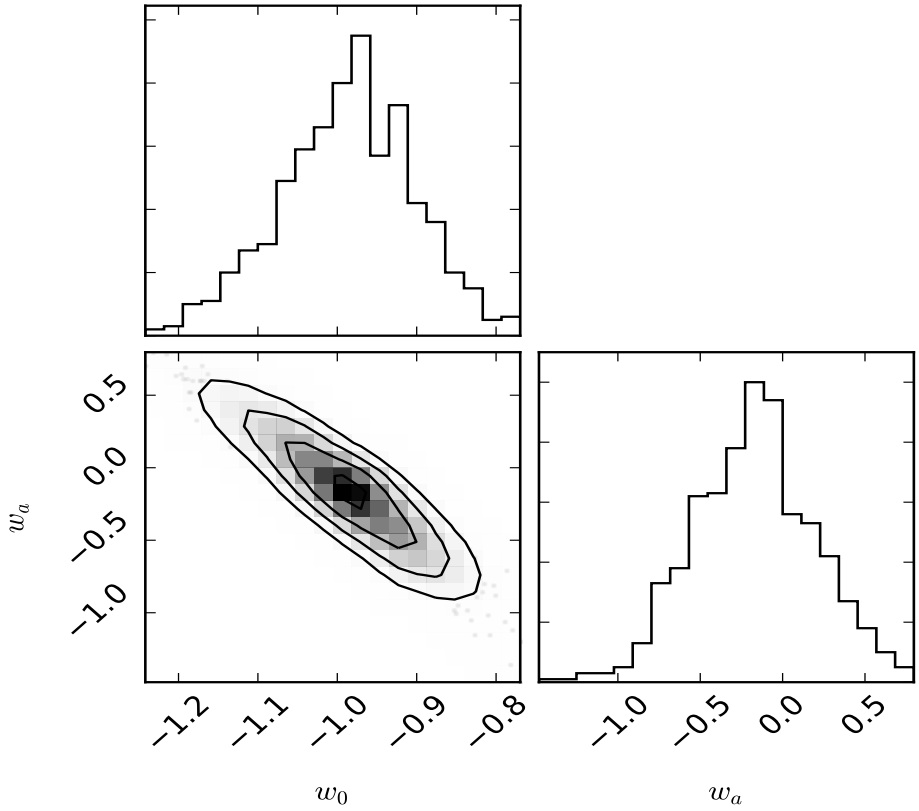

Figure 7.17.: (w_0, w_a) contours for a combination of SN constraints from Y and J band observations with the Euclid DDF+JWST and a distance prior from CMB observations.

Table 7.7.: wCDM model constraints from SN Ia only. The mock sample consists of 200 low-z SNe (z <0.1), SNe discovered in the Euclid Deep Fields and the high-z arm observed with JWST. The SNe alone can constrain constant w to $\sim$ 10% or better (assuming flatness).

N_{SN}	$\frac{\Delta_w}{w}$
200	0.101
300	0.097
500	0.095

Table 7.8.: Constraints on time-varying dark energy from a combination of Euclid DDF+JWST SN Ia and a distance prior from CMB observations.

N_{SN}	$\frac{\Delta w_0}{w_0}$	Δw_a
200	0.108	0.449
300	0.099	0.427
500	0.095	0.400

7.7. Discussion

Future supernova surveys are designed to provide excellent multi-band photometry for large sample of SN Ia, increase the total number of known SN events by 1 or 2 orders of magnitude. Using well-calibrated photometric systems, these surveys (e.g. DES, LSST), aim to significantly improve the constraints on the equation of state of dark energy and its time variability. Moreover, an improvement in the measurements of complementary cosmological probes (e.g. Baryon Acoustic Oscillations, Weak Lensing) will further bolster the constraining power of future surveys to understand the nature of dark energy.

We have studied the constraints on standard cosmological models from future SN surveys designed to return data in the *rest-frame* Near Infrared. A reduced contribution from host galaxy dust and a smaller intrinsic scatter in the absolute magnitudes makes this an ideal wavelength region to use SN Ia as distance indicators in cosmology. We present the final constraints on Ω_m, w and time-varying equation of state $w(a)$ in combination with a distance prior from the CMB compressed likelihood.

We note that the rms scatter for our mock Hubble diagrams is ~ 0.11. A recent study by Barone-Nugent et al. [15] found an rms scatter in the H band of 0.085 mag for 12 SNe in the Hubble flow (i.e. z>0.03). Hence, with a larger sample of NIR observations for SN Ia in Hubble flow (e.g. the recently concluded Carnegie Supernova Project - II), one can test the effect of peculiar velocity errors on the final value of the intrinsic scatter in the peak luminosity of the SNe.

In this section, we discuss our findings in context of current constraints and forecasts presented in the literature. We also discuss the use of complementary distance indicators recently proposed to further augment the constraints from SN Ia.

7.7.1. Impact of K-correction errors on cosmology

Light from distant supernovae is significantly redshifted by expansion of universe by the time it reaches the telescope. Hence, the SED is significantly shifted with respect to the SN rest frame and the fluxes measured in the passbands on earth do not correspond to the SN rest frame flux, which is the quantity of interest for cosmological (and physical) constraints.

In order to 'shift' the observed fluxes to the 'original' rest frame filters, we apply K-corrections. Indeed, this is the method for light curve fitting used by MLCS2k2 [142], but not by other light curve fitters e.g. SALT2 [107], which models the SN magnitudes at different redshifts with different training sets for each redshift region (e.g. SDSS, SNLS to create intermediate and high-z templates).

As a result of this application, it is imperative to know the underlying SED very well. For this purpose, authors have previously constructed template SED's from a library of spectra (Nugent et al. [218], Hsiao et al. [132]).

For our investigations we require a template SED in the NIR in order to K-correct the observed J and H band photometry to the rest frame Y band (and also calculate K_{YY} for the low-z sample).

Here, we look at the effect of the K-correction errors in the NIR on cosmological parameters estimation. The cross-filter K-corrections are evaluated as given in Equation 7.20

$$K_{AB}(t) = 2.5 \cdot \log\left((1+z) \cdot \frac{\int F_B(\lambda)\phi(\lambda;t)\lambda d\lambda}{\int F_A(\lambda)\phi(\lambda(1+z);t)\lambda d\lambda}\right) + Z_A - Z_B \quad (7.20)$$

where A : (Y,J,H) and B:Y. F_A and F_B are the filter transmission functions and ϕ is the template SED. Z_A and Z_B are the filter zero-points.

Dispersions in K-corrections

K-correction dispersions are quantified here are the differences between the K-correction calculated using a particular observed spectrum $\phi^S(\lambda)$ and that calculated using an assumed template spectrum $\phi^T(\lambda)$. Hence, the K-correction dispersion can be written as

$$\Delta K_{AB} = 2.5 \cdot \log\left(\frac{\int \lambda \phi^S(\lambda) F_B(\lambda) d\lambda}{\int \lambda \phi^T(\lambda) F_B(\lambda) d\lambda}\right) - 2.5 \cdot \log\left(\frac{\int \lambda \phi^S(\lambda/(1+z)) F_A(\lambda) d\lambda}{\int \lambda \phi^T(\lambda) F_A(\lambda) d\lambda}\right) \tag{7.21}$$

As can be seen in Equation 7.21, the definition of the K-correction dispersion removes the dependence on the zero points and focuses on the effects of an assumed spectral template and the alignment of the rest-frame and observed filters

In this investigation we use two approximations for the error on the K-term. Firstly, we use a constant term added in quadrature to the errors from the fit. In the second case, we use a linearly increasing error term with redshift as demonstrated in Boldt et al. [30] for Y, J, H, K filters.

In Freedman et al. [89], the authors find a maximum error in the K-correction of ~ 0.1 mag. We apply 0.1 mag as an additional error to all SNe (conservatively). We also look at the effect of larger K-correction errors on the value of w. The resulting effect on the best estimate and error on w in flat wCDM model is presented in Table 7.7.1.

We also calculate the impact of the K-correction dispersion on the precision of estimating w_a. Using the Euclid DDF+JWST SN catalog and a CMB distance prior, we find that $\sigma(w_a)$ is 0.55 for an additional systematic uncertainty of 0.1 mag. For a smaller uncertainty of 0.05 mag, the error on w_a is 0.45. We note that the main limiting factor in calculating the dispersion of the K-correction terms is the number of NIR spectra available to create accurate templates as a function of phase and $\Delta m_{15}(B)$.

We calculate more realistic dispersions in the K-correction as a function of redshift. For a given redshift, we determine the spread in the possible values of

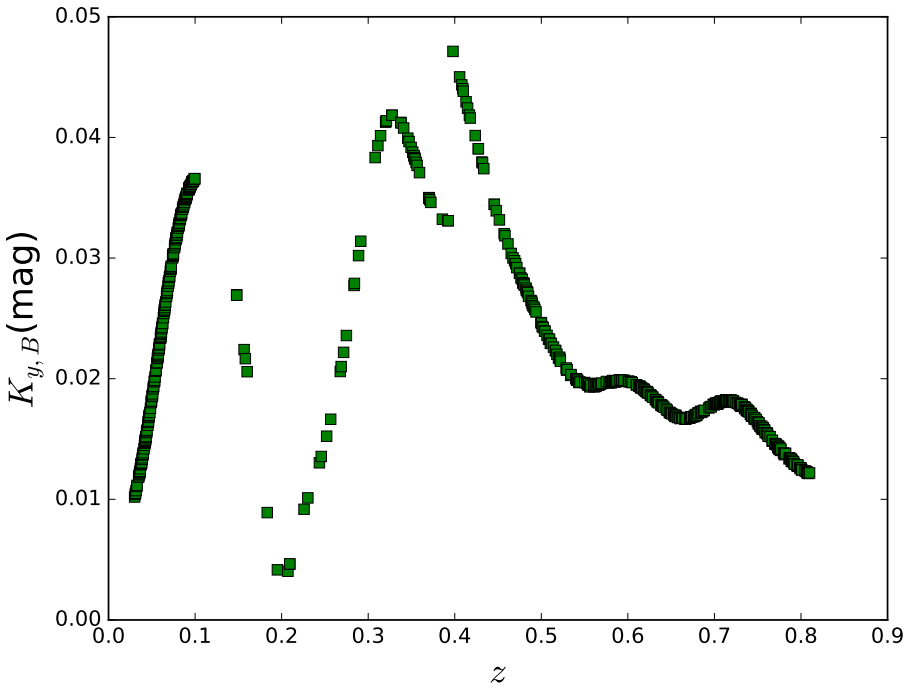

Figure 7.18.: The spread in the calculated K-correction versus redshift. The K-correction spread is calculated by "mangling" the template spectrum to the observed colours for SNe with observations near the epoch of interest. The "jumps" observed in the dispersion occur due to the rest-frame filter shift from y to J band (at z $\sim$ 0.1) and J to H (at z $\sim$ 0.3)

the K-correction by matching the template spectrum to the observed colours of the SNe in the sample described above for calculating the mean curve. For each matched spectrum we calculate the K-correction as described in Equation 7.20. The range of K-correction values is then assumed as an additional error term, added in quadrature for the final estimation of cosmological parameters.

We compare the resulting constraints on w from the forecast Euclid survey to those from the Joint LightCurve Analysis (JLA) sample presented by Betoule et al. [21]. Firstly, we compare the estimates on w and $\Omega_{\rm m}$ from our nested sampling MCMC (see Appendix A and [74, 75]) method to those presented in the literature for the JLA sample and find a very good agreement. The constraints from SNe-alone as will be observed by Euclid are marginally better

Table 7.9.: The functional form and scale of the error in the K-correction, median value for w and σ are presented. "const" refers to a constant error added in quadrature to the error on the distance modulus, whereas "lin" uses a simple linear function with the maximum value mentioned in column 1.

K_{err}	Func	w	σ
0.0	...	-0.99	0.24
0.1	const	-1.01	0.27
0.15	const	-1.04	0.31
0.2	const	-1.07	0.41
0.1	lin	-0.99	0.24
0.15	lin	-1.05	0.28
0.2	lin	-1.08	0.31

than those from the JLA sample (see Figures 7.6 and 7.8). We note that the NIR light curves are built from very few observations and can even yield distances with only a single observation as long as there is a prior on the time of B-maximum and a spectroscopic classification of the SN.

Combining the SN constraints with an orthogonal CMB distance prior from *Planck* , we find that the constraints on constant w from the Euclid + low-z survey are comparable to the JLA+CMB constraints. Since these NIR light curves come at essentially no additional cost to the Euclid survey (the Deep Drilling Fields are required to calibrate the measurements for the primary science goals of Euclid i.e. weak lensing and Baryon Acoustic Oscillations), such a survey is extremely advantageous to bolster the constraints on the dark energy equation of state.

Furthermore, we evaluate the constraints on time-varying dark energy from such an NIR survey. As is expected, the SNe alone are not sufficient to provide a precise constraint on the time-variability of dark energy, with $\sigma(w_a) \sim 1.8 \,\&\, 1.7$ for the JLA and Euclid NIR surveys respectively (see Figures 7.9 and 7.7, top panels). However, combining these constraints with a CMB prior, we find that the error on w_a is significantly reduced to ~ 0.9 (as is also seen in

the case for constant w; Table 7.5). The constraints on w_a from the NIR are slightly better than the current constraints from the optical, however, it is not a substantial improvement. This is most likely due to the Euclid NIR survey not extending to higher redshifts z>1.

In the rest frame Near Infrared at z>1, NIRCam on JWST will be an ideal instrument to obtain sparsely sampled light curves for measuring distances to SN Ia. With only 300 SNe, each with a *single* observation using the NIRCam, the JWST high-z lever allows us to constrain constant w in a flat universe (combined with the low-z anchor and the intermediate z observations from Euclid) to $\sim$ 10 % or better (*note*: the timing of B-band maximum and hence, the phase of observation is assumed to be known from complementary optical observations.).

Forecasts for the Dark Energy Survey (DES; [20]) predict a 10 % constraint on constant w, from a sample of $\sim$ 4000 SNe alone, comparable to the values we obtain here. Combining the results with a CMB prior from *Planck*, constant w can be constrained to $\sim$ 2 %, similar to what we obtain from the NIR.

The Science book for the Large Synoptic Survey Telescope (LSST) [187] has presented constraints on dark energy equation of state using SN Ia (Chapter 11). For a constant w, the errors are slightly larger than 10 % from SNe alone for a sample of 10,000 SN Ia, assuming spectroscopic redshifts for all host galaxies. This is a significant improvement on current constraints from the JLA sample ($\sim 25-30\%$ on constant w from SNe alone, see Table 7.5). Relaxing the assumption of spectroscopic redshifts for host galaxies of SNe discovered by LSST, the authors find that the more realistic case of photometric redshifts yields constraints of $\sim$ 20 % (see Figure 11.12 of [187]). We note that our results are comparable to, or slightly better than the best case scenario presented in the LSST science book. We stress as well that the NIR presents a complementary method to constrain the dark energy equation of state.

Bernstein et al. [20] forecast the error contours on the time-varying dark energy equation of state (assuming a Chevallier-Polarski-Linder parametrisation). Along with a Stage II Dark Energy Task Force + Planck Prior, the authors find $\sigma(w_a) \sim 0.5$ and $\sigma(w_0) \sim 0.1$, which is similar to the estimates forecast from the NIR. The LSST science book also forecasts constraints on $w(a)$ from SNe alone. They find $\sigma(w_a) \sim 1-2$ depending on the errors in the

photometric redshifts. It is worth noting, however, that for this forecast, they assume 50,000 SN Ia (about one-tenth of the total sample LSST is designed to find in its ten-year lifetime) which is a factor $\sim$ 50 larger than the total number of SNe in the NIR forecast.

WFIRST is a planned NASA Mission of an NIR wide-field imaging and spectroscopy satellite in space. Its main science goals concentrate on measuring the expansion history of the universe and galaxy clustering (exploring dark energy and modified gravity with weak lensing, BAO and supernovae). The forecast SN survey as described in the definition study report (Green et al. [105]) includes a low-z anchor of 800 SNe at z <0.1, 1400 SNe in the range 0.1 <z <0.8 and 700 SNe in the range 0.8 <z <1.65 measured in the J,H and K bands. Since the redshift range 0.1 <z <1.65 is broader than the span of measurements (J,H,K), Relative distances heavily rely on the SN model and are sensitive to the calibration uncertainties of the training sample. We note that in our forecast survey, the low, intermediate and high-redshift parts are all measured in the same rest frame wavelength region and hence are not prone to uncertainties arising from extrapolating the SED presuming an SN model. Astier et al. [8] use their simulator for a space-based high-z survey along with the WFIRST inputs and find that the systematic uncertainties from the training sample significantly increase the final errors on w_a hence, being a limiting factor for such an SN survey.

7.7.2. Further extension of the high-z arm

As mentioned above and detailed in the Definition Study Report ([105]), WFIRST will be surveying SN Ia in the optical to extremely high redshift $z_{max} = 1.7$ or even greater. In this discussion, we study the impact of following a subset of these high-z SNe discovered by WFIRST in the rest-frame NIR with JWST. Similar to the case mentioned in section 7.6, we draw a uniform redshift distribution $\mathcal{U}(0.8, 1.8)$ for 200 SNe. Since WFIRST is designed to discover $\sim$ 100 SN Ia in each redshift bin Δz of 0.1 (summing up to $\sim$ 1000 SNe in the specified redshift range), our estimate of 200 SNe followed up in the NIR is very conservative. We study the impact of such high-z observations with JWST. We test the wCDM and w_zCDM model with a combination of the EuclidDDF+JWST SNe.

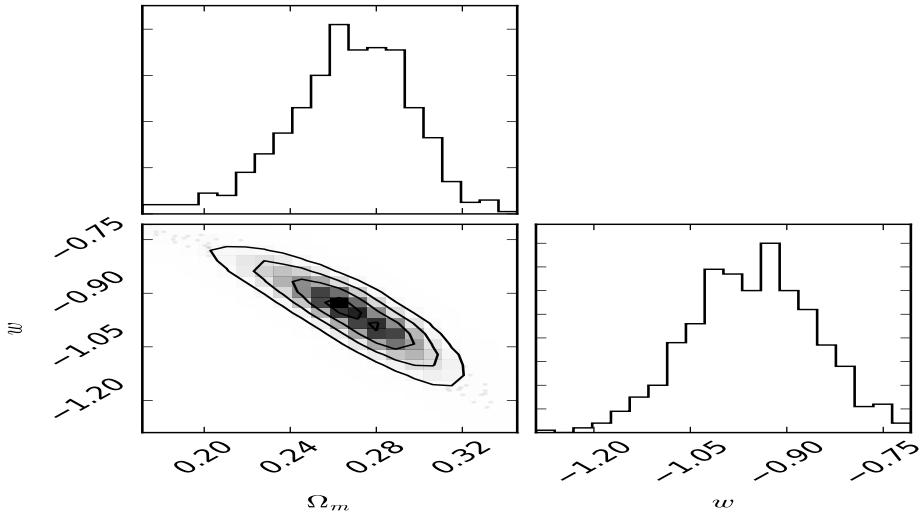

Figure 7.19.: (w-$\Omega_{\rm m}$) contours derived from SNe only with 200 SNe observed using JWST out to a maximum redshift of 1.8. The SNe alone yield $\sim 8\%$ constraints on constant w

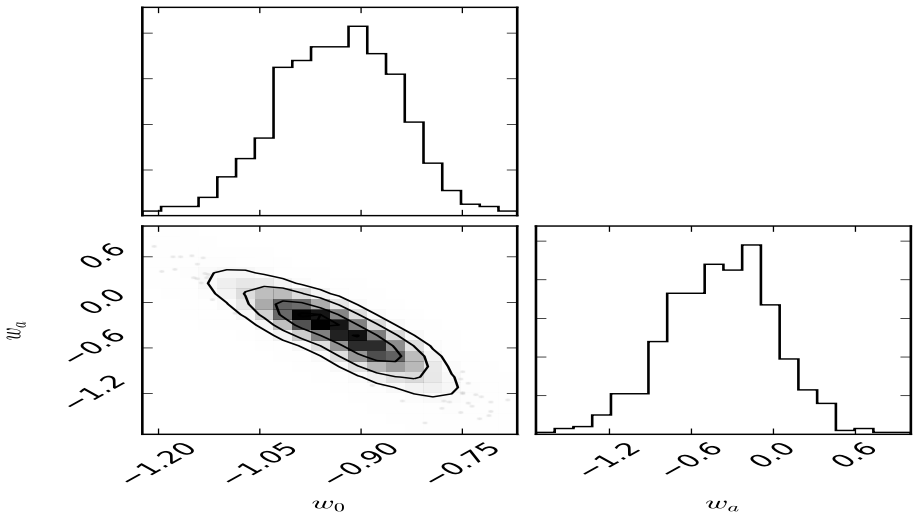

Figure 7.20.: (w_0-w_a) likelihood contours for SN Ia along with a CMB distance prior. With z_{max} of 1.8, the SNe+CMB yield a $\sigma(w_a) \sim 0.4$.

We find that extending the NIR Hubble diagram to a z_{max} of 1.8 leads to precise constraints on constant w of ~ 8 %. Combined with the CMB distance prior to test time-varying dark energy, we find that with $z_{max} = 1.8$, we get $\sigma(w_a)$ of 0.37, which is marginally better than observing 500 SNe out to a z_{max} of 1.4.

7.7.3. Fitting for the intrinsic scatter

In the analysis presented, we fix the value of the intrinsic scatter to the standard deviation of the peak magnitudes. This value is a conservative overestimation of the intrinsic scatter of the sample. Hence, we calculate the contours for the cosmological model by fitting for the intrinsic scatter as well. For this, the likelihood expression is as follows

$$\mathcal{L} = \sum_{i=0}^{N_{SN}} \frac{1}{\sqrt{2\pi\sigma^2}} exp(-(\mu_i - \mu_{model})^2/\sigma^2) \tag{7.22}$$

where $\sigma^2 = \sigma_i^2 + \sigma_{int}^2$, the error on the distance modulus and the intrinsic scatter respectively.

In this section we evaluate the contours with σ_{int} as a free parameter in the fit We use the w_zCDM model (to test how the uncertainty on w_0 and w_a changes) for the EuclidDDF + JWST SN with a CMB prior. The resulting likelihood contours are plotted in Figure 7.21. The 1-σ errors on w_0 and w_a are 0.08 and 0.35 respectively. These values are smaller than the errors of ~ 0.10 and 0.45 in the case that the standard deviation is used as the intrinsic scatter (see Figure 7.16 for a comparison). Hence, fitting for the intrinsic scatter yields smaller errors in the final estimate of w_0 and w_a.

We also note that adding a constant term of 0.1 mag in quadrature as a systematic uncertainty for the K-corrections (as done in section 7.7.1) increase the 1-σ errors on w_0 and w_a to 0.1 and 0.41 respectively.

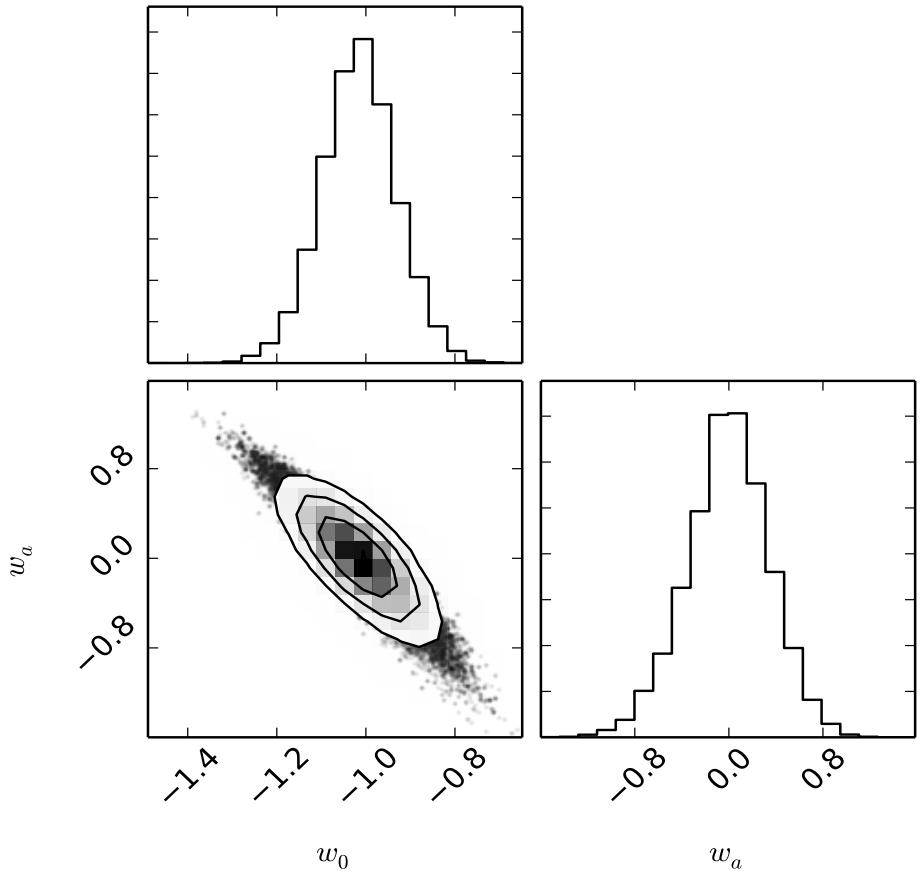

Figure 7.21.: (w_0-w_a) contours for Euclid DDF+JWST SNe along with the distance prior from *Planck*. The 1-D marginalised distributions for w_0 and w_a are also plotted along with. For this fit the σ_{int} term in the expression for the χ^2 is fitting as a free parameter instead of fixing it to the σ_{rms} of the peak magnitudes. Since the σ_{rms} is either equal to or larger than the σ_{int}, fitting for this parameter leads to smaller errors for w_0 and w_a.

7.8. Conclusion

In this chapter, we have presented constraints on standard cosmology and time-varying dark energy from SN surveys in the rest frame Near Infrared with future ground and space-based facilities. We restrict ourselves to the CPL parameterisation of time-variability since it is the most commonly used formalism in the literature, however, this prescription can be used for alternate paramterisations too for e.g. Wetterich paramterisation [316] or Jassal-Bagla-Padmnabhan parametrisation [138] . We note that the expression for the luminosity distance in Equations 7.5 and 7.6 assumes homogeneity and isotropy on large scales. Relaxing these assumptions, we can also use the SN datasets to test inhomogenous cosmology, e.g. the Lemaitre-Tolman-Bondi model (e.g. [73]) .

We find that an SN survey in the rest-frame Y band with the Deep Drilling Fields for the Euclid mission yields slightly improved constraints on constant w , when compared with the latest optical constraints from the JLA sample. The constraints from Euclid are derived for sparsely sampled light curves in a single filter, compared to the multi-band detailed light curves from the SDSS and SNLS surveys in the optical (see Table 7.5). Moreover, we stress that the DDF survey comes at essentially no additional cost to the Euclid mission since these fields will be visited for calibration of the primary science goals, i.e. BAOs and Weak Lensing. However, these constraints presume an accurate timing of the B-band maximum, derived from complementary optical light curves obtained from ground-based facilities.

Since the final aim is to constrain the time variability of dark energy, we estimate the error on w_a for the CPL formalism of the redshift dependence of dark energy equation of state (see Equation 7.13). Combining the SN Ia likelihood with a distance prior from the CMB we find a 1-σ error on w_a of ~ 0.9, which is again similar to the current best constraints from the optical (Table 15. Betoule et al. [21]).

To obtain more precise constraints on w_a, we require higher redshift observations of SN Ia in the Near Infrared. We find that an additional 300 SNe in the redshift range [0.8, 1.4], measured by a future satellite can provide stringent constraints on $w_a \sim 0.45$. These constraints are similar to those from ongoing and future surveys like DES and LSST.

Distance measurements to SN Ia in the NIR are complementary to measurements in the optical and offer a unique opportunity to compare the systematics in both methods by measuring a distance to the *same* SN. Additionally, the NIR offers an opportunity to constrain properties of SN host galaxy dust and to measure global parameters e.g. ^{56}Ni mass (e.g. [60]), if there is sufficient sampling around the timing of the second maximum. Therefore, the NIR appears to be an effective tool to constrain cosmology in the future.

8. Conclusions and Future Outlook

In this thesis, we analyse the Near Infrared and bolometric properties of Type Ia supernovae to understand the physics of the explosions, search for clues regarding the progenitor system and progenitor mass and to forecast the use of SN Ia as distance indicators in the *rest-frame* Near Infrared with future facilities.

The Near Infrared light curves are a unique opportunity to study both the physics of the explosions and to use them for precise distance measurements. We find that the light curves in the $YJHK$ filters are very uniform near maximum light and appear to diversify at ~ 2 weeks after maximum. In these filters (as well as the i and z bands), the light curves rebrighten to form a second peak between 15 and ~ 40 days from B-band maximum light (although see the recent study of peculiar, super-Chandra candidate SN 2012dn where the authors find an H-band second peak at $\sim +70$ days [331]). The timing of the second maximum correlates strongly with the post-peak optical decline such that more slowly declining SNe peak at a later epoch. This indicates that intrinsically brighter SN Ia would have a later second maximum and hence, the NIR late time diversity is governed by the main radioactive energy source, i.e. ^{56}Ni . This conclusion is further supported by the correlation between the timing of the second maximum and the epoch at which the optical $(B-V)$ colour is maximum, which traces the amount of ^{56}Ni produced in the explosion.

The Near Infrared colour curves ($J-H$, $Y-J$) are also extremely uniform near maximum light and start to show differences at later phases. The $J-H$ colour curves show a trough-like feature at ~ 1 month post-maximum light, which is attributed to the lack of emission lines in the J-band ([281]). The epoch at which this trough-like feature occurs in the colour curve is also correlated

strongly with the timing of the second maximum, indicating that the late time colour curve diversity is also a function of the ^{56}Ni mass.

Reddening-free estimate of ^{56}Ni mass We followed the study on NIR light curve properties by testing whether the derived ^{56}Ni masses for a sample of SN Ia correlate with t_2. The ^{56}Ni mass is derived from the bolometric light curve, since the output flux at maximum light equals the instantaneous energy decay rate from ^{56}Ni [92]. The construction of the bolometric light curves to derive the peak bolometric flux includes correcting the observed magnitudes for reddening from the host galaxy dust. Recent studies with large samples of nearby SN Ia have shown that the mean total to selective absorption ratio (R_V) that is significantly smalller than the mean Milky Way value of 3.1. Hence, using a galactic R_V value would yield incorrect bolometric fluxes, and hence, ^{56}Ni masses. In order to circumvent this problem, we selected a "calibration" sample of SNe with low host galaxy extinction. For this sample, we find a strong correlation between the derived ^{56}Ni mass and t_2, implying that SNe with later t_2 produce more ^{56}Ni . This relation was also used to derive a distribution of bolometric luminosities (and ^{56}Ni masses) for all SNe with a measured t_2. More recent compilations of NIR light curves (e.g. CfAIR2 [5]) and ongoing/concluded NIR programs, e.g. Carnegie Supernova Project - II will allow us to create a larger sample of objects from which to derive the luminosity distributions.

Fast-declining SN Ia The analysis of the NIR second maximum and correlations with optical and bolometric properties, by design, excludes SNe with only a single peak in the NIR. SN Ia with a single NIR peak are typically intrinsically faint, fast-declining and show spectra similar to the prototypical SN 1991bg. We studied the Near Infrared and bolometric properties of these SNe to shed light on the properties of the progenitor and to understand whether they form a distinct sub-population of SN Ia or if they are simply a low-luminosity, fast-declining extension of normal SN Ia. The bolometric peak luminosity versus a "colour-stretch" ordering parameter appears to show a "break" for SNe with peak luminosities below $0.5 \cdot 10^{43}$ erg s^{-1}. Furthermore, reconstructing the total ejecta mass for these explosion points towards a sub-Chandrasekhar progenitor. Within this class of fast-declining objects, we find a range of ^{56}Ni

mass values for all SNe that can be explained by the sub-Chandra progenitor. This could point towards different explosion mechanisms leading to different fast-declining SN Ia. A larger sample of SNe with $\Delta m_{15}(B)$ >1.6 will be crucial to further elucidate whether these SNe are indeed different explosions. The analysis can be expanded to include spectroscopic properties which will offer key insights into the explosion mechanism and physical conditions in the ejecta.

.

Nebular Phase Properties Most of our previous analysis of SN Ia data concentrated on the phases upto 100 days from B-band maximum light. At phases $\sim$ 1 year after explosion, most of the γ rays escape the ejecta and the light curves are powered by energy deposited from the positrons. We observed SN 2014J, a nearby supernova in M82 at epochs between +400 and +500 days and obtained three Near Infrared spectra. The inferred ^{56}Ni mass from the forbidden iron lines was consistent with the inference from the γ-ray spectrum near maximum light ($\sim$ 0.6 $M_{\odot}$). The NIR spectra at late phases provide an independent estimate of the total to selective absorption ratio for the dust in the environment of the SN. The R_V estimate from the NIR spectra appears to be consistent with the Milky Way value of 3.1 despite the optical colours at maximum light preferring much lower values of $\sim$ 1.5. This presents clear evidence for non-standard dust properties in the region around SN 2014J.

Ejecta mass estimates Furthermore, we also reconstructed the total ejecta mass for normal SN Ia with sufficient late time optical and NIR coverage to derive an estimate for the transparency timescale from the exponential tail of the (pseudo-)bolometric light curve. The transparency timescales range between $\sim$ 26- 42 days implying a range of ejecta masses from 0.7 - 1.7 $M_{\odot}$. We confront the observed M_{ej}- $M_{^{56}Ni}$ observation with state of the art model tracks from different explosion scenarios. From our analysis, we find that a combination of two or more explosion channels would best explain the observed trend. Chandrasekhar mass delayed detonation models seem to best represent the bright, high ^{56}Ni mass SNe, whereas a combination of sub-Chandra explosion mechanisms could explain the low-^{56}Ni end of the distribution. In our analysis we use the same value of the input parameters for the Jeffrey model

for each SN. A detailed modelling of the bolometric light curve and an addition of spectral information could provide smaller errors on the final M_{ej} estimates and hence, be a better discriminant of the different explosion mechanisms. Moreover, using a template for the NIR (and in certain cases u-band) contribution as a function of phase and light curve width would be important to increase the sample size and hence have better statistics.

Cosmology with Future Observatories Low-redshift surveys of SN Ia in the Near Infrared have demonstrated their ability to measure distances precisely *without* requiring corrections for stretch or colour. Moreover, recent studies also demonstrated that even sparsely sampled light curves in the J and H bands can provide accurate distances. We investigated the potential use of NIR observations of SN Ia with future satellites to constrain cosmology and the time-variability of dark energy. We formulated a survey with three components: a low-z anchor, similar to the recently concluded NIR surveys, an intermediate redshift component using the Deep Drilling Fields for Euclid survey and a high-z lever from JWST. The DDF survey assumes very sparse sampling for each SN ($\sim$ 2-4 points) whereas the JWST observations assume only a *single* point per SN. The ability to measure a distance with only a single observations makes the NIR a lucrative channel to use SN Ia for cosmology. We find that for such sparse light curves, the prior information on the date of B-band maximum is required from a spectrum or an optical light curve. Contemporaneous transient surveys like WFIRST or LSST will provide such information for the SNe followed-up with JWST. An extension of this analysis could be to optimize an SN survey with WFIRST. A recent definition study report has shown that a WFIRST SN survey in the optical, combined with priors from Planck returns 1-σ errors of $\sim$ 0.4 on w_a [278]. A possible channel to optimise the constraints from the WFIRST SN survey would be to observe the SNe in the rest-frame Near Infrared. Since the magnitude limits for the WFIRST survey are deeper than the Euclid calibration fields, this would yield more precise individual distances to the SNe. Moreover, the WFIRST SNe can also be combined with the high-z arm from JWST to gain precise constraints from a combination of such SN surveys. Future surveys will also be critical to test alternate cosmological models e.g. Lemaitre-Tolman-Bondi models [35], Dvali-Gabadadze-Porrati (DGP) cosmology [66]. Another future direction for this investigation could involve a consistent model selec-

tion for different parametrisations of the dark energy equation of state for a combination of SN, BAO and CMB data.

Bibliography

[1] E. A. Ajhar, J. L. Tonry, J. P. Blakeslee, A. G. Riess, and B. P. Schmidt. Reconciliation of the Surface Brightness Fluctuation and Type Ia Supernova Distance Scales. ApJ, 559:584–591, Oct. 2001.

[2] R. Amanullah, A. Goobar, J. Johansson, D. P. K. Banerjee, V. Venkataraman, V. Joshi, N. M. Ashok, Y. Cao, M. M. Kasliwal, S. R. Kulkarni, P. E. Nugent, T. Petrushevska, and V. Stanishev. The Peculiar Extinction Law of SN 2014J Measured with the Hubble Space Telescope. ApJ, 788:L21, June 2014.

[3] R. Amanullah, J. Johansson, A. Goobar, R. Ferretti, S. Papadogiannakis, T. Petrushevska, P. J. Brown, Y. Cao, C. Contreras, H. Dahle, N. Elias-Rosa, J. P. U. Fynbo, J. Gorosabel, L. Guaita, L. Hangard, D. A. Howell, E. Y. Hsiao, E. Kankare, M. Kasliwal, G. Leloudas, P. Lundqvist, S. Mattila, P. Nugent, M. M. Phillips, A. Sandberg, V. Stanishev, M. Sullivan, F. Taddia, G. Östlin, S. Asadi, R. Herrero-Illana, J. J. Jensen, K. Karhunen, S. Lazarevic, E. Varenius, P. Santos, S. S. Sridhar, S. H. J. Wallström, and J. Wiegert. Diversity in extinction laws of Type Ia supernovae measured between 0.2 and 2 μm. MNRAS, 453:3300–3328, Nov. 2015.

[4] W. D. Arnett. A Possible Model of Supernovae: Detonation of ^{12}C. Ap&SS, 5:180–212, Oct. 1969.

[5] W. D. Arnett. Type I supernovae. I - Analytic solutions for the early part of the light curve. ApJ, 253:785–797, Feb. 1982.

[6] W. D. Arnett, D. Branch, and J. C. Wheeler. Hubble's constant and exploding carbon-oxygen white dwarf models for Type I supernovae. Nature, 314:337, Mar. 1985.

[7] C. Ashall, P. Mazzali, D. Bersier, S. Hachinger, M. Phillips, S. Percival, P. James, and K. Maguire. Photometric and spectroscopic observations, and abundance tomography modelling of the Type Ia supernova SN 2014J located in M82. MNRAS, 445:4427–4437, Dec. 2014.

[8] P. Astier, C. Balland, M. Brescia, E. Cappellaro, R. G. Carlberg, S. Cavuoti, M. Della Valle, E. Gangler, A. Goobar, J. Guy, D. Hardin, I. M. Hook, R. Kessler, A. Kim, E. Linder, G. Longo, K. Maguire, F. Mannucci, S. Mattila, R. Nichol, R. Pain, N. Regnault, S. Spiro, M. Sullivan, C. Tao, M. Turatto, X. F. Wang, and W. M. Wood-Vasey. Extending the supernova Hubble diagram to z ˜ 1.5 with the Euclid space mission. A&A, 572:A80, Dec. 2014.

[9] P. Astier, J. Guy, N. Regnault, R. Pain, E. Aubourg, D. Balam, S. Basa, R. G. Carlberg, S. Fabbro, D. Fouchez, I. M. Hook, D. A. Howell, H. Lafoux, J. D. Neill, N. Palanque-Delabrouille, K. Perrett, C. J. Pritchet, J. Rich, M. Sullivan, R. Taillet, G. Aldering, P. Antilogus, V. Arsenijevic, C. Balland, S. Baumont, J. Bronder, H. Courtois, R. S. Ellis, M. Filiol, A. C. Gonçalves, A. Goobar, D. Guide, D. Hardin, V. Lusset, C. Lidman, R. McMahon, M. Mouchet, A. Mourao, S. Perlmutter, P. Ripoche, C. Tao, and N. Walton. The Supernova Legacy Survey: measurement of Ω_M, Ω_{Lambda} and w from the first year data set. *å*, 447:31–48, Feb. 2006.

[10] É. Aubourg, S. Bailey, J. E. Bautista, F. Beutler, V. Bhardwaj, D. Bizyaev, M. Blanton, M. Blomqvist, A. S. Bolton, J. Bovy, H. Brewington, J. Brinkmann, J. R. Brownstein, A. Burden, N. G. Busca, W. Carithers, C.-H. Chuang, J. Comparat, R. A. C. Croft, A. J. Cuesta, K. S. Dawson, T. Delubac, D. J. Eisenstein, A. Font-Ribera, J. Ge, J.-M. Le Goff, S. G. A. Gontcho, J. R. Gott, J. E. Gunn, H. Guo, J. Guy, J.-C. Hamilton, S. Ho, K. Honscheid, C. Howlett, D. Kirkby, F. S. Kitaura, J.-P. Kneib, K.-G. Lee, D. Long, R. H. Lupton, M. V. Magaña, V. Malanushenko, E. Malanushenko, M. Manera, C. Maraston, D. Margala, C. K. McBride, J. Miralda-Escudé, A. D. Myers, R. C. Nichol, P. Noterdaeme, S. E. Nuza, M. D. Olmstead, D. Oravetz, I. Pâris, N. Padmanabhan, N. Palanque-Delabrouille, K. Pan, M. Pellejero-Ibanez, W. J. Percival, P. Petitjean, M. M. Pieri, F. Prada, B. Reid, J. Rich, N. A. Roe, A. J. Ross, N. P. Ross, G. Rossi, J. A. Rubiño-

Martín, A. G. Sánchez, L. Samushia, R. T. G. Santos, C. G. Scóccola, D. J. Schlegel, D. P. Schneider, H.-J. Seo, E. Sheldon, A. Simmons, R. A. Skibba, A. Slosar, M. A. Strauss, D. Thomas, J. L. Tinker, R. Tojeiro, J. A. Vazquez, M. Viel, D. A. Wake, B. A. Weaver, D. H. Weinberg, W. M. Wood-Vasey, C. Yèche, I. Zehavi, G.-B. Zhao, and BOSS Collaboration. Cosmological implications of baryon acoustic oscillation measurements. Phys. Rev. D, 92(12):123516, Dec. 2015.

[11] T. S. Axelrod. *Late time optical spectra from the Ni-56 model for Type 1 supernovae*. PhD thesis, California Univ., Santa Cruz., 1980.

[12] W. Baade and F. Zwicky. On Super-novae. *Proceedings of the National Academy of Science*, 20:254–259, May 1934.

[13] W. Baade and F. Zwicky. Photographic Light-Curves of the Two Supernovae in IC 4182 and NGC 1003. ApJ, 88:411, Nov. 1938.

[14] R. Barbon, F. Ciatti, and L. Rosino. On the light curve and properties of type I supernovae. A&A, 25:241–248, 1973.

[15] R. L. Barone-Nugent, C. Lidman, J. S. B. Wyithe, J. Mould, D. A. Howell, I. M. Hook, M. Sullivan, P. E. Nugent, I. Arcavi, S. B. Cenko, J. Cooke, A. Gal-Yam, E. Y. Hsiao, M. M. Kasliwal, K. Maguire, E. Ofek, D. Poznanski, and D. Xu. Near-infrared observations of Type Ia supernovae: the best known standard candle for cosmology. MNRAS, 425:1007–1012, Sept. 2012.

[16] S. Benetti, P. Meikle, M. Stehle, G. Altavilla, S. Desidera, G. Folatelli, A. Goobar, S. Mattila, J. Mendez, H. Navasardyan, A. Pastorello, F. Patat, M. Riello, P. Ruiz-Lapuente, D. Tsvetkov, M. Turatto, P. Mazzali, and W. Hillebrandt. Supernova 2002bo: inadequacy of the single parameter description. MNRAS, 348:261–278, Feb. 2004.

[17] C. L. Bennett, D. Larson, J. L. Weiland, N. Jarosik, G. Hinshaw, N. Odegard, K. M. Smith, R. S. Hill, B. Gold, M. Halpern, E. Komatsu, M. R. Nolta, L. Page, D. N. Spergel, E. Wollack, J. Dunkley, A. Kogut, M. Limon, S. S. Meyer, G. S. Tucker, and E. L. Wright. Nine-year Wilkinson Microwave Anisotropy Probe (WMAP) Observations: Final Maps and Results. ApJS, 208:20, Oct. 2013.

[18] W. Benz, F.-K. Thielemann, and J. G. Hills. Three-dimensional hydrodynamical simulations of stellar collisions. II - White dwarfs. ApJ, 342:986–998, July 1989.

[19] L. Bergström and A. Goobar. *Cosmology and Particle Astrophysics*. 2004.

[20] J. P. Bernstein, R. Kessler, S. Kuhlmann, R. Biswas, E. Kovacs, G. Aldering, I. Crane, C. B. D'Andrea, D. A. Finley, J. A. Frieman, T. Hufford, M. J. Jarvis, A. G. Kim, J. Marriner, P. Mukherjee, R. C. Nichol, P. Nugent, D. Parkinson, R. R. R. Reis, M. Sako, H. Spinka, and M. Sullivan. Supernova Simulations and Strategies for the Dark Energy Survey. ApJ, 753:152, July 2012.

[21] M. Betoule, R. Kessler, J. Guy, J. Mosher, D. Hardin, R. Biswas, P. Astier, P. El-Hage, M. Konig, S. Kuhlmann, J. Marriner, R. Pain, N. Regnault, C. Balland, B. A. Bassett, P. J. Brown, H. Campbell, R. G. Carlberg, F. Cellier-Holzem, D. Cinabro, A. Conley, C. B. D'Andrea, D. L. DePoy, M. Doi, R. S. Ellis, S. Fabbro, A. V. Filippenko, R. J. Foley, J. A. Frieman, D. Fouchez, L. Galbany, A. Goobar, R. R. Gupta, G. J. Hill, R. Hlozek, C. J. Hogan, I. M. Hook, D. A. Howell, S. W. Jha, L. Le Guillou, G. Leloudas, C. Lidman, J. L. Marshall, A. Möller, A. M. Mourão, J. Neveu, R. Nichol, M. D. Olmstead, N. Palanque-Delabrouille, S. Perlmutter, J. L. Prieto, C. J. Pritchet, M. Richmond, A. G. Riess, V. Ruhlmann-Kleider, M. Sako, K. Schahmaneche, D. P. Schneider, M. Smith, J. Sollerman, M. Sullivan, N. A. Walton, and C. J. Wheeler. Improved cosmological constraints from a joint analysis of the SDSS-II and SNLS supernova samples. *A&A*, 568:A22, Aug. 2014.

[22] M. Betoule, J. Marriner, N. Regnault, J.-C. Cuillandre, P. Astier, J. Guy, C. Balland, P. El Hage, D. Hardin, R. Kessler, L. Le Guillou, J. Mosher, R. Pain, P.-F. Rocci, M. Sako, and K. Schahmaneche. Improved photometric calibration of the SNLS and the SDSS supernova surveys. A&A, 552:A124, Apr. 2013.

[23] L. Bildsten, K. J. Shen, N. N. Weinberg, and G. Nelemans. Faint Thermonuclear Supernovae from AM Canum Venaticorum Binaries. ApJ, 662:L95–L98, June 2007.

[24] I. Biscardi, E. Brocato, A. Arkharov, E. Di Carlo, G. di Rico, M. Dolci, N. V. Efimova, A. Pietrinferni, and G. Valentini. The slowly declining type Ia supernova 2008fv and the near-infrared second maximum. A&A, 537:A57, Jan. 2012.

[25] S. Blondin. Constraints on the explosion mechanism and progenitors of Type Ia supernovae. In F. Martins, S. Boissier, V. Buat, L. Cambrésy, and P. Petit, editors, *SF2A-2015: Proceedings of the Annual meeting of the French Society of Astronomy and Astrophysics*, pages 319–323, Dec. 2015.

[26] S. Blondin, T. M. Davis, K. Krisciunas, B. P. Schmidt, J. Sollerman, W. M. Wood-Vasey, A. C. Becker, P. Challis, A. Clocchiatti, G. Damke, A. V. Filippenko, R. J. Foley, P. M. Garnavich, S. W. Jha, R. P. Kirshner, B. Leibundgut, W. Li, T. Matheson, G. Miknaitis, G. Narayan, G. Pignata, A. Rest, A. G. Riess, J. M. Silverman, R. C. Smith, J. Spyromilio, M. Stritzinger, C. W. Stubbs, N. B. Suntzeff, J. L. Tonry, B. E. Tucker, and A. Zenteno. Time Dilation in Type Ia Supernova Spectra at High Redshift. ApJ, 682:724–736, Aug. 2008.

[27] S. Blondin, L. Dessart, and D. J. Hillier. A one-dimensional Chandrasekhar-mass delayed-detonation model for the broad-lined Type Ia supernova 2002bo. MNRAS, 448:2766–2797, Apr. 2015.

[28] S. Blondin, L. Dessart, D. J. Hillier, and A. M. Khokhlov. One-dimensional delayed-detonation models of Type Ia supernovae: confrontation to observations at bolometric maximum. MNRAS, 429:2127–2142, Mar. 2013.

[29] S. Blondin, T. Matheson, R. P. Kirshner, K. S. Mandel, P. Berlind, M. Calkins, P. Challis, P. M. Garnavich, S. W. Jha, M. Modjaz, A. G. Riess, and B. P. Schmidt. The Spectroscopic Diversity of Type Ia Supernovae. AJ, 143:126, May 2012.

[30] L. N. Boldt, M. D. Stritzinger, C. Burns, E. Hsiao, M. M. Phillips, A. Goobar, G. H. Marion, and V. Stanishev. Near-Infrared K Corrections of Type Ia Supernovae and their Errors. PASP, 126:324–337, Apr. 2014.

[31] D. Branch. The Hubble constant from nickel radioactivity in type IA supernovae. ApJ, 392:35–40, June 1992.

[32] D. Branch. Type IA Supernovae and the Hubble Constant. ARA&A, 36:17–56, 1998.

[33] P. J. Brown, M. T. Smitka, L. Wang, A. Breeveld, M. de Pasquale, D. H. Hartmann, K. Krisciunas, N. P. Kuin, P. A. Milne, M. Page, and M. Siegel. Swift Ultraviolet Observations of Supernova 2014J in M82: Large Extinction from Interstellar Dust. ApJ, 805:74, May 2015.

[34] J. Buchner, A. Georgakakis, K. Nandra, L. Hsu, C. Rangel, M. Brightman, A. Merloni, M. Salvato, J. Donley, and D. Kocevski. X-ray spectral modelling of the AGN obscuring region in the CDFS: Bayesian model selection and catalogue. A&A, 564:A125, Apr. 2014.

[35] P. Bull, T. Clifton, and P. G. Ferreira. Kinematic Sunyaev-Zel'dovich effect as a test of general radial inhomogeneity in Lemaître-Tolman-Bondi cosmology. Phys. Rev. D, 85(2):024002, Jan. 2012.

[36] C. R. Burns, M. Stritzinger, M. M. Phillips, E. Y. Hsiao, C. Contreras, S. E. Persson, G. Folatelli, L. Boldt, A. Campillay, S. Castellón, W. L. Freedman, B. F. Madore, N. Morrell, F. Salgado, and N. B. Suntzeff. The Carnegie Supernova Project: Intrinsic Colors of Type Ia Supernovae. ApJ, 789:32, July 2014.

[37] C. R. Burns, M. Stritzinger, M. M. Phillips, S. Kattner, S. E. Persson, B. F. Madore, W. L. Freedman, L. Boldt, A. Campillay, C. Contreras, G. Folatelli, S. Gonzalez, W. Krzeminski, N. Morrell, F. Salgado, and N. B. Suntzeff. The Carnegie Supernova Project: Light-curve Fitting with SNooPy. AJ, 141:19, Jan. 2011.

[38] C. R. Burns, M. Stritzinger, M. M. Phillips, S. Kattner, S. E. Persson, B. F. Madore, W. L. Freedman, L. Boldt, A. Campillay, C. Contreras, G. Folatelli, S. Gonzalez, W. Krzeminski, N. Morrell, F. Salgado, and N. B. Suntzeff. SNooPy: TypeIa supernovae analysis tools. Astrophysics Source Code Library, May 2015.

[39] H. Campbell, M. Fraser, and G. Gilmore. How SN Ia host-galaxy properties affect cosmological parameters. MNRAS, 457:3470–3491, Apr. 2016.

[40] Y. Cao, J. Johansson, P. E. Nugent, A. Goobar, J. Nordin, S. R. Kulkarni, S. B. Cenko, O. Fox, M. M. Kasliwal, C. Fremling, R. Amanullah,

E. Y. Hsiao, D. A. Perley, B. D. Bue, F. J. Masci, W. H. Lee, and N. Chotard. An Intermediate Type Ia Supernova Between Normal And Super-Chandrasekhar. *ArXiv e-prints*, Jan. 2016.

[41] J. A. Cardelli, G. C. Clayton, and J. S. Mathis. The relationship between infrared, optical, and ultraviolet extinction. ApJ, 345:245–256, Oct. 1989.

[42] V. F. Cardone, S. Spiro, I. Hook, and R. Scaramella. Testing the distance duality relation with present and future data. Phys. Rev. D, 85(12):123510, June 2012.

[43] S. M. Carroll, W. H. Press, and E. L. Turner. The cosmological constant. ARA&A, 30:499–542, 1992.

[44] R. Cartier, M. Hamuy, G. Pignata, F. Förster, P. Zelaya, G. Folatelli, M. M. Phillips, N. Morrell, K. Krisciunas, N. B. Suntzeff, A. Clocchiatti, P. Coppi, C. Contreras, M. Roth, K. Koviak, J. Maza, L. González, S. González, and L. Huerta. Persistent C II Absorption in the Normal Type Ia Supernova 2002fk. ApJ, 789:89, July 2014.

[45] M. Chevallier and D. Polarski. Accelerating Universes with Scaling Dark Matter. *International Journal of Modern Physics D*, 10:213–223, 2001.

[46] M. J. Childress, D. J. Hillier, I. Seitenzahl, M. Sullivan, K. Maguire, S. Taubenberger, R. Scalzo, A. Ruiter, N. Blagorodnova, Y. Camacho, J. Castillo, N. Elias-Rosa, M. Fraser, A. Gal-Yam, M. Graham, D. A. Howell, C. Inserra, S. W. Jha, S. Kumar, P. A. Mazzali, C. McCully, A. Morales-Garoffolo, V. Pandya, J. Polshaw, B. Schmidt, S. Smartt, K. W. Smith, J. Sollerman, J. Spyromilio, B. Tucker, S. Valenti, N. Walton, C. Wolf, O. Yaron, D. R. Young, F. Yuan, and B. Zhang. Measuring nickel masses in Type Ia supernovae using cobalt emission in nebular phase spectra. MNRAS, 454:3816–3842, Dec. 2015.

[47] N. Chotard, E. Gangler, G. Aldering, P. Antilogus, C. Aragon, S. Bailey, C. Baltay, S. Bongard, C. Buton, A. Canto, M. Childress, Y. Copin, H. K. Fakhouri, E. Y. Hsiao, M. Kerschhaggl, M. Kowalski, S. Loken, P. Nugent, K. Paech, R. Pain, E. Pecontal, R. Pereira, S. Perlmutter, D. Rabinowitz, K. Runge, R. Scalzo, G. Smadja, C. Tao, R. C. Thomas,

B. A. Weaver, C. Wu, and Nearby Supernova Factory. The reddening law of type Ia supernovae: separating intrinsic variability from dust using equivalent widths. A&A, 529:L4, May 2011.

[48] E. Churazov, R. Sunyaev, J. Isern, I. Bikmaev, E. Bravo, N. Chugai, S. Grebenev, P. Jean, J. Knödlseder, F. Lebrun, and E. Kuulkers. Gamma-rays from Type Ia Supernova SN2014J. ApJ, 812:62, Oct. 2015.

[49] E. Churazov, R. Sunyaev, J. Isern, J. Knödlseder, P. Jean, F. Lebrun, N. Chugai, S. Grebenev, E. Bravo, S. Sazonov, and M. Renaud. Cobalt-56 γ-ray emission lines from the type Ia supernova 2014J. Nature, 512:406–408, Aug. 2014.

[50] A. Conley, J. Guy, M. Sullivan, N. Regnault, P. Astier, C. Balland, S. Basa, R. G. Carlberg, D. Fouchez, D. Hardin, I. M. Hook, D. A. Howell, R. Pain, N. Palanque-Delabrouille, K. M. Perrett, C. J. Pritchet, J. Rich, V. Ruhlmann-Kleider, D. Balam, S. Baumont, R. S. Ellis, S. Fabbro, H. K. Fakhouri, N. Fourmanoit, S. González-Gaitán, M. L. Graham, M. J. Hudson, E. Hsiao, T. Kronborg, C. Lidman, A. M. Mourao, J. D. Neill, S. Perlmutter, P. Ripoche, N. Suzuki, and E. S. Walker. Supernova Constraints and Systematic Uncertainties from the First Three Years of the Supernova Legacy Survey. ApJS, 192:1, Jan. 2011.

[51] A. Conley, D. A. Howell, A. Howes, M. Sullivan, P. Astier, D. Balam, S. Basa, R. G. Carlberg, D. Fouchez, J. Guy, I. Hook, J. D. Neill, R. Pain, K. Perrett, C. J. Pritchet, N. Regnault, J. Rich, R. Taillet, E. Aubourg, J. Bronder, R. S. Ellis, S. Fabbro, M. Filiol, D. Le Borgne, N. Palanque-Delabrouille, S. Perlmutter, and P. Ripoche. The Rise Time of Type Ia Supernovae from the Supernova Legacy Survey. AJ, 132:1707–1713, Oct. 2006.

[52] A. Conley, M. Sullivan, E. Y. Hsiao, J. Guy, P. Astier, D. Balam, C. Balland, S. Basa, R. G. Carlberg, D. Fouchez, D. Hardin, D. A. Howell, I. M. Hook, R. Pain, K. Perrett, C. J. Pritchet, and N. Regnault. SiFTO: An Empirical Method for Fitting SN Ia Light Curves. ApJ, 681:482–498, July 2008.

[53] G. Contardo, B. Leibundgut, and W. D. Vacca. Epochs of maximum light and bolometric light curves of type Ia supernovae. A&A, 359:876–886, July 2000.

[54] C. Contreras, M. Hamuy, M. M. Phillips, G. Folatelli, N. B. Suntzeff, S. E. Persson, M. Stritzinger, L. Boldt, S. González, W. Krzeminski, N. Morrell, M. Roth, F. Salgado, M. José Maureira, C. R. Burns, W. L. Freedman, B. F. Madore, D. Murphy, P. Wyatt, W. Li, and A. V. Filippenko. The Carnegie Supernova Project: First Photometry Data Release of Low-Redshift Type Ia Supernovae. AJ, 139:519–539, Feb. 2010.

[55] P. S. Corasaniti and A. Melchiorri. Testing cosmology with cosmic sound waves. Phys. Rev. D, 77(10):103507, May 2008.

[56] S. Dado and A. Dar. Analytical Expressions for Light Curves of Ordinary and Superluminous Type Ia Supernovae. ApJ, 809:32, Aug. 2015.

[57] T. M. Davis, L. Hui, J. A. Frieman, T. Haugbølle, R. Kessler, B. Sinclair, J. Sollerman, B. Bassett, J. Marriner, E. Mörtsell, R. C. Nichol, M. W. Richmond, M. Sako, D. P. Schneider, and M. Smith. The Effect of Peculiar Velocities on Supernova Cosmology. ApJ, 741:67, Nov. 2011.

[58] K. S. Dawson, G. Aldering, R. Amanullah, K. Barbary, L. F. Barrientos, M. Brodwin, N. Connolly, A. Dey, M. Doi, M. Donahue, P. Eisenhardt, E. Ellingson, L. Faccioli, V. Fadeyev, H. K. Fakhouri, A. S. Fruchter, D. G. Gilbank, M. D. Gladders, G. Goldhaber, A. H. Gonzalez, A. Goobar, A. Gude, T. Hattori, H. Hoekstra, X. Huang, Y. Ihara, B. T. Jannuzi, D. Johnston, K. Kashikawa, B. Koester, K. Konishi, M. Kowalski, C. Lidman, E. V. Linder, L. Lubin, J. Meyers, T. Morokuma, F. Munshi, C. Mullis, T. Oda, N. Panagia, S. Perlmutter, M. Postman, T. Pritchard, J. Rhodes, P. Rosati, D. Rubin, D. J. Schlegel, A. Spadafora, S. A. Stanford, V. Stanishev, D. Stern, M. Strovink, N. Suzuki, N. Takanashi, K. Tokita, M. Wagner, L. Wang, N. Yasuda, H. K. C. Yee, and T. Supernova Cosmology Project. An Intensive Hubble Space Telescope Survey for z>1 Type Ia Supernovae by Targeting Galaxy Clusters. AJ, 138:1271–1283, Nov. 2009.

[59] L. Dessart, D. J. Hillier, S. Blondin, and A. Khokhlov. Critical ingredients of Type Ia supernova radiative-transfer modelling. MNRAS, 441:3249–3270, July 2014.

[60] S. Dhawan, B. Leibundgut, J. Spyromilio, and S. Blondin. A reddening-free method to estimate the ^{56}Ni mass of Type Ia supernovae. A&A, 588:A84, Apr. 2016.

[61] S. Dhawan, B. Leibundgut, J. Spyromilio, and K. Maguire. Near-infrared light curves of Type Ia supernovae: studying properties of the second maximum. MNRAS, 448:1345–1359, Apr. 2015.

[62] T. R. Diamond, P. Hoeflich, and C. L. Gerardy. Late-time Near-infrared Observations of SN 2005df. ApJ, 806:107, June 2015.

[63] R. Diehl, T. Siegert, W. Hillebrandt, S. A. Grebenev, J. Greiner, M. Krause, M. Kromer, K. Maeda, F. Röpke, and S. Taubenberger. Early ^{56}Ni decay gamma rays from SN2014J suggest an unusual explosion. *Science*, 345:1162–1165, Sept. 2014.

[64] R. Diehl, T. Siegert, W. Hillebrandt, M. Krause, J. Greiner, K. Maeda, F. K. Röpke, S. A. Sim, W. Wang, and X. Zhang. SN2014J gamma rays from the ^{56}Ni decay chain. A&A, 574:A72, Feb. 2015.

[65] B. Dilday, M. Smith, B. Bassett, A. Becker, R. Bender, F. Castander, D. Cinabro, A. V. Filippenko, J. A. Frieman, L. Galbany, P. M. Garnavich, A. Goobar, U. Hopp, Y. Ihara, S. W. Jha, R. Kessler, H. Lampeitl, J. Marriner, R. Miquel, M. Mollá, R. C. Nichol, J. Nordin, A. G. Riess, M. Sako, D. P. Schneider, J. Sollerman, J. C. Wheeler, L. Östman, D. Bizyaev, H. Brewington, E. Malanushenko, V. Malanushenko, D. Oravetz, K. Pan, A. Simmons, and S. Snedden. Measurements of the Rate of Type Ia Supernovae at Redshift lsim0.3 from the Sloan Digital Sky Survey II Supernova Survey. ApJ, 713:1026–1036, Apr. 2010.

[66] G. Dvali, G. Gabadadze, and M. Porrati. 4D gravity on a brane in 5D Minkowski space. *Physics Letters B*, 485:208–214, July 2000.

[67] D. J. Eisenstein, I. Zehavi, D. W. Hogg, R. Scoccimarro, M. R. Blanton, R. C. Nichol, R. Scranton, H.-J. Seo, M. Tegmark, Z. Zheng, S. F. Anderson, J. Annis, N. Bahcall, J. Brinkmann, S. Burles, F. J. Castander, A. Connolly, I. Csabai, M. Doi, M. Fukugita, J. A. Frieman, K. Glazebrook, J. E. Gunn, J. S. Hendry, G. Hennessy, Z. Ivezić, S. Kent, G. R. Knapp, H. Lin, Y.-S. Loh, R. H. Lupton, B. Margon, T. A. McKay, A. Meiksin, J. A. Munn, A. Pope, M. W. Richmond, D. Schlegel, D. P. Schneider, K. Shimasaku, C. Stoughton, M. A. Strauss, M. SubbaRao, A. S. Szalay, I. Szapudi, D. L. Tucker, B. Yanny, and D. G. York. Detection of the Baryon Acoustic Peak in the Large-Scale Correlation Function of SDSS Luminous Red Galaxies. ApJ, 633:560–574, Nov. 2005.

[68] O. Elgarøy and T. Multamäki. On using the cosmic microwave background shift parameter in tests of models of dark energy. A&A, 471:65–70, Aug. 2007.

[69] J. H. Elias, J. A. Frogel, J. A. Hackwell, and S. E. Persson. Infrared light curves of Type I supernovae. ApJ, 251:L13–L16, Dec. 1981.

[70] J. H. Elias, K. Matthews, G. Neugebauer, and S. E. Persson. Type I supernovae in the infrared and their use as distance indicators. ApJ, 296:379–389, Sept. 1985.

[71] N. Elias-Rosa, S. Benetti, E. Cappellaro, M. Turatto, P. A. Mazzali, F. Patat, W. P. S. Meikle, M. Stehle, A. Pastorello, G. Pignata, R. Kotak, A. Harutyunyan, G. Altavilla, H. Navasardyan, Y. Qiu, M. Salvo, and W. Hillebrandt. Anomalous extinction behaviour towards the Type Ia SN 2003cg. MNRAS, 369:1880–1900, July 2006.

[72] G. F. R. Ellis. Relativistic cosmology - Its nature, aims and problems. In B. Bertotti, F. de Felice, and A. Pascolini, editors, *General Relativity and Gravitation Conference*, pages 215–288, 1984.

[73] K. Enqvist. Lemaitre Tolman Bondi model and accelerating expansion. *General Relativity and Gravitation*, 40:451–466, Feb. 2008.

[74] F. Feroz and M. P. Hobson. Multimodal nested sampling: an efficient and robust alternative to Markov Chain Monte Carlo methods for astronomical data analyses. MNRAS, 384:449–463, Feb. 2008.

[75] F. Feroz, M. P. Hobson, and M. Bridges. MULTINEST: an efficient and robust Bayesian inference tool for cosmology and particle physics. MNRAS, 398:1601–1614, Oct. 2009.

[76] A. V. Filippenko. Optical Spectra of Supernovae. ARA&A, 35:309–355, 1997.

[77] A. V. Filippenko, W. D. Li, R. R. Treffers, and M. Modjaz. The Lick Observatory Supernova Search with the Katzman Automatic Imaging Telescope. In B. Paczynski, W.-P. Chen, and C. Lemme, editors, *IAU Colloq. 183: Small Telescope Astronomy on Global Scales*, volume 246 of *Astronomical Society of the Pacific Conference Series*, page 121, 2001.

[78] A. V. Filippenko, M. W. Richmond, D. Branch, M. Gaskell, W. Herbst, C. H. Ford, R. R. Treffers, T. Matheson, L. C. Ho, A. Dey, W. L. W. Sargent, T. A. Small, and W. J. M. van Breugel. The subluminous, spectroscopically peculiar type IA supernova 1991bg in the elliptical galaxy NGC 4374. AJ, 104:1543–1556, Oct. 1992.

[79] A. V. Filippenko, M. W. Richmond, T. Matheson, J. C. Shields, E. M. Burbidge, R. D. Cohen, M. Dickinson, M. A. Malkan, B. Nelson, J. Pietz, D. Schlegel, P. Schmeer, H. Spinrad, C. C. Steidel, H. D. Tran, and W. Wren. The peculiar Type IA SN 1991T - Detonation of a white dwarf? ApJ, 384:L15–L18, Jan. 1992.

[80] M. Fink, F. K. Röpke, W. Hillebrandt, I. R. Seitenzahl, S. A. Sim, and M. Kromer. Double-detonation sub-Chandrasekhar supernovae: can minimum helium shell masses detonate the core? A&A, 514:A53, May 2010.

[81] R. E. Firth, M. Sullivan, A. Gal-Yam, D. A. Howell, K. Maguire, P. Nugent, A. L. Piro, C. Baltay, U. Feindt, E. Hadjiyksta, R. McKinnon, E. Ofek, D. Rabinowitz, and E. S. Walker. The rising light curves of Type Ia supernovae. MNRAS, 446:3895–3910, Feb. 2015.

[82] R. Fisher and K. Jumper. Single-degenerate Type Ia Supernovae Are Preferentially Overluminous. ApJ, 805:150, June 2015.

[83] G. Folatelli, N. Morrell, M. M. Phillips, E. Hsiao, A. Campillay, C. Contreras, S. Castellón, M. Hamuy, W. Krzeminski, M. Roth, M. Stritzinger, C. R. Burns, W. L. Freedman, B. F. Madore, D. Murphy, S. E. Persson, J. L. Prieto, N. B. Suntzeff, K. Krisciunas, J. P. Anderson, F. Förster, J. Maza, G. Pignata, P. A. Rojas, L. Boldt, F. Salgado, P. Wyatt, F. Olivares E., A. Gal-Yam, and M. Sako. Spectroscopy of Type Ia Supernovae by the Carnegie Supernova Project. ApJ, 773:53, Aug. 2013.

[84] G. Folatelli, M. M. Phillips, C. R. Burns, C. Contreras, M. Hamuy, W. L. Freedman, S. E. Persson, M. Stritzinger, N. B. Suntzeff, K. Krisciunas, L. Boldt, S. González, W. Krzeminski, N. Morrell, M. Roth, F. Salgado, B. F. Madore, D. Murphy, P. Wyatt, W. Li, A. V. Filippenko, and N. Miller. The Carnegie Supernova Project: Analysis of the First Sample of Low-Redshift Type-Ia Supernovae. AJ, 139:120–144, Jan. 2010.

[85] R. J. Foley, P. J. Challis, R. Chornock, M. Ganeshalingam, W. Li, G. H. Marion, N. I. Morrell, G. Pignata, M. D. Stritzinger, J. M. Silverman, X. Wang, J. P. Anderson, A. V. Filippenko, W. L. Freedman, M. Hamuy, S. W. Jha, R. P. Kirshner, C. McCully, S. E. Persson, M. M. Phillips, D. E. Reichart, and A. M. Soderberg. Type Iax Supernovae: A New Class of Stellar Explosion. ApJ, 767:57, Apr. 2013.

[86] R. J. Foley, O. D. Fox, C. McCully, M. M. Phillips, D. J. Sand, W. Zheng, P. Challis, A. V. Filippenko, G. Folatelli, W. Hillebrandt, E. Y. Hsiao, S. W. Jha, R. P. Kirshner, M. Kromer, G. H. Marion, M. Nelson, R. Pakmor, G. Pignata, F. K. Röpke, I. R. Seitenzahl, J. M. Silverman, M. Skrutskie, and M. D. Stritzinger. Extensive HST ultraviolet spectra and multiwavelength observations of SN 2014J in M82 indicate reddening and circumstellar scattering by typical dust. MNRAS, 443:2887–2906, Oct. 2014.

[87] F. Förster, S. González-Gaitán, G. Folatelli, and N. Morrell. On the Lira Law and the Nature of Extinction toward Type Ia Supernovae. ApJ, 772:19, July 2013.

[88] S. J. Fossey, B. Cooke, G. Pollack, M. Wilde, and T. Wright. Supernova 2014J in M82 = Psn J09554214+6940260. *Central Bureau Electronic Telegrams*, 3792, Jan. 2014.

[89] W. L. Freedman, C. R. Burns, M. M. Phillips, P. Wyatt, S. E. Persson, B. F. Madore, C. Contreras, G. Folatelli, E. S. Gonzalez, M. Hamuy, E. Hsiao, D. D. Kelson, N. Morrell, D. C. Murphy, M. Roth, M. Stritzinger, L. Sturch, N. B. Suntzeff, P. Astier, C. Balland, B. Bassett, L. Boldt, R. G. Carlberg, A. J. Conley, J. A. Frieman, P. M. Garnavich, J. Guy, D. Hardin, D. A. Howell, R. Kessler, H. Lampeitl, J. Marriner, R. Pain, K. Perrett, N. Regnault, A. G. Riess, M. Sako, D. P. Schneider, M. Sullivan, and M. Wood-Vasey. The Carnegie Supernova Project: First Near-Infrared Hubble Diagram to z ˜ 0.7. ApJ, 704:1036–1058, Oct. 2009.

[90] W. L. Freedman and B. F. Madore. The Hubble Constant. ARA&A, 48:673–710, Sept. 2010.

[91] W. L. Freedman, B. F. Madore, B. K. Gibson, L. Ferrarese, D. D. Kelson, S. Sakai, J. R. Mould, R. C. Kennicutt, Jr., H. C. Ford, J. A. Graham,

J. P. Huchra, S. M. G. Hughes, G. D. Illingworth, L. M. Macri, and P. B. Stetson. Final Results from the Hubble Space Telescope Key Project to Measure the Hubble Constant. ApJ, 553:47–72, May 2001.

[92] A. S. Friedman, W. M. Wood-Vasey, G. H. Marion, P. Challis, K. S. Mandel, J. S. Bloom, M. Modjaz, G. Narayan, M. Hicken, R. J. Foley, C. R. Klein, D. L. Starr, A. Morgan, A. Rest, C. H. Blake, A. A. Miller, E. E. Falco, W. F. Wyatt, J. Mink, M. F. Skrutskie, and R. P. Kirshner. CfAIR2: Near-infrared Light Curves of 94 Type Ia Supernovae. ApJS, 220:9, Sept. 2015.

[93] J. A. Frieman, B. Bassett, A. Becker, C. Choi, D. Cinabro, F. DeJongh, D. L. Depoy, B. Dilday, M. Doi, P. M. Garnavich, C. J. Hogan, J. Holtzman, M. Im, S. Jha, R. Kessler, K. Konishi, H. Lampeitl, J. Marriner, J. L. Marshall, D. McGinnis, G. Miknaitis, R. C. Nichol, J. L. Prieto, A. G. Riess, M. W. Richmond, R. Romani, M. Sako, D. P. Schneider, M. Smith, N. Takanashi, K. Tokita, K. van der Heyden, N. Yasuda, C. Zheng, J. Adelman-McCarthy, J. Annis, R. J. Assef, J. Barentine, R. Bender, R. D. Blandford, W. N. Boroski, M. Bremer, H. Brewington, C. A. Collins, A. Crotts, J. Dembicky, J. Eastman, A. Edge, E. Edmondson, E. Elson, M. E. Eyler, A. V. Filippenko, R. J. Foley, S. Frank, A. Goobar, T. Gueth, J. E. Gunn, M. Harvanek, U. Hopp, Y. Ihara, Ž. Ivezić, S. Kahn, J. Kaplan, S. Kent, W. Ketzeback, S. J. Kleinman, W. Kollatschny, R. G. Kron, J. Krzesiński, D. Lamenti, G. Leloudas, H. Lin, D. C. Long, J. Lucey, R. H. Lupton, E. Malanushenko, V. Malanushenko, R. J. McMillan, J. Mendez, C. W. Morgan, T. Morokuma, A. Nitta, L. Ostman, K. Pan, C. M. Rockosi, A. K. Romer, P. Ruiz-Lapuente, G. Saurage, K. Schlesinger, S. A. Snedden, J. Sollerman, C. Stoughton, M. Stritzinger, M. Subba Rao, D. Tucker, P. Vaisanen, L. C. Watson, S. Watters, J. C. Wheeler, B. Yanny, and D. York. The Sloan Digital Sky Survey-II Supernova Survey: Technical Summary. AJ, 135:338–347, Jan. 2008.

[94] J. A. Frieman, M. S. Turner, and D. Huterer. Dark Energy and the Accelerating Universe. ARA&A, 46:385–432, Sept. 2008.

[95] B. Friesen, E. Baron, J. P. Wisniewski, J. T. Parrent, R. C. Thomas, T. R. Miller, and G. H. Marion. Near-infrared Line Identification in

Type Ia Supernovae during the Transitional Phase. ApJ, 792:120, Sept. 2014.

[96] M. Ganeshalingam, W. Li, and A. V. Filippenko. The rise-time distribution of nearby Type Ia supernovae. MNRAS, 416:2607–2622, Oct. 2011.

[97] M. Ganeshalingam, W. Li, A. V. Filippenko, J. M. Silverman, R. Chornock, R. J. Foley, T. Matheson, R. P. Kirshner, P. Milne, M. Calkins, and K. J. Shen. The Low-velocity, Rapidly Fading Type Ia Supernova 2002es. ApJ, 751:142, June 2012.

[98] J. Gao, B. W. Jiang, A. Li, J. Li, and X. Wang. Physical Dust Models for the Extinction toward Supernova 2014J in M82. ApJ, 807:L26, July 2015.

[99] G. Garavini, S. Nobili, S. Taubenberger, A. Pastorello, N. Elias-Rosa, V. Stanishev, G. Blanc, S. Benetti, A. Goobar, P. A. Mazzali, S. F. Sanchez, M. Salvo, B. P. Schmidt, and W. Hillebrandt. ESC observations of SN 2005cf. II. Optical spectroscopy and the high-velocity features. A&A, 471:527–535, Aug. 2007.

[100] P. M. Garnavich, A. Z. Bonanos, K. Krisciunas, S. Jha, R. P. Kirshner, E. M. Schlegel, P. Challis, L. M. Macri, K. Hatano, D. Branch, G. D. Bothun, and W. L. Freedman. The Luminosity of SN 1999by in NGC 2841 and the Nature of "Peculiar" Type Ia Supernovae. ApJ, 613:1120–1132, Oct. 2004.

[101] M. Gilfanov and Á. Bogdán. An upper limit on the contribution of accreting white dwarfs to the typeIa supernova rate. Nature, 463:924–925, Feb. 2010.

[102] A. Goobar. Low R_V from Circumstellar Dust around Supernovae. ApJ, 686:L103, Oct. 2008.

[103] A. Goobar, J. Johansson, R. Amanullah, Y. Cao, D. A. Perley, M. M. Kasliwal, R. Ferretti, P. E. Nugent, C. Harris, A. Gal-Yam, E. O. Ofek, S. P. Tendulkar, M. Dennefeld, S. Valenti, I. Arcavi, D. P. K. Banerjee, V. Venkataraman, V. Joshi, N. M. Ashok, S. B. Cenko, R. F. Diaz,

C. Fremling, A. Horesh, D. A. Howell, S. R. Kulkarni, S. Papadogiannakis, T. Petrushevska, D. Sand, J. Sollerman, V. Stanishev, J. S. Bloom, J. Surace, T. J. Dupuy, and M. C. Liu. The Rise of SN 2014J in the Nearby Galaxy M82. ApJ, 784:L12, Mar. 2014.

[104] A. Goobar and B. Leibundgut. Supernova Cosmology: Legacy and Future. *Annual Review of Nuclear and Particle Science*, 61:251–279, Nov. 2011.

[105] J. Green, P. Schechter, C. Baltay, R. Bean, D. Bennett, R. Brown, C. Conselice, M. Donahue, X. Fan, B. S. Gaudi, C. Hirata, J. Kalirai, T. Lauer, B. Nichol, N. Padmanabhan, S. Perlmutter, B. Rauscher, J. Rhodes, T. Roellig, D. Stern, T. Sumi, A. Tanner, Y. Wang, D. Weinberg, E. Wright, N. Gehrels, R. Sambruna, W. Traub, J. Anderson, K. Cook, P. Garnavich, L. Hillenbrand, Z. Ivezic, E. Kerins, J. Lunine, P. McDonald, M. Penny, M. Phillips, G. Rieke, A. Riess, R. van der Marel, R. K. Barry, E. Cheng, D. Content, R. Cutri, R. Goullioud, K. Grady, G. Helou, C. Jackson, J. Kruk, M. Melton, C. Peddie, N. Rioux, and M. Seiffert. Wide-Field InfraRed Survey Telescope (WFIRST) Final Report. *ArXiv e-prints*, Aug. 2012.

[106] J. Guillochon, M. Dan, E. Ramirez-Ruiz, and S. Rosswog. Surface Detonations in Double Degenerate Binary Systems Triggered by Accretion Stream Instabilities. ApJ, 709:L64–L69, Jan. 2010.

[107] J. Guy, P. Astier, S. Baumont, D. Hardin, R. Pain, N. Regnault, S. Basa, R. G. Carlberg, A. Conley, S. Fabbro, D. Fouchez, I. M. Hook, D. A. Howell, K. Perrett, C. J. Pritchet, J. Rich, M. Sullivan, P. Antilogus, E. Aubourg, G. Bazin, J. Bronder, M. Filiol, N. Palanque-Delabrouille, P. Ripoche, and V. Ruhlmann-Kleider. SALT2: using distant supernovae to improve the use of type Ia supernovae as distance indicators. A&A, 466:11–21, Apr. 2007.

[108] J. Guy, P. Astier, S. Nobili, N. Regnault, and R. Pain. SALT: a spectral adaptive light curve template for type Ia supernovae. A&A, 443:781–791, Dec. 2005.

[109] J. Guy, M. Sullivan, A. Conley, N. Regnault, P. Astier, C. Balland, S. Basa, R. G. Carlberg, D. Fouchez, D. Hardin, I. M. Hook, D. A. Howell, R. Pain, N. Palanque-Delabrouille, K. M. Perrett, C. J. Pritchet,

J. Rich, V. Ruhlmann-Kleider, D. Balam, S. Baumont, R. S. Ellis, S. Fabbro, H. K. Fakhouri, N. Fourmanoit, S. González-Gaitán, M. L. Graham, E. Hsiao, T. Kronborg, C. Lidman, A. M. Mourao, S. Perlmutter, P. Ripoche, N. Suzuki, and E. S. Walker. The Supernova Legacy Survey 3-year sample: Type Ia supernovae photometric distances and cosmological constraints. A&A, 523:A7, Nov. 2010.

[110] S. Hachinger, P. A. Mazzali, S. Taubenberger, M. Fink, R. Pakmor, W. Hillebrandt, and I. R. Seitenzahl. Spectral modelling of the 'super-Chandrasekhar' Type Ia SN 2009dc - testing a 2 $M_{\odot}$ white dwarf explosion model and alternatives. MNRAS, 427:2057–2078, Dec. 2012.

[111] M. Hamuy, M. M. Phillips, N. B. Suntzeff, J. Maza, L. E. González, M. Roth, K. Krisciunas, N. Morrell, E. M. Green, S. E. Persson, and P. J. McCarthy. An asymptotic-giant-branch star in the progenitor system of a type Ia supernova. Nature, 424:651–654, Aug. 2003.

[112] M. Hamuy, M. M. Phillips, N. B. Suntzeff, R. A. Schommer, J. Maza, A. R. Antezan, M. Wischnjewsky, G. Valladares, C. Muena, L. E. Gonzales, R. Aviles, L. A. Wells, R. C. Smith, M. Navarrete, R. Covarrubias, G. M. Williger, A. R. Walker, A. C. Layden, J. H. Elias, J. A. Baldwin, M. Hernandez, H. Tirado, P. Ugarte, R. Elston, N. Saavedra, F. Barrientos, E. Costa, P. Lira, M. T. Ruiz, C. Anguita, X. Gomez, P. Ortiz, M. della Valle, J. Danziger, J. Storm, Y.-C. Kim, C. Bailyn, E. P. Rubenstein, D. Tucker, S. Cersosimo, R. A. Mendez, L. Siciliano, W. Sherry, B. Chaboyer, R. A. Koopmann, D. Geisler, A. Sarajedini, A. Dey, N. Tyson, R. M. Rich, R. Gal, R. Lamontagne, N. Caldwell, P. Guhathakurta, A. C. Phillips, P. Szkody, C. Prosser, L. C. Ho, R. McMahan, G. Baggley, K.-P. Cheng, R. Havlen, K. Wakamatsu, K. Janes, M. Malkan, F. Baganoff, P. Seitzer, M. Shara, C. Sturch, J. Hesser, A. N. P. Hartig, J. Hughes, D. Welch, T. B. Williams, H. Ferguson, P. J. Francis, L. French, M. Bolte, J. Roth, S. Odewahn, S. Howell, and W. Krzeminski. BVRI Light Curves for 29 Type IA Supernovae. AJ, 112:2408, Dec. 1996.

[113] M. Hamuy, M. M. Phillips, N. B. Suntzeff, R. A. Schommer, J. Maza, and R. Aviles. The Absolute Luminosities of the Calan/Tololo Type IA Supernovae. AJ, 112:2391, Dec. 1996.

[114] M. Hamuy, M. M. Phillips, N. B. Suntzeff, R. A. Schommer, J. Maza, and R. Aviles. The Hubble Diagram of the Calan/Tololo Type IA Supernovae and the Value of HO. AJ, 112:2398, Dec. 1996.

[115] M. Hamuy, M. M. Phillips, N. B. Suntzeff, R. A. Schommer, J. Maza, R. C. Smith, P. Lira, and R. Aviles. The Morphology of Type IA Supernovae Light Curves. AJ, 112:2438, Dec. 1996.

[116] M. Hamuy, S. C. Trager, P. A. Pinto, M. M. Phillips, R. A. Schommer, V. Ivanov, and N. B. Suntzeff. A Search for Environmental Effects on Type IA Supernovae. AJ, 120:1479–1486, Sept. 2000.

[117] B. T. Hayden, P. M. Garnavich, R. Kessler, J. A. Frieman, S. W. Jha, B. Bassett, D. Cinabro, B. Dilday, D. Kasen, J. Marriner, R. C. Nichol, A. G. Riess, M. Sako, D. P. Schneider, M. Smith, and J. Sollerman. The Rise and Fall of Type Ia Supernova Light Curves in the SDSS-II Supernova Survey. ApJ, 712:350–366, Mar. 2010.

[118] M. Hicken, P. Challis, S. Jha, R. P. Kirshner, T. Matheson, M. Modjaz, A. Rest, W. M. Wood-Vasey, G. Bakos, E. J. Barton, P. Berlind, A. Bragg, C. Briceño, W. R. Brown, N. Caldwell, M. Calkins, R. Cho, L. Ciupik, M. Contreras, K.-C. Dendy, A. Dosaj, N. Durham, K. Eriksen, G. Esquerdo, M. Everett, E. Falco, J. Fernandez, A. Gaba, P. Garnavich, G. Graves, P. Green, T. Groner, C. Hergenrother, M. J. Holman, V. Hradecky, J. Huchra, B. Hutchison, D. Jerius, A. Jordan, R. Kilgard, M. Krauss, K. Luhman, L. Macri, D. Marrone, J. McDowell, D. McIntosh, B. McNamara, T. Megeath, B. Mochejska, D. Munoz, J. Muzerolle, O. Naranjo, G. Narayan, M. Pahre, W. Peters, D. Peterson, K. Rines, B. Ripman, A. Roussanova, R. Schild, A. Sicilia-Aguilar, J. Sokoloski, K. Smalley, A. Smith, T. Spahr, K. Z. Stanek, P. Barmby, S. Blondin, C. W. Stubbs, A. Szentgyorgyi, M. A. P. Torres, A. Vaz, A. Vikhlinin, Z. Wang, M. Westover, D. Woods, and P. Zhao. CfA3: 185 Type Ia Supernova Light Curves from the CfA. ApJ, 700:331–357, July 2009.

[119] M. Hicken, P. Challis, R. P. Kirshner, A. Rest, C. E. Cramer, W. M. Wood-Vasey, G. Bakos, P. Berlind, W. R. Brown, N. Caldwell, M. Calkins, T. Currie, K. de Kleer, G. Esquerdo, M. Everett, E. Falco, J. Fernandez, A. S. Friedman, T. Groner, J. Hartman, M. J. Holman, R. Hutchins, S. Keys, D. Kipping, D. Latham, G. H. Marion, G. Narayan,

M. Pahre, A. Pal, W. Peters, G. Perumpilly, B. Ripman, B. Sipocz, A. Szentgyorgyi, S. Tang, M. A. P. Torres, A. Vaz, S. Wolk, and A. Zezas. CfA4: Light Curves for 94 Type Ia Supernovae. ApJS, 200:12, June 2012.

[120] W. Hillebrandt, M. Kromer, F. K. Röpke, and A. J. Ruiter. Towards an understanding of Type Ia supernovae from a synthesis of theory and observations. *Frontiers of Physics*, 8:116–143, Apr. 2013.

[121] W. Hillebrandt and J. C. Niemeyer. Type IA Supernova Explosion Models. ARA&A, 38:191–230, 2000.

[122] P. Hoeflich, A. M. Khokhlov, and J. C. Wheeler. Delayed detonation models for normal and subluminous type IA sueprnovae: Absolute brightness, light curves, and molecule formation. ApJ, 444:831–847, May 1995.

[123] P. Höflich, C. L. Gerardy, R. A. Fesen, and S. Sakai. Infrared Spectra of the Subluminous Type Ia Supernova SN 1999by. ApJ, 568:791–806, Apr. 2002.

[124] P. Höflich, C. L. Gerardy, K. Nomoto, K. Motohara, R. A. Fesen, K. Maeda, T. Ohkubo, and N. Tominaga. Signature of Electron Capture in Iron-rich Ejecta of SN 2003du. ApJ, 617:1258–1266, Dec. 2004.

[125] I. M. Hook. Supernovae and cosmology with future European facilities. *Philosophical Transactions of the Royal Society of London Series A*, 371, Apr. 2013.

[126] A. Horesh, S. R. Kulkarni, D. B. Fox, J. Carpenter, M. M. Kasliwal, E. O. Ofek, R. Quimby, A. Gal-Yam, S. B. Cenko, A. G. de Bruyn, A. Kamble, R. A. M. J. Wijers, A. J. van der Horst, C. Kouveliotou, P. Podsiadlowski, M. Sullivan, K. Maguire, D. A. Howell, P. E. Nugent, N. Gehrels, N. M. Law, D. Poznanski, and M. Shara. Early Radio and X-Ray Observations of the Youngest nearby Type Ia Supernova PTF 11kly (SN 2011fe). ApJ, 746:21, Feb. 2012.

[127] D. A. Howell, P. Höflich, L. Wang, and J. C. Wheeler. Evidence for Asphericity in a Subluminous Type Ia Supernova: Spectropolarimetry of SN 1999by. ApJ, 556:302–321, July 2001.

[128] D. A. Howell, M. Sullivan, E. F. Brown, A. Conley, D. Le Borgne, E. Y. Hsiao, P. Astier, D. Balam, C. Balland, S. Basa, R. G. Carlberg, D. Fouchez, J. Guy, D. Hardin, I. M. Hook, R. Pain, K. Perrett, C. J. Pritchet, N. Regnault, S. Baumont, J. LeDu, C. Lidman, S. Perlmutter, N. Suzuki, E. S. Walker, and J. C. Wheeler. The Effect of Progenitor Age and Metallicity on Luminosity and ^{56}Ni Yield in Type Ia Supernovae. ApJ, 691:661–671, Jan. 2009.

[129] D. A. Howell, M. Sullivan, P. E. Nugent, R. S. Ellis, A. J. Conley, D. Le Borgne, R. G. Carlberg, J. Guy, D. Balam, S. Basa, D. Fouchez, I. M. Hook, E. Y. Hsiao, J. D. Neill, R. Pain, K. M. Perrett, and C. J. Pritchet. The type Ia supernova SNLS-03D3bb from a super-Chandrasekhar-mass white dwarf star. Nature, 443:308–311, Sept. 2006.

[130] F. Hoyle and W. A. Fowler. Nucleosynthesis in Supernovae. ApJ, 132:565, Nov. 1960.

[131] E. Y. Hsiao, C. R. Burns, C. Contreras, P. Höflich, D. Sand, G. H. Marion, M. M. Phillips, M. Stritzinger, S. González-Gaitán, R. E. Mason, G. Folatelli, E. Parent, C. Gall, R. Amanullah, G. C. Anupama, I. Arcavi, D. P. K. Banerjee, Y. Beletsky, G. A. Blanc, J. S. Bloom, P. J. Brown, A. Campillay, Y. Cao, A. De Cia, T. Diamond, W. L. Freedman, C. Gonzalez, A. Goobar, S. Holmbo, D. A. Howell, J. Johansson, M. M. Kasliwal, R. P. Kirshner, K. Krisciunas, S. R. Kulkarni, K. Maguire, P. A. Milne, N. Morrell, P. E. Nugent, E. O. Ofek, D. Osip, P. Palunas, D. A. Perley, S. E. Persson, A. L. Piro, M. Rabus, M. Roth, J. M. Schiefelbein, S. Srivastav, M. Sullivan, N. B. Suntzeff, J. Surace, P. R. Woźniak, and O. Yaron. Strong near-infrared carbon in the Type Ia supernova iPTF13ebh. A&A, 578:A9, June 2015.

[132] E. Y. Hsiao, A. Conley, D. A. Howell, M. Sullivan, C. J. Pritchet, R. G. Carlberg, P. E. Nugent, and M. M. Phillips. K-Corrections and Spectral Templates of Type Ia Supernovae. ApJ, 663:1187–1200, July 2007.

[133] W. Hu and N. Sugiyama. Small-Scale Cosmological Perturbations: an Analytic Approach. ApJ, 471:542, Nov. 1996.

[134] E. Hubble. A Relation between Distance and Radial Velocity among Extra-Galactic Nebulae. *Proceedings of the National Academy of Science*, 15:168–173, Mar. 1929.

[135] I. Iben, Jr. and A. V. Tutukov. Supernovae of type I as end products of the evolution of binaries with components of moderate initial mass (M not greater than about 9 solar masses). ApJS, 54:335–372, Feb. 1984.

[136] I. Iben, Jr. and A. V. Tutukov. On the evolution of close binaries with components of initial mass between 3 solar masses and 12 solar masses. ApJS, 58:661–710, Aug. 1985.

[137] D. Jack, P. H. Hauschildt, and E. Baron. Near-infrared light curves of type Ia supernovae. A&A, 538:A132, Feb. 2012.

[138] H. K. Jassal, J. S. Bagla, and T. Padmanabhan. WMAP constraints on low redshift evolution of dark energy. MNRAS, 356:L11–L16, Jan. 2005.

[139] D. J. Jeffery. Radioactive Decay Energy Deposition in Supernovae and the Exponential/Quasi-Exponential Behavior of Late-Time Supernova Light Curves. *ArXiv Astrophysics e-prints*, July 1999.

[140] J. B. Jensen, J. L. Tonry, B. J. Barris, R. I. Thompson, M. C. Liu, M. J. Rieke, E. A. Ajhar, and J. P. Blakeslee. Measuring Distances and Probing the Unresolved Stellar Populations of Galaxies Using Infrared Surface Brightness Fluctuations. ApJ, 583:712–726, Feb. 2003.

[141] S. Jha, D. Branch, R. Chornock, R. J. Foley, W. Li, B. J. Swift, D. Casebeer, and A. V. Filippenko. Late-Time Spectroscopy of SN 2002cx: The Prototype of a New Subclass of Type Ia Supernovae. AJ, 132:189–196, July 2006.

[142] S. Jha, A. G. Riess, and R. P. Kirshner. Improved Distances to Type Ia Supernovae with Multicolor Light-Curve Shapes: MLCS2k2. ApJ, 659:122–148, Apr. 2007.

[143] J. Jönsson, M. Sullivan, I. Hook, S. Basa, R. Carlberg, A. Conley, D. Fouchez, D. A. Howell, K. Perrett, and C. Pritchet. Constraining dark matter halo properties using lensed Supernova Legacy Survey supernovae. MNRAS, 405:535–544, June 2010.

[144] S. Justham. Single-degenerate Type Ia Supernovae Without Hydrogen Contamination. ApJ, 730:L34, Apr. 2011.

[145] P. Kahabka and E. P. J. van den Heuvel. Luminous Supersoft X-Ray Sources. ARA&A, 35:69–100, 1997.

[146] I. D. Karachentsev and O. G. Kashibadze. Masses of the local group and of the M81 group estimated from distortions in the local velocity field. *Astrophysics*, 49:3–18, Jan. 2006.

[147] D. Kasen. Secondary Maximum in the Near-Infrared Light Curves of Type Ia Supernovae. ApJ, 649:939–953, Oct. 2006.

[148] D. Kasen, F. K. Röpke, and S. E. Woosley. The diversity of type Ia supernovae from broken symmetries. Nature, 460:869–872, Aug. 2009.

[149] D. Kasen and S. E. Woosley. On the Origin of the Type Ia Supernova Width-Luminosity Relation. ApJ, 656:661–665, Feb. 2007.

[150] M. M. Kasliwal, E. O. Ofek, A. Gal-Yam, A. Rau, P. J. Brown, S. B. Cenko, P. B. Cameron, R. Quimby, S. R. Kulkarni, L. Bildsten, P. Milne, and G. Bryngelson. SN 2007ax: An Extremely Faint Type Ia Supernova. ApJ, 683:L29, Aug. 2008.

[151] S. Kattner, D. C. Leonard, C. R. Burns, M. M. Phillips, G. Folatelli, N. Morrell, M. D. Stritzinger, M. Hamuy, W. L. Freedman, S. E. Persson, M. Roth, and N. B. Suntzeff. The Standardizability of Type Ia Supernovae in the Near-Infrared: Evidence for a Peak-Luminosity Versus Decline-Rate Relation in the Near-Infrared. PASP, 124:114–127, Feb. 2012.

[152] K. S. Kawabata, H. Akitaya, M. Yamanaka, R. Itoh, K. Maeda, Y. Moritani, T. Ui, M. Kawabata, K. Mori, D. Nogami, K. Nomoto, N. Suzuki, K. Takaki, M. Tanaka, I. Ueno, S. Chiyonobu, T. Harao, R. Matsui, H. Miyamoto, O. Nagae, A. Nakashima, H. Nakaya, Y. Ohashi, T. Ohsugi, T. Komatsu, K. Sakimoto, M. Sasada, H. Sato, H. Tanaka, T. Urano, T. Yamashita, M. Yoshida, A. Arai, N. Ebisuda, Y. Fukazawa, A. Fukui, O. Hashimoto, S. Honda, H. Izumiura, Y. Kanda, K. Kawaguchi, N. Kawai, D. Kuroda, K. Masumoto, K. Matsumoto, T. Nakaoka, K. Takata, M. Uemura, and K. Yanagisawa. Optical and Near-infrared Polarimetry of Highly Reddened Type Ia Supernova 2014J: Peculiar Properties of Dust in M82. ApJ, 795:L4, Nov. 2014.

[153] P. L. Kelly, M. Hicken, D. L. Burke, K. S. Mandel, and R. P. Kirshner. Hubble Residuals of Nearby Type Ia Supernovae are Correlated with Host Galaxy Masses. ApJ, 715:743–756, June 2010.

[154] R. Kessler, A. C. Becker, D. Cinabro, J. Vanderplas, J. A. Frieman, J. Marriner, T. M. Davis, B. Dilday, J. Holtzman, S. W. Jha, H. Lampeitl, M. Sako, M. Smith, C. Zheng, R. C. Nichol, B. Bassett, R. Bender, D. L. Depoy, M. Doi, E. Elson, A. V. Filippenko, R. J. Foley, P. M. Garnavich, U. Hopp, Y. Ihara, W. Ketzeback, W. Kollatschny, K. Konishi, J. L. Marshall, R. J. McMillan, G. Miknaitis, T. Morokuma, E. Mörtsell, K. Pan, J. L. Prieto, M. W. Richmond, A. G. Riess, R. Romani, D. P. Schneider, J. Sollerman, N. Takanashi, K. Tokita, K. van der Heyden, J. C. Wheeler, N. Yasuda, and D. York. First-Year Sloan Digital Sky Survey-II Supernova Results: Hubble Diagram and Cosmological Parameters. ApJS, 185:32–84, Nov. 2009.

[155] A. Khokhlov, E. Mueller, and P. Hoeflich. Light curves of Type IA supernova models with different explosion mechanisms. A&A, 270:223–248, Mar. 1993.

[156] A. M. Khokhlov. Delayed detonation model for type IA supernovae. A&A, 245:114–128, May 1991.

[157] E. Komatsu, J. Dunkley, M. R. Nolta, C. L. Bennett, B. Gold, G. Hinshaw, N. Jarosik, D. Larson, M. Limon, L. Page, D. N. Spergel, M. Halpern, R. S. Hill, A. Kogut, S. S. Meyer, G. S. Tucker, J. L. Weiland, E. Wollack, and E. L. Wright. Five-Year Wilkinson Microwave Anisotropy Probe Observations: Cosmological Interpretation. ApJS, 180:330–376, Feb. 2009.

[158] E. Komatsu, K. M. Smith, J. Dunkley, C. L. Bennett, B. Gold, G. Hinshaw, N. Jarosik, D. Larson, M. R. Nolta, L. Page, D. N. Spergel, M. Halpern, R. S. Hill, A. Kogut, M. Limon, S. S. Meyer, N. Odegard, G. S. Tucker, J. L. Weiland, E. Wollack, and E. L. Wright. Seven-year Wilkinson Microwave Anisotropy Probe (WMAP) Observations: Cosmological Interpretation. ApJS, 192:18, Feb. 2011.

[159] C. T. Kowal. Absolute magnitudes of supernovae. AJ, 73:1021–1024, Dec. 1968.

[160] C. Kozma, C. Fransson, W. Hillebrandt, C. Travaglio, J. Sollerman, M. Reinecke, F. K. Röpke, and J. Spyromilio. Three-dimensional modeling of type Ia supernovae - The power of late time spectra. A&A, 437:983–995, July 2005.

[161] K. Krisciunas, P. M. Garnavich, V. Stanishev, N. B. Suntzeff, J. L. Prieto, J. Espinoza, D. Gonzalez, M. E. Salvo, N. Elias de la Rosa, S. J. Smartt, J. R. Maund, and R.-P. Kudritzki. The Type Ia Supernova 2004S, a Clone of SN 2001el, and the Optimal Photometric Bands for Extinction Estimation. AJ, 133:58–72, Jan. 2007.

[162] K. Krisciunas, G. H. Marion, N. B. Suntzeff, G. Blanc, F. Bufano, P. Candia, R. Cartier, N. Elias-Rosa, J. Espinoza, D. Gonzalez, L. Gonzalez, S. Gonzalez, S. D. Gooding, M. Hamuy, E. A. Knox, P. A. Milne, N. Morrell, M. M. Phillips, M. Stritzinger, and J. Thomas-Osip. The Fast Declining Type Ia Supernova 2003gs, and Evidence for a Significant Dispersion in Near-Infrared Absolute Magnitudes of Fast Decliners at Maximum Light. AJ, 138:1584–1596, Dec. 2009.

[163] K. Krisciunas, M. M. Phillips, and N. B. Suntzeff. Hubble Diagrams of Type Ia Supernovae in the Near-Infrared. ApJ, 602:L81–L84, Feb. 2004.

[164] K. Krisciunas, M. M. Phillips, N. B. Suntzeff, S. E. Persson, M. Hamuy, R. Antezana, P. Candia, A. Clocchiatti, D. L. DePoy, L. M. Germany, L. Gonzalez, S. Gonzalez, W. Krzeminski, J. Maza, P. E. Nugent, Y. Qiu, A. Rest, M. Roth, M. Stritzinger, L.-G. Strolger, I. Thompson, T. B. Williams, and M. Wischnjewsky. Optical and Infrared Photometry of the Nearby Type Ia Supernovae 1999ee, 2000bh, 2000ca, and 2001ba. AJ, 127:1664–1681, Mar. 2004.

[165] K. Krisciunas, J. L. Prieto, P. M. Garnavich, J.-L. G. Riley, A. Rest, C. Stubbs, and R. McMillan. Photometry of the Type Ia Supernovae 1999cc, 1999cl, and 2000cf. AJ, 131:1639–1647, Mar. 2006.

[166] K. Krisciunas, N. B. Suntzeff, M. M. Phillips, P. Candia, J. L. Prieto, R. Antezana, R. Chassagne, H.-W. Chen, M. Dickinson, P. R. Eisenhardt, J. Espinoza, P. M. Garnavich, D. González, T. E. Harrison, M. Hamuy, V. D. Ivanov, W. Krzemiński, C. Kulesa, P. McCarthy, A. Moro-Martín, C. Muena, A. Noriega-Crespo, S. E. Persson, P. A.

Pinto, M. Roth, E. P. Rubenstein, S. A. Stanford, G. S. Stringfellow, A. Zapata, A. Porter, and M. Wischnjewsky. Optical and Infrared Photometry of the Type Ia Supernovae 1991T, 1991bg, 1999ek, 2001bt, 2001cn, 2001cz, and 2002bo. AJ, 128:3034–3052, Dec. 2004.

[167] M. Kromer, S. T. Ohlmann, R. Pakmor, A. J. Ruiter, W. Hillebrandt, K. S. Marquardt, F. K. Röpke, I. R. Seitenzahl, S. A. Sim, and S. Taubenberger. Deflagrations in hybrid CONe white dwarfs: a route to explain the faint Type Iax supernova 2008ha. MNRAS, 450:3045–3053, July 2015.

[168] M. Kromer and S. A. Sim. Time-dependent three-dimensional spectrum synthesis for Type Ia supernovae. MNRAS, 398:1809–1826, Oct. 2009.

[169] M. Kromer, S. A. Sim, M. Fink, F. K. Röpke, I. R. Seitenzahl, and W. Hillebrandt. Double-detonation Sub-Chandrasekhar Supernovae: Synthetic Observables for Minimum Helium Shell Mass Models. ApJ, 719:1067–1082, Aug. 2010.

[170] M. J. Kuchner, R. P. Kirshner, P. A. Pinto, and B. Leibundgut. Evidence for Ni-56 yields Co-56 yields Fe-56 decay in type IA supernovae. ApJ, 426:89–92, May 1994.

[171] R. Laureijs, J. Amiaux, S. Arduini, J. . Augueres, J. Brinchmann, R. Cole, M. Cropper, C. Dabin, L. Duvet, A. Ealet, and et al. Euclid Definition Study Report. *ArXiv e-prints*, Oct. 2011.

[172] J. Leaman, W. Li, R. Chornock, and A. V. Filippenko. Nearby supernova rates from the Lick Observatory Supernova Search - I. The methods and data base. MNRAS, 412:1419–1440, Apr. 2011.

[173] B. Leibundgut. *Light curves of supernovae type, I.* PhD thesis, PhD thesis. Univ. Basel.137 pp. , (1988), 1988.

[174] B. Leibundgut. Type Ia Supernovae. A&A Rev., 10:179–209, 2000.

[175] B. Leibundgut, R. P. Kirshner, M. M. Phillips, L. A. Wells, N. B. Suntzeff, M. Hamuy, R. A. Schommer, A. R. Walker, L. Gonzalez, P. Ugarte, R. E. Williams, G. Williger, M. Gomez, R. Marzke, B. P. Schmidt, B. Whitney, N. Coldwell, J. Peters, F. H. Chaffee, C. B. Foltz,

D. Rehner, L. Siciliano, T. G. Barnes, K.-P. Cheng, P. M. N. Hintzen, Y.-C. Kim, J. Maza, J. W. Parker, A. C. Porter, P. C. Schmidtke, and G. Sonneborn. SN 1991bg - A type IA supernova with a difference. AJ, 105:301–313, Jan. 1993.

[176] B. Leibundgut, R. Schommer, M. Phillips, A. Riess, B. Schmidt, J. Spyromilio, J. Walsh, N. Suntzeff, M. Hamuy, J. Maza, R. P. Kirshner, P. Challis, P. Garnavich, R. C. Smith, A. Dressler, and R. Ciardullo. Time Dilation in the Light Curve of the Distant Type IA Supernova SN 1995K. ApJ, 466:L21, July 1996.

[177] G. Leloudas, M. D. Stritzinger, J. Sollerman, C. R. Burns, C. Kozma, K. Krisciunas, J. R. Maund, P. Milne, A. V. Filippenko, C. Fransson, M. Ganeshalingam, M. Hamuy, W. Li, M. M. Phillips, B. P. Schmidt, J. Skottfelt, S. Taubenberger, L. Boldt, J. P. U. Fynbo, L. Gonzalez, M. Salvo, and J. Thomas-Osip. The normal Type Ia SN 2003hv out to very late phases. A&A, 505:265–279, Oct. 2009.

[178] G. Lemaître. Un Univers homogène de masse constante et de rayon croissant rendant compte de la vitesse radiale des nébuleuses extra-galactiques. *Annales de la Société Scientifique de Bruxelles*, 47:49–59, 1927.

[179] W. Li, A. V. Filippenko, R. Chornock, E. Berger, P. Berlind, M. L. Calkins, P. Challis, C. Fassnacht, S. Jha, R. P. Kirshner, T. Matheson, W. L. W. Sargent, R. A. Simcoe, G. H. Smith, and G. Squires. SN 2002cx: The Most Peculiar Known Type Ia Supernova. PASP, 115:453–473, Apr. 2003.

[180] W. Li, A. V. Filippenko, E. Gates, R. Chornock, A. Gal-Yam, E. O. Ofek, D. C. Leonard, M. Modjaz, R. M. Rich, A. G. Riess, and R. R. Treffers. The Unique Type Ia Supernova 2000cx in NGC 524. PASP, 113:1178–1204, Oct. 2001.

[181] W. Li, J. Leaman, R. Chornock, A. V. Filippenko, D. Poznanski, M. Ganeshalingam, X. Wang, M. Modjaz, S. Jha, R. J. Foley, and N. Smith. Nearby supernova rates from the Lick Observatory Supernova Search - II. The observed luminosity functions and fractions of supernovae in a complete sample. MNRAS, 412:1441–1472, Apr. 2011.

[182] E. V. Linder. Exploring the Expansion History of the Universe. *Physical Review Letters*, 90(9):091301, Mar. 2003.

[183] P. Lira. Light curves of the supernovae 1990N and 1990T. Master's thesis, MS thesis. Univ. Chile (1996), 1996.

[184] W. Liu, D. J. Jeffery, and D. R. Schultz. Nebular Spectra of Type IA Supernovae. ApJ, 483:L107–L110, July 1997.

[185] M. Livio. The Progenitors of Type Ia Supernovae. In J. C. Niemeyer and J. W. Truran, editors, *Type Ia Supernovae, Theory and Cosmology*, page 33, 2000.

[186] M. Livio and J. W. Truran. Type I supernovae and accretion-induced collapses from cataclysmic variables? ApJ, 389:695–703, Apr. 1992.

[187] LSST Science Collaboration, P. A. Abell, J. Allison, S. F. Anderson, J. R. Andrew, J. R. P. Angel, L. Armus, D. Arnett, S. J. Asztalos, T. S. Axelrod, and et al. LSST Science Book, Version 2.0. *ArXiv e-prints*, Dec. 2009.

[188] K. Lundmark. Nebulæ, The motions and the distances of spiral. MNRAS, 85:865, June 1925.

[189] K. Maeda, S. Benetti, M. Stritzinger, F. K. Röpke, G. Folatelli, J. Sollerman, S. Taubenberger, K. Nomoto, G. Leloudas, M. Hamuy, M. Tanaka, P. A. Mazzali, and N. Elias-Rosa. An asymmetric explosion as the origin of spectral evolution diversity in type Ia supernovae. Nature, 466:82–85, July 2010.

[190] K. Maeda, G. Leloudas, S. Taubenberger, M. Stritzinger, J. Sollerman, N. Elias-Rosa, S. Benetti, M. Hamuy, G. Folatelli, and P. A. Mazzali. Effects of the explosion asymmetry and viewing angle on the Type Ia supernova colour and luminosity calibration. MNRAS, 413:3075–3094, June 2011.

[191] K. Maguire, M. Sullivan, F. Patat, A. Gal-Yam, I. M. Hook, S. Dhawan, D. A. Howell, P. Mazzali, P. E. Nugent, Y.-C. Pan, P. Podsiadlowski, J. D. Simon, A. Sternberg, S. Valenti, C. Baltay, D. Bersier, N. Blagorodnova, T.-W. Chen, N. Ellman, U. Feindt, F. Förster, M. Fraser,

S. González-Gaitán, M. L. Graham, C. Gutiérrez, S. Hachinger, E. Hadjiyska, C. Inserra, C. Knapic, R. R. Laher, G. Leloudas, S. Margheim, R. McKinnon, M. Molinaro, N. Morrell, E. O. Ofek, D. Rabinowitz, A. Rest, D. Sand, R. Smareglia, S. J. Smartt, F. Taddia, E. S. Walker, N. A. Walton, and D. R. Young. A statistical analysis of circumstellar material in Type Ia supernovae. MNRAS, 436:222–240, Nov. 2013.

[192] K. Maguire, S. Taubenberger, M. Sullivan, and P. A. Mazzali. Searching for swept-up hydrogen and helium in the late-time spectra of 11 nearby Type Ia supernovae. MNRAS, 457:3254–3265, Apr. 2016.

[193] K. S. Mandel, W. M. Wood-Vasey, A. S. Friedman, and R. P. Kirshner. Type Ia Supernova Light-Curve Inference: Hierarchical Bayesian Analysis in the Near-Infrared. ApJ, 704:629–651, Oct. 2009.

[194] D. Maoz, F. Mannucci, and G. Nelemans. Observational Clues to the Progenitors of Type Ia Supernovae. ARA&A, 52:107–170, Aug. 2014.

[195] R. Margutti, J. Parrent, A. Kamble, A. M. Soderberg, R. J. Foley, D. Milisavljevic, M. R. Drout, and R. Kirshner. No X-Rays from the Very Nearby Type Ia SN 2014J: Constraints on Its Environment. ApJ, 790:52, July 2014.

[196] E. Marietta, A. Burrows, and B. Fryxell. Type IA Supernova Explosions in Binary Systems: The Impact on the Secondary Star and Its Consequences. ApJS, 128:615–650, June 2000.

[197] G. H. Marion, P. J. Brown, J. Vinkó, J. M. Silverman, D. J. Sand, P. Challis, R. P. Kirshner, J. C. Wheeler, P. Berlind, W. R. Brown, M. L. Calkins, Y. Camacho, G. Dhungana, R. J. Foley, A. S. Friedman, M. L. Graham, D. A. Howell, E. Y. Hsiao, J. M. Irwin, S. W. Jha, R. Kehoe, L. M. Macri, K. Maeda, K. Mandel, C. McCully, V. Pandya, K. J. Rines, S. Wilhelmy, and W. Zheng. SN˜2012cg: Evidence for Interaction Between a Normal Type Ia Supernova and a Non-degenerate Binary Companion. ApJ, 820:92, Apr. 2016.

[198] G. H. Marion, P. Höflich, C. L. Gerardy, W. D. Vacca, J. C. Wheeler, and E. L. Robinson. A Catalog of Near-Infrared Spectra from Type Ia Supernovae. AJ, 138:727–757, Sept. 2009.

[199] G. H. Marion, D. J. Sand, E. Y. Hsiao, D. P. K. Banerjee, S. Valenti, M. D. Stritzinger, J. Vinkó, V. Joshi, V. Venkataraman, N. M. Ashok, R. Amanullah, R. P. Binzel, J. J. Bochanski, G. L. Bryngelson, C. R. Burns, D. Drozdov, S. K. Fieber-Beyer, M. L. Graham, D. A. Howell, J. Johansson, R. P. Kirshner, P. A. Milne, J. Parrent, J. M. Silverman, R. J. Vervack, Jr., and J. C. Wheeler. Early Observations and Analysis of the Type Ia SN 2014J in M82. ApJ, 798:39, Jan. 2015.

[200] R. E. Mason, S. Côté, M. Kissler-Patig, N. A. Levenson, A. Adamson, C. Emmanuel, and D. Crabtree. The Gemini Observatory fast turnaround program. In *Observatory Operations: Strategies, Processes, and Systems V*, volume 9149 of Proc. SPIE, page 914910, Aug. 2014.

[201] T. Matheson, R. R. Joyce, L. E. Allen, A. Saha, D. R. Silva, W. M. Wood-Vasey, J. J. Adams, R. E. Anderson, T. L. Beck, M. C. Bentz, M. A. Bershady, W. S. Binkert, K. Butler, M. A. Camarata, A. Eigenbrot, M. Everett, J. S. Gallagher, P. M. Garnavich, E. Glikman, D. Harbeck, J. R. Hargis, H. Herbst, E. P. Horch, S. B. Howell, S. Jha, J. F. Kaczmarek, P. Knezek, E. Manne-Nicholas, R. D. Mathieu, M. Meixner, K. Milliman, J. Power, J. Rajagopal, K. Reetz, K. L. Rhode, A. Schechtman-Rook, M. E. Schwamb, H. Schweiker, B. Simmons, J. D. Simon, D. Summers, M. D. Young, A. Weyant, E. M. Wilcots, G. Will, and D. Williams. The Infrared Light Curve of SN 2011fe in M101 and the Distance to M101. ApJ, 754:19, July 2012.

[202] J. R. Maund, P. Höflich, F. Patat, J. C. Wheeler, P. Zelaya, D. Baade, L. Wang, A. Clocchiatti, and J. Quinn. The Unification of Asymmetry Signatures of Type Ia Supernovae. ApJ, 725:L167–L171, Dec. 2010.

[203] P. A. Mazzali, E. Cappellaro, I. J. Danziger, M. Turatto, and S. Benetti. Nebular Velocities in Type IA Supernovae and Their Relationship to Light Curves. ApJ, 499:L49–L52, May 1998.

[204] P. A. Mazzali, F. K. Röpke, S. Benetti, and W. Hillebrandt. A Common Explosion Mechanism for Type Ia Supernovae. *Science*, 315:825, Feb. 2007.

[205] P. A. Mazzali, M. Sullivan, A. V. Filippenko, P. M. Garnavich, K. I. Clubb, K. Maguire, Y.-C. Pan, B. Shappee, J. M. Silverman, S. Benetti,

S. Hachinger, K. Nomoto, and E. Pian. Nebular spectra and abundance tomography of the Type Ia supernova SN 2011fe: a normal SN Ia with a stable Fe core. MNRAS, 450:2631–2643, July 2015.

[206] P. Meikle, Y. Khreegi, and R. Kotak. Multiband Observations of Type Ia Supernovae at Late Times. In M. Turatto, S. Benetti, L. Zampieri, and W. Shea, editors, *1604-2004: Supernovae as Cosmological Lighthouses*, volume 342 of *Astronomical Society of the Pacific Conference Series*, page 217, Dec. 2005.

[207] W. P. S. Meikle. The absolute infrared magnitudes of type Ia supernovae. MNRAS, 314:782–792, June 2000.

[208] G. Miknaitis, G. Pignata, A. Rest, W. M. Wood-Vasey, S. Blondin, P. Challis, R. C. Smith, C. W. Stubbs, N. B. Suntzeff, R. J. Foley, T. Matheson, J. L. Tonry, C. Aguilera, J. W. Blackman, A. C. Becker, A. Clocchiatti, R. Covarrubias, T. M. Davis, A. V. Filippenko, A. Garg, P. M. Garnavich, M. Hicken, S. Jha, K. Krisciunas, R. P. Kirshner, B. Leibundgut, W. Li, A. Miceli, G. Narayan, J. L. Prieto, A. G. Riess, M. E. Salvo, B. P. Schmidt, J. Sollerman, J. Spyromilio, and A. Zenteno. The ESSENCE Supernova Survey: Survey Optimization, Observations, and Supernova Photometry. ApJ, 666:674–693, Sept. 2007.

[209] R. Minkowski. Spectra of Supernovae. PASP, 53:224, Aug. 1941.

[210] K. Motohara, K. Maeda, C. L. Gerardy, K. Nomoto, M. Tanaka, N. Tominaga, T. Ohkubo, P. A. Mazzali, R. A. Fesen, P. Höflich, and J. C. Wheeler. The Asymmetric Explosion of Type Ia Supernovae as Seen from Near-Infrared Observations. ApJ, 652:L101–L104, Dec. 2006.

[211] P. Mukherjee, M. Kunz, D. Parkinson, and Y. Wang. Planck priors for dark energy surveys. Phys. Rev. D, 78(8):083529, Oct. 2008.

[212] P. Mukherjee, D. Parkinson, P. S. Corasaniti, A. R. Liddle, and M. Kunz. Model selection as a science driver for dark energy surveys. MNRAS, 369:1725–1734, July 2006.

[213] D. K. Nadyozhin. The properties of NI to CO to Fe decay. ApJS, 92:527–531, June 1994.

[214] S. Nobili, R. Amanullah, G. Garavini, A. Goobar, C. Lidman, V. Stanishev, G. Aldering, P. Antilogus, P. Astier, M. S. Burns, A. Conley, S. E. Deustua, R. Ellis, S. Fabbro, V. Fadeyev, G. Folatelli, R. Gibbons, G. Goldhaber, D. E. Groom, I. Hook, D. A. Howell, A. G. Kim, R. A. Knop, P. E. Nugent, R. Pain, S. Perlmutter, R. Quimby, J. Raux, N. Regnault, P. Ruiz-Lapuente, G. Sainton, K. Schahmaneche, E. Smith, A. L. Spadafora, R. C. Thomas, L. Wang, and Supernova Cosmology Project. Restframe I-band Hubble diagram for type Ia supernovae up to redshift z $\sim$ 0.5. A&A, 437:789–804, July 2005.

[215] S. Nobili, V. Fadeyev, G. Aldering, R. Amanullah, K. Barbary, M. S. Burns, K. S. Dawson, S. E. Deustua, L. Faccioli, A. S. Fruchter, G. Goldhaber, A. Goobar, I. Hook, D. A. Howell, A. G. Kim, R. A. Knop, C. Lidman, J. Meyers, P. E. Nugent, R. Pain, N. Panagia, S. Perlmutter, D. Rubin, A. L. Spadafora, M. Strovink, N. Suzuki, and Supernova Cosmology Project. Constraining Dust and Color Variations of High-z SNe Using NICMOS on the Hubble Space Telescope. ApJ, 700:1415–1427, Aug. 2009.

[216] S. Nobili and A. Goobar. The colour-lightcurve shape relation of type Ia supernovae and the reddening law. A&A, 487:19–31, Aug. 2008.

[217] K. Nomoto and Y. Kondo. Conditions for accretion-induced collapse of white dwarfs. ApJ, 367:L19–L22, Jan. 1991.

[218] P. Nugent, A. Kim, and S. Perlmutter. K-Corrections and Extinction Corrections for Type Ia Supernovae. PASP, 114:803–819, Aug. 2002.

[219] P. E. Nugent, M. Sullivan, S. B. Cenko, R. C. Thomas, D. Kasen, D. A. Howell, D. Bersier, J. S. Bloom, S. R. Kulkarni, M. T. Kandrashoff, A. V. Filippenko, J. M. Silverman, G. W. Marcy, A. W. Howard, H. T. Isaacson, K. Maguire, N. Suzuki, J. E. Tarlton, Y.-C. Pan, L. Bildsten, B. J. Fulton, J. T. Parrent, D. Sand, P. Podsiadlowski, F. B. Bianco, B. Dilday, M. L. Graham, J. Lyman, P. James, M. M. Kasliwal, N. M. Law, R. M. Quimby, I. M. Hook, E. S. Walker, P. Mazzali, E. Pian, E. O. Ofek, A. Gal-Yam, and D. Poznanski. Supernova SN 2011fe from an exploding carbon-oxygen white dwarf star. Nature, 480:344–347, Dec. 2011.

[220] H. Nussbaumer and P. J. Storey. Transition probabilities for forbidden Fe II infrared lines. A&A, 193:327–333, Mar. 1988.

[221] R. Pakmor, S. Hachinger, F. K. Röpke, and W. Hillebrandt. Violent mergers of nearly equal-mass white dwarf as progenitors of subluminous Type Ia supernovae. A&A, 528:A117, Apr. 2011.

[222] R. Pakmor, M. Kromer, F. K. Röpke, S. A. Sim, A. J. Ruiter, and W. Hillebrandt. Sub-luminous type Ia supernovae from the mergers of equal-mass white dwarfs with mass ˜0.9M_{solar}. Nature, 463:61–64, Jan. 2010.

[223] R. Pakmor, M. Kromer, S. Taubenberger, S. A. Sim, F. K. Röpke, and W. Hillebrandt. Normal Type Ia Supernovae from Violent Mergers of White Dwarf Binaries. ApJ, 747:L10, Mar. 2012.

[224] R. Pakmor, M. Kromer, S. Taubenberger, and V. Springel. Helium-ignited Violent Mergers as a Unified Model for Normal and Rapidly Declining Type Ia Supernovae. ApJ, 770:L8, June 2013.

[225] A. Pastorello, P. A. Mazzali, G. Pignata, S. Benetti, E. Cappellaro, A. V. Filippenko, W. Li, W. P. S. Meikle, A. A. Arkharov, G. Blanc, F. Bufano, A. Derekas, M. Dolci, N. Elias-Rosa, R. J. Foley, M. Ganeshalingam, A. Harutyunyan, L. L. Kiss, R. Kotak, V. M. Larionov, J. R. Lucey, N. Napoleone, H. Navasardyan, F. Patat, J. Rich, S. D. Ryder, M. Salvo, B. P. Schmidt, V. Stanishev, P. Székely, S. Taubenberger, S. Temporin, M. Turatto, and W. Hillebrandt. ESC and KAIT observations of the transitional Type Ia SN 2004eo. MNRAS, 377:1531–1552, June 2007.

[226] F. Patat, D. Baade, P. Höflich, J. R. Maund, L. Wang, and J. C. Wheeler. VLT spectropolarimetry of the fast expanding type Ia SN 2006X. A&A, 508:229–246, Dec. 2009.

[227] F. Patat, P. Chandra, R. Chevalier, S. Justham, P. Podsiadlowski, C. Wolf, A. Gal-Yam, L. Pasquini, I. A. Crawford, P. A. Mazzali, A. W. A. Pauldrach, K. Nomoto, S. Benetti, E. Cappellaro, N. Elias-Rosa, W. Hillebrandt, D. C. Leonard, A. Pastorello, A. Renzini, F. Sabbadin, J. D. Simon, and M. Turatto. Detection of Circumstellar Material in a Normal Type Ia Supernova. *Science*, 317:924, Aug. 2007.

[228] F. Patat, M. A. Cordiner, N. L. J. Cox, R. I. Anderson, A. Harutyunyan, R. Kotak, L. Palaversa, V. Stanishev, L. Tomasella, S. Benetti, A. Goobar, A. Pastorello, and J. Sollerman. Multi-epoch high-resolution spectroscopy of SN 2011fe. Linking the progenitor to its environment. A&A, 549:A62, Jan. 2013.

[229] F. Patat, P. Höflich, D. Baade, J. R. Maund, L. Wang, and J. C. Wheeler. VLT Spectropolarimetry of the Type Ia SN 2005ke. A step towards understanding subluminous events. A&A, 545:A7, Sept. 2012.

[230] F. Patat, S. Taubenberger, N. L. J. Cox, D. Baade, A. Clocchiatti, P. Höflich, J. R. Maund, E. Reilly, J. Spyromilio, L. Wang, J. C. Wheeler, and P. Zelaya. Properties of extragalactic dust inferred from linear polarimetry of Type Ia Supernovae. A&A, 577:A53, May 2015.

[231] J. A. Peacock, P. Schneider, G. Efstathiou, J. R. Ellis, B. Leibundgut, S. J. Lilly, and Y. Mellier. ESA-ESO Working Group on "Fundamental Cosmology". Technical report, Oct. 2006.

[232] R. Penney and P. Hoeflich. Thermonuclear Supernovae: Probing Magnetic Fields by Positrons and Late-time IR Line Profiles. ApJ, 795:84, Nov. 2014.

[233] R. Pereira, R. C. Thomas, G. Aldering, P. Antilogus, C. Baltay, S. Benitez-Herrera, S. Bongard, C. Buton, A. Canto, F. Cellier-Holzem, J. Chen, M. Childress, N. Chotard, Y. Copin, H. K. Fakhouri, M. Fink, D. Fouchez, E. Gangler, J. Guy, W. Hillebrandt, E. Y. Hsiao, M. Kerschhaggl, M. Kowalski, M. Kromer, J. Nordin, P. Nugent, K. Paech, R. Pain, E. Pécontal, S. Perlmutter, D. Rabinowitz, M. Rigault, K. Runge, C. Saunders, G. Smadja, C. Tao, S. Taubenberger, A. Tilquin, and C. Wu. Spectrophotometric time series of SN 2011fe from the Nearby Supernova Factory. A&A, 554:A27, June 2013.

[234] S. Perlmutter, G. Aldering, G. Goldhaber, R. A. Knop, P. Nugent, P. G. Castro, S. Deustua, S. Fabbro, A. Goobar, D. E. Groom, I. M. Hook, A. G. Kim, M. Y. Kim, J. C. Lee, N. J. Nunes, R. Pain, C. R. Pennypacker, R. Quimby, C. Lidman, R. S. Ellis, M. Irwin, R. G. McMahon, P. Ruiz-Lapuente, N. Walton, B. Schaefer, B. J. Boyle, A. V. Filippenko, T. Matheson, A. S. Fruchter, N. Panagia, H. J. M. Newberg,

W. J. Couch, and T. S. C. Project. Measurements of Ω and Λ from 42 High-Redshift Supernovae. *ApJ*, 517:565–586, June 1999.

[235] K. Perrett, M. Sullivan, A. Conley, S. González-Gaitán, R. Carlberg, D. Fouchez, P. Ripoche, J. D. Neill, P. Astier, D. Balam, C. Balland, S. Basa, J. Guy, D. Hardin, I. M. Hook, D. A. Howell, R. Pain, N. Palanque-Delabrouille, C. Pritchet, N. Regnault, J. Rich, V. Ruhlmann-Kleider, S. Baumont, C. Lidman, S. Perlmutter, and E. S. Walker. Evolution in the Volumetric Type Ia Supernova Rate from the Supernova Legacy Survey. AJ, 144:59, Aug. 2012.

[236] J. M. M. Pfannes, J. C. Niemeyer, and W. Schmidt. Thermonuclear explosions of rapidly rotating white dwarfs. II. Detonations. A&A, 509:A75, Jan. 2010.

[237] M. M. Phillips. The absolute magnitudes of Type IA supernovae. ApJ, 413:L105–L108, Aug. 1993.

[238] M. M. Phillips. Near-Infrared Properties of Type Ia Supernovae. PASA, 29:434–446, Feb. 2012.

[239] M. M. Phillips, K. Krisciunas, N. B. Suntzeff, R. G. Abraham, M. G. Beckett, M. Bonati, P. Candia, T. M. Corwin, D. L. Depoy, J. Espinoza, A. E. Firth, W. L. Freedman, G. Galaz, L. Germany, D. Gonzalez, M. Hamuy, N. C. Hastings, A. L. Hungerford, V. D. Ivanov, E. Labbé, R. O. Marzke, P. J. McCarthy, R. G. McMahon, R. McMillan, C. Muena, S. E. Persson, M. Roth, M. T. Ruiz, R. C. Smith, R. Smith, L.-G. Strolger, and C. Stubbs. Optical and Near-Infrared Observations of the Peculiar Type ia Supernova 1999ac. AJ, 131:2615–2627, May 2006.

[240] M. M. Phillips, W. Li, J. A. Frieman, S. I. Blinnikov, D. DePoy, J. L. Prieto, P. Milne, C. Contreras, G. Folatelli, N. Morrell, M. Hamuy, N. B. Suntzeff, M. Roth, S. González, W. Krzeminski, A. V. Filippenko, W. L. Freedman, R. Chornock, S. Jha, B. F. Madore, S. E. Persson, C. R. Burns, P. Wyatt, D. Murphy, R. J. Foley, M. Ganeshalingam, F. J. D. Serduke, K. Krisciunas, B. Bassett, A. Becker, B. Dilday, J. Eastman, P. M. Garnavich, J. Holtzman, R. Kessler, H. Lampeitl, J. Marriner, S. Frank, J. L. Marshall, G. Miknaitis, M. Sako, D. P. Schneider, K. van der Heyden, and N. Yasuda. The Peculiar SN 2005hk: Do Some Type Ia Supernovae Explode as Deflagrations? PASP, 119:360–387, Apr. 2007.

[241] M. M. Phillips, P. Lira, N. B. Suntzeff, R. A. Schommer, M. Hamuy, and J. Maza. The Reddening-Free Decline Rate Versus Luminosity Relationship for Type IA Supernovae. AJ, 118:1766–1776, Oct. 1999.

[242] M. M. Phillips, A. C. Phillips, S. R. Heathcote, V. M. Blanco, D. Geisler, D. Hamilton, N. B. Suntzeff, F. J. Jablonski, J. E. Steiner, A. P. Cowley, P. Schmidtke, S. Wyckoff, J. B. Hutchings, J. Tonry, M. A. Strauss, J. R. Thorstensen, W. Honey, J. Maza, M. T. Ruiz, A. U. Landolt, A. Uomoto, R. M. Rich, J. E. Grindlay, H. Cohn, H. A. Smith, J. H. Lutz, R. J. Lavery, and A. Saha. The type 1a supernova 1986G in NGC 5128 - Optical photometry and spectra. PASP, 99:592–605, July 1987.

[243] M. M. Phillips, J. D. Simon, N. Morrell, C. R. Burns, N. L. J. Cox, R. J. Foley, A. I. Karakas, F. Patat, A. Sternberg, R. E. Williams, A. Gal-Yam, E. Y. Hsiao, D. C. Leonard, S. E. Persson, M. Stritzinger, I. B. Thompson, A. Campillay, C. Contreras, G. Folatelli, W. L. Freedman, M. Hamuy, M. Roth, G. A. Shields, N. B. Suntzeff, L. Chomiuk, I. I. Ivans, B. F. Madore, B. E. Penprase, D. Perley, G. Pignata, G. Preston, and A. M. Soderberg. On the Source of the Dust Extinction in Type Ia Supernovae and the Discovery of Anomalously Strong Na I Absorption. ApJ, 779:38, Dec. 2013.

[244] M. M. Phillips, L. A. Wells, N. B. Suntzeff, M. Hamuy, B. Leibundgut, R. P. Kirshner, and C. B. Foltz. SN 1991T - Further evidence of the heterogeneous nature of type IA supernovae. AJ, 103:1632–1637, May 1992.

[245] G. Pignata, S. Benetti, P. A. Mazzali, R. Kotak, F. Patat, P. Meikle, M. Stehle, B. Leibundgut, N. B. Suntzeff, L. M. Buson, E. Cappellaro, A. Clocchiatti, M. Hamuy, J. Maza, J. Mendez, P. Ruiz-Lapuente, M. Salvo, B. P. Schmidt, M. Turatto, and W. Hillebrandt. Optical and infrared observations of SN 2002dj: some possible common properties of fast-expanding Type Ia supernovae. MNRAS, 388:971–990, Aug. 2008.

[246] Planck Collaboration, P. A. R. Ade, N. Aghanim, C. Armitage-Caplan, M. Arnaud, M. Ashdown, F. Atrio-Barandela, J. Aumont, C. Baccigalupi, A. J. Banday, and et al. Planck 2013 results. XVI. Cosmological parameters. A&A, 571:A16, Nov. 2014.

[247] Planck Collaboration, P. A. R. Ade, N. Aghanim, M. Arnaud, M. Ashdown, J. Aumont, C. Baccigalupi, A. J. Banday, R. B. Barreiro, J. G. Bartlett, and et al. Planck 2015 results. XIII. Cosmological parameters. *ArXiv e-prints*, Feb. 2015.

[248] Planck Collaboration, P. A. R. Ade, N. Aghanim, M. Arnaud, M. Ashdown, J. Aumont, C. Baccigalupi, A. J. Banday, R. B. Barreiro, N. Bartolo, and et al. Planck 2015 results. XIV. Dark energy and modified gravity. *ArXiv e-prints*, Feb. 2015.

[249] C. Raskin and D. Kasen. Tidal Tail Ejection as a Signature of Type Ia Supernovae from White Dwarf Mergers. ApJ, 772:1, July 2013.

[250] A. Rau, S. R. Kulkarni, N. M. Law, J. S. Bloom, D. Ciardi, G. S. Djorgovski, D. B. Fox, A. Gal-Yam, C. C. Grillmair, M. M. Kasliwal, P. E. Nugent, E. O. Ofek, R. M. Quimby, W. T. Reach, M. Shara, L. Bildsten, S. B. Cenko, A. J. Drake, A. V. Filippenko, D. J. Helfand, G. Helou, D. A. Howell, D. Poznanski, and M. Sullivan. Exploring the Optical Transient Sky with the Palomar Transient Factory. PASP, 121:1334–1351, Dec. 2009.

[251] A. G. Riess, A. V. Filippenko, P. Challis, A. Clocchiatti, A. Diercks, P. M. Garnavich, R. L. Gilliland, C. J. Hogan, S. Jha, R. P. Kirshner, B. Leibundgut, M. M. Phillips, D. Reiss, B. P. Schmidt, R. A. Schommer, R. C. Smith, J. Spyromilio, C. Stubbs, N. B. Suntzeff, and J. Tonry. Observational Evidence from Supernovae for an Accelerating Universe and a Cosmological Constant. *AJ*, 116:1009–1038, Sept. 1998.

[252] A. G. Riess, A. V. Filippenko, W. Li, R. R. Treffers, B. P. Schmidt, Y. Qiu, J. Hu, M. Armstrong, C. Faranda, E. Thouvenot, and C. Buil. The Rise Time of Nearby Type IA Supernovae. AJ, 118:2675–2688, Dec. 1999.

[253] A. G. Riess, A. V. Filippenko, M. C. Liu, P. Challis, A. Clocchiatti, A. Diercks, P. M. Garnavich, C. J. Hogan, S. Jha, R. P. Kirshner, B. Leibundgut, M. M. Phillips, D. Reiss, B. P. Schmidt, R. A. Schommer, R. C. Smith, J. Spyromilio, C. Stubbs, N. B. Suntzeff, J. Tonry, P. Woudt, R. J. Brunner, A. Dey, R. Gal, J. Graham, J. Larkin, S. C. Odewahn, and B. Oppenheimer. Tests of the Accelerating Universe with Near-Infrared

Observations of a High-Redshift Type IA Supernova. ApJ, 536:62–67, June 2000.

[254] A. G. Riess, L. Macri, S. Casertano, H. Lampeitl, H. C. Ferguson, A. V. Filippenko, S. W. Jha, W. Li, and R. Chornock. A 3% Solution: Determination of the Hubble Constant with the Hubble Space Telescope and Wide Field Camera 3. ApJ, 730:119, Apr. 2011.

[255] A. G. Riess, L. M. Macri, S. L. Hoffmann, D. Scolnic, S. Casertano, A. V. Filippenko, B. E. Tucker, M. J. Reid, D. O. Jones, J. M. Silverman, R. Chornock, P. Challis, W. Yuan, P. J. Brown, and R. J. Foley. A 2.4% Determination of the Local Value of the Hubble Constant. *ArXiv e-prints*, Apr. 2016.

[256] A. G. Riess, W. H. Press, and R. P. Kirshner. A Precise Distance Indicator: Type IA Supernova Multicolor Light-Curve Shapes. ApJ, 473:88, Dec. 1996.

[257] A. G. Riess, L.-G. Strolger, S. Casertano, H. C. Ferguson, B. Mobasher, B. Gold, P. J. Challis, A. V. Filippenko, S. Jha, W. Li, J. Tonry, R. Foley, R. P. Kirshner, M. Dickinson, E. MacDonald, D. Eisenstein, M. Livio, J. Younger, C. Xu, T. Dahlén, and D. Stern. New Hubble Space Telescope Discoveries of Type Ia Supernovae at z >= 1: Narrowing Constraints on the Early Behavior of Dark Energy. ApJ, 659:98–121, Apr. 2007.

[258] A. G. Riess, L.-G. Strolger, J. Tonry, S. Casertano, H. C. Ferguson, B. Mobasher, P. Challis, A. V. Filippenko, S. Jha, W. Li, R. Chornock, R. P. Kirshner, B. Leibundgut, M. Dickinson, M. Livio, M. Giavalisco, C. C. Steidel, T. Benítez, and Z. Tsvetanov. Type Ia Supernova Discoveries at z > 1 from the Hubble Space Telescope: Evidence for Past Deceleration and Constraints on Dark Energy Evolution. ApJ, 607:665–687, June 2004.

[259] M. Rigault, G. Aldering, M. Kowalski, Y. Copin, P. Antilogus, C. Aragon, S. Bailey, C. Baltay, D. Baugh, S. Bongard, K. Boone, C. Buton, J. Chen, N. Chotard, H. K. Fakhouri, U. Feindt, P. Fagrelius, M. Fleury, D. Fouchez, E. Gangler, B. Hayden, A. G. Kim, P.-F. Leget, S. Lombardo, J. Nordin, R. Pain, E. Pecontal, R. Pereira, S. Perlmutter, D. Rabinowitz, K. Runge, D. Rubin, C. Saunders, G. Smadja,

C. Sofiatti, N. Suzuki, C. Tao, and B. A. Weaver. Confirmation of a Star Formation Bias in Type Ia Supernova Distances and its Effect on the Measurement of the Hubble Constant. ApJ, 802:20, Mar. 2015.

[260] S. A. Rodney, A. G. Riess, D. M. Scolnic, D. O. Jones, S. Hemmati, A. Molino, C. McCully, B. Mobasher, L.-G. Strolger, O. Graur, B. Hayden, and S. Casertano. Two SNe Ia at Redshift ∼2: Improved Classification and Redshift Determination with Medium-band Infrared Imaging. AJ, 150:156, Nov. 2015.

[261] F. K. Röpke, W. Hillebrandt, W. Schmidt, J. C. Niemeyer, S. I. Blinnikov, and P. A. Mazzali. A Three-Dimensional Deflagration Model for Type Ia Supernovae Compared with Observations. ApJ, 668:1132–1139, Oct. 2007.

[262] S. Rosswog, D. Kasen, J. Guillochon, and E. Ramirez-Ruiz. Collisions of White Dwarfs as a New Progenitor Channel for Type Ia Supernovae. ApJ, 705:L128–L132, Nov. 2009.

[263] A. J. Ruiter, S. A. Sim, R. Pakmor, M. Kromer, I. R. Seitenzahl, K. Belczynski, M. Fink, M. Herzog, W. Hillebrandt, F. K. Röpke, and S. Taubenberger. On the brightness distribution of Type Ia supernovae from violent white dwarf mergers. MNRAS, 429:1425–1436, Feb. 2013.

[264] P. Ruiz-Lapuente and L. B. Lucy. Nebular spectra of type IA supernovae as probes for extragalactic distances, reddening, and nucleosynthesis. ApJ, 400:127–137, Nov. 1992.

[265] D. J. Sand, E. Y. Hsiao, D. P. K. Banerjee, G. H. Marion, T. R. Diamond, V. Joshi, J. T. Parrent, M. M. Phillips, M. D. Stritzinger, and V. Venkataraman. Post-maximum near infrared spectra of SN 2014J: A search for interaction signatures. *ArXiv e-prints*, Mar. 2016.

[266] R. Scalzo, G. Aldering, P. Antilogus, C. Aragon, S. Bailey, C. Baltay, S. Bongard, C. Buton, A. Canto, F. Cellier-Holzem, M. Childress, N. Chotard, Y. Copin, H. K. Fakhouri, E. Gangler, J. Guy, E. Y. Hsiao, M. Kerschhaggl, M. Kowalski, P. Nugent, K. Paech, R. Pain, E. Pecontal, R. Pereira, S. Perlmutter, D. Rabinowitz, M. Rigault, K. Runge, G. Smadja, C. Tao, R. C. Thomas, B. A. Weaver, C. Wu, and T. Nearby

Supernova Factory. A Search for New Candidate Super-Chandrasekhar-mass Type Ia Supernovae in the Nearby Supernova Factory Data Set. ApJ, 757:12, Sept. 2012.

[267] R. Scalzo, G. Aldering, P. Antilogus, C. Aragon, S. Bailey, C. Baltay, S. Bongard, C. Buton, F. Cellier-Holzem, M. Childress, N. Chotard, Y. Copin, H. K. Fakhouri, E. Gangler, J. Guy, A. G. Kim, M. Kowalski, M. Kromer, J. Nordin, P. Nugent, K. Paech, R. Pain, E. Pecontal, R. Pereira, S. Perlmutter, D. Rabinowitz, M. Rigault, K. Runge, C. Saunders, S. A. Sim, G. Smadja, C. Tao, S. Taubenberger, R. C. Thomas, B. A. Weaver, and Nearby Supernova Factory. Type Ia supernova bolometric light curves and ejected mass estimates from the Nearby Supernova Factory. MNRAS, 440:1498–1518, May 2014.

[268] R. A. Scalzo, G. Aldering, P. Antilogus, C. Aragon, S. Bailey, C. Baltay, S. Bongard, C. Buton, M. Childress, N. Chotard, Y. Copin, H. K. Fakhouri, A. Gal-Yam, E. Gangler, S. Hoyer, M. Kasliwal, S. Loken, P. Nugent, R. Pain, E. Pécontal, R. Pereira, S. Perlmutter, D. Rabinowitz, A. Rau, G. Rigaudier, K. Runge, G. Smadja, C. Tao, R. C. Thomas, B. Weaver, and C. Wu. Nearby Supernova Factory Observations of SN 2007if: First Total Mass Measurement of a Super-Chandrasekhar-Mass Progenitor. ApJ, 713:1073–1094, Apr. 2010.

[269] R. A. Scalzo, A. J. Ruiter, and S. A. Sim. The ejected mass distribution of Type Ia supernovae: a significant rate of non-Chandrasekhar-mass progenitors. MNRAS, 445:2535–2544, Dec. 2014.

[270] D. M. Scolnic, A. G. Riess, R. J. Foley, A. Rest, S. A. Rodney, D. J. Brout, and D. O. Jones. Color Dispersion and Milky-Way-like Reddening among Type Ia Supernovae. ApJ, 780:37, Jan. 2014.

[271] I. R. Seitenzahl, G. Cescutti, F. K. Röpke, A. J. Ruiter, and R. Pakmor. Solar abundance of manganese: a case for near Chandrasekhar-mass Type Ia supernova progenitors. A&A, 559:L5, Nov. 2013.

[272] K. Serkowski, D. S. Mathewson, and V. L. Ford. Wavelength dependence of interstellar polarization and ratio of total to selective extinction. ApJ, 196:261–290, Feb. 1975.

[273] B. J. Shappee, K. Z. Stanek, R. W. Pogge, and P. M. Garnavich. No Stripped Hydrogen in the Nebular Spectra of Nearby Type Ia Supernova 2011fe. ApJ, 762:L5, Jan. 2013.

[274] H. Shariff, X. Jiao, R. Trotta, and D. A. van Dyk. BAHAMAS: new SNIa analysis reveals inconsistencies with standard cosmology. *ArXiv e-prints*, Oct. 2015.

[275] S. A. Sim, F. K. Röpke, W. Hillebrandt, M. Kromer, R. Pakmor, M. Fink, A. J. Ruiter, and I. R. Seitenzahl. Detonations in Sub-Chandrasekhar-mass C+O White Dwarfs. ApJ, 714:L52–L57, May 2010.

[276] J. Skilling. Nested Sampling. In R. Fischer, R. Preuss, and U. V. Toussaint, editors, *American Institute of Physics Conference Series*, volume 735 of *American Institute of Physics Conference Series*, pages 395–405, Nov. 2004.

[277] J. Sollerman, J. Lindahl, C. Kozma, P. Challis, A. V. Filippenko, C. Fransson, P. M. Garnavich, B. Leibundgut, W. Li, P. Lundqvist, P. Milne, J. Spyromilio, and R. P. Kirshner. The late-time light curve of the type Ia supernova 2000cx. A&A, 428:555–568, Dec. 2004.

[278] D. Spergel, N. Gehrels, C. Baltay, D. Bennett, J. Breckinridge, M. Donahue, A. Dressler, B. S. Gaudi, T. Greene, O. Guyon, C. Hirata, J. Kalirai, N. J. Kasdin, B. Macintosh, W. Moos, S. Perlmutter, M. Postman, B. Rauscher, J. Rhodes, Y. Wang, D. Weinberg, D. Benford, M. Hudson, W.-S. Jeong, Y. Mellier, W. Traub, T. Yamada, P. Capak, J. Colbert, D. Masters, M. Penny, D. Savransky, D. Stern, N. Zimmerman, R. Barry, L. Bartusek, K. Carpenter, E. Cheng, D. Content, F. Dekens, R. Demers, K. Grady, C. Jackson, G. Kuan, J. Kruk, M. Melton, B. Nemati, B. Parvin, I. Poberezhskiy, C. Peddie, J. Ruffa, J. K. Wallace, A. Whipple, E. Wollack, and F. Zhao. Wide-Field InfrarRed Survey Telescope-Astrophysics Focused Telescope Assets WFIRST-AFTA 2015 Report. *ArXiv e-prints*, Mar. 2015.

[279] J. Spyromilio, R. Gilmozzi, J. Sollerman, B. Leibundgut, C. Fransson, and J.-G. Cuby. Optical and near infrared observations of SN 1998bu. A&A, 426:547–553, Nov. 2004.

[280] J. Spyromilio, W. P. S. Meikle, D. A. Allen, and J. R. Graham. A large mass of iron in supernova 1991T. MNRAS, 258:53P–56P, Oct. 1992.

[281] J. Spyromilio, P. A. Pinto, and R. G. Eastman. On the Origin of the 1.2-MICRON Feature in Type-Ia Supernova Spectra. MNRAS, 266:L17, Jan. 1994.

[282] V. Stanishev, A. Goobar, R. Amanullah, B. Bassett, Y. T. Fantaye, P. Garnavich, R. Hlozek, J. Nordin, P. M. Okouma, L. Ostman, M. Sako, R. Scalzo, and M. Smith. Type Ia Supernova Cosmology in the Near-Infrared. *ArXiv e-prints*, May 2015.

[283] M. Stehle, P. A. Mazzali, S. Benetti, and W. Hillebrandt. Abundance stratification in Type Ia supernovae - I. The case of SN 2002bo. MNRAS, 360:1231–1243, July 2005.

[284] A. Sternberg, A. Gal-Yam, J. D. Simon, D. C. Leonard, R. M. Quimby, M. M. Phillips, N. Morrell, I. B. Thompson, I. Ivans, J. L. Marshall, A. V. Filippenko, G. W. Marcy, J. S. Bloom, F. Patat, R. J. Foley, D. Yong, B. E. Penprase, D. J. Beeler, C. Allende Prieto, and G. S. Stringfellow. Circumstellar Material in Type Ia Supernovae via Sodium Absorption Features. *Science*, 333:856, Aug. 2011.

[285] M. Stritzinger, B. Leibundgut, S. Walch, and G. Contardo. Constraints on the progenitor systems of type Ia supernovae. A&A, 450:241–251, Apr. 2006.

[286] M. Stritzinger, P. A. Mazzali, J. Sollerman, and S. Benetti. Consistent estimates of ^{56}Ni yields for type Ia supernovae. A&A, 460:793–798, Dec. 2006.

[287] M. Stritzinger and J. Sollerman. Late-time emission of type Ia supernovae: optical and near-infrared observations of SN 2001el. A&A, 470:L1–L4, July 2007.

[288] M. D. Stritzinger, M. M. Phillips, L. N. Boldt, C. Burns, A. Campillay, C. Contreras, S. Gonzalez, G. Folatelli, N. Morrell, W. Krzeminski, M. Roth, F. Salgado, D. L. DePoy, M. Hamuy, W. L. Freedman, B. F. Madore, J. L. Marshall, S. E. Persson, J.-P. Rheault, N. B. Suntzeff, S. Villanueva, W. Li, and A. V. Filippenko. The Carnegie Supernova

Project: Second Photometry Data Release of Low-redshift Type Ia Supernovae. AJ, 142:156, Nov. 2011.

[289] M. Sullivan, A. Conley, D. A. Howell, J. D. Neill, P. Astier, C. Balland, S. Basa, R. G. Carlberg, D. Fouchez, J. Guy, D. Hardin, I. M. Hook, R. Pain, N. Palanque-Delabrouille, K. M. Perrett, C. J. Pritchet, N. Regnault, J. Rich, V. Ruhlmann-Kleider, S. Baumont, E. Hsiao, T. Kronborg, C. Lidman, S. Perlmutter, and E. S. Walker. The dependence of Type Ia Supernovae luminosities on their host galaxies. MNRAS, 406:782–802, Aug. 2010.

[290] M. Sullivan, J. Guy, A. Conley, N. Regnault, P. Astier, C. Balland, S. Basa, R. G. Carlberg, D. Fouchez, D. Hardin, I. M. Hook, D. A. Howell, R. Pain, N. Palanque-Delabrouille, K. M. Perrett, C. J. Pritchet, J. Rich, V. Ruhlmann-Kleider, D. Balam, S. Baumont, R. S. Ellis, S. Fabbro, H. K. Fakhouri, N. Fourmanoit, S. González-Gaitán, M. L. Graham, M. J. Hudson, E. Hsiao, T. Kronborg, C. Lidman, A. M. Mourao, J. D. Neill, S. Perlmutter, P. Ripoche, N. Suzuki, and E. S. Walker. SNLS3: Constraints on Dark Energy Combining the Supernova Legacy Survey Three-year Data with Other Probes. ApJ, 737:102, Aug. 2011.

[291] M. Sullivan, D. Le Borgne, C. J. Pritchet, A. Hodsman, J. D. Neill, D. A. Howell, R. G. Carlberg, P. Astier, E. Aubourg, D. Balam, S. Basa, A. Conley, S. Fabbro, D. Fouchez, J. Guy, I. Hook, R. Pain, N. Palanque-Delabrouille, K. Perrett, N. Regnault, J. Rich, R. Taillet, S. Baumont, J. Bronder, R. S. Ellis, M. Filiol, V. Lusset, S. Perlmutter, P. Ripoche, and C. Tao. Rates and Properties of Type Ia Supernovae as a Function of Mass and Star Formation in Their Host Galaxies. ApJ, 648:868–883, Sept. 2006.

[292] N. B. Suntzeff. Observations of Type IA Supernovae. In R. McCray and Z. Wang, editors, *IAU Colloq. 145: Supernovae and Supernova Remnants*, page 41, 1996.

[293] N. B. Suntzeff. Optical, Infrared, and Bolometric Light Curves of Type Ia Supernovae. In W. Hillebrandt and B. Leibundgut, editors, *From Twilight to Highlight: The Physics of Supernovae*, page 183, 2003.

[294] N. Suzuki, D. Rubin, C. Lidman, G. Aldering, R. Amanullah, K. Barbary, L. F. Barrientos, J. Botyanszki, M. Brodwin, N. Connolly, K. S.

Dawson, A. Dey, M. Doi, M. Donahue, S. Deustua, P. Eisenhardt, E. Ellingson, L. Faccioli, V. Fadeyev, H. K. Fakhouri, A. S. Fruchter, D. G. Gilbank, M. D. Gladders, G. Goldhaber, A. H. Gonzalez, A. Goobar, A. Gude, T. Hattori, H. Hoekstra, E. Hsiao, X. Huang, Y. Ihara, M. J. Jee, D. Johnston, N. Kashikawa, B. Koester, K. Konishi, M. Kowalski, E. V. Linder, L. Lubin, J. Melbourne, J. Meyers, T. Morokuma, F. Munshi, C. Mullis, T. Oda, N. Panagia, S. Perlmutter, M. Postman, T. Pritchard, J. Rhodes, P. Ripoche, P. Rosati, D. J. Schlegel, A. Spadafora, S. A. Stanford, V. Stanishev, D. Stern, M. Strovink, N. Takanashi, K. Tokita, M. Wagner, L. Wang, N. Yasuda, H. K. C. Yee, and T. Supernova Cosmology Project. The Hubble Space Telescope Cluster Supernova Survey. V. Improving the Dark-energy Constraints above z $>$ 1 and Building an Early-type-hosted Supernova Sample. ApJ, 746:85, Feb. 2012.

[295] D. A. Swartz, P. G. Sutherland, and R. P. Harkness. Gamma-Ray Transfer and Energy Deposition in Supernovae. ApJ, 446:766, June 1995.

[296] R. E. Taam. Helium runaways in white dwarfs. ApJ, 237:142–147, Apr. 1980.

[297] S. Taubenberger, S. Benetti, M. Childress, R. Pakmor, S. Hachinger, P. A. Mazzali, V. Stanishev, N. Elias-Rosa, I. Agnoletto, F. Bufano, M. Ergon, A. Harutyunyan, C. Inserra, E. Kankare, M. Kromer, H. Navasardyan, J. Nicolas, A. Pastorello, E. Prosperi, F. Salgado, J. Sollerman, M. Stritzinger, M. Turatto, S. Valenti, and W. Hillebrandt. High luminosity, slow ejecta and persistent carbon lines: SN 2009dc challenges thermonuclear explosion scenarios. MNRAS, 412:2735–2762, Apr. 2011.

[298] S. Taubenberger, N. Elias-Rosa, W. E. Kerzendorf, S. Hachinger, J. Spyromilio, C. Fransson, M. Kromer, A. J. Ruiter, I. R. Seitenzahl, S. Benetti, E. Cappellaro, A. Pastorello, M. Turatto, and A. Marchetti. Spectroscopy of the Type Ia supernova 2011fe past 1000 d. MNRAS, 448:L48–L52, Mar. 2015.

[299] S. Taubenberger, S. Hachinger, G. Pignata, P. A. Mazzali, C. Contreras, S. Valenti, A. Pastorello, N. Elias-Rosa, O. Bärnbantner, H. Barwig, S. Benetti, M. Dolci, J. Fliri, G. Folatelli, W. L. Freedman, S. Gonzalez,

M. Hamuy, W. Krzeminski, N. Morrell, H. Navasardyan, S. E. Persson, M. M. Phillips, C. Ries, M. Roth, N. B. Suntzeff, M. Turatto, and W. Hillebrandt. The underluminous Type Ia supernova 2005bl and the class of objects similar to SN 1991bg. MNRAS, 385:75–96, Mar. 2008.

[300] S. Taubenberger, M. Kromer, S. Hachinger, P. A. Mazzali, S. Benetti, P. E. Nugent, R. A. Scalzo, R. Pakmor, V. Stanishev, J. Spyromilio, F. Bufano, S. A. Sim, B. Leibundgut, and W. Hillebrandt. 'Super-Chandrasekhar' Type Ia Supernovae at nebular epochs. MNRAS, 432:3117–3130, July 2013.

[301] C. M. Telesco, P. Höflich, D. Li, C. Álvarez, C. M. Wright, P. J. Barnes, S. Fernández, J. H. Hough, N. A. Levenson, N. Mariñas, C. Packham, E. Pantin, R. Rebolo, P. Roche, and H. Zhang. Mid-IR Spectra of Type Ia SN 2014J in M82 Spanning the First 4 Months. ApJ, 798:93, Jan. 2015.

[302] J. L. Tonry, A. Dressler, J. P. Blakeslee, E. A. Ajhar, A. B. Fletcher, G. A. Luppino, M. R. Metzger, and C. B. Moore. The SBF Survey of Galaxy Distances. IV. SBF Magnitudes, Colors, and Distances. ApJ, 546:681–693, Jan. 2001.

[303] J. L. Tonry, B. P. Schmidt, B. Barris, P. Candia, P. Challis, A. Clocchiatti, A. L. Coil, A. V. Filippenko, P. Garnavich, C. Hogan, S. T. Holland, S. Jha, R. P. Kirshner, K. Krisciunas, B. Leibundgut, W. Li, T. Matheson, M. M. Phillips, A. G. Riess, R. Schommer, R. C. Smith, J. Sollerman, J. Spyromilio, C. W. Stubbs, and N. B. Suntzeff. Cosmological Results from High-z Supernovae. ApJ, 594:1–24, Sept. 2003.

[304] C. Travaglio, W. Hillebrandt, M. Reinecke, and F.-K. Thielemann. Nucleosynthesis in multi-dimensional SN Ia explosions. A&A, 425:1029–1040, Oct. 2004.

[305] R. Trotta. Bayes in the sky: Bayesian inference and model selection in cosmology. *Contemporary Physics*, 49:71–104, Mar. 2008.

[306] J. W. Truran, A. S. Glasner, and Y. Kim. ^{56}Ni, Explosive Nucleosynthesis, and SNe Ia Diversity. *Journal of Physics Conference Series*, 337(1):012040, Feb. 2012.

[307] R. B. Tully. *Nearby galaxies catalog*. 1988.

[308] M. Turatto. Classification of Supernovae. In K. Weiler, editor, *Supernovae and Gamma-Ray Bursters*, volume 598 of *Lecture Notes in Physics, Berlin Springer Verlag*, pages 21–36, 2003.

[309] W. D. Vacca, R. T. Hamilton, M. Savage, S. Shenoy, E. E. Becklin, I. S. McLean, S. E. Logsdon, G. H. Marion, N. M. Ashok, D. P. K. Banerjee, A. Evans, O. D. Fox, P. Garnavich, R. D. Gehrz, M. Greenhouse, L. A. Helton, R. P. Kirshner, D. Shenoy, N. Smith, J. Spyromilio, S. Starrfield, D. H. Wooden, and C. E. Woodward. Observations of Type Ia Supernova 2014J with FLITECAM/SOFIA. ApJ, 804:66, May 2015.

[310] G. Valentini, E. Di Carlo, F. Massi, M. Dolci, A. A. Arkharov, V. M. Larionov, A. Pastorello, A. Di Paola, S. Benetti, E. Cappellaro, M. Turatto, F. Pedichini, F. D'Alessio, A. Caratti o Garatti, G. Li Causi, R. Speziali, I. J. Danziger, and A. Tornambé. Optical and Near-Infrared Photometry of the Type Ia Supernova 2000E in NGC 6951. ApJ, 595:779–793, Oct. 2003.

[311] M. H. van Kerkwijk, P. Chang, and S. Justham. Sub-Chandrasekhar White Dwarf Mergers as the Progenitors of Type Ia Supernovae. ApJ, 722:L157–L161, Oct. 2010.

[312] L. Wang, D. Baade, and F. Patat. Spectropolarimetric Diagnostics of Thermonuclear Supernova Explosions. *Science*, 315:212, Jan. 2007.

[313] X. Wang, W. Li, A. V. Filippenko, K. Krisciunas, N. B. Suntzeff, J. Li, T. Zhang, J. Deng, R. J. Foley, M. Ganeshalingam, T. Li, Y. Lou, Y. Qiu, R. Shang, J. M. Silverman, S. Zhang, and Y. Zhang. Optical and Near-Infrared Observations of the Highly Reddened, Rapidly Expanding Type Ia Supernova SN 2006X in M100. ApJ, 675:626–643, Mar. 2008.

[314] D. H. Weinberg, M. J. Mortonson, D. J. Eisenstein, C. Hirata, A. G. Riess, and E. Rozo. Observational probes of cosmic acceleration. Phys. Rep., 530:87–255, Sept. 2013.

[315] D. E. Welty, A. M. Ritchey, J. A. Dahlstrom, and D. G. York. Diffuse Interstellar Bands versus Known Atomic and Molecular Species in the Interstellar Medium of M82 toward SN 2014J. ApJ, 792:106, Sept. 2014.

[316] C. Wetterich. Phenomenological parameterization of quintessence. *Physics Letters B*, 594:17–22, July 2004.

[317] A. Weyant, M. Wood-Vasey, L. Wasserman, and P. Freeman. An Unbiased Method of Modeling the Local Peculiar Velocity Field with Type Ia Supernovae. ApJ, 732:65, May 2011.

[318] A. Weyant, W. M. Wood-Vasey, L. Allen, P. M. Garnavich, S. W. Jha, R. Joyce, and T. Matheson. SweetSpot: Near-infrared Observations of 13 Type Ia Supernovae from a New NOAO Survey Probing the Nearby Smooth Hubble Flow. ApJ, 784:105, Apr. 2014.

[319] J. C. Wheeler and R. P. Harkness. Type I supernovae. *Reports on Progress in Physics*, 53:1467–1557, Dec. 1990.

[320] J. C. Wheeler, P. Höflich, R. P. Harkness, and J. Spyromilio. Explosion Diagnostics of Type IA Supernovae from Early Infrared Spectra. ApJ, 496:908–914, Mar. 1998.

[321] J. Whelan and I. Iben, Jr. Binaries and Supernovae of Type I. ApJ, 186:1007–1014, Dec. 1973.

[322] D. C. B. Whittet, editor. *Dust in the galactic environment*, 2003.

[323] J. A. Willick, S. Courteau, S. M. Faber, D. Burstein, A. Dekel, and M. A. Strauss. Homogeneous Velocity-Distance Data for Peculiar Velocity Analysis. III. The Mark III Catalog of Galaxy Peculiar Velocities. ApJS, 109:333–366, Apr. 1997.

[324] W. M. Wood-Vasey, A. S. Friedman, J. S. Bloom, M. Hicken, M. Modjaz, R. P. Kirshner, D. L. Starr, C. H. Blake, E. E. Falco, A. H. Szentgyorgyi, P. Challis, S. Blondin, K. S. Mandel, and A. Rest. Type Ia Supernovae Are Good Standard Candles in the Near Infrared: Evidence from PAIRITEL. ApJ, 689:377–390, Dec. 2008.

[325] W. M. Wood-Vasey, G. Miknaitis, C. W. Stubbs, S. Jha, A. G. Riess, P. M. Garnavich, R. P. Kirshner, C. Aguilera, A. C. Becker, J. W. Blackman, S. Blondin, P. Challis, A. Clocchiatti, A. Conley, R. Covarrubias, T. M. Davis, A. V. Filippenko, R. J. Foley, A. Garg, M. Hicken, K. Krisciunas, B. Leibundgut, W. Li, T. Matheson, A. Miceli, G. Narayan, G. Pignata, J. L. Prieto, A. Rest, M. E. Salvo, B. P. Schmidt, R. C. Smith,

J. Sollerman, J. Spyromilio, J. L. Tonry, N. B. Suntzeff, and A. Zenteno. Observational Constraints on the Nature of Dark Energy: First Cosmological Results from the ESSENCE Supernova Survey. ApJ, 666:694–715, Sept. 2007.

[326] S. E. Woosley. Delayed Detonation Mode For Type Ia Supernovae. In *Bulletin of the American Astronomical Society*, volume 22 of BAAS, page 1221, Sept. 1990.

[327] S. E. Woosley and D. Kasen. Sub-Chandrasekhar Mass Models for Supernovae. ApJ, 734:38, June 2011.

[328] S. E. Woosley, D. Kasen, S. Blinnikov, and E. Sorokina. Type Ia Supernova Light Curves. ApJ, 662:487–503, June 2007.

[329] S. E. Woosley, R. E. Taam, and T. A. Weaver. Models for Type I supernova. I - Detonations in white dwarfs. ApJ, 301:601–623, Feb. 1986.

[330] S. E. Woosley and T. A. Weaver. Sub-Chandrasekhar mass models for Type IA supernovae. ApJ, 423:371–379, Mar. 1994.

[331] M. Yamanaka, K. Maeda, M. Tanaka, N. Tominaga, K. S. Kawabata, K. Takaki, M. Kawabata, T. Nakaoka, I. Ueno, H. Akitaya, T. Nagayama, J. Takahashi, S. Honda, T. Omodaka, R. Miyanoshita, T. Nagao, M. Watanabe, M. Isogai, A. Arai, R. Itoh, T. Ui, M. Uemura, M. Yoshida, H. Hanayama, D. Kuroda, N. Ukita, K. Yanagisawa, H. Izumiura, Y. Saito, K. Masumoto, R. Ono, R. Noguchi, K. Matsumoto, D. Nogami, T. Morokuma, Y. Oasa, and K. Sekiguchi. OISTER optical and near-infrared observations of the super-Chandrasekhar supernova candidate SN 2012dn: Dust emission from the circumstellar shell. PASJ, May 2016.

[332] W. Zheng, I. Shivvers, A. V. Filippenko, K. Itagaki, K. I. Clubb, O. D. Fox, M. L. Graham, P. L. Kelly, and J. C. Mauerhan. Estimating the First-light Time of the Type Ia Supernova 2014J in M82. ApJ, 783:L24, Mar. 2014.

A. Nested Sampling for Cosmological Parameter Estimation

In this Appendix, we describe the Nested Sampling Markov Chain Monte Carlo algorithm used for cosmological parameter estimation in Chapter 7.

The application of numerical methods has flourished in cosmology and astrophysics in the past decade, owing to the large size and complexity of datasets. These numerical methods can broadly be characterised into two classes based on their functionality, namely, *parameter estimation* and *model selection*. Here, we will discuss nested sampling (introduced by J. Skilling in 2004 [276]) and its application for sampling multi-modal distributions in MultiNest. Nested sampling was developed as a method in order to perform model selection, but it also calculates the posterior distribution samples as a by-product for a given set of parameters. A review of Bayesian inference for cosmology and astrophysics (both for parameter estimation and model selection) can be found in [305].

However, before we discuss the details of the method implemented here for cosmological inference, we would like to define the quantities used in the derivation of the method.

The probabilistic context for such a sampling method is usually in the form of Bayes' theorem. In the Bayesian approach to probabilities, a probability is defined as a degree of belief in a proposition as opposed to the frequency of occurrence of a favourable outcome. Bayes' theorem is as follows

$$\begin{aligned} \Pr(D|\theta, I) \times \Pr(\theta|I) &= \Pr(\theta|D, I) \times \Pr(D|I) \\ \text{Likelihood} \times \text{Prior} &= \text{Posterior} \times \text{Evidence} \\ L(\theta) \times \pi(\theta) d\theta &= Z \times p(\theta) d\theta \end{aligned} \tag{A.1}$$

D are the data that allow us to modulate our prior belief $dX = \pi(\theta)d\theta$ into posterior $dP = p(\theta)d\theta$. I is the initial hypothesis being tested. The inputs L and π yield outputs Z and p.

For executing the nested sampling algorithm, we use the publicly available software, MultiNest (Feroz et al. [74, 75]), along with the Python wrapper PyMultiNest (Buchner et al. [34])

We note here, that for our analysis of cosmological parameter, we use uniform priors and define the Likelihood $L(\theta)$ simply as $\exp(-\chi^2/2)$. However, since the high-redshift SNe are not sufficient as standalone probes for time-variability, we need to combine constraints from the SNe with external priors, e.g. from the Cosmic Microwave Background. For this purpose, multiplying the defined likelihood in MultiNest is a useful method to get the combined constraints on the cosmological parameters.

A.1. Nested Sampling Algorithm

The final quantity of interest for model selection is the Bayesian Evidence, Z defined as

$$Z = \int L(\theta)\Pi(\theta)d^{N_d}\theta \tag{A.2}$$

where L is the likelihood of parameters θ, Π is the prior and N_d is the number of dimensions. We stress, here, however, that we are implementing this algorithm to evaluate the posterior distribution which is a by-product of the evidence

calculation. As the average likelihood over the prior, the evidence implements Occam's razor.

The nested sampling algorithm uses the relation between prior and likelihood to transform the multi-D integral A.2 to a 1-D integral

$$X(\lambda) = \int_{L(\theta)>\lambda} \Pi(\theta) d^{N_d}\theta \tag{A.3}$$

which is the integral of the prior mass within the region of the iso-likelihood contour $L(\theta) = \lambda$. The evidence then becomes

$$Z = \int_0^1 L(X) dX \tag{A.4}$$

where $L(X)$ is an ever decreasing monotonic function of X. Hence if $L(X_i)$ is evaluated at decreasing values $0 <\mathrm{X}_M <\ldots <\mathrm{X}_2 <\mathrm{X}_1 <\mathrm{X}_0 = 1$

$$Z = \sum_i L_i w_i \tag{A.5}$$

since the trapezoidal rule is used for approximation $w_i = \frac{1}{2}(X_{i-1} - X_{i+1})$.

A.1.1. Stopping Condition

Sampling the likelihood and calculating the evidence should be stopped when the evidence is calculated to a certain, pre-determined precision. However, this is not the most effective criterion in cases where there are narrow peaks near the maximum. Hence, the key question is how to do the summation in Equation A.5. For this purpose, N "active" (or "live") points are drawn from the full prior $\Pi(\theta)$ (often, as in the case presented here, this is uniform distribution over the prior range).

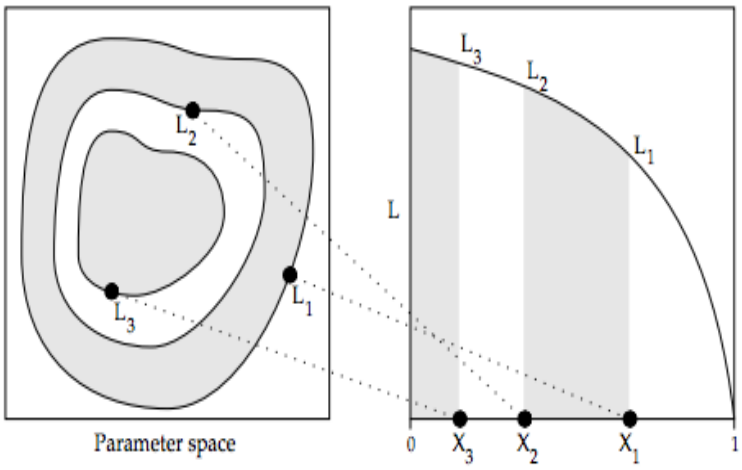

Figure A.1.: Nested likelihood contours are sorted to enclosed prior mass X. Credits: Skilling 2004 [276]

The initial prior volume $X_{i=0}$ is 1 (since its the full prior mass). N samples are sorted by their likelihood $L_n = P_n(D|\theta, H)$ and the lowest is discarded from the "active set" making is "inactive".

This point is replace by a point drawn from the prior subject to the constraint that its likelihood $L<L_0$ (which is the lowest likelihood value in the previous iteration, i.e. the likelihood of the now "inactive" point). The corresponding prior volume within this iso-likelihood contour will be a random variable $X_1 = t_1 X_0$ where t_1 follows the distribution

$$Pr(t) = Nt^{N-1} \tag{A.6}$$

i.e. the probability distribution for the largest of N samples drawn uniformly from the interval [0, 1].

For each subsequent iteration

1. L_i is the lowest likelihood which is discarded.
2. The prior volume reduced to $X_i = t_i X_{i-1}$

till the complete prior volume has been traversed.

The mean and standard deviation of logt, which dominates the exploration are

$$E[\log] = -\frac{1}{N} \tag{A.7}$$

i.e. as N $\rightarrow \infty$; E(log t) $\rightarrow 0$

$$\sigma(\log t) = \frac{1}{N} \tag{A.8}$$

similarly as N $\rightarrow \infty$; $\sigma(\log t) \rightarrow 0$

The algorithm for nested sampling is terminated when Z is evaluated with a pre-determined precision, which, for our estimation of cosmological parameters, is $\sigma(lnZ)$ of 0.5. For the ith iteration, the largest contribution that can be made by the remaining portion of the posterior is

$$\Delta Z_i = L_{max} X_i \tag{A.9}$$

where L_{max} is max$\{L(X_i)\}$

$$\Delta = \sum_{j=1}^{N} L_j w_{m+j} \tag{A.10}$$

Hence, the posterior inference is given by

$$P_j = \frac{L_j w_j}{Z} \tag{A.11}$$

where j = 1 $\rightarrow$ M+N, the total number of sampled points.

We note that the point at which the integration error for the evidence calculation is below the threshold, the samples for the posterior distribution have also converged, which is the quantity of interest for our analysis. For fine resolved samples in Chapter 7 we use 400 live points.

Acknowledgements

First and foremost I would like to thank my supervisor Dr. Bruno Leibundgut for his unending guidance and patience during the course of the PhD. I would like to thank Bruno for extremely helpful comments on paper and proposal drafts. I would also like to thank him for allowing me the freedom to pursue my own projects and build collaborations by myself. Moreover, amongst other things, I would like to thank Bruno for the trip to Australia at Mt. Stromlo Observatory, for introducing me to the first two seasons of *The Newsroom* and for showing me his observing logs from the MMT run in 1991.

I would like to thank my doktorvater Prof. Wolfgang Hillebrandt for his feedback and opinion at various stages of the project. I would also like to extend my gratitude to Jason Spyromilio for his help with Near Infrared spectroscopy, feedback on paper drafts, several long discussions in his office about ejecta mass calculations. I would like to thank Stephane Blondin for his help with the Nickel mass calculations, providing outputs from his models and encouraging emails during the postdoc application season. Thanks also to Nando Patat for discussions on spectropolarimetry of fast-declining SN Ia.

I would like to thank Bruno, Jason and Stephane for writing reference letters for postdoctoral positions, especially during the holiday period. I would also like to thank Ariel Goobar for offering me a postdoc position in his group at the Oskar Klein Center in Stockholm.

The data reduction described in Chapter 5 would not have been possible with the help of Stefan Taubenberger. Thanks to him for several important meetings to reduce the data and write follow-up proposals. I would also like to acknowledge my fellow mentors during the course of my time at ESO, Kate Maguire and Wolfgang Kerzendorf for their advice on data reduction, coding, jobs and for always being welcoming when I dropped by their offices. A big thank you to my office mates Bernd, Sarolta and now Annagrazia during the course of my PhD at ESO. Thanks to all friends at ESO who made for an exciting scientific environment to work. To Christine Schulz and Kate Pitchord for decorating my office with the most atypical collection of animal photos.

Thanks to the baristas at Lost Weekend on Schellingstrasse for fantastic Sunday morning filter coffees and for bearing with me when I swore softly at my computer screen.

Lastly, thanks to my family for supporting me throughout with my choices, being at the other end of long phone calls back home and just being wonderful people who have had the misfortune of having to deal with me.